THE UNIVERSITY *of* EDINBURGH

Assessment of MRI Scanner Performance for Preclinical Functional Studies

Gavin David Merrifield

B.Sc. (Hons) PgDip AMInstP

Doctor of Philosophy

University of Edinburgh

2014

Abstract of Thesis

Functional Magnetic Resonance Imaging (fMRI) based studies are rapidly expanding in the field of preclinical research. The majority of these studies use Echo Planar Imaging (EPI) to measure Blood Oxygenation Level Dependent (BOLD) signal contrasts in the brain. In such studies the magnitude and statistical significances of these contrasts are then related to brain function and cognition. It is assumed that any observed signal contrast is ultimately due to differences in biological state and that scanner performance is stable and repeatable between subjects and studies. However, due to confounding issues introduced by *in vivo* subjects, little work has been undertaken to test this basic assumption. As the BOLD signal contrasts generated in such experiments are often very low, even small changes in scanner performance may dominate the BOLD contrast, distorting any biological conclusions drawn.

A series of fMRI phantoms were produced to measure scanner performance independent of biological subjects. These phantoms produce specified signal contrast levels on demand during an fMRI scan by means of current-induced magnetic field gradients. These were used to generate data sets that emulated the BOLD signal contrast of *in vivo* imaging. Two studies examining scanner performance were then conducted on high-field preclinical MRI scanners. Firstly, in a longitudinal study on a single scanner, measurements were taken over a number of days across a week long period and then every two months over a year long period. Secondly, the behaviour of four preclinical scanners (three at 7T, one at 9.4T) was comparatively assessed. Measurements of several imaging parameters including contrast generated and functional contrast to noise ratio (fCNR) were obtained in both studies. If the scanners involved are truly comparable then they should generate similar measurement values.

Across both studies parameter measurements showed significant differences for identical contrast settings on the phantom. Although signal contrast itself proved very comparable across the studies fCNR proved to be highly variable. As well as these measurements of longer tem behaviour proving variable, short and mid-term signal stability displayed a wide range of variability. Variations in the level and quality of both signal and noise were observed. Modelling of signal changes based on fundamental physical principles was also performed for comparison.

The impact of these behaviours and variations on *in vivo* studies could result in skewed biological conclusions at any single site, with some sites exhibiting greater problems than others. The multisite results suggest potential difficulties when comparing biological conclusions between sites, even when using identical imaging parameters.

In summary, these results suggest that a cautious approach should be taken with the conclusions of both fMRI and associated resting state connectivity studies that use EPI as their acquisition sequence. Improvements to both the experimental design of studies and regular quality monitoring of scanners should be undertaken to minimise these effects. Clinical MRI scanners should also be assessed for similar aberrations in behaviour.

Declaration

I declare that:

i) The thesis that follows has been composed by myself as the student.

ii) That the body of work contained within is my own.

iii) That this body of work has not been submitted for any other degree or professional qualification except as specified.

Gavin D. Merrifield BSc. (Hons) PgDip AMInstP

Edinburgh

9th January 2014

To the Glory of God

Father,

Son,

Spirit.

Contents Page

Acknowledgements

At the end of a little over three years and three months of PhD related activity it is now time to sit down and rightly give thanks to all those who have been involved along the way. Any fevered imaginings of profound or immortal words of splendour that I entertained in anticipation of this moment have gone out of the window as another long night of tweaking the final version of my thesis (I have a PhD thesis?! Blimey...) has again consumed my time and energy. And with a promise of cake for all in the morning to celebrate (walnut and carrot cake for someone if the printer breaks in a few minutes time…) it is the moment to draw things to a close. There are many people to thank and mention so let's get to it.

Firstly I must thank my two primary PhD supervisors here in Edinburgh, Professor Ian Marshall and Dr Maurits Jansen. Not only have they both guided me through the last few years of this PhD project but also for a number of years beforehand. They introduced me to the world of MRI research and gave me the chance to become a professional scientist. I have always maintained that I although had earned science qualifications before coming to Edinburgh, it was working here - primarily with Ian and Maurits - that taught me how to actually 'do' science and how to be a working scientist. Although I am now moving on to other MRI projects elsewhere I look forward to opportunities to work with both again. Hopefully that I am staying in MRI can be taken as the compliment it is to their tutorage. Special recognition must also be noted for managing to keep me on the straight and narrow during the PhD, especially when there are so many other tantalizing… side projects… around…

My PhD project has been carried out through SINAPSE so a hearty tip of the hat also goes to my wider SINAPSE supervisors Professor Barry Condon and Dr William Holmes (both of the University of Glasgow). The project was also sponsored by Agilent Technologies so of course thanks must go to them for making it possible at all. Special thanks to my onsite contacts there Drs Michael Gyngell, Paul Kinchesh and Amy Herlihy.

Two other people who have worked away to support me in the background must, of course, be rightly mentioned. Firstly, Dr Carmel Moran who has been my PhD mentor and has provided a much needed watchful pair of eyes in general and been a centre of calm and support in periods of unanticipated stress. Many thanks for everything! And secondly, thanks to Mrs Irene Craig for various administrative and supportive assistance (and banter) over the

years of my time in Edinburgh. One of the big disappointments of finishing and leaving Edinburgh is the end of an era supported by these two wise and generous people.

Those who have performed the necessary practical evils that come with a PhD should also be thanked as it must normally be a fairly thankless task at points. So I would like to thank Professor Peter Hoskins and Dr Mark Bastin for their input via my PhD Committee over the earlier part of the PhD. I also thank my two thesis examiners for their willingness to assess this project – Professor Steve Williams (KCL) and Dr Michael 'Horrible' Thrippleton (Edinburgh). Hopefully you have both found this project of sufficient interest to warrant spending your valuable time on it.

One of the enjoyable aspects of this PhD has been the Multisite Study. This has been a great opportunity to not only get out and about and see some other preclinical MRI labs at work from a professional point of view, but also to get to know the people at those sites as well. Therefore I am especially grateful to Michael, Amy and Paul (Agilent/Oxford), William (Glasgow) Po-Wah So (KCL) and Jack Wells (UCL). Thanks to you all for opening your scanners up to testing by me. Hopefully we can all remember that the phantom doesn't make anything personal…

These visits would not have been possible without the generosity of friends in the area providing good company and a place to stay numerous times throughout the project. Thanks to Dr Hugh and Mrs Lesley Reynolds for a London home away from home. And Oxford thanks go to Dr Paul and Mrs Sarah Dodson. Thanks also to Naomi Dodson for reminding me that a five year old will always find the most public place possible in which to lambast you for not 'sleeping over' no matter how genuine your reason. I want make that mistake again in a hurry.

Undertaking a PhD is no small thing and it becomes extraordinarily consuming both in terms of time and physical/mental energy. The inclination is to shy away from friends in order to stay focussed and conserve energy. Of course that is pretty much the opposite of what you need to be doing so I want to thank a long list of friends who have given me space (when I have needed it), but who have also not let me vanish either. I will inevitably miss someone out by mistake (don't worry, there is always the next thesis…), but if you find your name here then know that I am very grateful for all your support and friendship other the last few years. In no particular order: Gregorio Naredo, Ross Lennen (Real Lemon), Michael Bennett, Ralph Burns (The Fool/Chumpanion), Andy Turnbull, Nick Davidson, Karl Thurgood (The Kaptain), Beth Wilson, Catherine Rose, an assortment of Andrews

(Thompson, Lister and Bretherick), Alex and Jen Scott, Anjie Fitch (don't drink from *that* cup!), Nichola Brydges, Anoop (Superboy) Shah, Laurie MacKay, Harry and Janet Braden, Lindsey Murray, Neville Cobbe, Dave Col(d)ridge, the Pullmans, Phil Holland, Lauren Thomas-Searle, Antonios Perperidis (thanks for the thesis beard inspiration!), Andreas Glatz, Duncan Giles and David Hamilton. Thanks also to those I have shared different offices with for chat and making things a bit more fun than they would otherwise have been – especially Nik Joshi, Shirjel Alam, Steve Morley, Amanda Hunter, Fiona Strachan. Adrian Thomson and Dave Hardman.

Special mentions must go to Mairead, Chris and Matthew Johnson whose unflinching support, especially over the last few months has been invaluable. Special thanks also to Professor Norman McDicken. Not so much for the regular verbal abuse or the constant drinking of my tea, but more so for those moments of encouragement over the years - however much it was a 'mistake' that they slipped out! Thanks also to Tom Anderson, the very definition of a 21st Century techno-mage with his various electronic wizardry skills.

A huge thank you must also go to my family for accepting my long periods of absence (especially over the last year) as I knuckled down a bit in order to get this project finished. I will however return to get the family cat back into shape and will be more than ready to finally beat my niece at that Hello Kitty memory game. Just watch.

Finally, I want to thank Professor Roy Sambles (Exeter). Roy not only gave me the chance to study physics as an undergraduate, but is also an old family friend from many moons ago who it turned out was the inspiration for my interest in science back when I was a nipper and too young to remember who he was at the time. He then lectured me on electrodynamics back in 2003 in my final year as an undergraduate. Something must have sunk in as it all came in very useful in my PhD. Full circle.

- Gavin Merrifield

Edinburgh, 9th January 2014

Abbreviations Used

$\|\Delta S\|$	=	Magnitude of the change in signal
P	=	Imaging Efficiency of one MRI sequence to another.
BOLD	=	Blood Oxygen Level Dependent
B_0	=	Primary magnetic field of the scanner
B_z	=	Magnetic field running parallel to the axis of the scanner bore
CAT	=	Coil Around Tube
CCCS	=	Computer Controlled Current Source
EPI	=	Echo Planar Imaging
EPIP	=	Echo Planar Imaging (Pulse/Paul/Prototype)
FA	=	Flip Angle
fCNR	=	Functional Contrast-to-Noise Ration
fCNRI	=	Functional Contrast-to-Noise Ratio per unit of applied current to phantom
FID	=	Free Induction Decay
FLASH	=	Fast Low Angle SHot Magnetic Resonance Imaging
FOV	=	Field of View
FSEMS	=	Fast Spin Echo Multislice
GE	=	Gradient Echo
GE3D	=	Gradient Echo 3D
GE-EPI	=	Gradient-Echo Echo Planar Imaging
HRF	=	Haemodynamic Response Function

KCL	=	King’s College London
NE	=	Number of Echoes
PEC	=	Pearson’s Correlation Coefficient
PRESS	=	Point REsolved SpectroScopy
QA	=	Quality Assurance
RF	=	Radio Frequency
ROI	=	Region of Interest
SNR	=	Signal-to-Noise Ratio
TE	=	Echo Time
TR	=	Relaxation time
UCL	=	University College London
VnmrJ	=	Agilent user interface software for scanners.
WIT	=	Wire in Tube

"… the absence of a signal should never be used as a signal."

Julian Bigelow, Jan. 1, 1947.

Interim Progress Report on the Physical Realization of an Electronic Computing Instrument.
Institute for Advanced Study, Princeton, N.J.

Chapter 1 Introduction to Preclinical fMRI

1.1 Imaging

1.1.1 Introducing Imaging

Modern medical health care services increasing rely on a range of non-invasive imaging techniques to diagnose injury or disease within the human body. Such imaging techniques been deployed across a diverse range of environments including the expected clinic and hospital environment, to more unusual venues such as major sporting events [Bethapudi 2013] and military combat centres [Jaffer 2012]. Basic portable systems for some modalities have even been placed on expeditions to low-Earth orbit onboard various human spaceflight missions and habitats where they form an important aspect of tele-medicine in such practically inaccessible environments [Sargsyan 2006, Hamilton 2011, 2012].

Today's techniques allow for the characterisation of most body tissue types dependent on the modality used. Imaging is also used to track the progression or remission of disease in order to evaluate the effectiveness of appropriate treatments by imaging the same subject across multiple sessions while undergoing therapy. As imaging techniques continue to advance they can only continue to find an increasing role in an expanding range of situations.

1.1.2 Small Animal Imaging

The same imaging techniques used for medical diagnosis can also be used as a research tool in the development of new biomedical therapies at the preclinical stage of treatment development. Additionally, they can also serve as a platform for further basic research into more fundamental biological processes such as basic neuroscience or organism level gene-expression.

Much of this research is performed in appropriate small animal models (typically rodents) rather than in human patient populations [Benveniste 2002]. This allows such processes to be studied in a more detailed and controllable manner than can be accomplished by passive surveying of a comparative human population. Experimental elucidation of mechanism and treatment also become viable research opportunities, whereas interventional studies in human populations are necessarily treated with a degree of higher ethical and moral caution.

Biologically there is great translational potential in comparative investigations between humans and rodents. However, the small size of such animal subjects can place challenging

requirements on imaging equipment necessitating the use of animal specific imaging scanners that have been optimised for such small subjects [Steward 2005, Schröder 2011].

The specifications and operating regimes of such scanners can bring both advantages and disadvantages when it comes to rodent-based preclinical studies. Translating the results from such studies back into the clinical environment may not always be as direct as might be first imagined. For example the high magnetic fields associated with small animal Magnetic Resonance Imaging (MRI) scanners compared to clinical MRI scanners (typically >4.7T vs. 1.5-3.0T) facilitates increases in image resolution and signal strength, but enhance other sources image artefacts that are less severe in clinical systems. The experimental settings used at one field strength are not necessarily directly transferable to other field strengths.

1.2 The Use of Animals in Scientific Experimentation

Although the use of animals in early stages of biomedical research is perhaps preferable to experimentation on human subjects, the use of animals in preclinical studies is not without serious ethical concerns and challenges of its own. If using animals in research that ethical concern must be kept in mind throughout in any study.

The matter of animal conscience and its associated implications for the use of animals in biomedical experimentation is rightly a matter of ongoing scientific, philosophical and theological debate. [Nagal 1974, Deanne-Drummond 2009]. However, there is currently broad agreement within the scientific community that unlike a handful of other animal species rodents lack a sufficiently developed level of sentience and an ability to engage in a significantly reflective way with the theory of mind and associated cognitive awareness to become voluntary participants in an experimental study. They are also subject to immediate experiences of pain and are capable of anxiety and suffering induced by experimental procedures that can negatively impact their longer-term mental wellbeing [Brydges 2012]. Any researcher using them is therefore under a robust ethical obligation to minimise such suffering to any animals used over the duration of an experiment.

Although this obligation may at times be an experimental limitation that could potentially frustrate a researcher, it also makes sound scientific sense. Since a distressed or suffering animal is unlikely to give the same response in an experiment as a relaxed and unstressed animal it is in the researchers own interests to ensure that their experimental animals are well treated and cared for.

In the United Kingdom (UK) all experiments involving animals are highly regulated by the Home Office via the *Animals (Scientific Procedures) Act 1986*. This act requires that every animal experiment performed in the UK is licenced at multiple levels and has a robust aim of gaining some significant scientific knowledge.

Ultimately studies must be conducted in such a way that minimises any suffering to the individual animal if it becomes necessary to use them. Study designs must be carefully considered so that a study can also be performed with the minimum number of animals while remaining statistically valid.

No matter where someone may sit on the spectrum of opinion about the use of animals in biomedical experiments, it is clear that properly conducted imaging studies have much to contribute towards Home Office priorities of experimental refinement, subject replacement and reduction of animals used in studies.

Most obviously non-invasive imaging is a much less traumatic experience for an animal than investigative surgery or an invasive biopsy would be. Additionally, the ability to non-invasively examine the same animal subject across multiple time points provides clear opportunity for reducing the total number of animals in an individual study. Without imaging to gather the equivalent data numerous animals would have to be sacrificed for every time point sampled. The quality of scientific data gathered is also increased in such re-examinations as each animal in a study can act as its own control. As the data from multiple time points now comes from the same individual animals each time, the data will have a greater internal consistency than if each individual time point was sampled from a multiple fresh groups of animals.

1.3 Magnetic Resonance Imaging

1.3.1 Introduction

MRI is an imaging technique developed in the second half of the 20th century, originally proposed as method for non-invasively quantifying pathology within a living body. The highly successful modern form of the technique, utilising magnetic field gradient spatial encoding, can be most strongly linked to research conducted by Paul Lauterbur and Peter Mansfield who developed the technique in the 1970s. This led to the clinical uptake of MRI in the early 1980s [Nobel Prize 2003]. The basic physical principles of MRI are relatively simple, being taught in many modern pre-undergraduate school courses, but MRI has

constantly been finding new applications and making advances far beyond its original ambitions.

Amongst the current range of imaging modalities MRI has rapidly risen in popularity, becoming the first choice of high quality imaging of the soft tissues of the body. As MRI relies on the water content of a subject to generate a signal from which the technique then constructs an image, MRI's imaging potential is only limited in areas of the body that are low in water content such as the bones or in air cavities like the lungs. As the technique continues to develop even these areas are beginning to be imaged through novel techniques such as ultrashort echo time imaging [Reichert 2005] and the use of hyper-polarised gases [van Beek 2004, Fain 2007].

1.3.2 Uses/Advantages/Disadvantages

MRI is highly attractive as an imaging modality for a number of reasons.

Patient Safety

The technique is non-invasive which insures a minimum of physical trauma to any subject being scanned. Unlike other imaging techniques such as Positron Emission Tomography (PET) or X-ray based Computed Tomography (CT), MRI involves no potentially damaging ionising radiation dose. This also allows for multiple MRI scans to be performed on the same subject in rapid succession if need be without concern about a cumulative radiation dose.

Image Acquisition Flexibility

Secondly, MRI is a very flexible imaging technique providing great freedom to generate different contrast parameters in order to preferentially highlight different tissues as required. This is simply achieved by changing the length and/or duration of the inputted radio pulses. These can be adjusted in quick succession allowing a wide variety of scans to be taken efficiently from a single patient in a single session. For example a succession of scans may highlight the grey then white matter of the brain in a single scan session. In other imaging modalities contrasts are either not so strong or readily achievable without the use of additional biochemical contrast agents.

Chemical Information

The MRI scanner is at heart a chemical spectrometer, using radio waves to characterise the local biological make-up of a subject. This allows for the acquisition of chemical data as well as image data. This information can reveal unique or complementary chemical data

about a scanned subject which is simply impossible to acquire using other imaging modalities.

Additionally many research level MRI scanners can also be tuned to detect signals from atomic nuclei other than the standard water-based signal. For example a scanner can be sensitised to phosphorus nuclei for monitoring cardiac energetics [Chacko 2000, Dobbins 2003] or to sodium for example to assess myocardial infarction [Jansen 2004]. While imaging can also be performed with these so called 'x-nuclei' the signal generated from them is typically much weaker than with standard MRI, so there is a current tendency to use them in chemical spectroscopic assessment of subjects in either global or image guided localised fashions.

Functional Imaging

By sequentially acquiring a sequence of repeated images across a single scan session and then analysing changes in the resultant series of images it is possible to quantify biological function as well as structure in a subject. These image changes can be related to function that may be either passive (as in resting state functional MRI [White 2011]) or induced through a variety of measures including chemical or environmental cues [Jackson 2011, Kida 2011, Brydges 2013] or through mental task based interaction [Pessoa 2002, Zheng 2010].

1.3.3 Scanner Hardware Configuration

MRI works by using a combination of static and switching magnetic fields, externally inputted radio energy and computational processing of the resultant radio signals from a subject.

An MRI scanner consists of essentially five systems:

- **Superconducting Electromagnet** – This is the most visible part of the MRI scanner. A cryogenically cooled superconducting electromagnetic produces a strong magnetic field in the bore of the scanner and in the surrounding vicinity. At the centre of the bore there is a region of relative magnetic homogeneity where subjects are positioned for imaging. For orientations in MRI typically the z-axis is described as running parallel to the central bore of the scanner. This large static field aligns the spin of the hydrogen atom based protons in the subject's water molecules into two 'population' states – spin up and spin down and causes this spins to precess around a central axis parallel to the scanner bore at the Larmor frequency (*f*), which then induces a matching radio frequency signal in the receiver coil of the MRI scanner

setup. This frequency has an associated energy with it (ΔE) which is the energy difference associated between the two quantised spin states (E_{UP} and E_{DOWN}) when the sample is present in the B_0 field.

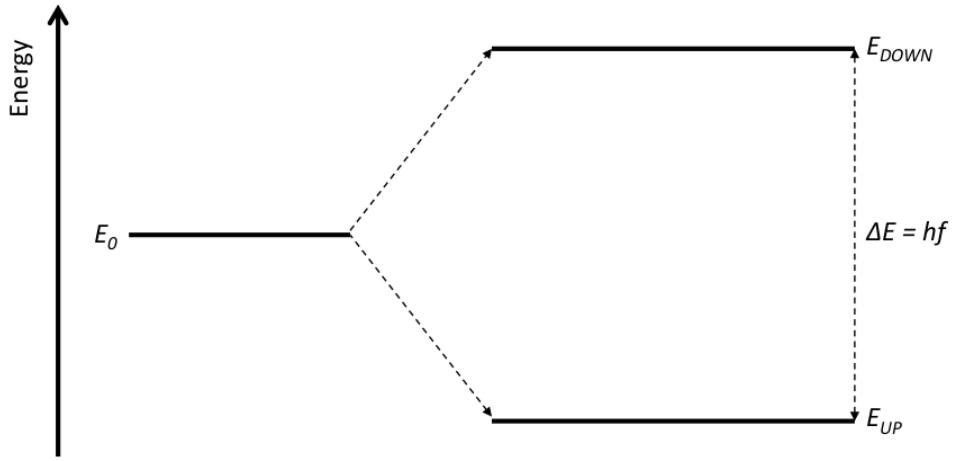

Fig. 1.1 *– When spins are exposed to an external magnetic field (B_0) they are aligned from an initial energy state (E_0) into two new quantised energy states (E_{DOWN} and E_{UP}). A small spin population difference between these two states generates a net signal with associated energy ΔE.*

- **Radio Transmitter** – This is used generate radiofrequency (RF) pulses which excite the aligned protons in the scanned subject. The RF pulses flip the spins of the protons from the z direction into a perpendicular x-y plane.. An aerial, known as a coil, emits the final RF pulses is positioned near the scan subject. The coil often takes the forms of wire loops placed over the surface of a subject or alternatively a 'cage' design that completely surrounds a subject.
- **Radio Receiver** – The flipped spins realign with the main static magnetic field. And as they do so, due to a small net imbalance in the two spin populations, a secondary RF signal is emitted from the spins. This signal is detected by another aerial (sometimes the same one as the transmitter but now in a 'receive' mode) and is used to reconstruct the MRI image.
- **Electromagnetic Field Gradients** – Typically located around the central bore of the scanner, surrounding both the subject and coil. These are used to encode three-dimensional spatial information onto the MRI signal.
- **Shim Gradients** – Another set of electromagnets, these are instead used to increase the homogeneity of the primary magnetic field by introducing corrective fields that

counteract inhomogeneity introduced by the presence of the scan subject themselves. This is necessary to optimise the imaging conditions to reduce potential artefacts inherent to the MRI process.

Fig. 1.2 *– The 7T Preclinical MRI Scanner at Edinburgh*

1.3.4 MRI Safety

Although MRI is a safe technique to use from a biological perspective there are safety precautions that must be adhered to as the scanner is a massively powerful magnet which introduces its own set of practical hazards. Primarily this is from the attractive nature of the scanner to metal objects turning them into potentially lethal missiles. The induction of motion-resisting eddy currents formed as metallic objects move within the magnetic field of the scanner also present a further non-intuitive danger that can often catch users and patience unaware..

There is also the potential for burns to be caused by the build up of heat originating from the high energy RF pulses being used in the scans. Additionally there is speculation that the rapid switching of the electromagnetic field gradients used in MRI may cause biological problems to regular scanner users. Although this has not been scientifically established, a precautionary principle is perhaps wise until it has definitely been proven otherwise.

These hazards can usually be eliminated with patient screening protocols in operation at all MRI laboratories and facilities. Anybody entering the vicinity of the scanner's magnetic influence (the fringe field) should be screened beforehand. A small subset of the population (those with some types of medical implants or embedded metallic debris) must be refused MRI scans as these objects cannot be removed from the subjects and the scanners will cause injury to an individual containing such objects.

1.3.5 Small Animal MRI

Using MRI on small animals comes with a unique set of requirements compared to regular clinical MRI.

- **Resolution** – Image voxels in human MRI are of the order of <1.0mm or more in plane and larger in terms of slice thickness even in higher field systems (i.e. 3T). In rodents it is typically 0.1 - 0.2 mm in plane with slice thicknesses of 0.5 – 1.0 mm to obtain a comparative anatomical resolution due to the smaller size of comparative physiological structures. This requires much stronger magnetic field gradients in order to encode spatial information onto the MRI signal. fMRI voxel resolution on both human and preclinical systems if usually much less – 0.40-50mm on preclinical systems.
- **Signal Strength** – With these smaller imaging voxels comes a drop in signal strength since signal is dependent on the volume of material being imaged. Sources of noise in the system however remain comparative, giving rodent MRI comparatively lower Signal-to-Noise values.
- **Higher Static Magnetic Field Strength** - Rodent MRI scanners operate at much higher field strengths in order to boost signal strength. This however can create problems with chemical shift artefacts as well as increasing the safety hazards of working with higher magnetic field strengths.
- **Field of View** – These higher field strengths and stronger gradients are difficult to achieve and maintain. Consequently the usable field of views of animal scanners are much smaller than those of clinical systems. The small size of the rodent helps to offset this, but suitably positioning rodent subjects can be a difficulty when the imaging target of interest is not externally obvious.

1.3.6 MRI Image Generation

At the basis of all MRI is the generation of radio signals emitted by excited water-based protons. This signal than has spatial information imposed upon it and the final total signal is then undergoes a Fourier transform in order to produce the final MRI image. MRI signals from different biochemical environments in a subject will create different MRI signals. By careful adjustment of MRI acquisition parameters different *image contrasts* can be created that can emphasise different structures or functionality in the subject as desired by a researcher.

1.3.6.1 Generation of the MR Signal

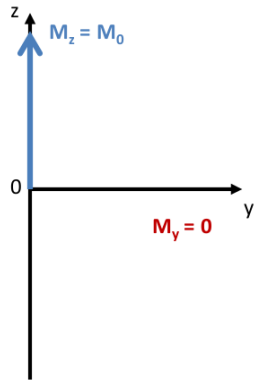	When placed within the magnetic environment of an MRI scanner a collection of water molecules with a net magnetisation in the z-direction (M_z) possess an initial magnetisation value (M_0) due to the primary scanner magnetic field B_0 (running parallel to the z-axis). Initially: $M_z = M_{Total} = M_0$. (Eq. 1.1) At this point the magnetisation in the orthogonal plane (M_{xy}) is zero.
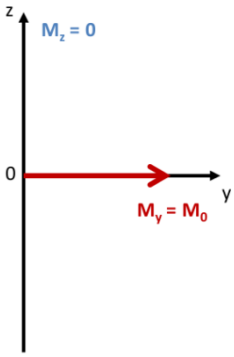	A pulse of radiofrequency (RF) energy is inputted into the system. This pulse is associated with a secondary time-varying magnetic field, B_1. This field flips M_z into the xy-plane by an amount according to: $\theta = \gamma B_1 t_p$ (Eq. 1.2) [Gadian 1985] θ = The Flip angle formed as Mz is tilted into the M_{xy} plane by the B_1 radio pulse. γ = Gyromagnetic Ratio. t_p = time the B_1 pulse is active. In the case of the figure to the left this is 90° so that M_z is completely flipped into the xy plane along the y-axis.

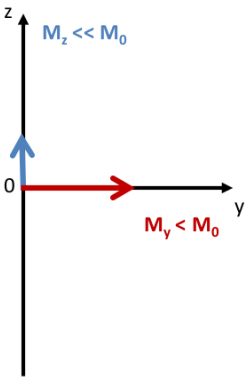	At the end of the pulse the value of M_y begins to decay away according to: $$M_y = M_0 e^{-t/T_2}$$ (Eq 1.3) Simultaneously the value of M_z begins to recover according to: $$M_z = M_0 \left(1 - e^{-\frac{t}{T_1}}\right)$$ (Eq. 1.4) The rate at which M_z recovers and M_y decays are controlled by values known as the T_1 and T_2 rates.
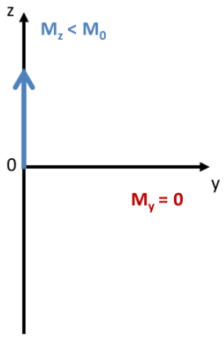	My decays at a faster rate than M_z recovers, so eventually $M_y = 0$ while M_z is still $<M_0$.
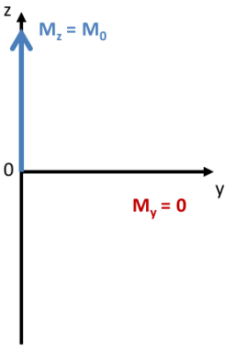	Eventually both M_y and M_z both return to the original pre-B_1 pulse magnetisation states.

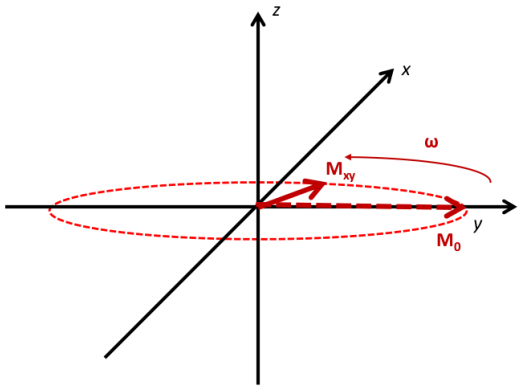

During these decay processes the net magnetisation vector M_z precesses around the z-axis with a frequency (ω_0) given by to the Larmor Equation:

$$\omega_0 = \gamma B_0 \text{ (Eq. 1.5)}$$

This precession of charge generates radio waves whose frequency (and so associated energy) is tied to the rate of procession. The radio signal detected must then undergo a Fourier transform in order to be turned into a useful imaging signal.

For simplicity discussions about the physics of signal generation of MRI are often held in the 'rotating frame' which is a frame of reference that precesses around the z-axis at the Lamor frequency, ω_0. This returns the equations to simpler one dimensional exponential decay equations as before.

The signal from a collection of spins experiencing no additional gradient or relaxation effects and with spin density $\rho(\boldsymbol{r})$, at a time t and from a volume $d\boldsymbol{r}$ can detected can be calculated via:

$$S(t) = \iiint \rho(\boldsymbol{r})\, e^{[-i\omega_0 t]} d\boldsymbol{r} \qquad \text{Eq.1.6}$$

1.3.6.2 Creating Contrast

The excited water protons will relax at fixed rates that are dependent on the molecular bimolecular environment in which they are located. Water molecules that are found in blood will relax at a faster rate compared to those in fatty tissues for example. The different relaxation rates produce different signal intensities and across the full recovery time produce different contrasts between the different substances (Figure. 1.3). By selectively choosing different sampling times different contrasts can be selected and emphasised in the resultant MRI images.

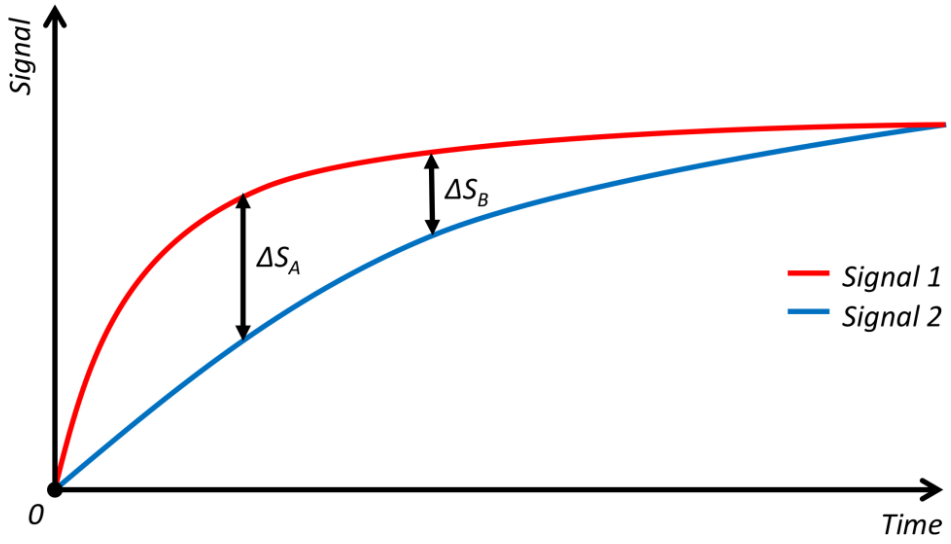

Fig. 1.3 *– Signals are generated by the relaxing spin states of protons. Differ relaxation rates for different biological materials allow for contrasts (ΔS) to be created between different materials. By signal sampling at different time points different value of ΔS can be created. In this example* $\Delta S_A > \Delta S_B$.

1.3.6.3 MRI Pulse Sequences

Magnetic field gradients can affect the final MRI signal in a number of ways. If uncorrected for their effect is to reduce the net signal from the excited proton spin states. In the presence of a magnetic field gradient the signal from the excited spins will begin to shift out of phase with one another depending on their physical position in the scanner. This is a process known as signal dephasing.

Magnetic field gradients are deliberately applied to the spin system to encode spatial information onto the signal, allowing images to be constructed from the signal information. They also occur by virtue of distortions in the linearity of the primary magnetic field (B_0) field caused by the physical presence of the subject being scanned. Subject-induced magnetic inhomogeneities in the primary magnetic field are corrected for using electromagnet 'shim' gradients. Orthogonal sets of these gradients are used to generate a three dimensional magnetic field that to a large extent restores the homogeneity of the primary field.

1.3.6.4 Signal Spatial Encoding

Without the addition of spatial encoding to the MRI signal all we will collect will be global chemically-environmentally modulated spectroscopic signal data from the subject. Signal must be localised to a specific spatial region so that an array of signal can be created. This

array is in the form of frequency information within a mathematical space known as k-space. This array undergoes a Fourier transformation resulting in the final MRI image. Localisation for this array must occur in all three spatial dimensions.

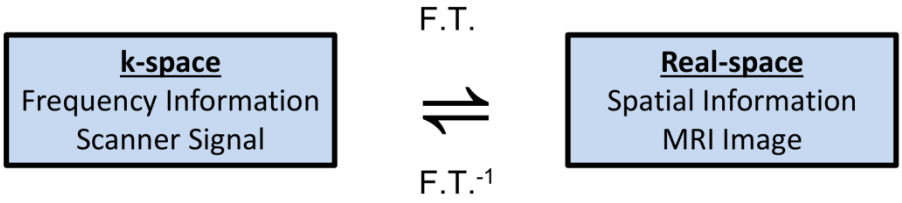

Fig. 1.4 *– Conversion of received MRI signal to displayed MRI image via mathematical Fourier transform.*

Spatial position is encoded using sequences of magnetic field gradients in to alter the local magnetic environment around the subject. This alters the resonant frequency ω_0 needed to create a signal in a position dependent manner. For a magnetic field gradient $\boldsymbol{G}$:

$$\omega(\boldsymbol{r}) = \gamma \boldsymbol{B_0} + \gamma \boldsymbol{G} \cdot \boldsymbol{r} \qquad \textbf{(}\text{Eq. 1.7}\textbf{)} \qquad \text{[Callaghan 2006a]}$$

For a particular resonant frequency this results in a change in signal according to:

$$S(t) = \iiint \rho(\boldsymbol{r})\, e^{[i\gamma \boldsymbol{G} \cdot \boldsymbol{r} t]} d\boldsymbol{r} \qquad \text{(Eq. 1.8)} \qquad \text{[Callaghan 2006b]}$$

Slice Selection Gradient (G_z)

Selecting a slice in the z-plane is achieved by applying a magnetic field gradient, G_z, along the z-axis of the scanner. This alters the resonant frequency of spins along this axis in a predictable way so that by transmitting the initial RF pulse at particular range of frequencies then only spins with a matching frequency (and so location) will be excited. To select a different slice an RF pulse with a different resonate frequency is used.

Phase Encoding Gradient (G_y)

k_y encoding is performed with a second magnetic field gradient pulse, but this time the gradient introduces a position dependent predictable phase modulation to the signal. When the pulse is turned off this phase change remains 'frozen' into the underlying signal allowing localisation allowing the position to be 'read off'.

Frequency Encoding Gradient (G_x)

The remaining k_x axis is selected for by simply applying a constant magnetic field gradient immediately after phase encoding, perpendicular to both slice selection and phase encoding gradients over the entire signal acquisition period. When this signal undergoes a Fourier transform to turn it into image data the result is a one dimensional projection of the sample.

By using combinations of these three encoding techniques to raster through all points in k-space the signal can be sampled at all points and then reconstructed in an image array made up out of three-dimensional voxels.

The combination of RF pulse followed by the x, y and z encoding gradients is known as an MRI pulse sequence. A Gradient Echo pulse sequence is often shown as in Fig. 1.5 below.

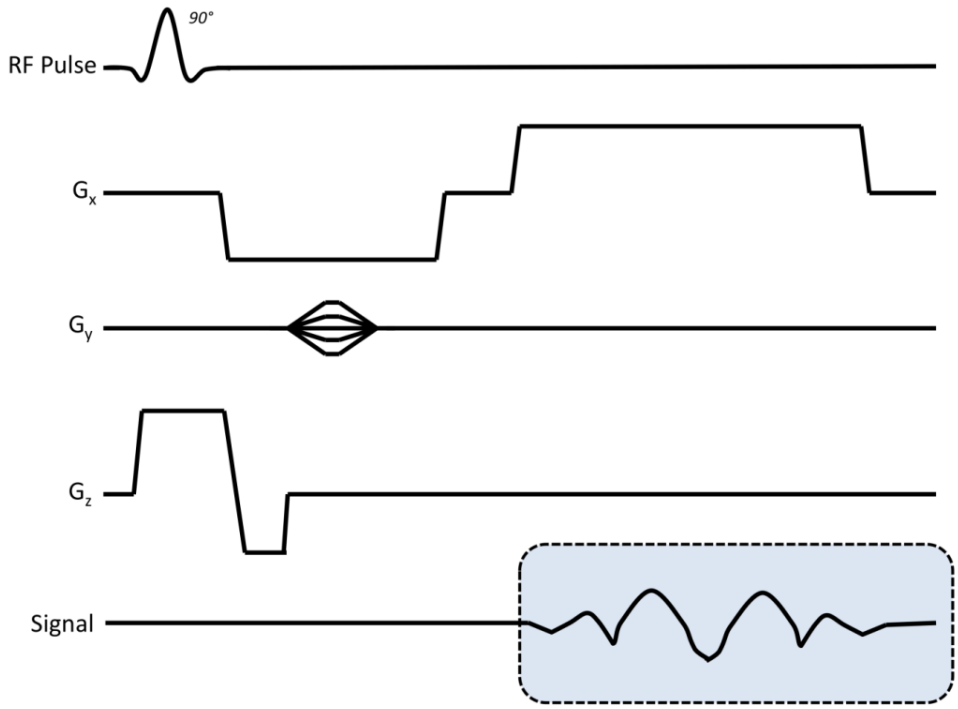

Fig. 1.5 *– A Gradient Echo MRI pule sequence. Signal acquisition occurs in the shaded box region. This sequence reads out one line of k_y in the k-space array. The sequence is repeated to fill the array, adjusting the phase encode gradient each time.*

A two dimensional Fourier transform is then performed on the final k-space array which resultants in a magnitude image composed of data from both real and imaginary parts of the signal such that:

$$Magnitude = (Real^2 + Imaginary^2)^{\frac{1}{2}} \qquad \text{(Eq. 1.9)}$$

1.3.6.5 Image Noise and Artefacts

A significant limitation on MRI signals are sources of noise or artefacts that result in unwanted background signal and/or distortions to the images. Artefacts can arise for a number of reasons and are often pulse sequence specific. Noise can come from either the subject in the form of physiological noise (e.g. movement or internal fluid flow), or from background process and physical phenomena associated with the scanner operation (e.g. electronic and thermal noise present in the system).

Any signal received is always a combination of both the MRI derived signal and the various sources of noise that act to distort or mask that signal. Rather than just measuring absolute signal strength, what is often more important is the Signal-to-Noise ratio (SNR). This gives an important measure for how significant the signal is compared to the latent noise of the total system. In functional MRI studies this becomes particularly important in fMRI experimental reporting.

1.4 Functional MRI (fMRI)

1.4.1 Introduction

fMRI involves the repeated imaging of the same subject in a single scan session. Subsequent computational analysis of the resultant volumes of images, on a voxel by voxel basis, is used to measure and map functional activity in the subject being scanned. These parameters are then related to biological function in order to search for biologically relevant patterns or abnormalities.

Often short-term changes in biological function are stimulated artificially either through the introduction of a chemical contrast agent (as in perfusion MRI [Petersen 2006] or cell tracking [Ahrens 2013] or through temporary alteration of the subject's MRI properties (such as in Arterial Spin Labelling [Petersen 2006]). Other ways of tracking more complex function such as in neuroscience or cognition involve the interactive presentation of stimuli to induce temporary physiological changes which are then measured and correlated with underlying neural and cognitive function [Kannurpatti 2003, Xu 2010, 2012]. Resting state fMRI has also become a popular area of research in recent years [Biswal 1995, De Martino 2011], where no stimulation is provided, but fMRI scans of the brain are processed using multidimensional correlation analysis techniques to reveal underlying background neurological networks at work in the brain.

fMRI studies of the human brain have found widespread use in a range of neuroscience applications and have been conducted now for over twenty years, beginning in 1991 [Belliveau 1991]. In humans they are commonly used to study a wide range of cognitive functions primarily through task based approaches [Fu 2008, Axmacher 2009, Horikawa 2013] or to correlate such cognition effects with underlying structural data and to monitor cognitive health and decline [Mitterschiffthaler 2006, Hampel 2011, Dichter 2012, Ray 2012]. At a more basic level fMRI is used to study somewhat more passive brain activity in either neutral or stressed environmental conditions [Xu F 2010, Min DK 2011, Loggia 2012].

1.4.2 Small Animal fMRI

fMRI techniques have been widely applied in animal studies [Lowe 2007, Guilfoyle 2013]. Due to ethical and legal constraints the majority of these studies are typically done with the animal under anaesthesia. The use of conscious animal fMRI is however beginning to become more common as problems with degraded image quality (primarily due to rodent movement when conscious) and animal welfare (the loud, dark and unfamiliar environment of an MRI scanner easily stress rodents) are beginning to be overcome [Peetersa 2001, Ferris 2006]. Even when using conscious animals as subjects the vast majority of presented tasks to date have been purely responsive. It is only very recently that learnt responses have been practically demonstrated within fMRI studies [Brydges 2013].

Conscious animal imaging also avoids need for and subsequent undesirable effects on brain biochemistry associated with the use of anaesthesia agents. This also permits task-based challenges rather than just monitoring passive responses. Preparing animals for conscious imaging however does depend on a detailed acclimatisation and training regime adding complication to a study. Currently there is no standard protocol for this in use across MRI sites globally. Often what is used depends heavily on local animal experimentation restrictions which can vary quite considerably across countries.

1.4.3 fMRI Signal Response

The fMRI signal time course extracted from an individual imaging voxel is the sum of three individual components.

- **The Stimulus Function** – This is the pattern of stimulus inputted into the system. In many fMRI experiments it is a simple box car function.

- **The Response Function** – This is a characteristic response of the biological material in question to the presented stimulus, driven by underlying biological mechanisms. The two main possible mechanisms in the brain are those of the haemodynamic response function (HRF) and the possibility of neural action potentials. These further discussed in section 1.4.3.1 and 1.4.3.2.

- **Noise** – All fMRI studies experience noise in the signal as an unavoidable consequence of the nature of both subject and equipment.

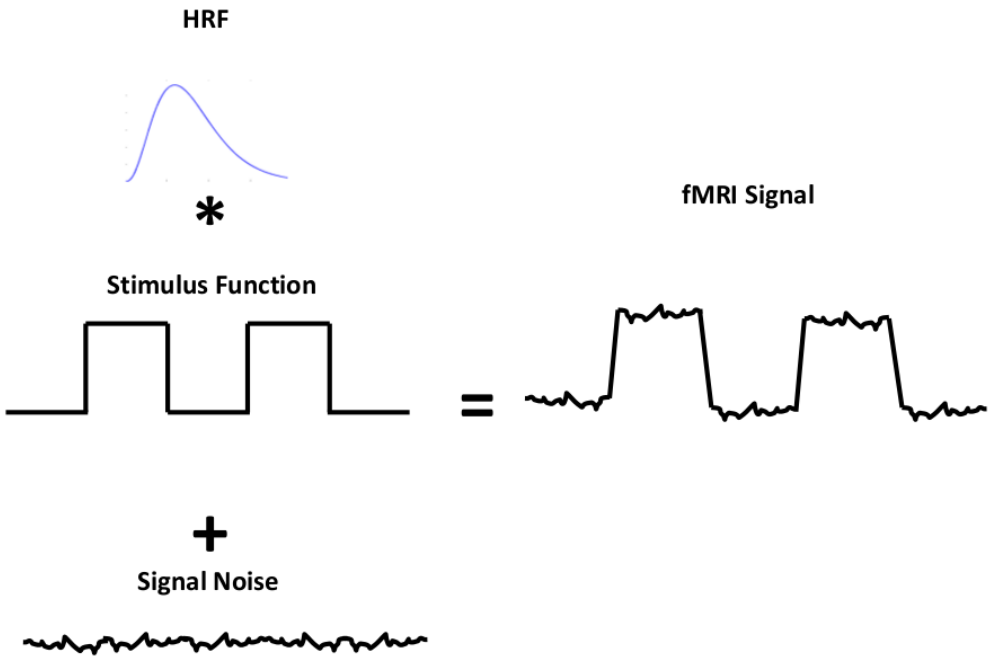

Fig. 1.6 *– Breakdown of components of final received fMRI signal.*

Statistical analysis using a General Linear Model is performed on this combined response to extract neurologically relevant measures. In broad terms however the signal at rest is compared to the maximum stimulated signal. Experimental designs are optimised to ensure good measures of both of these signals are obtained for analysis.

1.4.3.1 Response - BOLD fMRI

The most popular method of fMRI studies *in vivo* is to study the contrast generated by oxygenated and deoxygenated blood in the brain. This is known as Blood Oxygenation Level Dependent (BOLD) fMRI. The BOLD signal is relatively accessible to fMRI studies and the underlying biology behind the effect is now considered to be well understood [Fox 2012]. BOLD signal changes occur because of a contrast in signal between oxygenated and deoxygenated forms of the oxygen-carrying molecule haemoglobin contained within the

blood. Differing ratios of these two forms of haemoglobin will give rise to different MRI signals.

The major assumption used in BOLD neural fMRI is that changes in haemoglobin ratios are caused by the activity of the underlying neuronal tissue. This activity causes a change in the accompanying vasculature and hence the MRI signal. This vascular change gives a characteristic response curve to a momentary stimulus known as the Haemodynamic Response Function (HRF) which is illustrated in Fig. 1.7.

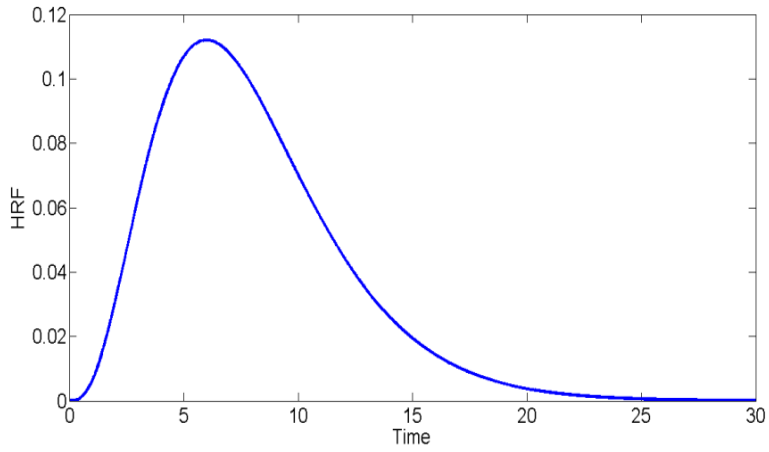

Fig. 1.7 *– Theoretical pure HRF.*

At time = 0 stimulus is presented. Initially there is no HRF response (Signal = 0 = S_A). After a delay (typically 2-3 seconds *in vivo*) the HRF starts to rise. Signal peaks and then plateaus at a higher level than original signal amount (Signal = Maximum = S_B). The stimulus is ceased (time = 50 in Fig. 1.8 below), but it takes a few seconds for the HRF to respond and start to decay back to S_A.

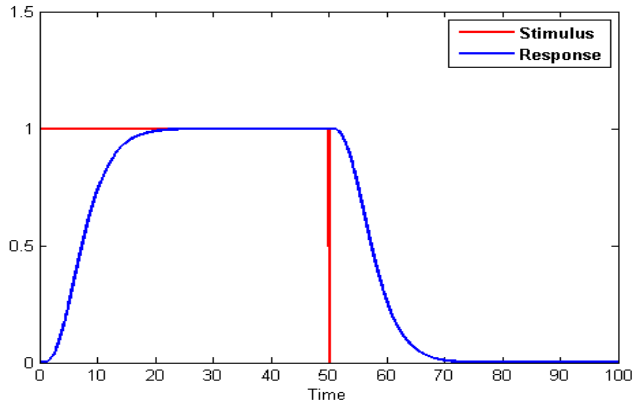

Fig. 1.8 *– Theoretical convolved HRF with driving stimulus of duration 50.*

Analysing the exact response of the HRF to stimuli is usually through General Linear Modelling – a process well described in numerous fMRI related textbooks. [Lazar 2008, Ashby 2011].

Although BOLD-based fMRI presents a readily detectable and well characterised response function that has proven invaluable in fMRI studies, it must always be born in mind that it is not a direct measure of neuronal response. Rather it is a collective after effect of the underlying biochemistry at work in the operation of the brain. The response duration of the effect is also much greater than the firing time of the corresponding neuronal action potentials. This temporal resolution limitation is another factor to consider when asking what is practically achievable using fMRI BOLD techniques.

1.4.3.2 Response - Neurological Action Potentials

Ideally an fMRI experiment would be able to directly detect brain activity due to changes in action potentials as functional relevant collections of neurons fire rather than the BOLD effect. The collective change in neural magnetic field which would cause a signal change however is very low, typically quoted as 10^{-9} – 10^{-10}T [Bodurka 2002]. This is typically reported as resulting in MRI signal changes on the order of fractions of a per cent at temporal resolutions useful enough to replace BOLD-based fMRI techniques [Xiong 2003, Sekino 2009]. These requirements are somewhat challenging even for the most advanced and sensitive MRI scanners to successfully meet.

MRI scan protocols must be working at their current limits in order to stand any chance of detecting such fleeting signal changes. Additionally in vertebrates the oxygenation and deoxygenation of haemoglobin, produces a much larger signal change over a longer time period. This swamps out the weaker action potential signal.

In animal studies there are also additional challenges to overcome even if reliable direct neural detection was demonstrated in humans. Higher resolution requirements and correspondingly smaller voxel sizes used in animal experiments mean that there would be a lower signal level compared to humans due to there being a smaller physical volume of material within the voxel to generate a detectable signal with. The signal would be further reduced due to the lower density of neurons and interconnections in the rodent brain further lowering the potential to generate a BOLD signal contrast.

Despite these limitations there have been numerous attempts to measure this source of contrast in humans, animals and *ex vivo* stimulation of animal parts [Park 2006, Huang 2013, Jiang 2013]. This have all met meeting with differing amounts of success with some

claiming positive evidence and others negative for the effect. Often the results are heavily processed and result in non-initiative measurement parameters making their practical utility uncertain.

Perhaps the most convincing results have been in artificially stimulated ex vivo sections of invertebrate neural tissue. By using this source material experimenters gain total causal control over the system being investigated, but also by using invertebrate tissue they avoid any BOLD confound. Hemocyanin which is a copper-based invertebrate equivalent of iron-based haemoglobin, doesn't produce a signal contrast between its oxy- and deoxy- states [Rawlinson 1941], suggesting there would be no BOLD-equivalent contrast effect to swamp out the direct neuronal signal in invertebrates. While clearly not a realistic experimental set up such examples do at least demonstrate the possibility for direct detection of neural derived signal changes with MRI. However, even in this area of work examples can still be found producing negative results, so even this selected system of investigation is not yet a wholly reliable route [Xia Jiang 2013].

1.4.4 fMRI Signal Analysis

There are various measurements used to report fMRI results in the literature. Often only a single one of these measurements will be reported since an individual paper is more often concerned with its own internal changes between conditions or subject group. Additionally, a wide variety of software packages and associated plugins are in widespread use throughout the fMRI community. Two of the leading packages are SPM [Friston 2007, Ashburner 2012] and FSL [Jenkinson 2012]. This gives rise to a diverse range of reporting styles and variable image analysis techniques and focus within the fMRI community.

fMRI analysis includes many preprocessing steps designed to control for many structural differences between animals as well as motion differences between subjects. These refined data sets are also typically mapped to existing structural data that has been pre-created from other groups of matching subjects. This allows fMRI data sets to be standardised in terms of its structural nature, leaving any remaining significantly changed signals from individual voxels to be accounted purely from functional-related events.

Maps of significantly activated brain regions are often graphically overlaid onto structural images to facilitate the identification of brain regions in which activations are occurring as in Fig. 1.9.

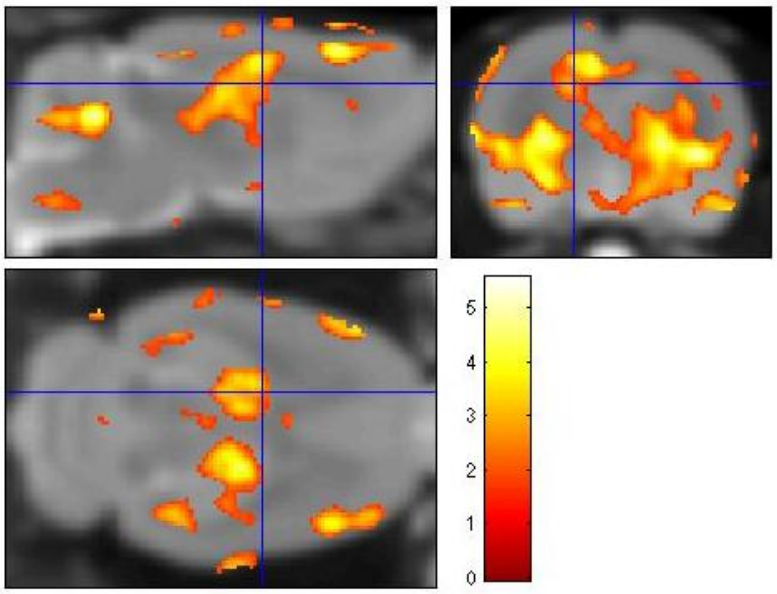

Fig. 1.9 *– Activated brain regions (orange) in response to a hypercapnic challenge in a single rat brain overlaid on a greyscale structural image of the same animal (scale is the t-statistic for a ON>OFF contrast).*

Experimental measures that are often obtained from functional images include:

- **Change in Signal (ΔS)** – This is given as a percentage change, representing the amount of signal difference observed between the activated and non-activated brain states.
- **Noise** – This is the background signal level that is a composite of a number of different sources. These include inherent imperfections in the construction and set up of the scanner hardware. Another noise component is caused by the inherent and unavoidable noise properties associated with the operation of electronic circuits.
- **Signal-to-Noise Ratio (SNR)** – This is the mean signal divided by the background level of signal and gives a measure of whether a significant signal can be detected against the natural variation in the signal noise.
- **Functional Contrast-to-Noise Ratio (fCNR)** – This is the difference between two signal levels divided by the background level of that signal and gives a measure of whether a significant signal change in signal between two activations can be discriminated against the underlying variation in the signal noise.
- **Cluster Size** – This is often used as a measure of the significance of an activation i.e. the larger the clusters the higher the probability that voxels in a localised area are 'activated' by the stimulus and so the stronger the effect is.

Trends in both noise and signal are also often investigated to authenticate the reliability of the above measures across the duration of an experiment.

1.4.5 Echo Planar Imaging

Although many pulses sequences can be used for BOLD fMRI not all of them are capable of the temporal resolution demanded by the neurophysiology at work in fMRI experiments. For this reason a rapid acquisition pulse sequence known as Echo Planar Imaging (EPI) is often used [Mansfield 1977, Ordidge 1999] which is sensitive to T2* contrast effects..

A major advantage of using EPI-based imaging techniques over other sequences is the incredible speed that EPI can gather a set of data from the whole brain. Typically with non-EPI methods a single slice can take- at sufficient quality - seconds to acquire as the sequence works its way through all lines of k-space, one RF excitation at a time. To get good T2* contrast and to cover a whole brain in this manner can take several seconds, often limiting the amount of brain coverage acquired by non-EPI sequences. EPI by contrast is fast enough to acquire data with whole brain coverage in a single RF excitation. Only 2-3 seconds is typical of the time needed to acquire a volume of fMRI data using EPI.

EPI achieves this by sampling the signal for all phase and frequency encode values from a single RF pulse as shown in Fig. 1.10:

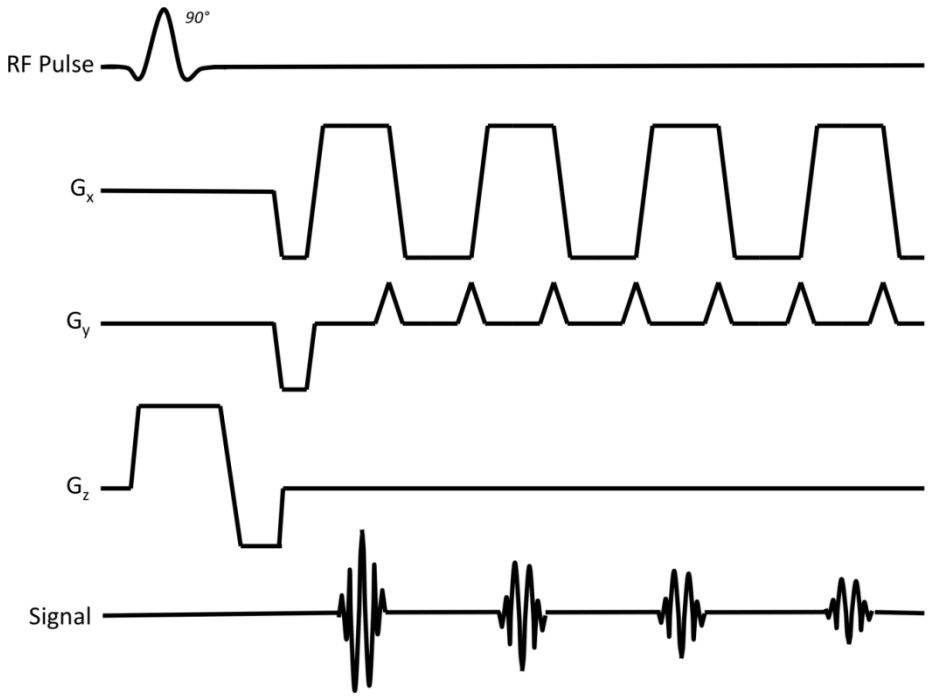

Fig. 1.10 *– 'Blipped' Gradient Echo EPI Sequence.*

As with any animal MRI imaging there are particular challenges involved with rodent EPI fMRI. With EPI however many of the standard challenges are enhanced. In particular the requirement to have large gradient strengths sufficient for animal-resolution imaging is increased further by the need of EPI in general to have both high gradient strength and the ability to rapidly switch between different gradient values. The technical ability to do this has been the main limitation in the deployment of EPI techniques in animal imaging.

1.5 Discussion

1.5.1 fMRI Quality Assurance

Although there is an extensive literature of examining the variability of various fMRI processing methodologies alongside *in vivo* intra- and inter-scan repeatability [Friedman 2006, 2008, Gradin 2010, McGonigle 2012] and potential effects of physiological noise on that variability [Bianciardi 2009, Hutton 2011, Iacovella 2011] there has been little work performed that examines the physical performance of the MRI scanner itself separate to *in vivo* subjects in relation to the unique measurements of fMRI studies. This would seem to be particularly important as minor fluctuations in either signal or noise levels could lead to activation-like false positives in results that could be incorrectly attributed to the subject's neurophysiology.

In other areas of imaging research efforts to ensure scanner quality and performance has become a small industry in itself and MRI is no exception to this. Most of these quality assurance (QA) measures have focused on assessing basic signal stability or structural properties with little work attention paid to measures of particular relevance to functional imaging. There has been an assumption that existing QA examinations double up and provide reassurance for fMRI investigations.

Existing QA tests are in a large part performed by scanning static samples known as phantoms. This has the immediate advantage of eliminating biological noise and variability from the system. Any remaining variations are then due to scanner performance. While this neatly removes the effects of biological noise it leaves only a static signal to analyse whereas fMRI is concerned with changes in signal.

1.5.2 The Need for an fMRI specific QA Phantom

fMRI uses several parameters that the results of existing QA tests are either not routinely examined for or are incapable of detecting – e.g. the stability of rapid switching between various signal states. Additionally the statistical nature of MRI results often means that they

are reported in study-specific relative terms or probabilities without reference to any universally validated standard.

To test the whether fluctuations in the remaining equipment noise are a problem for *in vivo* fMRI experiments an appropriate QA phantom must replicate the ability to change signal that the is observed in fMRI scans. Ideally the signal changes should be tuneable over a range of appropriate signal changes that are comparable to what would be expected *in vivo*. These remaining changes in signal must also be above signal changes due to background fluctuations in the noise of the system to show a meaningful and statistically valid signal change that can be used to assess scanner performance.

As well as assessing absolute signal changes such a device should also be capable of providing measures of SNR and fCNR so that the statistical significance of fMRI results can be judged.

Ideally the fMRI phantom should be deployable across a number of MRI sites in order to check for consistency of fMRI measures across those sites.

1.5.3 Applications of an fMRI Phantom

Different designs of phantom devices are a widespread tool for instrument calibration, monitoring and development. In MRI such phantoms are usually static objects whose properties are stable and emulate those found within a typical scanner subject.

Phantoms also enable the development of new sequences without the use of in vivo subjects and the accompanying complications of biological based sources of noise associated with them. In preclinical scanners where animal subjects are used this avoids unnecessary procedures from being carried out on animal subjects. Regular QA checks with phantoms also benefit animal welfare by helping to ensure that that scanners are operating at peak performance for when animals are used. This protects and safeguards animals used in scientific research in line with national and international ethical guidelines.

Phantoms are also ideal for calibrating experimental studies between multiple MRI sites. This allows for comparative performance to be judged, potentially allowing the distributing of imaging workloads across sites. This has a duel benefit of sharing the experimental load and also minimising any site or user specific bias in large studies.

A static phantom is only of limited use when monitoring the performance of fMRI related scans. Instead to provide insight and monitoring into the fMRI performance of a scanner a phantom capable of adopting a number of signal states and switching between them is

necessary. Such a phantom could also be used to optimise signal stability spatial and temporal resolution and potential pick up effects from equipment degradation that would be unobservable in a static phantom.

Such a device would also allow the exploration of signal sensitivity limits to be placed on an individual scanner or pulse sequence. As well as being useful for monitoring stability over time this would also help inform the design stage of an fMRI experimental study allowing more accurate estimations of subject group sizes based on known limits of signal change detectability. Together this could lead to improved experimental set ups for MRI systems and verified study designs and protocols well before the use of any animal subjects in such systems. This has the potential to lead to a more realistic judgement of the number of animals used in a study and improved confidence in the scientific output from those subjects that are scanned.

In the MRI-extreme environment of preclinical MRI the continual need for monitoring the stability of MRI scanners used for fMRI studies combined with the obvious benefits to animal subjects provides good justification for the development of fMRI specific phantoms.

1.5.4 fMRI Phantoms Overview

To date there have only been a limited number of studies in the literature concerning phantoms that might be described as 'functional' rather than static. Past studies have also all been performed on clinical scanners operating at lower values of B_0 in the range of 1.5-3.0T, far below those utilised in preclinical MRI scanners.

Designs tend to be split between static designs and designs that incorporate some form of active signal switching.

- Static designs tend to consist of an array of elements where each element has a slightly different MR property due to differences in the material compositions of the medium occupying each element. Relative image contrasts are generated by comparing different elements of the array to one another [Olsrud 2008].
- Switching designs involve the ability to alter the MR properties of a region of the phantom. Typically this is accomplished either through mechanically switching a volume of a specific medium for one of another or through the use of magnetic fields to alter the properties of the medium already present [Cheng 2006, Renvall 2006, 2009a, 2009b, 2010].

Static/Chemical

Systems with static components are not truly comparable. No matter how well shimmed the systems is two different regions of the phantom will occupy two different spatial regions of the scanner field which will have non-identical magnetic field properties. This will result in changes in the MR signal from these differing regions not solely attributable to the differing MR properties of the different materials involved.

Mechanical

Mechanical switching of voxel content (i.e. the physical rearrangement of elements of a static array) has an advantage in that the individual elements can be easily loaded with different materials as desired. Measurements are conducted in the same region of the scanner field and so should experience closely matching field properties. However a mechanical fMRI based phantom with moving parts would need robust construction and material choice to work in the high magnetic field environment of a preclinical MRI scanner. Potentially these devices could also break down during a scan. Long term reliability of precise switching would also be difficult to maintain over time as components wore out or degraded through regular use.

Electromagnetic

Designs that utilise electromagnetic switching to create signal changes via phase alteration of a signal within a voxel offer many advantages. The construction of such designs can also be greatly simplified compared due to a lack of moving parts. In addition contrasts can be changed *in situ* by precise externally applied magnetic fields rather than by creating a series of chemically different substances that may vary over time. The electrical currents that create the applied magnetic fields and their associated signal effects can also be predicted in theory from first principles.

Some phase inducing designs that have been used in the past [Bodurka 1999] have not been used as fMRI phantoms as such themselves, but to investigate detection limits of scanners using similar principles.

1.6 Chapter Summary and Project Aims

fMRI is a technique that is already widely deployed globally in a range of research activities in both the clinical and preclinical setting. Although aspects of data extraction and comparative testing have been assessed at later stages of the fMRI study process, there

remains a critical lack of relevant and rigorous testing at the key stage of image acquisition in regards to scanner performance. Imperfections or anomalies here could undermine results at later stages and compromise any biological conclusions drawn from such potential distorted results.

To investigate the significance of this (if any) over the course of this project we will:

- Design and test a range of suitable fMRI phantoms appropriate for use in preclinical MRI scanners.

- Use a finalised phantom to assess the performance of a preclinical MRI scanner in regards to fMRI relevant parameters.

- Consider theoretical aspects of phantom performance and compare these with the practical phantom.

- Initiate a program of long-term monitoring on an MRI scanner to assess behaviour and performance over an extended period.

- Compare the comparative performance of MRI scanners at different sites to see how closely they match each other in terms of fMRI relevant measures.

Ideally measures such as ΔS, SNR and fCNR should be comparable between sites and certainly any variation in them should be well below the variation caused by biological noise in an *in vivo* scan. Scanners should also possess similar performances in terms of noise behaviour across the duration of typical fMRI scans.

Returning briefly to the role of animal usage in experimental procedures, there is a strong ethical driver here to pursue this research along with scientific integrity. It is ethically essential that if animals are going to be used in the course of an experiment that useful results can not only be obtained, but that the comparative use and role of those results in future studies, whether they be at the same facility or as part of the larger scientific literature, can be relied upon to give reliable and believable conclusions.

If however MRI facilities at different locations or other time points report differing results from identical experimental procedures, then the use of animals in such systems because ethically disingenuous and the value of that data becomes scientifically questionable.

Chapter 2 EPI Set Up and Operation

2.1 EPI Initial Observations

Although EPI was installed on the Edinburgh system it had yet to be deployed in any studies. Local experience with EPI on preclinical scanners was also limited at best. However, EPI is the preferred sequence for preclinical fMRI studies so the implementation of the sequence was a priority for the facility as it had recently been conducting its first fMRI based studies using an Fast Spin Echo based protocol [Brydges 2013]. The existence in the literature of several papers and reports from groups working with EPI on MRI scanners of the same type and field strength as the Edinburgh scanner provided encouragement to invest time and energy on fully implementing this sequence at Edinburgh.

EPI scan parameters were based around several examples from the literature and requested requirements in terms of spatial and temporal resolution selected by interested researchers.

Parameter	**Value**
TR	3000ms
TE	14.02ms (system minimum)
k_o (central line of k-space)	32
Volumes	200
Gain	10
Field of View	25.6 x 25.6 mm
Matrix Size	64 x 64
No. of Slices	27
Slice Thickness	1.00mm
Slice Interleaving	Yes

Table 2.1 *– Imaging Parameters used in EPI optimisation scans.*

Unless otherwise stated all scans in this chapter were performed using these parameters and a hardware set up of a 72mm volume coil for transmission and a two channel phased array coil optimised for rat neurological studies for reception (both Rapid Biomedical). Initial trial scans in both animal cadavers and with static phantoms quickly illustrated just how difficult it might be to generate usable data with the EPI sequence.

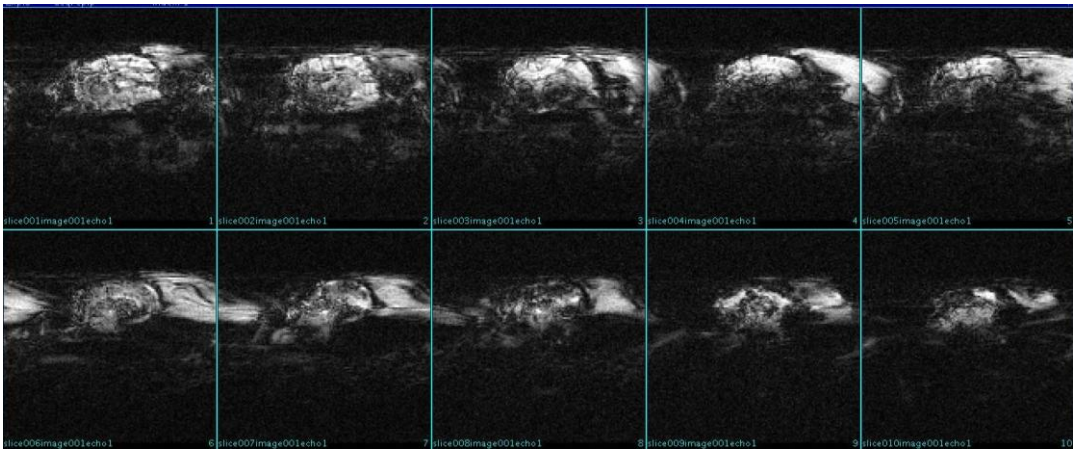

Fig. 2.1 *– Images from initial EPI scan of first rat cadaver.*

2.2 EPI Artefacts

EPI is subject to more pronounced artefact problems compared to other MRI sequences. As with all MRI artefacts the causes of these artefacts can include physiological noise from an *in vivo* subject or can originate from the interaction of the subject with the EPI sequence. In the case of EPI there are also some unique image artefacts caused by the rapid acquisition method of the sequence.

Artefacts in EPI images appear more prominent in the phase encode direction compared to the Read Out direction as in this direction the equivalent frequency spacing between one point and the next is very much smaller than in the read out direction.

Accumulations of gradient mistiming over the duration of an EPI acquisition can cause the appearance of Nyquist ghosting artefacts (sometimes referred to as N/2 ghosting) [Zhakor 1991]. This produces ghost-like images in the phase encode direction that are shifted by half the numbers of pixels in the phase encode direction. This results in fainter duplicate images whose centre is shifted by N/2 pixels (with N being the number of phase encode steps) and so the artefact image appears to wraps around either side of the primary image. This ghosting is caused by an gradient imbalance as they sweep back and forth during EPI acquisition. Accumulation of timing differences between each direction result in a phase difference between gradient directions appearing which is interpreted as a change in spatial position during image reconstruction. On Agilent systems these gradient imbalances can be partially corrected for by running the TEP prescan option prior to an EPI scan. This however is not always fully successful as magnetic field inhomogenities, which vary across a subject, can also induce similar phase shift effects. A full mathematical treatment of this artefact can be found in Bernstein MA et al., 2004 [Bernstein 2004a].

As with other MRI sequences chemical shift artefacts can also result in ghost like duplicate images, again primarily in the phase encode direction of the acquisition. These artefacts can be overcome to an extent by applying suppression techniques to reduce their effects during image acquisition.

Field inhomogenities can cause both signal drop outs and geometric distortions in the images to occur. These inhomogenities result in intrinsic phase differences to the MR signal rather than phase differences caused by spatial encoding. However, the scanner reconstructs the images as if they were all due to spatial encoding resulting in distortions in the resultant images. Good quality shimming is essential to reduce this inhomogeneity and so associated image artefacts. If only distortion occurs with no signal dropout it is sometimes possible to 'unwrap' such distortions during post-processing.

Variations in T2* values, often caused by highly localised magnetic field inhomogenities, produce regions of signal dropout [Buxton 2002]. These often occur at air-tissue boundaries such as around the sinus cavities and temporal lobes where the air from the ear canals comes close to the brain.

Artefacts and distortions can also arise from the physiological process and/or motions of the subject being scanned since even an anesthetised and restrained animal moves a small amount within the scanner. Blood, other fluids and organs such as the heart also continue to move internally while the subject is inside the scanner.

2.3 Optimising EPI For In Vivo Scanning

It is unfortunately difficult to disentangle the various causes of these different artefacts as they often interact with one another. A combination of optimisation techniques must be applied to reduce their detrimental effects.

Additionally to produce fMRI data that minimises the need for the most extensive image post-processing realignment after image acquisition it is important to ensure that the practical nature of the experimental set up is as similar as possible for each animal. This includes both positioning of the animal within the scanner and adjustment of scanner pre-scan settings such as power calibrations and shimming. In an ideal system the process should be identical each time leading to identical results between subjects and across scan sessions excepting any intended experimental effect.

Some variability in subject positioning is to be expected as positioning techniques typically rely on manually aligning sets of pre-measured markings on animal holding equipment.

These markings are used to align coils, animal holders and animals themselves with the centre of the scanner B_0 field. While not necessarily strictly repeatable, coil performance is assumed to be identical across a specified region where the animal may be positioned. Variations in animal size will also lead to small differences in positioning and subsequent system calibration. An MRI system must be able to produce repeatable results while accommodating this variability.

The exact techniques and protocols for scanner set ups tend to vary from site-to-site. However common measures of scanner set up such as peak power required for a 90° RF pulse and measures of the 50% water peak linewidth in an acquired MR spectrum are measurable at most sites allowing comparison of scanner set up across sites.

2.3.1 Shimming

Shimming is a process by which the homogeneity of the primary magnetic field of the scanner is optimised by adding strategically shaped and calibrated secondary magnetic fields to the primary field. As discussed earlier given the particular susceptibility of EPI sequences to magnetic field inhomogeneity an optimal B_0 field shim is essential for EPI imaging.

Shimming on preclinical MRI scanners can be accomplished manually by altering currently levels in the specialist shim coils using an interface in the scanner control software. Shim quality is monitored by inspecting the shape of the sample's signal free induction decay curve and/or by monitoring the spectral linewidth of water. Manual shimming of this kind was the primary shim method deployed on the Edinburgh scanner prior to the start of this project.

An alternative is to use on-board software to automatically shim the system. This has the primary advantage of systematic reproducibility as well as freeing a scanner user to perform other tasks such as animal monitoring during the initial set up stages of a scan session.

Agilent preclinical systems operating the VnmrJ software are equipped with an auto-shimming package based around a gradient echo 3d shimming (GE3D) technique [van Zijl et al, 1994]. This is a localised field map based technique where the system iteratively attempts to minimise the variation produced in those maps over a specified region over successive shim iterations and sampling points.

Using the opportunity presented by concurrent neurological studies occurring at Edinburgh, data were gathered to compare the GE3D shimming technique with the manual methods used up until that time at Edinburgh. The two techniques were tested in both rat (n=5 GE3D, n=30

manual shim) and mouse (n=5 GE3D, n=33 manual shim) subjects. Manual shimming was performed by an experienced scanner operator for approximately the same time as the GE3D shimming procedure took to be run by the scanner computer. Results are summarised below in Fig. 2.2.

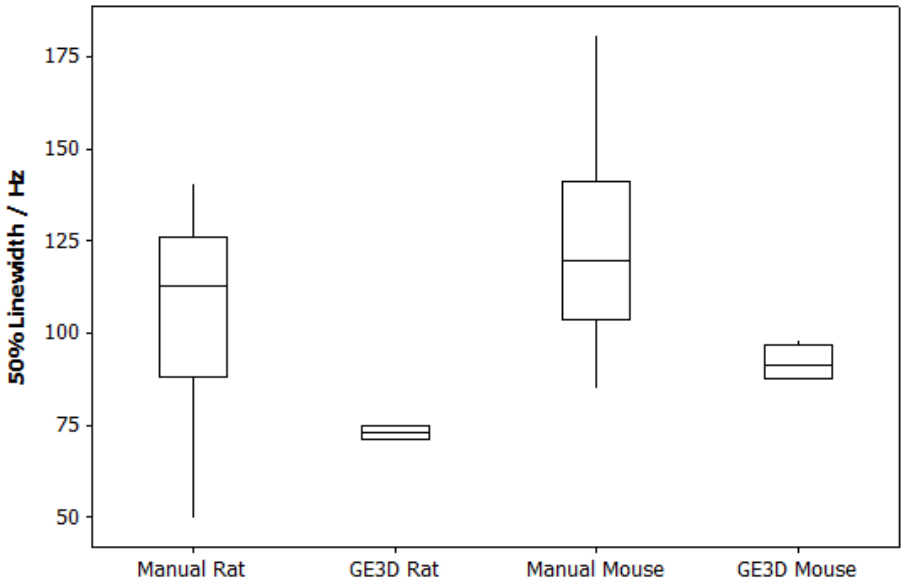

Fig. 2.2 *– Comparison of shimming techniques based on measuring the 50% linewidth of the sample spectral water peak. Under the GE3D shim technique the standard deviation of the mean 50% linewidth of the proton peak in localised voxel spectra for the two animal types groups were 1.84 (rat) and 4.64 (mouse).*

GE3D shimming gave statistically significantly improved shimming values compared to the manual method for each animal species ($p<0.005$, student's t-test). Not only were mean shim values improved but the standard deviation of the shim value across the group was also dramatically narrowed, demonstrating that the GE3D method produced more consistent shim values from animal to animal than the manual method.

The improvements in shim quality and consistency alongside the lack of need for direct user intervention during the shim process led us to adopt the GE3D method for this project. GE3D is also now in use in many other projects running on the Edinburgh scanner.

2.3.2 Orientation Shim Studies

No matter what holding device is used to position the animal within the scanner there will be some variation in the physical positioning of the animal. From one subject to the next animals can be relatively rotated in all three spatial planes.

To generate images in matching orientations typically a stack of prescribed image slices are rotated until they run approximately parallel to the axis of the subject brain. This greatly assists in the processing of fMRI images in the post-processing of such data as less extrapolation and treatment of image data is needed across a group to translate individual animal data into a universal shared orientation space.

However, obliquely angled slices of this type place additional strains on the encoding gradients, which for EPI imaging are already running at high capacity. To minimise inhomogeneity artefacts shim quality should therefore also remain optimal no matter the position of the animal or the slice prescription.

Two studies were therefore conducted to investigate the effect of subject orientation on the quality of the shim obtained. Firstly, a study was conducted where the prescription angle of the shim voxel used in the GE3D shim method was systematically altered in three perpendicular planes to place varying amounts of strain on the encoding gradients to see if gradient performance affected shim quality. A second study was also conducted where a static phantom within the scanner was physically rotated in perpendicular planes to the scanner bore axis and similarly measuring the effect - if any - on shim quality.

- **Effect of Voxel Orientation**

  A standard water sphere phantom (diameter = 49mm) was positioned at the centre of the scanner. A GE3D shim voxel (15mm x 15mm x 15mm) was then prescribed onto the centre of this phantom and the scanner was shimmed for this voxel using the GE3D protocol. The linewidth of the shim voxel was then measured using a localised PRESS spectroscopy sequence. Five separate shim set up experiments (resetting the shims to zero between each) were performed and measured. The voxel was then rotated by 15° in a single plane and the process repeated. This continued in an angle range of -180° to 180°. This was then repeated in the other two planes. Results from these tests suggest little variation in shim quality due to voxel orientation changes as outlined in Table 2.2.

Plane	Mean 50% Linewidth / Hz	Standard Deviation / Hz
Axial	1.88	0.14
Coronal	2.12	0.43
Sagittal	2.53	0.17

Table 2.2 *– Mean shim linewidth obtained from slice prescription reorientation study. Change in shim quality with voxel prescription change is low.*

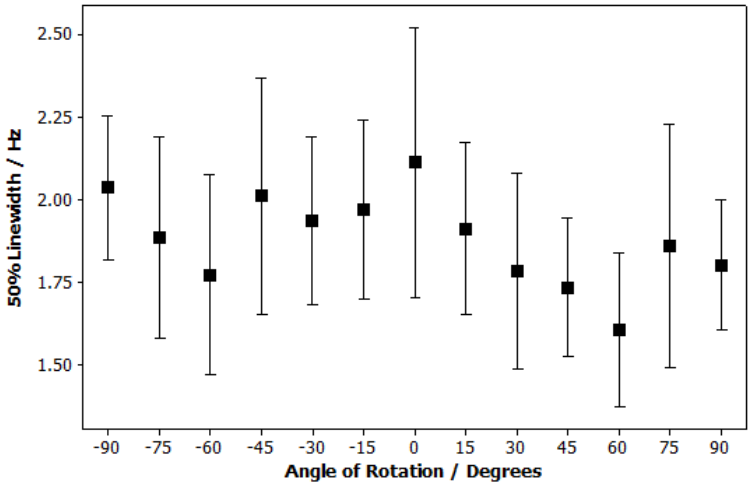

Fig. 2.3 *– Shim variation due to rotation of image stack in axial plane.*

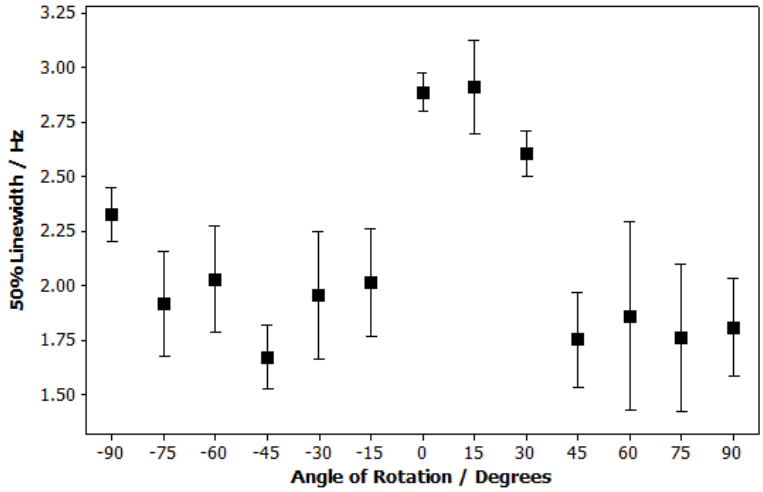

Fig. 2.4 *– Shim variation due to rotation of image stack in coronal plane.*

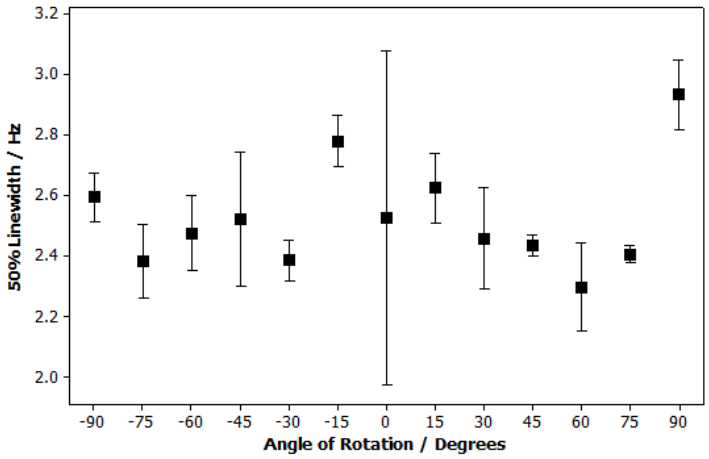

Fig. 2.5 *– Shim variation due to rotation of image stack in sagittal plane.*

Although there is some variation related to the shim voxel orientation angle the overall standard deviations of linewidth values of all three planes are well below the standard deviations found across each animal groups as outlined in section 2.2.1 above. This suggests that the extra work the gradients must perform, while introducing some non-significant variations (in most cases) to the shim value is well within the normal biological limits found when using animal subjects. This means that in terms of imaging set up the shim voxel orientation is of no concern in terms of image quality.

Although oblique angles introduce no new magnetic inhomogeneity field artefacts, the extra strain on the gradients may still worsen other artefacts such as Nyquist ghosting (which is caused by gradient imbalances).

- **Effect of Physical Orientation**

  The second study followed a similar protocol to the Slice Orientation study. In this case however a small tube (length = 122mm, diameter =15.0mm) was filled with water and placed at the centre of the scanner. This tube was then rotated around the centre of the tube between an initial position in line with the scanner bore and a series of rotations through to the tube being perpendicular to the bore in the plane of rotation. The tube was rotated in the coronal and sagittal planes only as there was no need to rotate the tube in the axial plane due to the rotational symmetry of the tube cross-section in that plane.

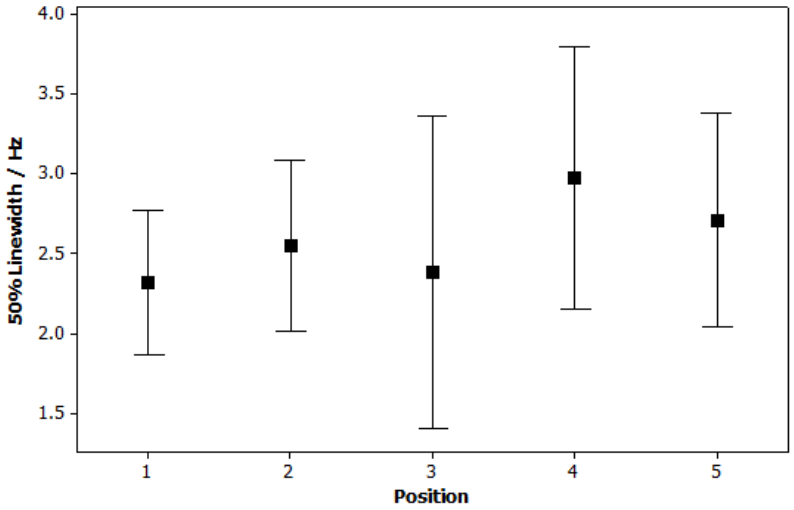

Fig. 2.6 *– 50% Linewidth values obtained from five different positions in the coronal plane, sweeping out an arc from 0° to ~90°.*

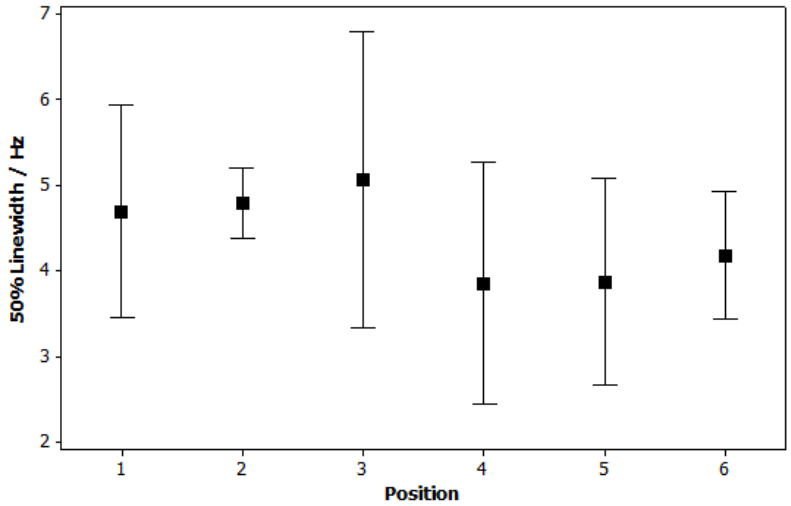

Fig. 2.7 *– 50% Linewidth values obtained from five different positions in the sagittal plane, sweeping out an arc from 0° to ~90°.*

Orientation	Position	Mean Linewidth / Hz	S.D.
Coronal	1	2.32	0.36
Coronal	2	2.5	0.43
Coronal	3	2.38	0.79
Coronal	4	2.97	0.66
Coronal	5	2.71	0.54
Sagittal	1	4.69	1.00
Sagittal	2	4.79	0.33
Sagittal	3	5.07	1.40
Sagittal	4	3.86	1.13
Sagittal	5	3.87	0.97
Sagittal	6	4.12	0.97

Table 2.3 *– 50% Linewidth value results from the physical orientation study.*

Although there were some minor changes to shim values in the different positions none of these changes were significant in the range of responses returned. It can be concluded (at least for the phantom used) that physical orientation has minimal effect on the shim performance of the GE3D sequence.

2.3.3 Practical Improvements to Images

Temporal resolution of functional changes in the brain is often the key requirement in fMRI experiments. This however must be balanced with both a reduction in image artefacts and a maximisation of fCNR.

In addition to the improved shimming available through the GE3D auto-shimming, the Agilent EPI sequence (more technically the EPIP sequence on VnmrJ 3.2 onwards) comes with a variety of options that can be employed in different combinations to improve image results.

Phase Encoding Direction

Blurring artefacts are primarily generated by signal corruption caused by phase changes such as those experienced when a voxel contains an abrupt change in tissue contrast with within one voxel. Voxels containing air-tissue boundaries for example are particularly susceptible to this for example. These artefacts were found to reduce when the phase encode direction was rotated by 90°, so that the direction now ran vertically through the animal's head rather than running laterally. This would reduce the number of air/tissue interfaces running through a single phase encode line and so reduce the number of potential source of field inhomogeneity per phase encode line. This resulted in less phase accumulation error per phase encode line, reducing artefacts caused by field inhomogeneity.

Referencing Schemes

The EPIP sequence is able to make use of different options to provide additional reference scans that are used to attempt to correct for the accumulation of various phase errors in both the readout and phase encode directions. As phase errors are more prominent in the phase encode direction more options have been developed by the scanner manufacturer to gather data to correct for these. These additional scans are generally performed before the main EPI acquisition takes place. The exception to this is the scheme known as 'Full Triple Referencing' on Agilent scanners running iterations of the VnmrJ software package.

Reference data is acquired either with Read Out and/or Phase Encode gradient direction inverted to that of the subsequent scan (which accounts for directional effects on the subsequent actual scan acquisition) or with the Phase Encode gradient tuned off entirely (to sample 'native' distortions in the phase encode direction that don't depend on the phase encode gradient itself).

Although the intention of these schemes is to provide improvements in image quality they also impact on both the total time needed to complete a scan and also the time per volume.

In the case of Full Triple referencing reference scans are taken before the EPI acquisition, but also prior to every *individual EPI volume.* This substantially increases the total acquisition time for a scan and halves the functional temporal resolution as well. Proportionately functional data is also sampled from only 50% of the scan time.

Choosing this scheme has a number of significant consequences that researchers might want to avoid. The lower temporal resolution limits the biological paradigms that might be suitably tested under such temporal constraints. A researcher will also have to choose

between doubling their acquisition time (and so costs as well) or settling for only half the number of acquired volumes, reducing the statistical usefulness of the experiment. Additional scan time also places additional physiological stress on an animal subject. As well as perhaps being ethically unacceptable this in itself could affect biological results from such subjects.

Referencing Scheme Name	Read Out Inverted	Phase Encode Off	Phase Encode Inverted	Additional Time for Scan
None	No	No	No	None
Single	No	Yes	No	1 TR
Triple	Yes	Yes	Yes	3 TR
Full Triple	Yes	Yes	Yes – for every volume	(3 TR) + (TR*NV)

Table 2.4 *– Details of different referencing schemes available with Agilent EPIP sequence. NV = number of volumes acquired in the EPIP scan.*

Since there is very little difference in acquisition time between the Single and Triple referencing schemes, the Triple scheme should always be used by preference to give the more comprehensive correction options. If the Full Triple scheme is to be used it must present significant advantage over the faster Triple scheme.

SNR values for the three schemes (Table 2.5 below) were also very comparative, so there is no obvious gain in choosing one scheme over another based exclusively on SNR properties.

Reference Scheme	Signal	Noise ($x10^{-3}$)	SNR
Single	0.24	1.16	209
Triple	0.25	1.28	193
Full Triple	0.24	1.14	213

Table 2.5 *– SNR values obtained under different EPI Referencing Schemes for a static water filled spherical phantom.*

Example scans using the two types of referencing schemes are shown below in Figures 2.8 (Triple referencing option) and 2.9 (Full Triple Referencing).

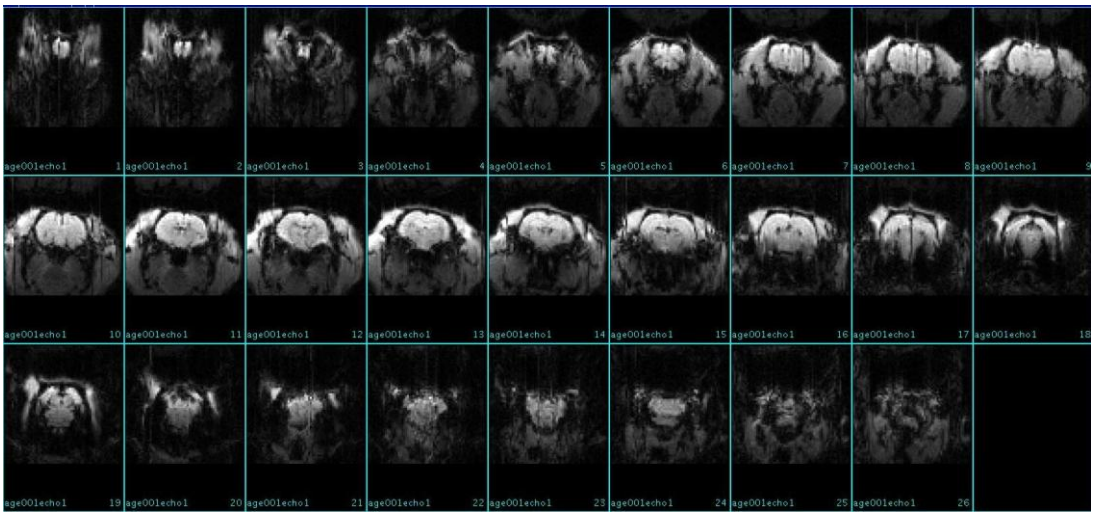

Fig. 2.8 *– EPIP scan with Triple Referencing. Rat cadaver, TR = 3000ms, Axial 90 orientation.*

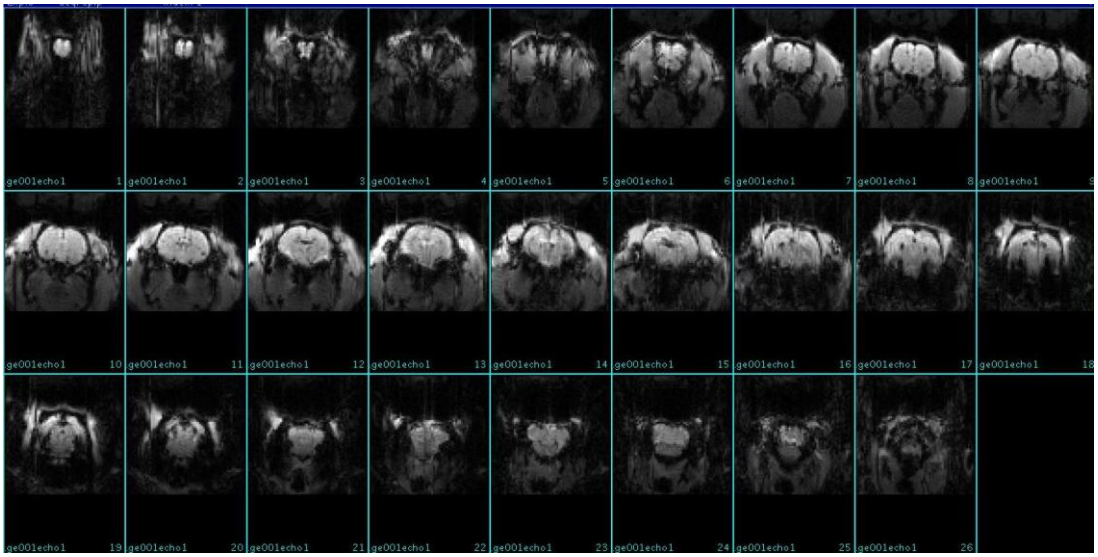

Fig. 2.9 *– EPIP scan with Full Triple Referencing. Rat cadaver, TR = 3000ms, Axial 90 orientation.*

Visually there is a slight improvement in the severity of blooming artefacts at the base of the brain when using the Full Triple Referencing. However, given that otherwise there appears to be only minor differences in image quality deployment of the Full Triple Reference scheme was not considered to be a useful trade off in terms of improved image quality when considering the extended acquisition time, costs and burden on the animal subject.

Appearance of 'Streak' Artefact

In both referencing schemes once the phase encode direction had been switched to the vertical direction a novel artefact was first noticed that was referred to as the streak artefact. This artefact manifested itself as a small number of unusually bright and/or dark lines in the phase encode direction. Fig. 2.10 illustrates some examples.

a)  b) 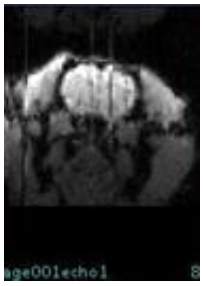 c) 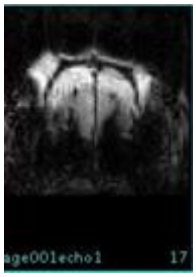

Fig. 2.10 *– Examples of streak artefact appearing in different regions of the brain a) forebrain, b) mid-brain and c) rear of brain. Artefact varies in severity and position from subject to subject.*

This artefact appears in slices where there are large air/tissue boundaries simultaneously around the animal head and inside it, such as in slices containing the inner ear canals. The artefact appears in such slices, but can appear in varying positions within the slice both inside and outside the brain and not necessarily in regions of air/tissue boundary.

This can also be seen in the appearance of the streak artefact in images of a water sphere phantom with an air bubble. The streak is most prominent at the air-water boundary of the air bubble.

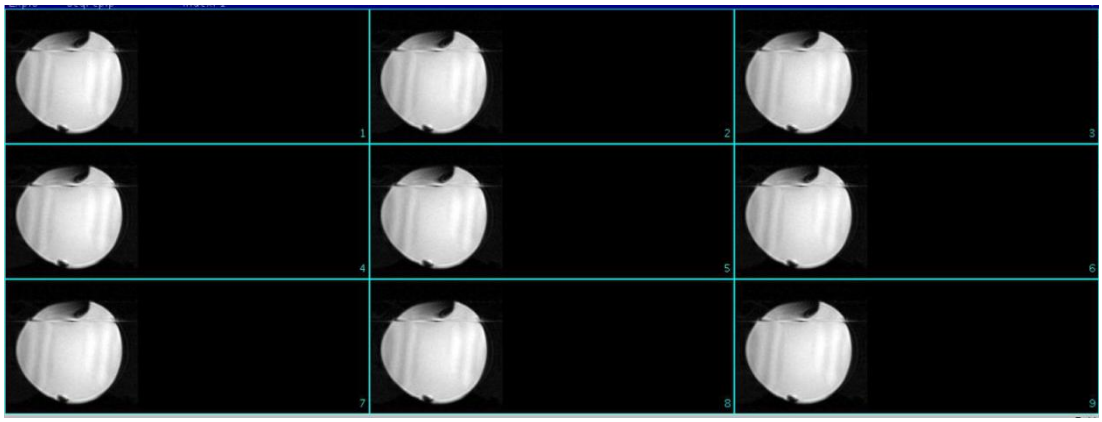

Figure 2.11 *- Appearance of the streak artefact in a water sphere. Phase encoding is Left-Right in this scan and the artefact runs in parallel with the phase encoding.*

There is little in the literature on this artefact but enquires were made to other centres using EPI on systems similar to the Edinburgh scanner. When queried this artefact was also reported as present in at least two other Agilent equipped MRI facilities (University College London, UK and The Nathan S. Kline Institute for Psychiatric Research, USA). Both of these groups reported taking no measures to minimise this artefact as it was persistent in their images and data was analysed under the assumption that it would not affect any final functional results obtained.

Discussions with Agilent led to the conclusion that the EPIP reconstruction software was misinterpreting this boundaries resulting in the incorrect phase values being assigned to some lines in the image reconstruction process. This phase error alters the signal intensity assigned to these regions generating the streak artefact.

Moving to *in vivo* subjects

Further improvements in image quality were obtained by 'piggy backing' onto the end of scan sessions for other existing fMRI projects to obtain *in vivo* EPI images which would have been difficult to obtain otherwise due to regulatory issues. Results from using *in vivo* subjects yielded improved image quality as can be seen in Fig. 2.12. Not only are geometric distortions on the brains now minimal, but the images are crisper and the extent of blooming artefacts towards the base of the brain is also reduced. The streak artefact however still manifests itself in regions of the images containing brain material.

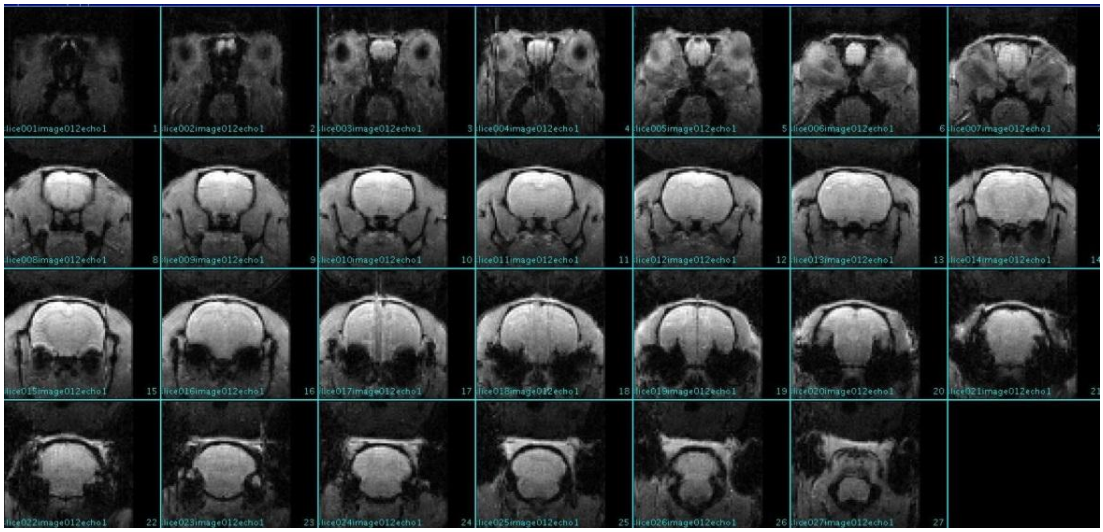

Fig. 2.12 *– Example Rat in vivo EPIP images using Full Triple Referencing. TR = 3000ms, Axial 90 orientation. Triple Referencing.*

Multishot Options

Accumulating EPI readout train timing errors can be reduced by using a multi-shot approach to gathering EPI data. Multiple signal shots (of number *n)* are generated over successive echos and a different shot acquires every *n*th line of k-space. This reduces the timing error per k-space line and so reduces the amount of phase discrepancy per line across the whole of k-space, reducing signal distortion due to phase accumulation effects.

This multi-shot approach to k-space data acquisition comes with a penalty as the total acquisition time per volume is multiplied by *n* as well. A typically value for *n* is three. In the case of Edinburgh this results in a study temporal resolution almost equal to that of the originally used FSEMS sequence, which is what improvements were sought on.

Higher temporal resolution can still be maintained through the use of a compressed, segmented multishot technique [Guilfoyle 2006]. In this approach a single echo acquires all lines of k-space in the trajectory manner of a multishot technique that gathers every *n*th line over *n* shots. In the compressed scheme however the intervening lines are gathered on the same original echo rather than on successive echoes. While this approach maintains the higher temporal resolution of single shot EPI, SNR is reduced by a factor known as the imaging efficiency (ρ) [Johnson 1999]. In EPI imaging TR >> T1 as the EPI scan is usually T2-weighted for BOLD imaging. Therefore the imaging efficiency of the interleaved multishot EPIP sequence compared with the single shot EPIP sequence (η_{NON}) can be given by:

$$\rho = \frac{n_{NON}}{n_{SEG}} = \sqrt{\frac{TR_{SEG}}{TR_{NON}}} \qquad \textbf{(}\text{Eq. 2.1)}$$

where TR_{SEG} = TR_{NON} x total number of shots.

Using this it can be seen that ρ will decrease with increased *n* according to the values given in Table 2.6.

TR_{NON} / ms	Shots	TR_{SEG}	Imaging Efficiency (ρ)
3000	1	3000	1.00
3000	3	9000	0.58
3000	5	15000	0.45

Table 2.6 *– Theoretical calculations of ρ using compressed multishot EPI for different numbers of shots. There is a sharp drop in ρ as shot number increases.*

EPIP images generated using a 3-shot compressed scheme (Fig. 2.13) showed improvements in both blooming and streak artefacts although both were still present. These artefacts were further reduced with 5 shots but the drop of ρ to of 55% was judged to be an unacceptable amount and was very noticeable in generated images.

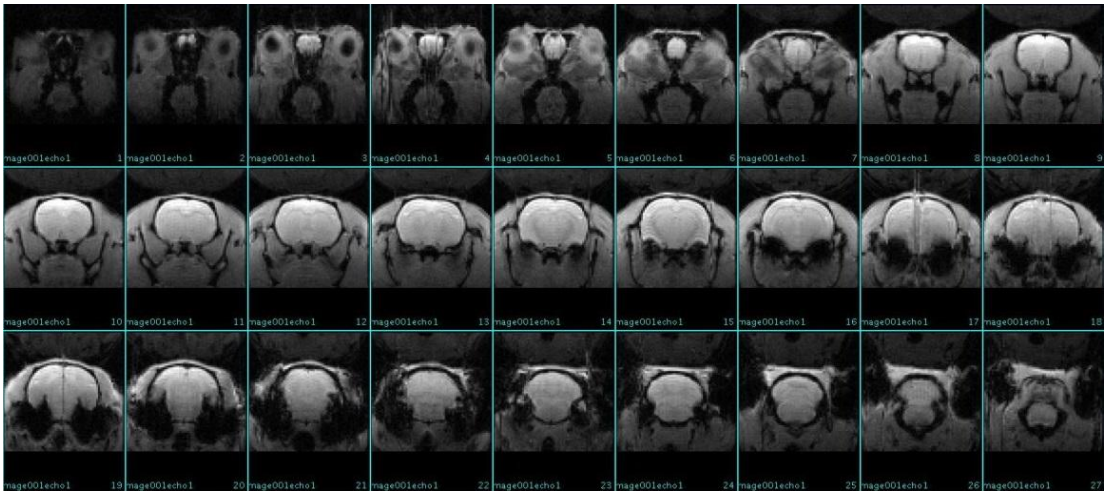

Fig. 2.13 – In vivo *rat EPIP scan with Triple Referencing and 3 x compressed segmented multishot acquisition. TR = 3000ms, Axial 90 orientation.*

Removal of Streak Artefact

The persistent presence of the streak artefact despite optimisation of set up parameters and testing presented a problem. Although other groups at other MRI centres felt happy to ignore the artefact and continue analysis with it present, this was an unsatisfactory conclusion. Given that it was thought to occur due to the presence of intravoxel air-tissue interfaces the position of the imaging FOV was lowered so that the head filled the imaging area as much as

possible. This reduced the proportion of the volume of the slice containing air. This does however move the centre of the brain itself away from the centre of the FOV.

Images generated using this new FOV positioning appeared free of the streak artefact. This technique was repeated over a number of different animals who all generated streak free images. On a handful of occasions streaks were observed, but these were outside of regions containing brain tissue so not considered problematic.

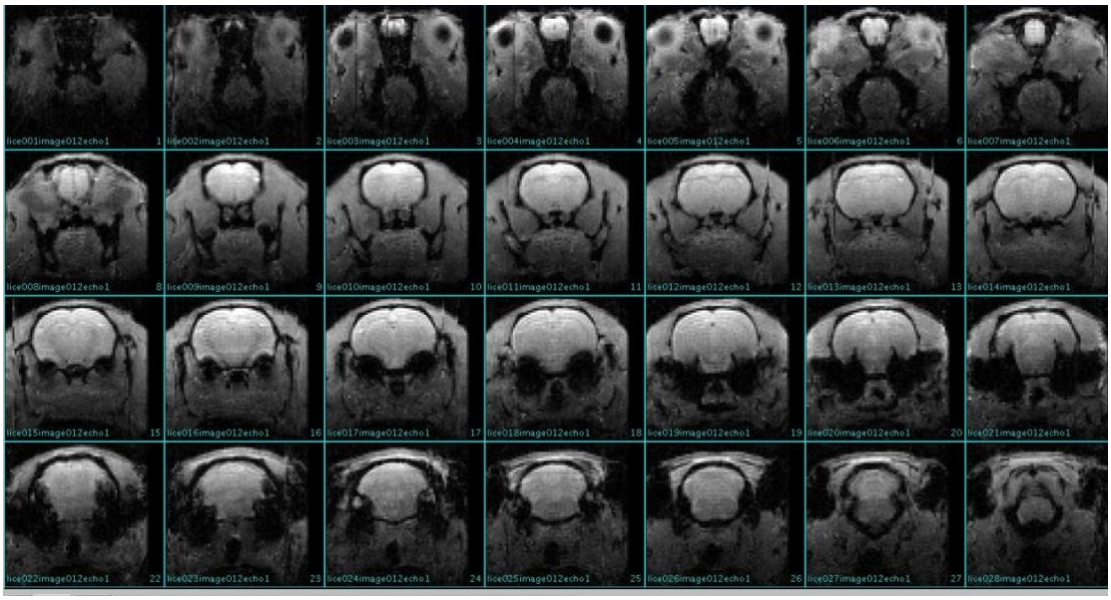

Fig. 2.14 *– in vivo rat EPIP, TR = 3000ms, Axial 90 Orientation with FOV aligned with top of rat head. Brains appear clear of artefacts.*

2.3.4 SNR Measurements of Different EPI Schemes

Using the methods outlined above we were able to successfully replicate artefact free EPI images on several *in vivo* subjects with a minimum of extra time for referencing scans. Although we expected a drop in SNR due to using the segmented multi-shot approach it was important to gain confirmation that these values were what they were expected to be. Deviation from expectation could provide a sensitive marker for scanner performance.

To this end we scanned the same spherical water phantom from before across a single session with both the Single and Triple reference schemes combined with different combinations of shots. SNR values were obtained by using an identically sized Region of Interest (ROI) to measure signal from within the phantom and comparing it with the background noise value obtained by sampling a region outside the phantom and off-centre to the phase encode direction to minimise skewing via ghosting artefacts. This technique is

outlined in more detail in Appendix 1.1 and used extensively in studies contained within Chapters 3-6.

The results from these tests are outlined below in Fig 2.15.

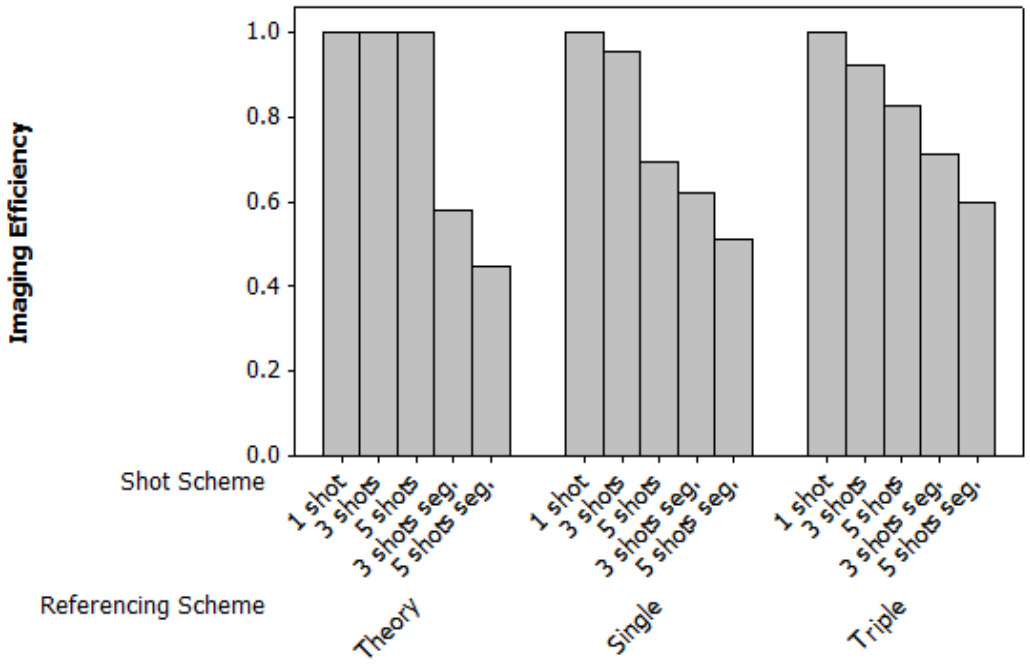

Fig. 2.15 *– Experimental Measurements of ρ on an in vivo subject using various EPI acquisition schemes. Imaging efficiency is relative to a theoretical single shot acquisition.*

In both the Single and Triple referencing schemes SNR values are elevated compared to what theory predicts. All SNR values decay with increasing shot number and the addition of shot segmentation. Superior SNR is achieved in the Triple scheme compared to the Single scheme. This justifies the usage of the Triple scheme despite the additional two TRs worth of time needed for this scheme.

2.4 Transferability of Technique

With an optimised and validated EPI set up protocol now outlined as above, opportunities arose throughout the PhD project to test the technique on other coils used in the Edinburgh lab.

The first coil tried was a coil set up used in conscious animal fMRI studies (coil supplied by Insight MRI). This coil is a volume/surface coil combination that also incorporates a restraint system to minimise animal motion in the stressful environment of the MRI scanner.

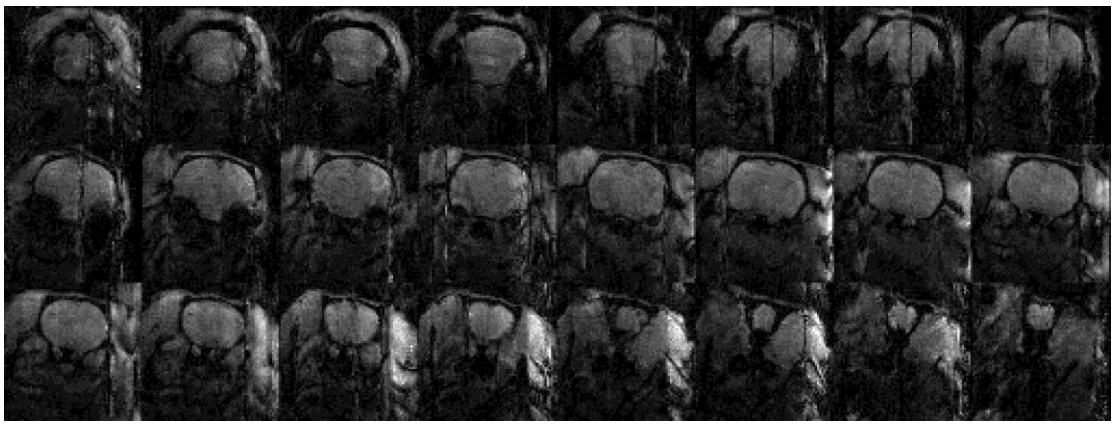

Fig. 2.16 – *EPIP* in vivo *rat scan with standard EPIP rat protocol using Insight fMRI coil.*

Comparing the resultant images from the Insight coil with those gained on the Rapid coil using the same protocol (Fig. 2.14) it is clear that the image quality on the Insight coil is poorer overall and with prominent appearance of the streak artefact.

We also tested the protocol on mice modifying the field of view to give a similar image filling proportion to the rat tests. Again, despite the similarity of protocol and technique resultant images were of poorer quality exhibiting significant blurring around the edges of the mid brain as well as the streak artefact.

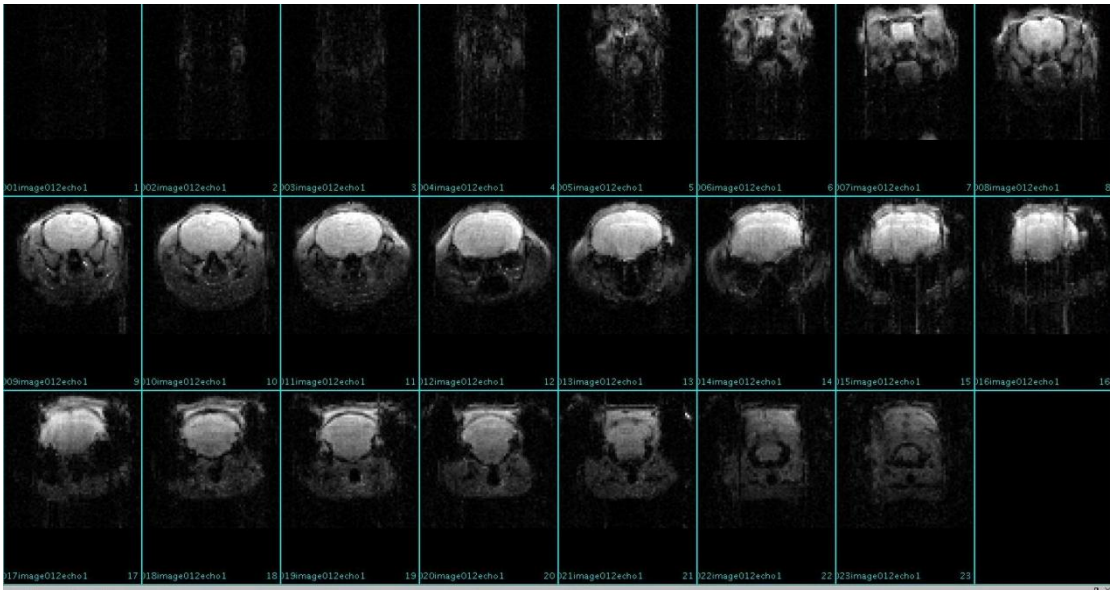

Fig. 2.17 – In vivo *mouse EPIP, TR = 3000ms, Axial 90 orientation, Triple Referencing. Note the presence of both the familiar streak artefact and also a more general 'blurring' in the centre slices.*

These results would seem to suggest that coil specific protocols must be developed and optimised before EPI is deployed onto a new coil set up. While many of the protocols may have similar justifications in terms of artefact origin their exact practical working out may be considerably variable.

2.5 Chapter Summary

The experimental methodology worked out in the course of the studies presented in this chapter produced good quality EPI images. These successful results were able to be replicated across multiple subjects on widely separated scanning dates, suggesting the methodology implied is robust.

However, the variability of results with different coil set ups combined with the rather convoluted and temperamental nature of the procedure for suppressing the image artefacts suggested that there is significant worth in investigating these variations in a more controlled environment away from the physiologically noisy and variable conditions of an *in vivo* subject.

This then is where the rest of the PhD project led with the development of an fMRI phantom and subsequent studies investigating scanner performance and reliability. This was especially of interest given the ethical demands of using animals to generate scientifically useful and reliable data.

Chapter 3 Preclinical fMRI Phantoms Design and Testing

3.1 Development Outline Discussion

Chapter 2 illustrated the difficulties encountered with optimising EPI for a particular set of equipment and then showed how a particular set up configuration was not suitable when applied to other coils etc. This lead to us questioning why that might be, what factors might be involved and where they significant when it came to the study of *in vivo* subjects.

It was clear that to investigate this systematically it would be necessary to separate the variability of scanner performance from any variability caused by the object being scanned. Because of this it was decided that studies would (at least initially) be carried out using phantom devices of known properties.

3.1.1 Specifications and Requirements for high-field preclinical fMRI Phantom

To be most useful for fMRI QA an fMRI phantom would have to meet a number of requirements.

- The phantom must be capable of remotely activated switching between various signal states in order to create image contrasts that mimic stimulus induced activation states in *in vivo* fMRI studies.
- These different signal states must be distinguishable in EPI images so that they can be individually measured for use in signal assessment.
- The signal generated should be stable with a minimum of drift and fluctuation attributable to the phantom itself.
- The phantom must be robust to handling so that day-to-day use does not damage or degrade the performance of the device.
- Its material properties should be stable so that it can be used for like for like monitoring of scanner performance over long periods of time.
- Any electronic noise due to the operation of the phantom itself should be minimised so that noise due to the scanner itself can be properly characterised.
- The construction of the phantom should be reproducible so that copies of the same device give the same results. To aid this simplicity of design and assembly are key.

3.1.2 fMRI Phantom Design Discussion

3.1.2.1 Type of fMRI Phantom

Various types of existing fMRI phantom designs were briefly outlined in Chapter 1.5.4 and an electromagnetic type was selected as the most suitable for development. In this chapter we utilise two designs outlined for use as fMRI phantoms by Renvall consisting of a Wire in Tube (WIT) design and a Coil Around Tube (CAT) design [Renvall 2006, 2009b]. These designs use the presence of induced magnetic field gradients to cause signal dephasing leading to a lower signal level when the device is active compared to when it is inactive. The amount of dephasing is determined by the level of current running through the wires of each device.

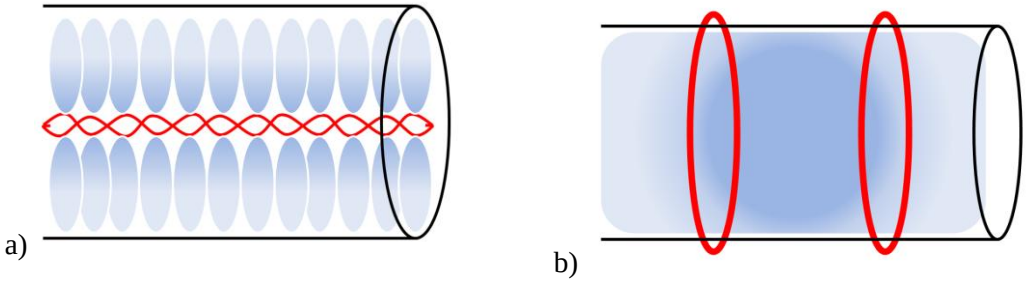

Fig. 3.1 *– Basic designs for the fMRI phantoms - a) The WIT design consists of a twisted wire (red) folded back on itself running down the centre of a tube filled with rape seed oil. Current in the wire creates regions of dipole shaped signal drop out along the length of the tube (blue shaded regions), that rotate around the length of the wire with the twist of the wire. b) In the CAT design two wire coils (red) surround a tube of Gd-doped water. Current in the wire coils (red) causes a magnetic field gradient to form between the wires (blue shaded region). This gradient attenuates the MR signal coming from the water located between the two coils.*

In the studies that form this project experiments using the phantoms are expanded across a much wider range of experimental situations and theoretical understanding of the phantom device is explored in greater detail than Renvall's papers [Renvall 2006, 2009a, 2009b] and PhD thesis [Renvall 2010] engage in. A variety of power sources, configurations and multiple MRI scanner sites are used to more fully evaluate both the potential of these designs and to uncover new information about MRI scanner performance.

Both the WIT and CAT designs were tested in early trials. Although the simplicity of the CAT design was attractive, the WIT design, if successful, could in theory be miniaturised

sufficiently to allow for simultaneous imaging with an *in vivo* subject. This would permit *in situ* quantification of scanner performance alongside an active *in vivo* scan, providing a means to validate *in vivo* data against scanner performance at any particular time. Miniaturising the WIT design would simply be a matter of reducing the resonator medium tube size, whereas the CAT design would require smaller physical coils and smaller voxel sizes in the acquisition stage in order to maintain a comparative level of statistically validity during image analysis.

As both designs are based around an electromagnetic effect it is important to provide a current source to the phantom that is constant, reproducible and precisely controllable. It should also have high temporal stability so as to be immune to random current spiking and fluctuations. As outlined more fully in Chapter 4 any changes in phantom current will result in changes in the magnetic fields produced by the phantom. These changes will then alter the phase dispersion caused by that magnetic field change and thus cause signal changes in the EPI images obtained.

The presence of the wiring involved in the construction of the phantoms can also create image distortions. However, with careful design of the phantom and subsequent region-of-interest selection their effects can be minimised in regions of actual measurement.

3.1.2.2 Phantom Construction

- **Size**

  A suitably sized phantom would also be able to be placed within the field of view of an *in vivo* subject being scanned allowing for simultaneous experimental data acquisition from both the subject and a constant reference image source that can be activated/deactivated in time with biological subject stimulation.

  This would allow for an absolute measure of signal change over the length of a scan to be integrated into the data analysis of the resultant images. Volumes showing out of the ordinary spikes in the signal could also be checked for and eliminated from analysed data sets. It could also be used to monitor for changes in the basic responsiveness of scanner components or measurements of a systems total electronic noise during a scan.

  Otherwise the only size constraints are such that the phantom can comfortable fit and be positioned in the coils and other equipment used in rodent fMRI scans.

- **Materials Used**

  As with any device placed within the strong magnetic field of an MRI scanner, the materials chosen for it must not respond to that field to avoid create a potential hazard to either the scanner or scanner users working in the immediate area. In general plastics and water-based liquids are safe to use. There are some safety problems with ferromagnetic materials which include many metals. Therefore as a useful rule of thumb the use of metals in general in the scanner environment should be limited where possible. If used then they should be secured in such a way so as not to create an unnecessary hazard.

  Materials used should minimally affect the image quality of the MRI scans. Metals again can be a considerable problem here as they absorb radio frequency waves, leading to regions of signal drop out in MRI images in areas adjacent to any metal in the phantom. The intensity of this drop out depends on the distance from the distorting material as well as imaging details such as the phase encode direction.

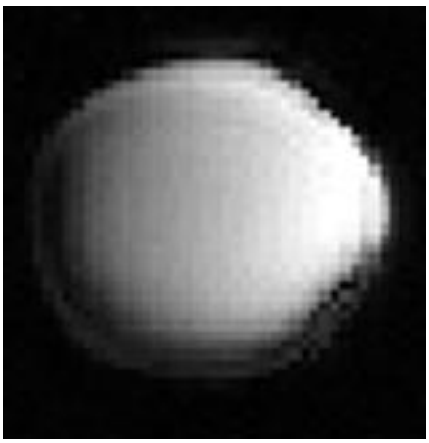

Fig. 3.2 *– Cross-sectional slice of CAT phantom with coil in plane. Signal drop out around the edge of the image can be clearly seen around the edge of the phantom. This is due to the presence of the coil wrapping around the perimeter of the resonator tube.*

- **Temporal Stability**

  The material properties of the phantom should be stable over both the duration of an individual scan (typically ~20mins), but also over repeated scans over longer periods of time. These include multiple scans on a single day and also long term performance over periods of months and years.

In order to ensure that any variations or anomalies seen are produced solely by scanning equipment the phantom should produce robust identical results over repeated use, including being removed and repositioned in the scanner from one scanning session to the next.

If variations in phantom performance are noticed, then subsequent constructions of the phantom should produce similar results so that replacement phantoms can be bought on-stream in good time during long-term monitoring of an MRI system.

- **Simplicity of Construction / Replication**

  Any phantom device should be simple to construct. Not only would this support the likely repeatability of results between different phantoms, but it also facilitates straight-forward repairs to an individual phantom when it might malfunction.

- **Cost**

  Costs for the phantom should be minimised if possible. This will to some extent depend on material choices used and the quality of electronic control desired over the phantom. A cheap, easy to construct (and repair) fMRI phantom would also encourage wider uptake of the device by other MRI centres.

3.1.2.3 Statistical Robustness for Sampling ROI

ROIs that are used to measure image properties should be positioned in regions of uniform signal intensity where possible. Concurrently the ROI should be positioned as close as possible to regions of maximum magnetic field gradient linearity. Together these measures would ensure that extracted image values are not unduly influenced by the position of the ROI within the image.

In the WIT phantom this must be in close proximity to the wire of the phantom as the magnetic field generated by the wire rapidly decays away when moving off-axis from the wire. Care should also be taken to avoid incorporating any voxels containing the wire itself into a ROI as this will lead to impure sampling of the induced signal changes.

For the CAT design ROIs should be placed at the centre of the activated region between the two coils. At the edges of slices, away from the centre, voxels will include elements of the coil wires themselves or varying magnetic field gradient values due to the geometry of the coils. (Fig. 3.2). Signal changes near these edges will also be distorted due to these differences and also imperfections in the construction of the coils around the tube. Towards

the centre of the tubes these effects are less of a concern as the uniformity of the magnetic field gradient increases towards the centre of the CAT coils.

ROI's should also contain a sufficient number of pixels to insure a statistically valid sampling occurs, in order to ensure that results are less susceptible to noise-based fluctuations in individual pixels.

3.2 Data Analysis Methods

3.2.1 Method 1: Manual ROI Measurements

This was the primary method used to analyse the fMRI phantom data generated in this project. The following is the image analyse procedure used to produce the measurements used in all subsequent results sections. Although more time consuming and user interactive than more automated fMRI packages (such as FSL and SPM), manual processing of the data allows the analysis chain to be easily interrogated and intuitively understood without the complexities involved in processing data through dedicated software packages that are unsuited to handling such relatively non-complex data as generated by the phantom.

1) Acquired EPI data is converted from the Agilent native FDF format into the Analyze format in order to be processed offline with a wider range of image analysis programs such as MATLAB, Mricro and ImageJ.

2) Visual inspection of the images is carried out to assess which image slice to use. For the WIT phantom this should enable the ROI to be placed in a clear region of signal change in close proximity to, but not overlapping, the central wire. This is usually clearly identifiable as a darkened dipole lobe shape in images when the phantom is activated. For the CAT phantom this is the slice closest to the middle position of the two coils. This image will be the image that is the least distorted by the two coils. Due to manual slice prescribing and inaccuracies in coil construction this is not necessarily the central slice of the image stack.

a) 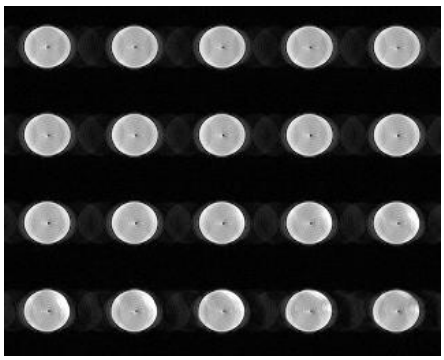 b) 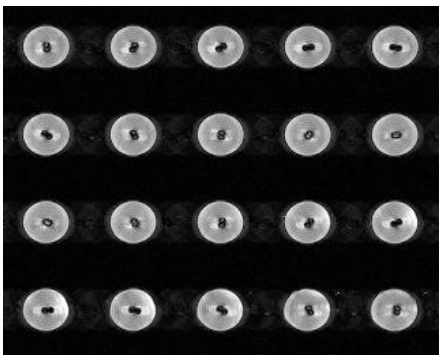

Fig. 3.3 *– Example montage of slices from a single volume of a WIT EPI scan. a) Phantom current OFF. The central wire is visible as the small distortion near the centre of each slice. b) Phantom current = 107mA. Signal attenuation is clearly visible as the darkened region around the wire position at the centre of each slice.*

a) 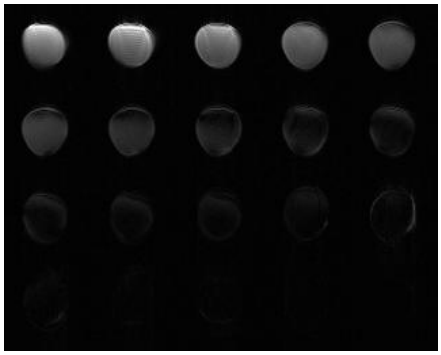 b) 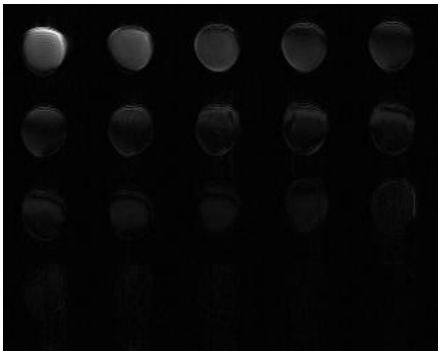

Fig. 3.4 *– Example montage of slices from a single volume of an early test of a Multicoil CAT EPI scan. Stack was not correctly aligned but is an example showing an obvious signal attenuation. Later CAT scans were performed with low currents and so not easily distinguishable to the eye. a) Phantom in state. b) Phantom in the ON state (I=20mA) showing darkened images demonstrating slice wide signal attenuation.*

3) Once the correct slice has been identified a ROI is selected as per the requirements of Chapter 3.1.1 to give signal or noise traces from that ROI over the scan period (Fig. 3.5). Values for ROI signal mean and standard deviation for each volume are measured using a MATLAB script.

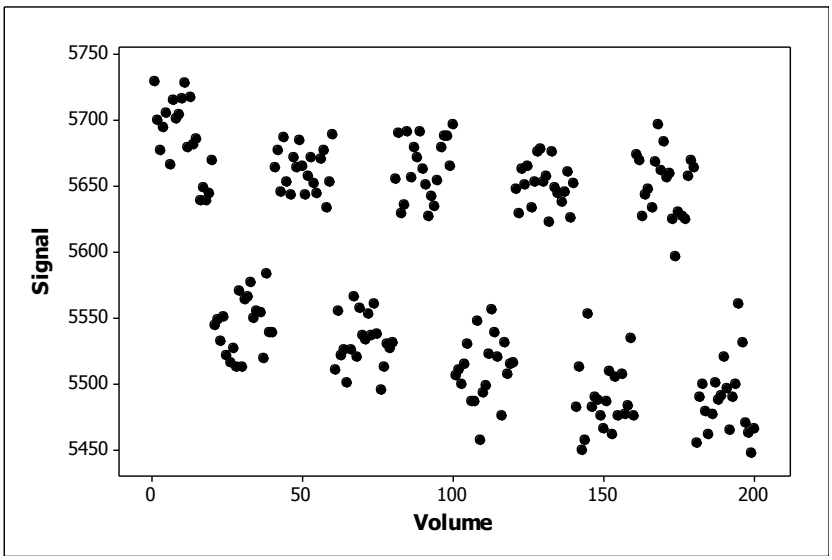

Fig. 3.5 *– Example signal trace from fMRI Phantom experiment. (Experiment GL.1 I = 3.0mA)*

4) These measurements were then inputted into statistics package (Minitab 16.1.1) to calculate a number of descriptive statistics used to assess image quality. These include the mean difference in signal between the ON/OFF phantom states (|ΔS|), the overall Response of the system to generated signal contrast, Signal-to-Noise Ratio (SNR) for both current states and functional Contrast-to-Noise Ratio (fCNR), etc. These measures are explained in more detail in Chapter 3.5 below.

5) A 2-Sample T-Test is used to check for statistically significant differences between the ON/OFF signal states using a threshold of $p \leq 0.05$. The data is also visualised so any volumes exhibiting unusual behaviour, sudden signal change 'steps' and other anomalous features across the duration of the scan can be identified. Histograms of the data from individual states are also generated to visually check that the populations of each signal state are distributed approximately normally.

3.2.2 Method 2: SPM

MATLAB can be equipped with a software suite known as the Statistical Parametric Modelling toolbox (SPM 8 used). This toolbox is commonly used in the neuroscience community for the processing of functional brain data from a variety of sources including fMRI as well as other functional brain imaging modalities such as magnetoencephalography (MEG). It performs the same basic statistical operations that the manual method outlined

above does, but over a whole stack of slices rather than just one. In addition SPM also includes a tool set for the preparation of *in* vivo animal data for fMRI analysis.

These steps are unnecessary with the fMRI phantom due to the simple structure of the phantom and its lack of physiological noise. In fact the signal change generated by the phantom data is mistaken by SPM's standard realignment pre-processing algorithms to be motion noise and thus eliminated if pre-processing is applied. Because of this many of the normal pre-processing steps that would be performed with an *in vivo* subject, including motion realignment of images, are deliberately not implemented on the fMRI phantom data. It is acceptable to do this as we can assume there has been little to no movement over the duration of the scan that those algorithms usually track and correct for.

As SPM is designed to operate with human brain sized data all image sets are rescaled by a factor of 10 in order to bring them up to an image scale more in line with what SPM is optimised for. An additional toolbox, MarsBaR [Brett 2002], allows measurements of signal change in percentages for specified ROIs. This output is comparable with the signal change results from the manual method outlined earlier.

3.3 Data Analysis Outputs

A number of useful image quality and performance parameters can be extracted from these methods.

1) **|ΔS|** - The percentage change in signal between the activated and non-activated signal states for a specified ROI.

$$|\mathbf{\Delta S}| = \left(1 - \left(\frac{SIGNAL_{ON} - SIGNAL_{OFF}}{SIGNAL_{ON}}\right)\right) * 100 \qquad \text{(Eq. 3.1)}$$

2) **Contrast Response** – An overall measure of the contrast response of the scanner to the phantom. Assessed by measuring a least squares fit to a linear regression model for a values of |ΔS| over a range of currents assuming |ΔS| = 0% when I = 0mA. Measured in units of % mA^{-1}. Since the Contrast Response should be independent of scanner field strength, depending only on the contrast generated by the phantom, the Response should be independent of coil used, scanner field strength or site location. It is preferable to use this value as an overall indicator

of scanner performance rather than individual values of |ΔS| at a particular current as these are subject to minor run-to-run differences.

3) **Standard Error** – A measure of how close the fit of the individual values of |ΔS| are to the Response line. Ideally this should be as small as possible. A large error would suggest a lot of electronic noise in the system.

4) **Pearson Correlation Coefficient (PCC)** – A measure describing the linear correlation between the applied current of the phantom and the signal change in resultant images. Small changes in the value of this could indicate either the beginnings of changes in the behaviour of either the phantom or the scanner. This measure is only valid in current regimes where linear behaviour is approximate. This was the case with the majority of data taken during this project with the final design of the fMRI phantom.

5) **Signal-to-Noise Ratio (SNR)** – Measured for both the ON and OFF states of the phantom individually.

$$SNR = \frac{SIGNAL}{\sigma_{Noise}}$$

where σ_{Noise} is the variance of the signal sampled in a noise ROI.

As changes in SNR are behind the signal switching behaviour of the phantom, SNR should drop when the the current in the ON state. Ideally values for the OFF state should be the same from one experimental run to the next. Extraction of image data to make this measurement is explained in Appendix 1.1

6) **Functional Contrast-to-Noise Ratio (fCNR)**

$$fCNR = \frac{SIGNAL_{ON} - SIGNAL_{OFF}}{\sigma_{NOISE}}$$

This is very similar to the SNR but measures instead the signal difference between the two current states divided by the average noise in the image. For calculation methodology see Appendix 1.1. fCNR is a measurement of how

significant a signal change from a particular current is compared to the normal background noise fluctuations present in the image. If scanner performance is repeatable identical values should be returned for identical current values using the same experimental set up. fCNR should only change when using different coils.

For measurements taken using the fMRI phantom any changes or differences to these parameters across time or between sites would indicate variations in scanner performance that are independent of any *in vivo* subject physiological noise variations. If there are variations present then it would suggest that the performance of the scanner and associated equipment is changing. Ideally these parameters should stay at constant levels so that confidence in scanner performance over extended periods can be assured and therefore *in vivo* experimental results acquired at multiple sites at different times can be considered genuinely comparable.

A commonly used measure of assessing fMRI results is the cluster size of significant activations [Heller 2006, Mezer 2009]. This hasn't been explored here in themselves as the fMRI phantoms (particularly the CAT design) produce a 'slab' of uniform activation rather than individual localised clusters of activation. Additionally the measures outlined above provide a somewhat more intuitive understanding of scanner performance outside of the biological arena. However, the statistical techniques that underlie the clustering technique rely on measurements of SNR and fCNR in order to judge which image voxels they consider to be in a significantly activated state or not. Thus clustering ultimately depends on the stability and repeatability of the image parameters outlined above.

3.4 Noise and Detection Limits

The electronic, mechanical and thermal noise of any MRI system will place limits on the minimum statistically significant signal change detectable in addition to any physiological noise from the subject being scanned. As we are attempting to measure small signal changes of only a few percent, levels of noise induced signal fluctuation in the system should be at even lower levels. Signal changes of less than the noise value in the images will not be visible in the data. This places a detection threshold limit on the minimum $|\Delta S|$ that can be detected.

Spatial measurements of noise were performed on the MRI data rather than measurements of temporal noise since for spatial SNR values at the level obtained in this study temporal SNR becomes saturated and unchanging [Murphy 2007]. Noise sampling must be made in a

region outside of the phantom and to the side of the phantom so that any ghosting artefacts in the phase encode direction are minimised in the noise measurement.

Detection threshold limits for |ΔS| will be dependent on the performance and specification of the coil used for signal detection at the time of acquisition. Although many of the sites that scans were performed at had coils of the same manufacturing specifications and origins, they were manufactured at different times and had been subjected to different experimental loads over their usage. The differing sites also tended to have different past maintenance histories for the coils which could lead to subtle differences effecting fMRI performance.

The minimum |ΔS| and associated current can be measured experimentally by reducing the phantom current successively over a number of EPI scans. This can be done by monitoring the magnitude of |ΔS| as input current to the phantom is reduced, and noting when fCNR reaches a statistical significance value of $p>0.05$ (or another chosen statistical threshold value).

Measurements of detection limits are particularly important when consolidating data in fMRI studies across multiple sites. What appears on one system as a statistically significant result at one site may have less statistical power or even an insignificant value at another site working with a system that generates a greater amount of noise. If differences in the minimum |ΔS| vary too greatly between sites then it is likely that some *in vivo* effects will go unnoticed at some sites increasing the likelihood that erroneous biological conclusions will be drawn.

Additionally if noise increases over a system's lifetime what may have once been a significant result at one time point may not be at a future point. This is of particular concern for smaller effects with values of |ΔS| that might be close to the detection limit of a scanner.

3.5 Experimental Parameters and Procedure

Other than for the Multisite study using the final CAT design (Chapter 6) scans were performed using the7MRI scanner at the Edinburgh Preclinical Imaging Centre, University of Edinburgh, UK. The Edinburgh scanner is a preclinical 7T MRI system (Direct Drive, Agilent Technologies). For fMRI phantom experiments it was equipped with a 205 gradient (gradient strength = 1000mT m^{-1}). Two coils were used - a two channel rat brain phased array coil (Rapid Biomedical) in combination with a 72mm volume transmit coil.

The phantom is loaded into the scanner, securely fixed in position against the surface of the phased array coil for the duration of an experiment. For WIT experiments the region of

twisted wires is placed directly beneath the imaging sensitive region of the phased array coil. Similarly, the CAT coils are located either side of the centre of the expected imaging area.

The system is then optimised for scanning using standard procedures of frequency optimisation, power calibration and automated shimming (Chapter 2.3.1). Two slightly different orientation and MRI acquisition protocols were used for the two different types of phantom and these are outlined in the appropriate sections later in this chapter.

3.6 fMRI Phantom Prototypes

3.6.1 Design 1 – WIT fMRI Phantom

3.6.1.1 WIT Basics

This design consists of a tube of rape seed oil as a resonating medium with a wire running down the centre of the tube. The wire is folded back and twisted around itself, entering and exiting the phantom at one end of the device, while hooked onto the interior base of the tube on a suitable attachment point. Current flowing in this wire induces signal dropout in the regions immediately surrounding it by creating signal altering magnetic field gradients emanating away from the wire.

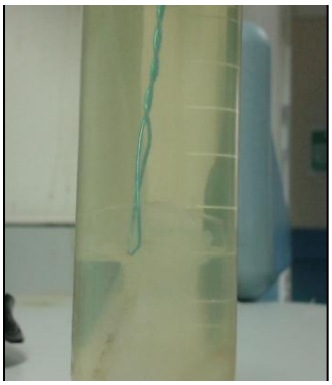

Fig. 3.6 *–Example WIT phantom used in experiments. Compare with Fig. 3.1a.*

Two lobes of signal dropout appear around the twisted wire, appearing as a dipole shape around the wire (highlighted in yellow square in Fig. 3.7). As scans are taking along the length of the wire the lobes of the can be seen rotating with position around the central axis as the wire twists over itself.

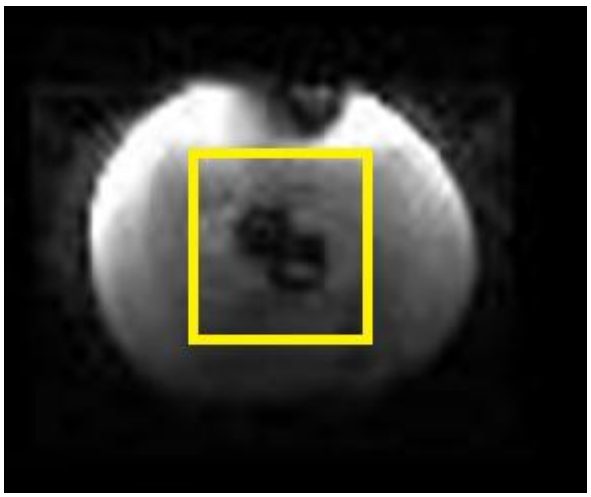

Fig. 3.7 *– Axial cross-sectional scan of WIT phantom when activated. Signal drop out in regions surrounding the central wire are clearly visible within the yellow square.*

The signal decays away from the wire coil rapidly and so there is only a limited distance from which a measurement can be made. Because of this any magnetic influence it might have on nearby potential animal subjects or equipment should be limited. The phantom that was constructed and tested had a diameter much larger than it needed to be. This was primarily for ease of construction and fixation within the scanner.

The potential for image artefacts caused by the currents running into and out of the image plane (and so along the z-axis) is greatly reduced by having the twisted pair as most effects of the current going in will be negated by the close proximity of the wire carrying current out.

3.6.1.2 Construction

Construction of three WIT design phantoms was attempted which resulted in one device that was deemed suitable for EPI testing in the scanner. Construction of the phantom proved somewhat problematic. It required the simultaneous assembly and manipulation of a number of crude hand-made parts, alongside the use of oil-based liquids that hindered the fusing of the phantom components into the final device.

It was especially difficult to correctly recreate identical twisted wire pair geometries over multiple phantoms. Even within a single phantom the node-to-node spacing of the small wire loops varied along the length of the phantom. This would affect the properties of the magnetic field gradient produced, thus altering signal properties between phantom units. In addition when the phantoms had been assembled and the bonding agents that were used to

fix components together were setting there was a tendency for the twisted wire to untwist within the tube and disrupt the rest of the phantom assembly in doing so.

If the WIT design was to be carried forward then several improvements to the manufacturing process would be necessary. For example the phantom tube could be 3D printed as one component rather than by assembling several interdependent components. A simple solution to the wire untwisting would have been to fix the wire into a more rigid position prior to inserting it into the phantom tube - perhaps by spreading a thin layer of glue or resin along the length of the twisted wire when it was originally twisted and under tension. However this might reduce the proximity with which useful measurements could be made to the wire which could impact on image parameters.

3.6.1.3 Experimental Testing Parameters

Images from the WIT experiments were acquired with the GE-EPIP sequence using the following parameters.

Parameter	**Value**
TR	3000ms
TE	12.14ms (minimum)
k_o	32
Shots	1
Volumes	105
Gain	10
Field of View (FOV)	51.2 x 51.2 mm
Matrix Size	64 x 64
No. of Slices	14
Slice Thickness	1mm
Interleaving	Yes
Referencing	Triple
Frequency Encode Bandwidth	250kHz

Table 3.1 *– WIT Phantom specific imaging protocol.*

Current was provided by a somewhat aged constant current source (Farnell FAO601 Tops 2). Switching between the current states was performed manually using the on-board switch of the power pack. Current levels were calculated by measuring the voltage across the current source terminals and dividing by the resistance of the circuit as a whole. The ordering of current values was not systematic at the point of acquisition in order to eliminate any trend from potential current bias. Circuit resistance was physically changed by swapping resistor components inserted into the circuit. Resistance from the wires involved in all phantom designs was negligible compared to the resistors inserted into the phantom electrical circuit.

Measurements were made within a single slice with a 3 x 3 pixel ROI positioned just off to one side of the central twisted wire in a region found to give a strong signal change.

3.6.1.4 Results and Discussion

Signal Change / %

Current / mA	**2.29**	**2.74**	**4.81**	**19.15**	**33.0**	**49.7**	**107**
|ΔS| / %	2.83	3.06	6.05	11.7	14.2	5.26	48.0
S1NR – ON	61.9	72.9	62.1	59.7	53.9	59.4	36.4
S2NR – OFF	63.7	75.2	66.1	67.6	62.8	62.7	70.0
fCNR	1.81	2.29	3.93	7.89	8.88	2575	33.9

Table 3.2 *– Summary of Results from Initial Trial of fMRI Phantom WIT Design*

Activation of current in the phantom caused signal drops as predicted. Values for both |ΔS| and fCNR increased as current applied increased as expected. High values of current produced very high levels of signal change approaching total attenuation values (up 92.3%).

|ΔS| and CNR were noticeably atypical in I=49.7mA. It is suspected that some of the components of the system were damaged in the experimental run immediately before this value was tried. Because of this values for 49.7mA have been excluded from subsequent signal response calculations.

Contrast Response

Linear regression values were obtained to give a measurement of the Contrast Response of the system.

	Contrast Response / % mA^{-1}	**Standard Error / % mA^{-1}**	**PCC**
WIT Test	0.45	0.05	0.98

Table 3.3 *– Summary of calculated response values for WIT design phantom.*

At the measured ROI the WIT phantom provides a strong response to current. The value of the PCC test is questionable at the high current regieme given the non-linear relationship between |ΔS| and current at high current values (Chapter 4.6). It can be seen (Fig. 3.8) that the remaining high current value is having a disproportionally stronger effect compared to lower current values on |ΔS|. This agrees well with later theoretical modelling of signal response (Chapter 4.6).

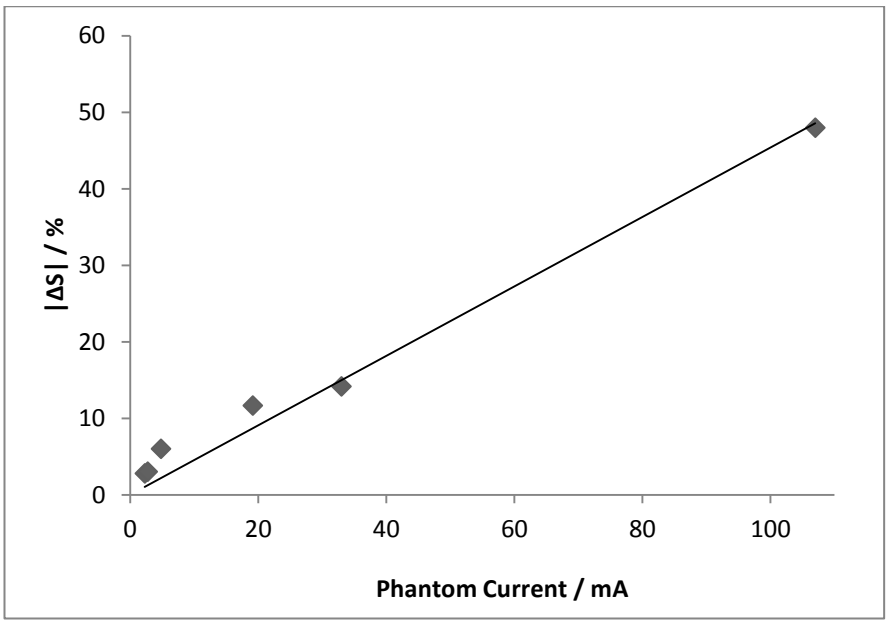

Fig. 3.8 *– Scatterplot of WIT |ΔS| Results*

3.6.1.5 WIT Conclusions and Summary

Although current induced signal change measurements can be performed with this design the rapid drop off in signal strength as the ROI moves away from the central axis of the twisted wire in the WIT design severely limits the size of ROI that can be used. This in turn limits the number of useful voxels it can contain and so it's statistical validity.

Since the twisted wire pair is acting as a rotating dipole, the signal strength for a particular ROI position also varies as a function of distance along the wires and axial position around the wires. This creates large problems for maintaining good signal repeatability when constructing and/or positioning the phantom. In addition the signal will also vary dependent on the physical configuration and geometry of each individual wire in different constructions of the phantom. These are all factors that are extremely difficult to control during the construction phase using locally available construction facilities. This makes creating like-for-like construction of WIT phantoms somewhat impractical at present.

It was also difficult to find a ROI of sufficient quality in a set of scan data to make like-for-like measurements at different selected ROI positions along the phantom wire. Further problems arise when attempting to compare data from separate scanning sessions when the phantom has been removed from and subsequently repositioned within the scanner. Some sort of labelling system for the ROI position being used in relation to the physical position in the coil would need to be created.

Additionally the central positioning of the twisted wire pair in the tube is difficult to reproduce between phantoms. This meant that the wires in different tubes occupy different 'lines-of-sight' down the scanner bore from one experimental run to another. This would alter the dephasing magnetic field gradient path from one phantom to another, altering the amount of signal change dependent on which phantom was used. This would make it difficult to establish or compare one set of phantom data to the next and to attribute any changes in performance solely to the scanner's performance.

One considerable positive of the WIT design is that the wires involved create little image distortion or artefact which enables scans to be taken using the Triple Referencing EPIP option, rather than the Full Triple Referencing needed for the CAT design. This results in an acquisition time of approximately half that of matching CAT EPIP scans.

3.7 Coil around Tube design

3.7.1 Design 2 – Multi-Loop CAT fMRI Phantom

3.7.1.1 CAT Basics

This design consists of two wire coils surrounding a 16mm diameter tube of Gd-doped water (doped with 279.32mgml^{-1} Gadoteric acid according to Ranvell 2009a) for the resonating medium. The two coils were positioned approximately ~1cm apart. The region between the two coils is then imaged.

When current is applied in opposite directions to each of the coils they create a magnetic field gradient between the coils, which introduces additional dephasing to the MR signal, leading to a net reduction in signal level. If the current is in the same direction a uniform magnetic field forms between the two coils instead. This field has a gradient of zero and so causes no signal dephasing. The properties of this field for a particular coil geometry and current pattern is described by the Biot-Savert Law (Chapter 4.3).

Fig. 3.9 *–Multi-Coil CAT fMRI phantom used in experiments. Compare with Figure 3.1b.*

Simulations of these current induced magnetic fields (Chapter 4.4) show that only at the centre of the inter-coil volume possesses an isotropic gradient and it is in this region that the sampling ROI is placed. The cross-sectional area of this region is less than that of the phantom itself. This combined with the desire to sample an adequate number of voxels with the ROI means that there is a minimum size necessary for the phantom. This will depend on the imaging resolution used. In realistic cases where resolutions match that of *in vivo* imaging and also simultaneously don't exasperate gradient-induced artefacts this means that a CAT phantom is unlikely to be constructed at a small enough scale to fit into a coil set up alongside a live animal subject.

3.7.1.2 Construction (Design 2 - Multicoil)

Production of the CAT-based phantoms is remarkably straightforward compared to that of the WIT phantom as there are a minimum of parts and the design is simple. A tube of suitable size to fit the phased array coil is filled with a resonating medium (water and Gd contrast agent). The tube is sealed to prevent leakage. Wire coils are then wrapped around the outer surface of the tube and bonded to it to hold the coils in place.

3.7.1.3 Experimental Testing Parameters

The phantom was set up in the scanner as per the WIT method

For the CAT phantom experiments a stack of 14 axial slices, prescribed along the central axis of the phantom, are acquired with Gradient-Echo EPIP (GE-EPIP) according to the parameters in Table 3.4 below.

Parameter	Value
TR	3000ms
TE	14.02ms (minimum)
Echo Train Length	64
Echo Spacing	0.376ms
k_o	32
Shots	1
Volumes	200
Gain	10
Field of View (FOV)	25.6 x 25.6 mm
Matrix Size	64 x 64
No. of Slices	14
Slice Thickness	1mm
Interleaving	Yes
Referencing	Full Triple
Dummy Scans	2
Spectral Width	250 kHz

Table 3.4 *- EPIP imaging protocol for CAT fMRI Phantom*

Matching fast-spin echo multi-slice (FSEMS) images were taken according to Table 3.5 for potential anatomical realignment and referencing.

Parameter	Value
TR	3000ms
TE	14.02ms
k_0	32
Shots	1
Volumes	200
Gain	10.0
TEP	AUTO-SET
FOV	25.6mm x 25.6mm
Matrix	64 x 64
Slices	14 or 15
Slice Th.	1.00mm
Interleave	YES
Dummy Scans	x 2
BW	250kHz
Referencing	Full Triple

Table 3.5 *- FSEMS imaging protocol for CAT fMRI Phantom*

Given the observed range of signal change experienced by the phantom during the WIT experiments, focus in the CAT experiments shifted to lower currents that would provide

more realistic matches to biological BOLD signal changes. Additionally focusing in this region where current change had been observed to be near linear, would also enable the reliable deployment of PCC measurements to monitor the performance of the phantom itself.

3.7.1.4 Study Results

Results from the initial CAT experiments are shown below in Table 3.6. Only five current samples were measured due to the increased time necessary for EPI acquisition as with the CAT phantom it was necessary to use the Full Triple Referencing options to reduce artefacts induced by the presence of the metallic coils in the FOV to a reasonable level.

Signal Change

Current / mA	**0.13**	**0.90**	**1.61**	**5.01**	**13.3**
Signal Change / %	0.12	0.86	1.43	4.18	10.9
S1NR – ON	42.2	42.6	41.6	43.1	35.8
S2NR – OFF	42.2	42.9	42.2	44.9	40.0
fCNR	0.05	0.36	0.60	1.80	3.88

Table 3.6 *– Summary Results for fMRI Phantom Design 2 CAT Design.*

Again, activation of current in the phantom caused signal drops as predicted. Values for both |ΔS| and fCNR increased as current applied increased as expected. Of particular note is the ability to measure very low statistically significant signal changes down as low as 0.12% in this example.

Contrast Response

Linear regression values were obtained to give a measurement of the response of the system as before. These results indicate both a strong response in line with that of the WIT phantom but also with a smaller amount of error involved. This is evidence suggesting that the enlarged ROI of the CAT phantom (10 x 10 voxels) compared to that of the WIT ROI (3 x 3 voxels) is indeed reducing the influence of background noise fluctuations on the measurements. The very high PCC value also suggests a strongly linear relationship between current and signal change within the range of currents specified.

	Contrast Response / % mA^{-1}	**Standard Error / % mA^{-1}**	**PCC**
ROI Method	0.82	0.01	1.00

Table 3.7 *– Summary of calculated response values for fMRI Phantom Design 2 – Multicoil CAT Design.*

This better fit to the data can be seen visually in Fig. 3.10 below contrasted with Fig. 3.8 from the WIT study.

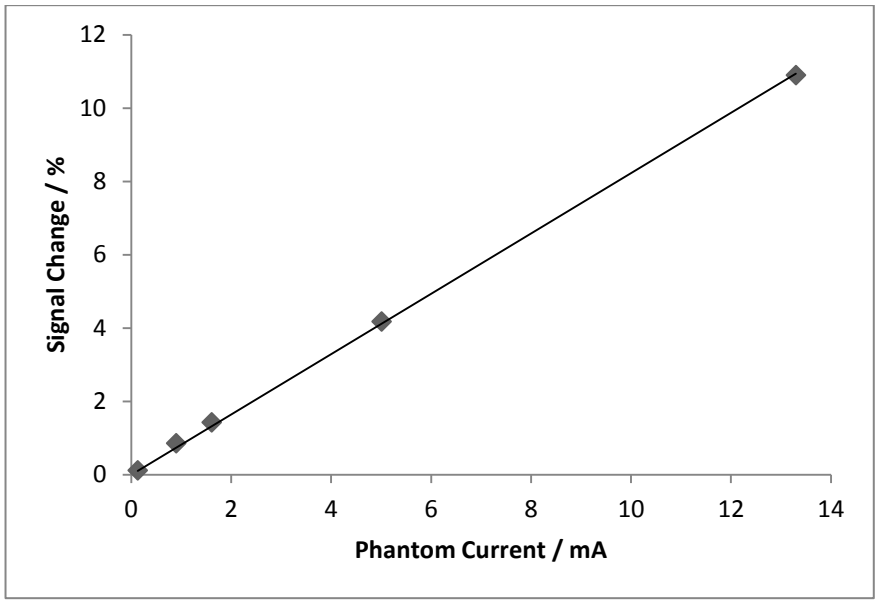

Fig. 3.10 *-|ΔS| vs. applied current for the Design 2 CAT phantom.*

3.7.1.5 General Conclusions and summary

Construction of the CAT phantom is fast, simple and low cost. The geometry of the wire coils around the phantom would be easy to replicate or modify depending on the precise tuning of the phantom characteristics one might desire. By having a comparatively large volume of material experience a uniform magnetic field gradient it becomes less important to position the phantom identically each time as ROI selection becomes more important in the image analysis stage rather than at acquisition. The cylindrical geometry of the phantom and accompanying coils also ensures that there is no preferential rotational position for the phantom that can be unintentionally varied between experimental sessions. This is provided of course that the two coils are correctly aligned on the surface of the phantom resonator.

The central slice of the image stack was selected by initially locating the gap between the coils on the FSEMS images (where the coils are visible) and then looking within this selection for the slice showing the least visual distortion in the GE-EPI images as the central slice typically exhibits the most circular cross section in the stack and has no (or minimal) inter-state signal transients when |ΔS| is plotted against time. Using MATLAB a mean image can be generated (as part of the output of the ROI selection script. This mean image can then be used to localise an area of relative image uniformity on which to make final ROI measurements.

Overall the construction of this design of phantom is simpler, measurement making is more repeatable and image performance improves on that of the WIT design. This justifies concentrating further efforts to solely develop the CAT design to generate a working fMRI phantom for use in subsequent studies.

3.7.2 Design 3 - Helmholtz Single Coil CAT Design

3.7.2.1 Modifications to CAT Design

Having selected the CAT design for further development two major modifications were made to Design 2 to generate the next CAT phantom iteration.

- In order to generate a properly configured uniform magnetic field gradient between the coils the coil geometry was specified to follow that of a Maxwell geometry. This is detailed more in Chapter 4, but essentially it involves positioning the coils a specific distance apart based on their diameter.
- Only a single loop of wire per coil was used rather than the multiple loops of Design 2. There were a number of good reasons for doing this. Firstly for providing a baseline minimum design and associated functional properties that could be enhanced upon, if necessary, by simply adding more coils to the phantom in a controlled manner once the properties of the single coil system were more fully understood. Secondly the multiple coils used before generated values of $|\Delta S|$ in a regime still higher than that typically seen *in vivo*. Fewer coils would mean less a weaker magnetic field gradient between the coils and so less signal attenuation due to dephasing. Thirdly a multiple loop phantom with the coils spread out along the length of the phantom resonator would be more complex to model in the MATLAB simulations. A single coil system would again simplify things greatly there.
- Since the coil number was now much reduced it becomes more difficult to locate the coils in either the FSEMS or GE-EPI images as the reduced number of coils produces lower image distortion. To location of the coils when the phantom was being scanned two small Eppendorf capsules were filled with water and secured to the side of the resonator. The tips of these were approximately positioned parallel with the coils and since they would be visible in both types of scans it became a simple matter to locate the coils within the scanner FOV.

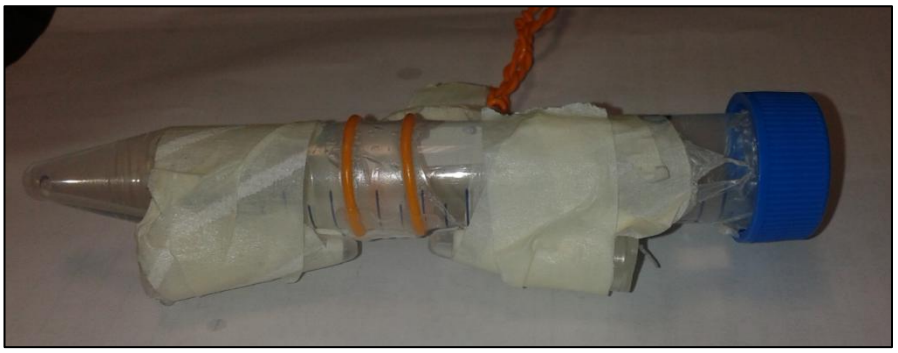

Fig. 3.11 *– Final Helmholtz CAT fMRI phantom resonator used in all subsequent experiments. Compare with Figure 3.1b.*

3.7.2.2 Construction

The construction process of this phantom was similar to Design 2. The only major difference was ensuring that the coils themselves matched the calculated Maxwell geometry positioning. This proved more difficult than anticipated and while the resultant device approximates the correct theoretical positioning of the coils, the actual coils are both at a very slight angle relative to the cross section of the tube. More advanced construction methods would overcome this problem.

The coils were fixed to the outside of the tube using a PVC plastic bonding agent (PVC Pipe Weld Extra Strong, Evo-Stiik) and then left to fix. The two lengths of wire coming from each coil were then twisted around each other to reduce signal interference from the long lengths of wire (>3m) needed to connect the coils to the current source located outside the scanner room.

For the new design current was supplied from single 9V batteries as an alternative to the mains supplied constant current power source used for the earlier tests. The two main reasons for doing this were to avoid signal spiking from possible voltage surges from the mains source and also to increase the overall portability of the system in anticipation of multisite studies. Switching was still performed manually but now using a separate switch inserted into a breadboard circuit set up. Circuit resistor values were selected to provide current levels to match those used in Design 2 experiments.

3.8 Multisite Testing of Design 3

The Design 3 phantom was initially tested at Edinburgh and then taken to three other preclinical MRI sites for comparative testing. If the behaviour of the phantom was identical at each site then the Contrast Response generated at each site should be identical. Other

results such as SNR and fCNR would obviously be dependent on different coils used. As this point however the primary interest was to ensure that the Contrast Response to the phantom is identical across the four sites in order to validate the phantom device itself rather than using it to begin interrogating scanner quality at this stage.

The Edinburgh results for this multisite study are those from the initial testing of Design 3 (Chapter 3.7.2).

3.8.1 Experimental Details

Exact equipment varied between the different sites but as close a match as possible to the Edinburgh set up was attempted to create as similar experimental conditions as possible. Improved SNR and fCNR would be expected at sites using phased array coils compared to those without. Further improvements would also be expected at sites with phased array coils that utilised higher numbers of coil elements.

Site	Scanner Type	B_0 Field Strength / T	Coil Used
Edinburgh Preclinical Imaging, University of Edinburgh, Edinburgh, UK	Agilent (Varian) Direct Drive	7	Rapid 72mm volume + 2-channel Rapid Rat Brain Phase Array.
Glasgow Experimental MRI Centre, University of Glasgow, Glasgow, UK	Bruker BioSpec	7	Rapid 72mm volume coil + Rapid 4-channel Rat Brain Phase Array.
Preclinical Imaging Unit, Kings College London, London, UK	Agilent (Varian) Direct Drive	7	Rapid 72mm volume.
Applications Lab, Agilent Technologies, Oxford, UK	Agilent (Varian) Direct Drive	7	Rapid 72mm volume + 4-channel Rat Brain Phase Array.

***Table 3.8** - Site specific details for the four MRI sites used in this initial multisite study.*

Experimental parameters and procedures used were there same as those for the Design 2 Multi-coil CAT Phantom (Chapter 3.7.1.3).

In Glasgow, as the system was manufactured and supplied by Bruker rather than Agilent, the scanner was not running the Agilent-specific EPIP sequence but a Bruker EPI equivalent sequence instead. The scans at Glasgow were run in a standard '*in vivo*' manner to match working conditions as close to local standard procedure as possible. These scans had a matrix of 96 x 96, but all other parameters were adjusted to match as closely as possible those used on the Agilent scanners at the other sites.

3.8.2 Results and Discussion

Signal Change

Current / mA	**0.90**	**1.61**	**5.01**	**13.3**
Edinburgh / %	0.25	0.55	1.81	5.54
Glasgow / %	0.58	0.72	1.76	10.3
KCL / %	-	-	1.80	2.43
Agilent / %	0.27	0.53	1.27	2.35

Table 3.9 *– Multisite results for |ΔS| from Design 3 at four different preclinical MRI sites*

Current values were not tested as low as in the Design 2 stage as there were equipment failures when visiting the first site external site. Because of this and in order to decrease the total testing time, the lowest current value was dropped from this initial multisite test. A fresh 9V battery was used at each site.

The signal change generated for a particular current value varied at each site. Although there are some points of cross over at some sites especially at the lower currents used. This was unexpected and implied the phantom was generating different dephasing effects at each site. Additionally at KCL no detectable signal change was identifiable at the two lowest current values attempted (0.90mA and 1.61mA) whereas they produced a detectable signal at all other sites. As the KCL experiments were performed without the benefit of a multi-channel phased array coil it is not too surprising to see some differences in performance between this site and the others. However this already provides early data that coil selection is critical for the interpretation of fMRI results.

S1NR - OFF

Current / mA	0.90	1.61	5.01	13.3
Edinburgh	168	172	166	168
Glasgow	28.9	30.4	31.7	31.9
KCL	-	-	95.1	93.9
Agilent	155	152	158	155

Table 3.10 *– Multisite SNR values with the phantom in the OFF state.*

S2NR - ON

Current / mA	0.90	1.61	5.01	13.3
Edinburgh	168	171	163	159
Glasgow	28.7	30.2	31.2	28.9
KCL	-	-	93.2	91.7
Agilent	155	151	156	151.5

Table 3.11 *– Multisite SNR values with the phantom in the ON state.*

With the phantom in the OFF state (i.e. a baseline level), SNR generally remains at a constant level at each individual site as would be expected. Actual SNR values vary between sites, noticeably decreased at Glasgow compared to Agilent where the equipment set up used is like-for-like. There is good agreement between Edinburgh and Agilent as well. KCL, using a volume coil, would be expected to give a lower OFF value of SNR which it does. The major difference at Glasgow however would imply something is creating a greater level of noise in this system. The gradients on this system are not as powerful and so shimming was not performed to as high a standard as on the Agilent systems. This would leave EPI data from Glasgow more likely to be affected by various EPI artefacts, possibly elevating background levels of image noise and ghosting.

fCNR

Current / mA	0.90	1.61	5.01	13.3
Edinburgh	0.42	0.93	2.94	8.81
Glasgow	0.17	0.22	0.55	2.98
KCL	-	-	1.69	2.24
Agilent	0.43	0.80	1.98	3.56

Table 3.12 *– Multisite fCNR values from the fMRI phantom.*

As expected from the widely varying values of |ΔS| the values for fCNR follow this variation as well. One particular surprise was the strong performance by the Edinburgh scanner in comparison to the Agilent system that utilised a phased array coil with twice as many receiver elements. This should have lowered the noise level in the combined coil resulting in a boosted fCNR at Agilent compared to Edinburgh. Despite some early level agreement at 13.3mA it is <50% of the value of Edinburgh's at the higher current levels.

Contrast Response

Site	Contrast Response / % mA^{-1}	Standard Error / % mA^{-1}	PCC
Edinburgh	0.41	0.01	0.999
Glasgow	0.72	0.08	0.978
Kings College London	0.21	0.05	0.930
Agilent (Oxford)	0.19	0.02	0.989

Table 3.13 *– Multisite Contrast Response from the fMRI Phantom.*

The Contrast Response varied across sites, which was not unexpected given the range of difference of |ΔS| across the sites. It is difficult to properly interpret the usefulness of the PCC measurement here and the accompanying assumption of signal linearity given the lack of mid-high current point within the data. Again there seems to be a 'clustering' of values at low current values and a potentially over influencing effect of the single high current value. The KCL data must also be treated with extra caution given that it is based only on two data points.

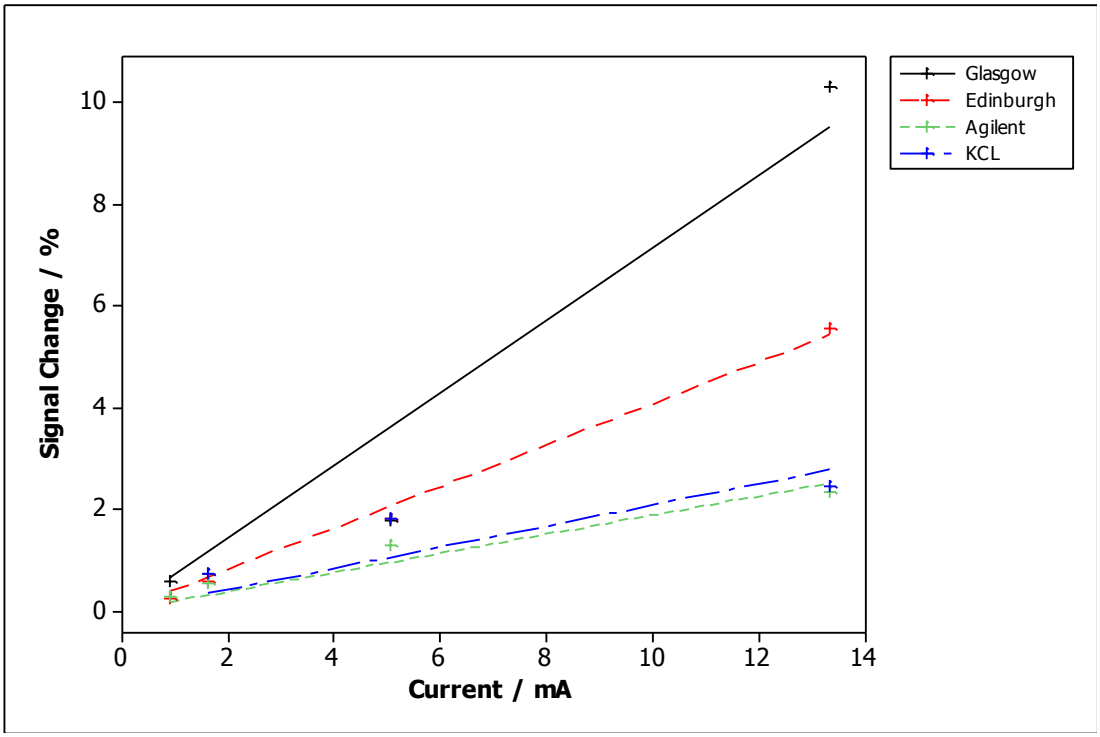

Figure 3.12 *– Linear fits to |ΔS| vs. phantom current for the initial battery powered Design 3 multisite testing. No site displays the same response from what were calculated to be same input currents.*

Despite the wide variation in Response all sites show a reduced Response compared to the multi-coil Design 2 which was as expected given the fewer number of turns of wire per coil compared to Design 3. At this point though, given the range of Response values, it is difficult to determine if this is more from design or just from good fortune.

The Contrast Response should be independent of scanner type, scanner primary field strength and coil set up used. The only reason for it to vary as dramatically as seen is if the input current was also varying. At each site a new battery from a standard 9V multipack battery set (Maplin) was used. It was not possible to measure the current of this set up directly during the EPI testing procedure. This unfortunately meant we had to rely on the commercial rating information on the battery labelling itself to provide information about the operating characteristics of the batteries and Ohm's Law (V=I*R) to calculate current values. It is likely that differences between the initial states of these batteries combined with the non-linear nature of the phantom response at high currents, which also only approximates a linear nature at low current values, (in fact a sinc function as realised after these particular experiments and subsequently outlined later in Chapter 4) are at the route of these discrepancies.

3.8.3 Comments on Inter-State Signal Spiking

Over the course of the three initial studies prototyping the phantom it was noticed that when switching phantom states there seemed to be a spike in signal attenuation during some of the inter-state volumes (Fig. 3.13). This spike was well outside the range of signal change created by dephasing by the phantom gradient. Initially it had been hoped that this was due to instability in the mains supply used on the constant current source and was one of the reasons for switching to the battery current source. Affected volumes were manually excluded from the data analysis procedure which was not only time consuming but also resulted in loss of data of up to 5% in terms of volumes gathered.

These intermittent inter-volume signal spikes, however, remained present with the battery source, suggesting this source as well was not immune to signal spiking. Their sporadic appearances suggested they were to do with the exact timing of the switching between states as well, which at this point was still performed manually at any point in the 6 seconds available during the switch over volume.

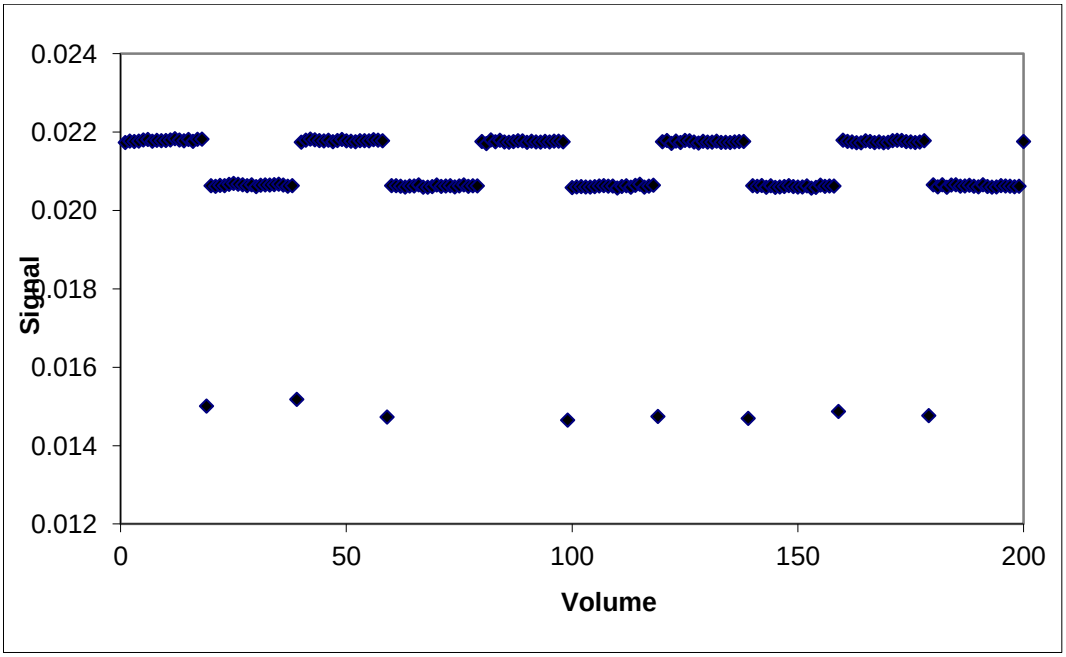

Fig. 3.13 *- Example of intermittent Inter-block signal spikes appearing in signal output. Design 3 CAT fMRI Phantom with battery power source.*

3.8.4 General Conclusions and Summary

Signal change was successfully accomplished at each site visited. However, all of the sites produced widely different results for all imaging output parameters. Some of these differences could be regarded as arising from differences in equipment available at the

different sites and/or different levels of quality in initial set up. The differences in Contrast Response suggest alternatively that much of the variation has come from non-identical current sources creating different effects on the MR signal at the different sites.

If the phantom performance is to be relied upon for routine quality assurance testing and inter-site calibration a more robust and reliable current source is therefore required.

3.9 Summary Discussion of fMRI Prototyping

Although the WIT design is the more plausible design for any future simultaneous phantom/subject scanning it is very impractical in terms of construction. Additionally ROI positioning is currently not robust and compounded by the inexact nature of phantom construction to be realistically useful in the short term.

The CAT design in contrast has a simple construction technique. Artefacts that are produced by the design's coil geometry can be repurposed to assist in correct ROI selection. The geometry of the system ensures a large pool of comparative sampling pixels is available. This results in a more repeatable data analysis technique allowing for measurements to be reliably taken from different scan sessions. Overall the CAT design proved both simpler to construct and subsequently to make measurements upon. Because of this the CAT phantom design was the design carried forward into future studies.

The battery based power supply and simple bread board circuitry set up used for Designs 2 and 3, although very portable, led to performance variations that are unacceptable in a QA device. For a true comparison between sites a new power source needed to be constructed so that there could be confidence in the phantom's performance. This needed to be done before the phantom could be deployed on any further studies investigating fMRI related performance of individual MRI scanners.

3.10 Computer Controlled Current Source (CCCS) Upgrade

Given the problems with the previously trialled current sources - the constant current source (age, lack of portability, signal spiking) and the 9V batteries (inconsistent image output, signal spiking) – there was a strong need to construct a more reliable current source yet one that was still portable enough to be used in multisite studies. In partnership with a local electronics expert (Mr Tom Anderson, University of Edinburgh) a computer controlled digital microelectronic controlled current source was built to meet these criteria.

The associated computer interface allows the setting of arbitrary current values in the range 0-15mA (to give a BOLD-like signal change range), rather than by physically replacing

circuit components haphazardly as before. This not only gave us increased confidence that our currents were real and not subject to the whims of human error in set up, but that they were also stable and repeatable from scan to scan. The new current source also enabled us to easily spread our current values more evenly over the range in which we were interested to provide a fairer sample of values for subsequently calculating the response of the scanner to signal change. This avoided the previous overt influence of single higher current values.

This new device also incorporated a new switching method into the phantom system. Previously the phantom was switched manually between states by an observer watching for the correct volume number to appear on an on-screen readout on the scanner control computer. Under the new design the phantom switching was triggered by the scanner itself. This involved a slight modification to the EPIP sequence so that it would output an extra triggering pulse for every volume of data acquired – modifying the EPIP sequence to one that was named EPIP-Pulse. This was partnered with a second in-house constructed electronic device that tracked these pulses and turned on/off the current source as appropriate. This ensured that current switching happened at the same time points during each scan. This also reduced the need for manual user intervention and associated human error during subsequent scans.

Under test conditions the computer controlled and operated switching system also seemed to eliminate the inter-state spiking previously observed (Fig. 3.13). This provides further evidence that in previous designs the spiking arose from the either or both the timing or choice of switching mechanism and/or choice of current source. The presence of signal spiking in the earlier work by Renvall [Renvall 2009b] that also utilised a battery-based current source also support this origin for the spiking. The inter-state volumes are still neither the signal value of one or the other two primary states, but at a third signal level. However, that signal is now confined to within the signal range of the two different states. It also now appears in every volume which makes data processing more straight forward as these volumes can now be excluded automatically without having to be manually assessed each time.

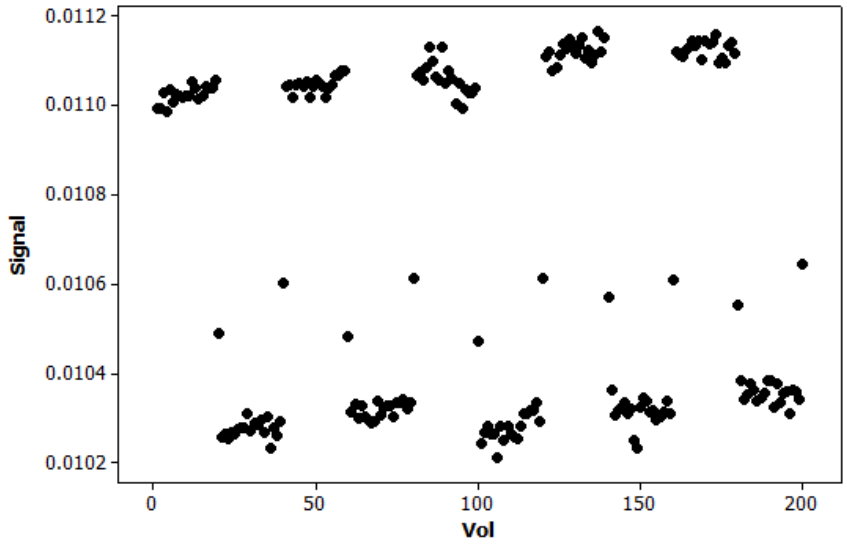

Fig. 3.14 *– Under the CCCS inter-block transients are confined in signal level between the ON/OFF signal state levels (CCCS with Single Coil CAT fMRI Phantom).*

Initially the phantom was in an OFF state when counting began (June 2012-November 2012). In December 2012 the switching circuitry was modified so that the phantom scans would begin in the ON state. Under this mode of operation the phantom no longer relied on receiving a set number of trigger pulses to activate and began scans in the activated state. This meant that we could maintain the ON state without needing trigger pulses. This allowed us to more easily perform non-switching measurements of the phantom in either state. This proved very useful when later making other basic MR material property measurements of the phantom using non-EPI sequences (Chapter 3.12).

This system of automated switching and the new current source is known as the Controlled Constant Current Source (CCCS). The entire fMRI phantom kit fits into a protective carry case that is easily transportable between sites (Fig. 3.15C).

a) 

b) 
c) 

Fig. 3.15 *– a) CCCS Single Coil CAT fMRI Phantom software interface b) hardware and c) packed into transport carry case .*

3.11 Finalised Coil EPI Testing (Design 3 + CCCS)

3.11.1 Experimental Procedure

Using the new CCCS system and switch box we ran a series of tests to check the repeatability of the signal changes generated by the phantom. The phantom was scanned over a three day period with three consecutive scans on the third day so that variations in both inter- and intraday performance might be assessed. During this period the phantom was not removed from the scanner.

Day	Experiment
1	EPIP 1
2	EPIP 2
3	EPIP 3a
3	EPIP 3b
3	EPIP 3c

Table 3.13 *– Experimental program for Finalised Coil Testing.*

Experiments were conducted as for Design 3 with matching imaging parameters. The same scan was repeated at five different current settings, the order of which was non-sequential. Using the CCCS system a range of currents was selected that spanned the full range available (0.01mA, 3.50mA, 7.50mA 10.0mA and 13.5mA) that provided approximate signal changes that could be expected to be observed *in vivo*.

3.11.2 Results and Discussion

Signal Change (|ΔS|)

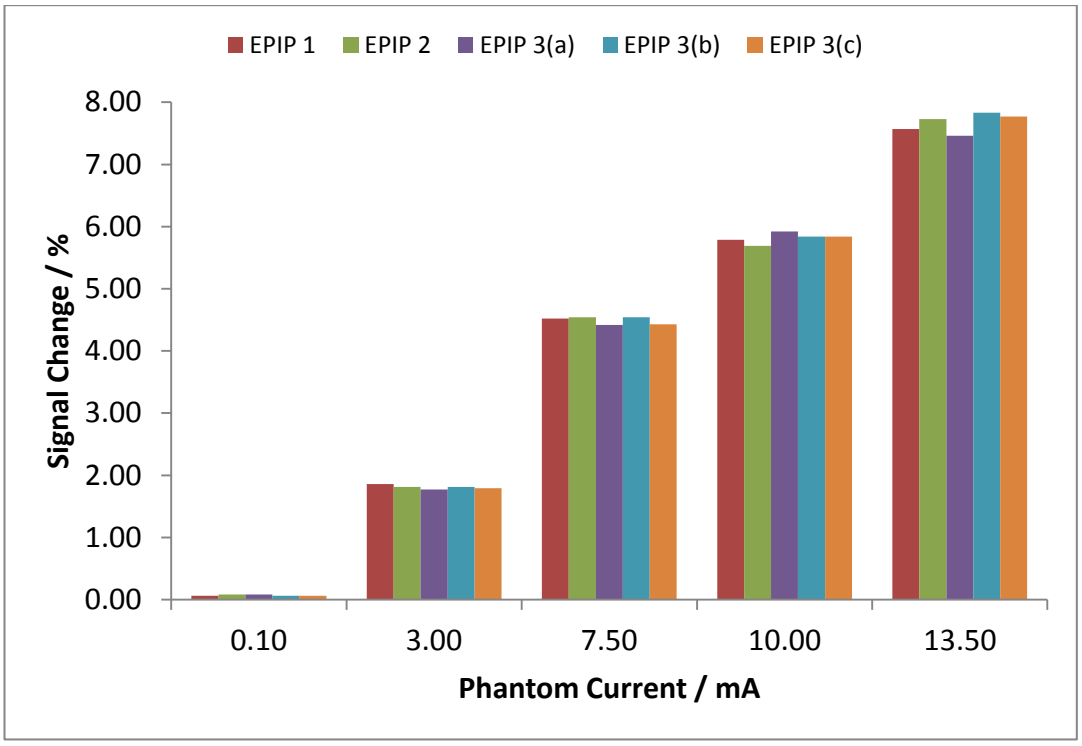

Fig. 3.16 *– Signal Change results for the initial Design 3 + CCCS experiments.*

Although there are some small differences at identical current values from scan to scan these are considerably smaller than differences observed between sites when using the battery power supply. Statistically significant signal changes are detected down to very lower current values (0.1mA) with matching changes in |ΔS| as low as 0.06%.

It was also noticed that one a particular scan was the first scan of the day (in **bold and underlined** in Table 3.14 below), the amount of |ΔS| was slightly depressed compared to other scans for that current value. Again, this is not by a relatively large amount and was only noticeable at higher currents (so for scans in EPIP 1 and 2 in this case), but the same effect was seen later in both the longitudinal study on the same scanner (Chapter 5) and at some of the other sites (Chapter 6).

Current / mA	0.10	3.00	7.50	10.0	13.5
EPIP 1	0.06	1.86	4.52	5.79	**7.57**
EPIP 2	0.08	1.81	4.54	**5.69**	7.73
EPIP 3(a)	**0.08**	1.77	4.42	5.92	7.46
EPIP 3(b)	0.06	1.81	4.54	**5.84**	7.83
EPIP 3(c)	0.06	1.79	**4.43**	5.84	7.77

Table 3.14 – Experimental Results for |ΔS| from Final Coil Test study.

Contrast Response

Experiment	Contrast Response / % mA^{-1}	Standard Error of Fit / % mA^{-1}	PCC
EPIP 1	0.57	0.01	0.999
EPIP 2	0.57	0.01	0.999
EPIP 3(a)	0.57	<0.01	0.999
EPIP 3(b)	0.59	<0.01	1.000
EPIP 3(c)	0.58	0.01	1.000

Table 3.15 *– Summary of Signal Response for Final Coil Testing. The high PCC values indicate a near perfect linear fit to the data.*

The Contrast Response stays almost identical across all five scans. The small variation across the three scans of Day 3 (EPIP 3a-c) is consistent with the variation later observed in the Edinburgh Longitudinal Study (Chapter 5). Visually the excellent repeatability can be seen more easily in Fig. 3.17. As current increases the variation between points does slightly increase.

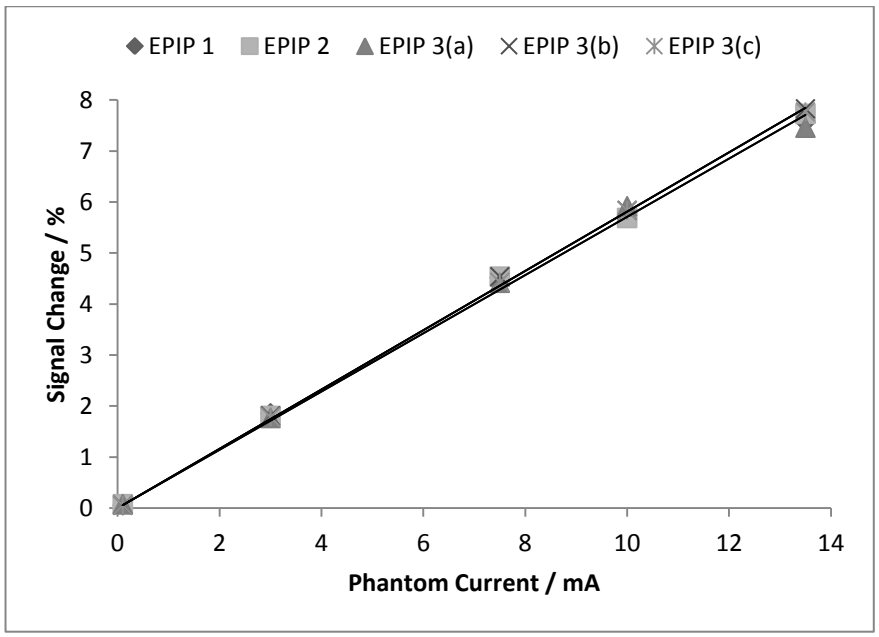

Fig. 3.17 *– Lines of best fit for data points from experiments EPIP 1 – 3c for |ΔS| against current for the Design 3 + CCCS experiments. The tight overlapping of these lines illustrates how the high standard of repeatability in the overall Contrast Response of the scanner-phantom system.*

The combination of the small Standard Error in the fit of the Response, combined with the near perfect unitary value for the Pearson's Correlation Coefficient, suggest that the Contrast Response across this current range is very nearly completely linear. The replacement of the battery power source with the CCCS appears to have minimised the variation seen between image parameters seen in the initial multisite study. This gave improved confidence that the response we were now observed is what should be expected each time and that the phantom is activated.

Signal-to-Noise Ratio

S1NR - ON

Current / mA	0.10	3.00	7.50	10.0	13.5
EPIP 1	96.4	95.1	94.4	93.2	**86.0**
EPIP 2	96.0	92.2	89.2	**84.1**	88.2
EPIP 3(a)	**77.7**	92.2	89.5	85.6	90.4
EPIP 3(b)	91.5	**90.0**	89.2	80.1	81.7
EPIP 3(c)	92.9	94.9	**80.9**	90.6	88.0

Table 3.16 *– Experimental Results for SNR with the phantom in the ON state during the Final Coil Test study.*

S2NR – OFF

Current / mA	0.10	3.00	7.50	10.0	13.5
EPIP 1	96.4	97.0	98.6	98.6	**92.5**
EPIP 2	96.0	93.9	93.2	**88.9**	95.0
EPIP 3(a)	**77.8**	93.9	93.5	90.9	97.1
EPIP 3(b)	91.5	**91.6**	93.2	85.4	88.1
EPIP 3(c)	92.9	96.6	**84.5**	95.9	94.8

Table 3.17 *– Experimental Results for SNR with the phantom in the OFF state during the Final Coil Test study.*

Functional Contrast-to-Noise Ratio (fCNR)

Current / mA	0.10	3.00	7.50	10.0	13.5
EPIP 1	0.06	1.77	4.27	5.40	**6.51**
EPIP 2	0.08	1.67	4.05	**4.78**	6.82
EPIP 3(a)	**0.07**	1.63	3.95	5.08	6.74
EPIP 3(b)	0.05	**1.63**	4.06	4.70	6.40
EPIP 3(c)	0.05	1.70	**3.59**	5.29	6.84

Table 3.18 *– Experimental Results for fCNR from Final Coil Test study.*

Deactivated SNR levels generally stay the same within an experimental run. However, as mentioned previously, the first scan of a run has a depressed SNR value compared to subsequent scans. While the effect was only noticeable at higher currents for |ΔS| for SNR it

is noticeable at all but the lowest current levels. These particular scans are again highlighted in **BOLD and underlined** in the SNR and fCNR tables**.**

Since these depressed readings occur for volumes where the phantom is inactive they can't be due to phantom activations, but must indicate an anomaly with scanner performance itself. With increased scanner usage it might be expected that SNR and corresponding fCNR would *drop* in subsequent scans compared to earlier scans, but here the reverse is true. This suggests that at the start of a day's study the system is either more subject to electronic noise or has a reduced signal output.

3.11.3 General Conclusions and Summary

The Maxwell coil design (Design 3) combined with the CCCS gives very reliable and repeatable measurements, both across a single day and over sequential days. This suggests that the phantom and associated CCCS devices are ready to be used as tools to study the performance of MRI scanners.

The noted differences in SNR and fCNR seen in the first experimental run of each day, while not greatly effecting values of |ΔS| itself, may well lead to alterations in t-statistics generated in more complicated data analysis methods (such as those used in SPM) as opposed to the simple ROI analysis method performed here. To avoid this it is suggested that before *in vivo* scanning takes place that the scanner should undergo a phantom scan to prepare it for more stable scanning afterwards. This can also be used as an opportunity to gather Quality Assurance data with either a static or functional phantom. As these depressed initial readings seem to take place at the start of each new study series, not just each day, it suggests that something is being reset in the scanner system whenever a new study is begun. To avoid this a day's scans might be contained within one study although this might decrease data integrity and archival security.

Although these first-scan depressions in SNR should be visible in a static phantom, their effect on both |ΔS| and fCNR is another new finding of anomalous behaviour in preclinical MRI scanners particularly noticeable due to the use of a functionally active phantom.

3.12 Signal Contrast Testing

The finalised Single-Coil CAT phantom also underwent T1, T2 and T2* star measurements to gain independent non-EPI measures of expected signal contrast. If the phantom signal attenuation effect is operating via the gradient dephasing effect then contrast should be

created in T2* scans that are sensitivity to changes in the magnetic environment of the scanner. There should be no change generated in either T1 or T2.

Experiments were performed at Edinburgh in November 2012 immediately after data collection from the corresponding EPIP experimental run. Tests were performed with a current of 13.5mA when the phantom was in the ON state. Five scans were taken for each phantom state for the T1, T2 and T2* measurement scans and statistical means were generated from these five sets of data. The associated error bars on Figs. 3.18-20 are the standard deviations of each point from those five scans. ROIs were applied in the same way as for extracting EPI data and appropriate curve fitting techniques in MATLAB were applied to extract T1, T2 and T2* values for each dataset generated. Descriptive statics were then generated for these data sets and a Two-Sample T-Test was performed to check for statistical significance between the relevant signal property values between the different phantom activation states.

3.12.1 T1 Contrast

T1 values were obtained using a Look-Locker inversion recovery pulse sequence. A correction to the T1 data was made based on the work of Deichmann [Deichmann 1992].

Experiment Parameters

TR / ms	7.5
TE / ms	2.27
FA / Degrees	20
Matrix	128 x 128
Field of View / mm	25.6 x 25.6
Number of Echoes	30

Table 3.19 *– T1 acquisition parameters.*

Results

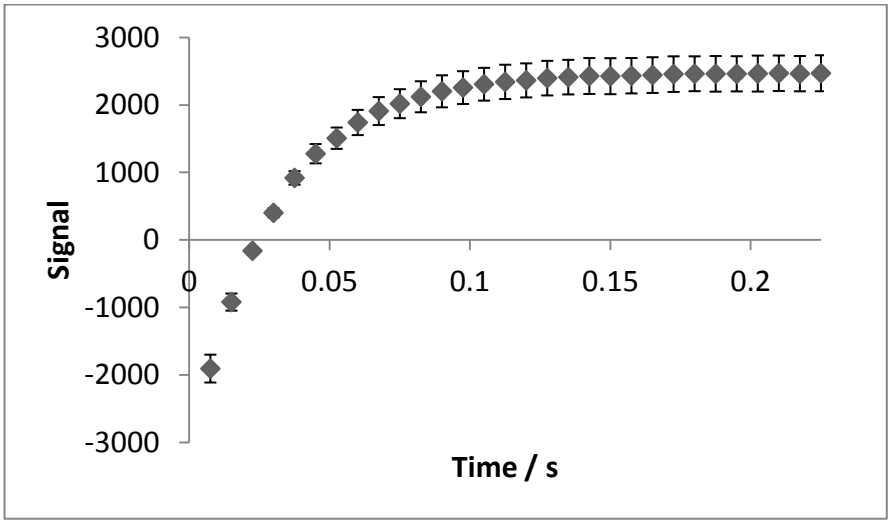

Fig. 3.18 *–Plot of data points obtained during T1 recovery using a Look-Locker sequence.*

State	Mean T1 / ms	Standard Deviation
ON	49.6	0.18
OFF	47.7	0.08

Table 3.20 *– T1 Signal in both states for the Single-Coil Helmholtz phantom.*

The mean difference between the values of T1 in the two phantom states is 0.96ms ($p < 0.0005$). Therefore there is a small but significant difference between the two states (~3.9%).

3.12.2 T2 Contrast

T2 measurements were performed using an Agilent multi-echo multi-slice spin echo sequence (MEMS). No significant difference in signal between the ON and OFF states of the phantom was expected.

Experiment Parameters

TR / ms	2285
TE / ms	10
Matrix	128 x 128
Field of View / mm	25.6 x 25.6
Number of Echos	16

Table 3.21 *– T2 acquisition parameters.*

Results

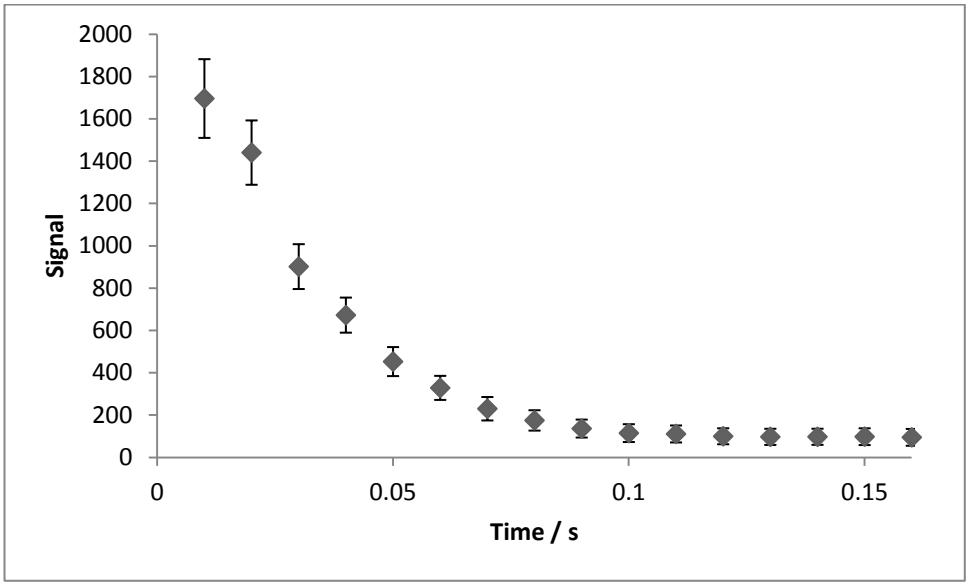

Fig. 3.19 *–Plot of data points obtained during T2 decay using a MEMS sequence.*

State	Mean T2 / ms	Standard Deviation
ON	31.6	0.20
OFF	31.5	0.71

Table 3.22 *– T2 Signal for the Single-Coil Helmholtz phantom.*

The mean difference in T2 between the two states is -0.09ms (p=0.796). Therefore there is no significant difference of T2 value between the two states of the phantom with the current being used as evidenced by prior EPI scans..

3.12.3 T2* Contrast

T2* measurements were performed using an Agilent multi-gradient-echo multi-slice (MGEMS) sequence. As values of T2* depends on any magnetic field inhomogeneities present there should be a significant difference in T2* between the ON and OFF states of the phantom.

Experiment Parameters

TR / ms	1145
TE / ms	5.00
FA	90
Matrix	128 x 128
Field of View / mm	25.6 x 25.6
Number of Echos	16

Table 3.23 *– T2* acquisition parameters.*

Results

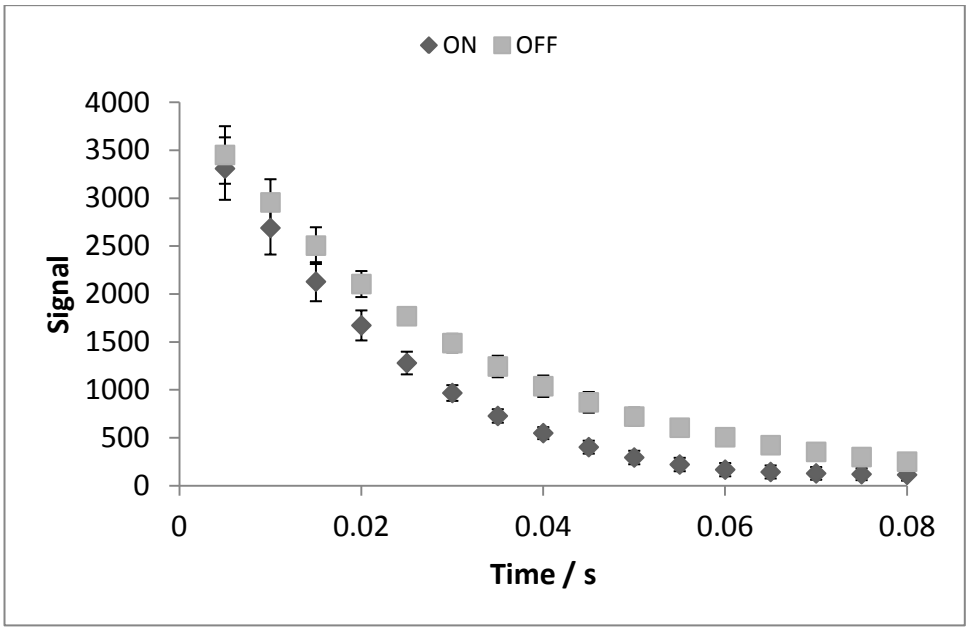

Fig. 3.20 *–Plot of data points obtained during T2* decay using ta MGEMS sequence.*

State	Mean T2* / ms	Standard Deviation
ON	19.5	0.05
OFF	28.4	0.03

Table 3.24 *– T2* Signal for the Single-Coil Helmholtz phantom*

The mean difference between the values of T2* in the two phantom states is 8.82ms ($p < 0.0005$) which is a significant difference as would be expected.

3.14 Comparison of Data Analysis Methods

Although the Manual ROI method of data analysis used in this project provides detailed control of all steps involved in the image analysis process it is a time consuming and requires a great deal of manual intervention.

SPM however is a faster, well tested and relied upon image analysis tool used widely in the fMRI field. MarsBaR [Brett 2002] is an additional toolbox for SPM that facilitiates ROI analysis of signal changes in absolute terms in a similar output to the Manual method used elsewhere in this project. Agreement between SPM/MarsBaR and the Manual method would provide a secondary confirmation that the method of image analysis used here is capable of speaking to alternate image analysis techniques such as SPM or FSL.

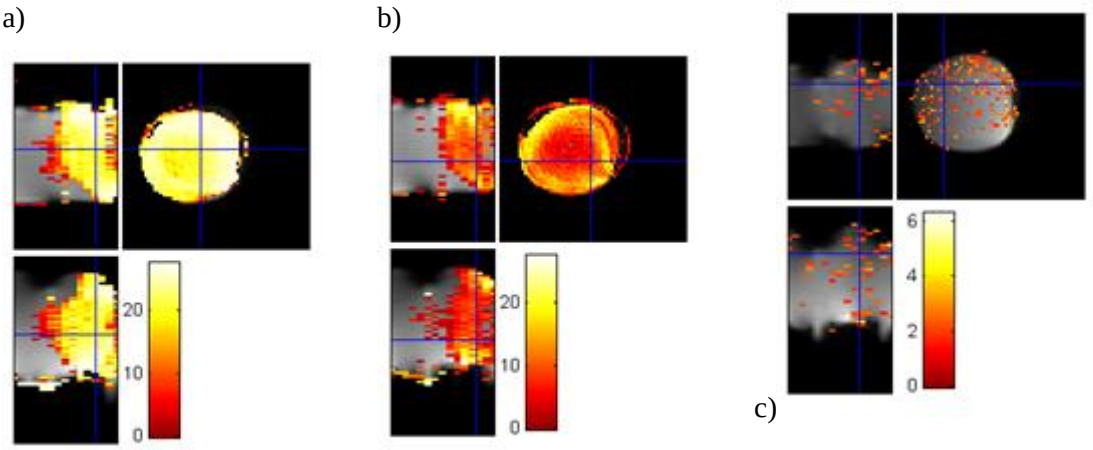

Fig. 3.21 *– Example SPM activation maps for three different current levels in the Design 3+CCCS phantom. a) 13.5mA, b) 3.00 mA and c) 0.01mA. Notice the very speckled appearance of the 0.01mA, supportive of the previously noted unreliability of imaging parameter results near the detection limit of a scanner (scale is the t-statistic for a ON>OFF contrast).*

SPM's main disadvantage is that a high degree of competence with the program is initially required before any useful results can emerge, hence why we used the simpler Manual method initially. However once the operation of SPM is learnt then many of the repetitive tasks needed for analysis can be saved and recalled in batch files that require a minimum of alterations from one set of data to the next.

	Response / % mA^{-1}	Standard Error in fit
Manual Method	**0.57**	**0.01**
SPM/Marsbar Method	**0.55**	**0.01**

Table 3.25 *– Comparison of Signal Response (EPIP 1) as measured via the two analysis techniques (Edinburgh June 2012 Run 1)*

Processing of phantom data with appropriate inputs via SPM and with matching ROIs shows good agreement with the Manual method outlined in this chapter. This gives confidence that the Manual method is reproducing a believable methodology for the phantom data.

3.15 Chapter Summary

Three prototypes phantom devices were successfully created and tested. Although each device produced signal change the Maxwell coil CAT design was selected as the final design, due to ease of construction and more rigorous image analysis attributes. Characterisation of both phantom resonator medium and coil current source was also undertaken.

Current sourced proved to be an important factor in producing reliable results to fulfil the requirements of an fMRI QA phantom. An appropriate source (the CCCS system) was created and partnered with the phantom. This combined device interfaces directly with scanner systems, reducing the need for user intervention and associated human errors.

The phantom is now ready to be deployed in QA studies (Chapters 5 and 6) and provides a finalised geometry for theoretical modelling studies (Chapter 4).

Chapter 4 fMRI Phantom Physics and Modelling

4.1 Introduction

The selected design for the fMRI phantom consists of a pair of wire coils arranged in a Maxwell configuration. These coils surround a tube of resonating medium which is visible in MRI images. Electrical current in these wire coils produces a linear magnetic field gradient between the coils. This gradient alters the MRI signal properties of the resonating medium so that a controllable change in image signal is produced on demand. This allows for the generation of user specified changes in image contrast allowing standard fMRI measures such as signal change and fCNR to be performed.

A computational model of the CAT fMRI phantom was constructed in a MATLAB environment to understand more fully and to simulate the contribution to changes in MRI signal that the current-induced magnetic field gradient produces. This allows us to model the behaviour of an ideal, perfectly constructed phantom and compare it to the real-life examples of this project. This in turn allows us to determine any remaining experimental signal fluctuations or behaviours as being due to individual scanner behaviour or to electronic noise and environmental effects.

The theoretical model is constructed around the principle of spin dephasing in the presence of a magnetic field gradient. This process results in a lower net magnetisation state when the phantom is activated compared to than what might be expected without the phantom gradient present. This results in an altered signal level when the gradient is present.

Because this dephasing effect is only dependent on the strength of the gradient applied, the resultant change in signal should be independent of coil type used or scanner B_0 magnetic field strength. This fulfils the requirements that the phantom is able to produce comparative effects over time and multiple scanner sites as outlined in Section 3.1.1 in order to create a gold standard device for fMRI QA.

4.2 fMRI Phantom Signal Attenuation

In order to understand the change in signal caused by the phantom it is prudent to examine more fully the generation of the magnetic resonance signal itself.

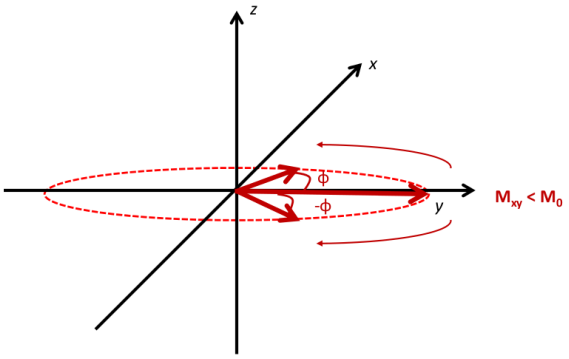

M_{xy} can be reduced through a process known as dephasing. This can be caused by a combination of local B_0 field inhomogeneities, the variable molecular environment that spins find themselves in and to the deliberately introduced magnetic field gradients used in spatial signal encoding (see Chapter 1.3.6.4). Because of this the collection of spins don't all precess at exactly the same rate.

This leads to a gradual dispersion of M_{xy} by ±φ as viewed in the rotating frame. The average sum of these dephased spins M_{xy} is less than the original unphased value of M_0.

$$\sum M_{xy} < M_0$$

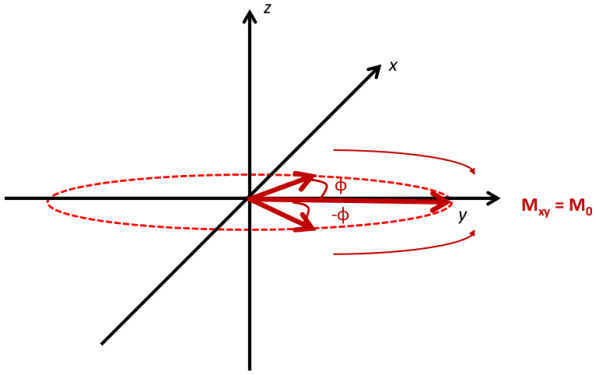

The reduced value of M_{xy} caused by a spatial encoding gradient dephasing can be counteracted (rephased) by the input of a second gradient immediately after the first that offsets the gradient dephasing effect such that:

$$\int_0^{TE} G^-(t)dt = -\int_0^{TE} G^+(t)dt \qquad \text{(Equation 4.1)}$$

After this rephasing to compensate for the signal encoding gradients M_{xy} is still less than M_0 due to the uncorrected for local field inhomogeneities and molecular differences. The resultant T_2 decay is moderated by the sum of these changes so that it then decays with a shorter time constant known as T_2* such that:

$$\frac{1}{T_2^*} = \frac{1}{T_2} + \frac{1}{T_2'} \qquad \text{(Equation 4.2)}$$

where T_2' is the relaxation time due to any remaining non-gradient offsets.

The presence of a second scanner-independent magnetic field gradient will induce additional dephasing that is uncorrected for by the scanner rephasing gradient operation. This additional dephasing induces a larger value of φ at the echo point where signal is gathered. This will alter T_2' resulting in an altered T_2^* that is different to the non-phantom 'native' T_2^*. This results in a relative drop in signal.

If this secondary gradient can be set on demand then it can give precisely controllable magnetic environments around the phantom and so a controllable signal from the phantom.

When the current in the phantom is activated an individual spin at a position *z* will experience a change in phase according to

$$\Delta\phi(z,t) = e^{-i\gamma.z.G_z.t} \qquad \text{(Equation 4.3)}$$

where G_z is the magnetic field gradient experienced by the spin over a period *t*, along *z*. G_z can in turn be calculated the Biot-Savert Law as outlined in section 4.3.2.

To calculate the total amount of signal attenuation caused by the presence of the phantom gradient induced phase dispersion across the sample, it is necessary sum the phase vectors of these individual spins in order to calculate the final voxel signal attenuation function (AF). Along a single dimension this can be approximated using

$$AF = \frac{1}{n}\sum e^{-i\phi} \qquad \text{(Equation 4.4)}$$

where *n* is the number of 'sub-voxels' So to create a map of phase difference between the two phantom states it is necessary to create one of magnetic field as well. Both matrices should have a higher resolution than the final map of Δφ since each element of the phase map will be an integral sum of the magnetic field gradient across this region. Since

maximum signal occurs when the phantom is OFF (i.e. no additional spin phase dispersion) then 0 < AF < 1 when the phantom is ON.

Since in the phantom the magnetic field gradient acts in a similar manner to that of gradient spoiling in a spoiled MRI pulse sequence the signal attenuation should have the form of a SINC response [Marshall 1998, Bernstein 2004b] since

$$\left|\overrightarrow{M_{\perp}}\right| = \left|\sum_{n}^{N} \vec{M}_{\perp,n}(\vec{z}_n)\right| \qquad \text{(Equation 4.5)}$$

$$\approx \frac{\int_{voxel} M_{\perp} e^{-i\phi_{ON}}}{\int_{voxel} dr} \qquad \text{(Equation 4.6)}$$

$$= M_{\perp}|SINC(\Delta\phi/2)| \qquad \text{(Equation 4.7)}$$

This response is confirmed in full simulations later in Chapter 4.6 and gives the magnetisation attenuation parallel to the xy-plane ($M_{\perp}$) for a calculated value of phase change (ϕ) in each voxel when the phantom is ON compared to when it is OFF (No attenuation).

4.3 fMRI Phantom Physics

4.3.1 Requirement to generate Magnetic Field Gradient

To create the additional gradient a constant current is applied to the phantom coils. This creates a magnetic field around the coils which can be computed using the Biot-Savert Law. As we are only interested in the field gradient along the z-axis, we need only calculate magnetic fields running parallel to the z-axis of the phantom and can ignore B_x and B_y field components which greatly simplifies the calculations involved.

To ensure measurements are made are in a region of maximum phase uniformity they must be made at the centre of the coils where the magnetic field generated is most constant (as shown in Fig. 4.6b.

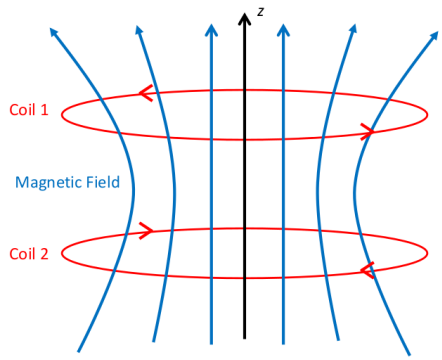

Fig. 4.1 *– Illustration of magnetic field lines generated by two current carrying coils. A region of relative uniformity occurs at the centre of the coils.*

4.3.2 Magnetic Fields of Current Carrying Wires

A magnetic field is generated by any current carrying source. For a wire carrying current I the total magnetic field B_z for a set of current elements dI along its length at a point P away from the wire can be calculated using the Biot-Savert Law [Griffiths DJ 1999].

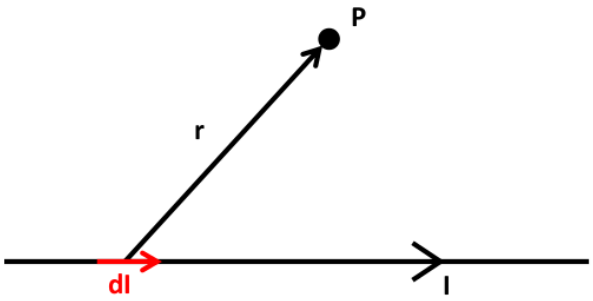

Fig. 4.2 *– A wire carries a current I past point P. A sequence of current elements, dI (r) can be taken along the wire's length (l).*

$$B_z = \frac{\mu_0}{4\pi}\int \frac{\boldsymbol{I}\, x\, \hat{\boldsymbol{r}}}{r^2} dl \qquad \text{(Equation 4.8)}$$

$$= \frac{\mu_0}{4\pi} I \int \frac{\boldsymbol{dI'}\, x\, \hat{\boldsymbol{r}}}{r^2} \qquad \text{(Equation 4.9)}$$

For the fMRI phantom we use two circular loops of current. For a single loop with radius R (Fig. 4.3) the on-axis magnetic field of such a coil can be calculated using:

$$B_Z = \frac{\mu_0}{4\pi}\frac{IR^2}{(R^2 + z^2)^{3/2}}\int_0^{\varphi} d\varphi \qquad \text{(Equation 4.10)}$$

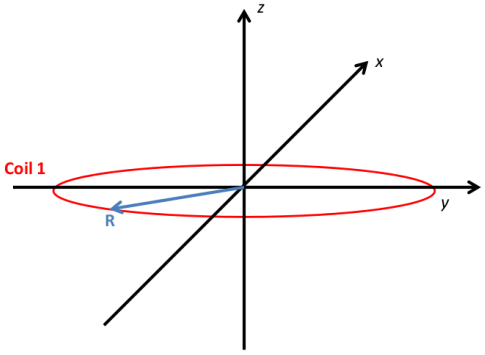

Fig. 4.3 *– Wire coil diagram, showing coil in the x-y plane. R is the distance to the wire coil in this plane*

As we are calculating the field contributions for the complete circular wire coil (i.e. dφ from 0 to 2π) this simplifies to:

$$B_z = \frac{\mu_0 IR^2}{2(R^2 + z^2)^{3/2}} \qquad \text{(Equation 4.11)}$$

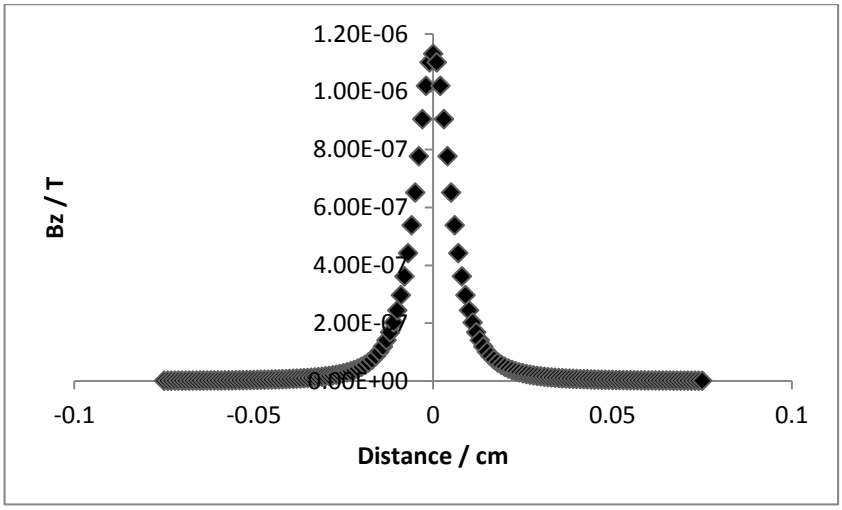

Fig. 4.3 *– Plot of magnetic field along z-axis for single coil, I = 13.5mA*

4.3.3 fMRI Phantom Coil Geometry

In order to produce a magnetic field gradient two magnetic field sources must be separated by a distance, L. In the case of the fMRI phantom two current carrying coils are used to form

a uniform gradient between the coils. In order to ensure gradient linearity the physical geometry of these coils must be precisely prescribed so that the distance between the two coils is equal to the radius of the coils.

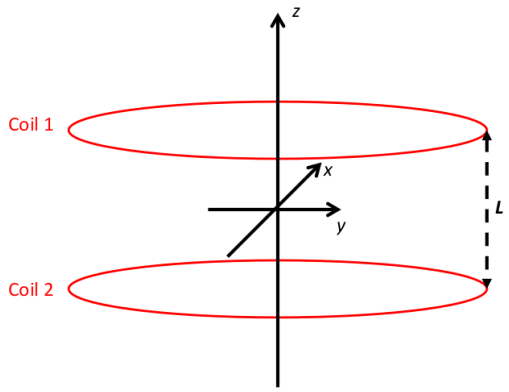

Fig. 4.4 *– Coil set up showing coils separated by distance L.*

This coil geometry is known as a Maxwell pair when current in the coils runs in opposite polarities (i.e. $I_{coil\ 1} = -I_{coil\ 2}$). This produces the required uniform magnetic field gradient between the coils. If current is run in the same direction in both the coils (i.e. $I_{coil\ 1} = I_{coil\ 2}$) no magnetic field gradient is formed. Instead a uniform magnetic field is produced in what is known as a Helmholtz coil configuration.

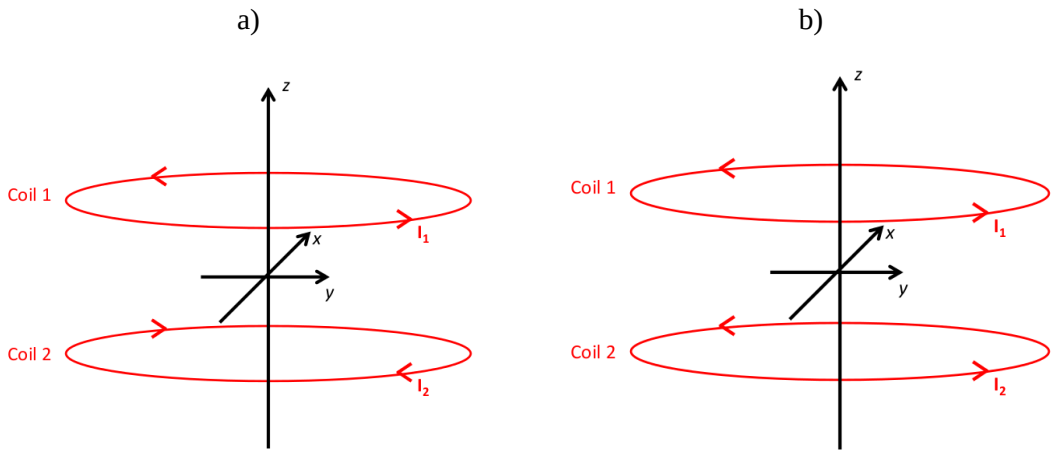

Fig. 4.5 *– Current configurations for a) Maxwell Coil and b) Helmholtz Coil*

The fMRI phantom is run in the Maxwell current configuration, although the physical geometry of the coils is identical between the two current configurations.

4.3.4 Field Calculations for fMRI Phantom Coils

As before for a single coil we can simply calculate the field along the z-axis of a pair of coils, separated by distance L, the contributions from both fields are added together so that:

$$B_z = \sum (B_{z-coil\ 1} + B_{z-coil\ 2}) \quad \text{(Equation 4.12)}$$

For a Helmholtz coil configuration the on-axis Biot-Savert equation is:

$$B_z = \frac{N\mu_0 I R^2}{2}\left[\frac{1}{\left(\left(z-\frac{L}{2}\right)^2 + R^2\right)^{3/2}} + \frac{1}{\left(\left(z+\frac{L}{2}\right)^2 + R^2\right)^{3/2}}\right]$$

(Equation 4.13)

And for the Maxwell coil configuration:

$$B_z = \frac{N\mu_0 I R^2}{2}\left[\frac{1}{\left(\left(z-\frac{L}{2}\right)^2 + R^2\right)^{3/2}} - \frac{1}{\left(\left(z+\frac{L}{2}\right)^2 + R^2\right)^{3/2}}\right]$$

(Equation 4.14)

A multiplication factor, *N*, can also be included where N equals the number of turns of wire per coil. In the final design of the phantom N=1, so for simplicity is dropped from subsequent B_z equations.

Fig. 4.6 displays the results of such a simulation for a geometry matching that of the final fMRI CAT phantom with I = 13.5mA.

a) b)

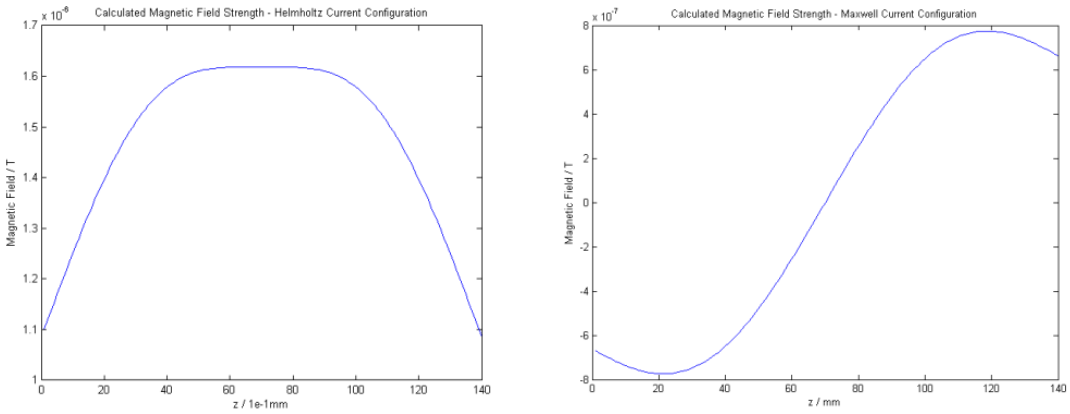

Fig. 4.6 *– B_z plots along the central z-axis for two coils in both the Helmholtz configuration (A)) and the Maxwell configuration (b). I = 13.5mA in both cases.*

From this it can be seen that for a properly configured Maxwell configuration at z=0 (z = 65-75 in above the examples) where the experimental ROI measurements are made the magnetic field should be zero. Conversely the magnetic field gradient is at maximum resulting in a signal change. In the Helmholtz configuration there should be no change as although the magnetic field is at maximum at z=0, there is no magnetic field gradient at that point.

To move off-axis and calculate B_z at an arbitrary point is more complicated and requires numerical integration methods using a computer. To do this a MATLAB script was written to plot the value of B_z for a 3D matrix of arbitrary chosen points [See Appendix 3.1].

Several other geometric parameters must be prescribed to allow position with respect to the wire coil to be defined in order to calculate B_z.

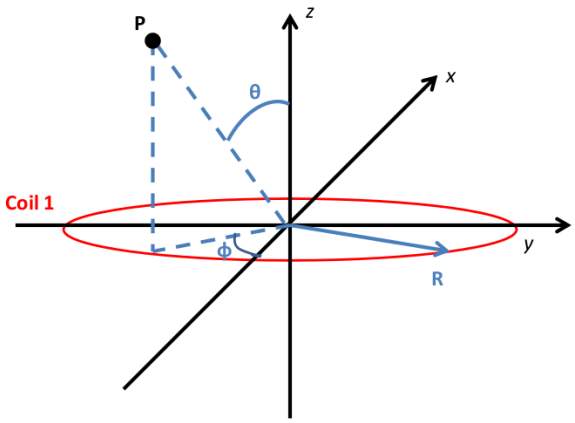

Fig. 4.7 *– Geometric parameters used in off-axis B_z calculations.*

φ defines the angle from the x-axis in the x-y plane. (This should not be confused with the signal phase also denoted with φ).

θ defines the angle from the z-axis in the z-plane.

For a single coil the $B_z(z, \varphi)$ at any point P(z, φ) [Lewin W. 2002]:

$$B_Z(z,\varphi) = \frac{\mu_0 IR}{4\pi}\int_0^{2\pi} \frac{R - y\sin\varphi\, d\varphi}{(R^2 + y^2 + z^2 - 2yR\sin\varphi)^{3/2}} \qquad \text{(Equation 4.15)}$$

For two coils in the Maxwell configuration:

$$\begin{aligned} & B_z(z,\varphi) \\ & = \sum (B_{Z-coil\,1} + B_{z-coil\,2}) \\ & = \left[\frac{\mu_0 IR}{4\pi}\int_0^{2\pi} \frac{R - y\sin\varphi\, d\varphi}{\left(R^2 + y^2 + \left(\frac{L}{2}\right)^2 - 2yR\sin\varphi\right)^{3/2}}\right] \\ & + \left[\frac{\mu_0 (-I)R}{4\pi}\int_0^{2\pi} \frac{R - y\sin\varphi\, d\varphi}{\left(R^2 + y^2 - \left(\frac{L}{2}\right)^2 - 2yR\sin\varphi\right)^{3/2}}\right] \end{aligned} \qquad \text{(Equation 4.16)}$$

4.4 fMRI Phantom Simulations

In order to then simulate the attenuation of MRI signal caused by the operation of the phantom three individual MATLAB scripts were prepared. The first generates a three dimensional matrix of the magnetic field caused by the coils of the phantom. The second converts this field matrix into a corresponding matrix of phase values and the third resamples this matrix to generate a matrix of signal attenuation. From this final matrix ROI measurements can then be made in a matching way to those of experimental data sets.

4.4.1 Magnetic Field Matrix

Three dimensional simulations of the magnetic field generated by the Maxwell pair were prepared using Equation 4.17. Simulations of the magnetic field were run at resolutions higher than experimental resolutions since the final phase effect that determines the level of

signal attenuation (Sections 4.4.3-4) depends on a averaging of localised phase dispersion via magnetic field gradient effects across an imaging voxel (Equation 4.5).

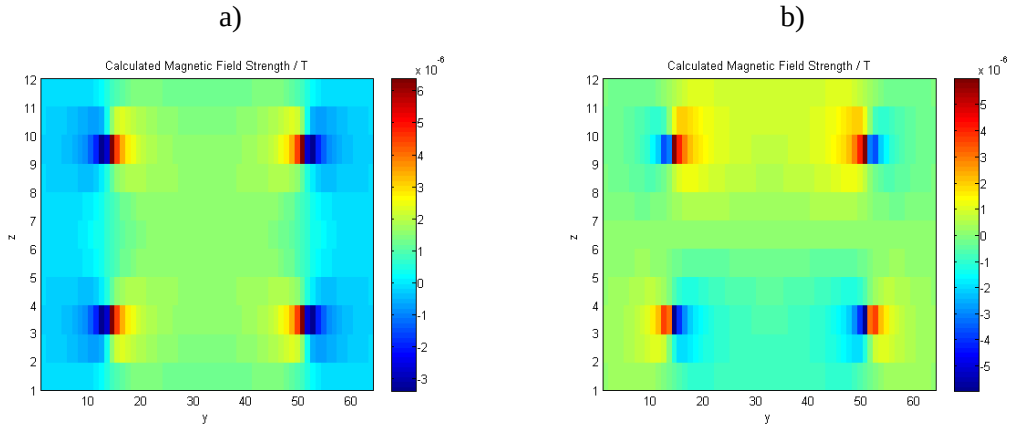

Fig. 4.8 *– Illustrative experimental resolution examples of B_z (T) simulations for both a) Helmholtz and b) Maxwell current configurations. Note both the narrow region of uniformity at the centre of example a) and also the matching region of zero magnetic field at the centre of the simulation for the Maxwell configuration simulation.*

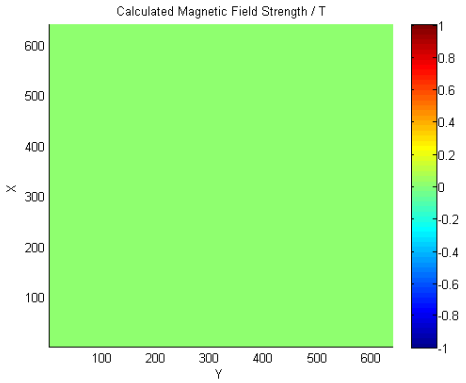

Fig.4.9 *- In the Maxwell configuration, the central slice (z = 60) displays a B_z = 0T (I=13.5mA) as expected.*

4.4.1.1 Simulation Resolution

A resolution of 10 x experimental resolution scanner resolution (640 in plane increments, 140 in the z-direction) with 360 current elements (dφ) was initially selected to provide a large number of sub-voxels within the final experimental resolution voxel. A high resolution for the first-step B_z simulation is needed as to calculate the phase offset of an individual experimental resolution pixel requires taking the average phase dispersion caused by the magnetic field across the different individual spins within the sample into account of the

phantom across that pixel (Equation 4.5). The higher the resolution the more accurate the experimental field will be simulated.

A check was performed to ensure that the selected higher resolution was at a sufficient level to ensure an accurate simulation. This was performed by running the scripts at half the resolution (i.e. 320 x 320 x 70) to the standard simulation resolution. The final experimental resolution matrix from which attenuation measurements are made therefore has less simulation resolution voxels per voxel compared to the higher resolution matrix. The results from the lower resolution simulation provided a close match for those from the higher resolution that was used throughout this study. This indicates that the high resolution simulations had at a sufficiently high level resolution to provide accurate simulations (Fig. 4.10).

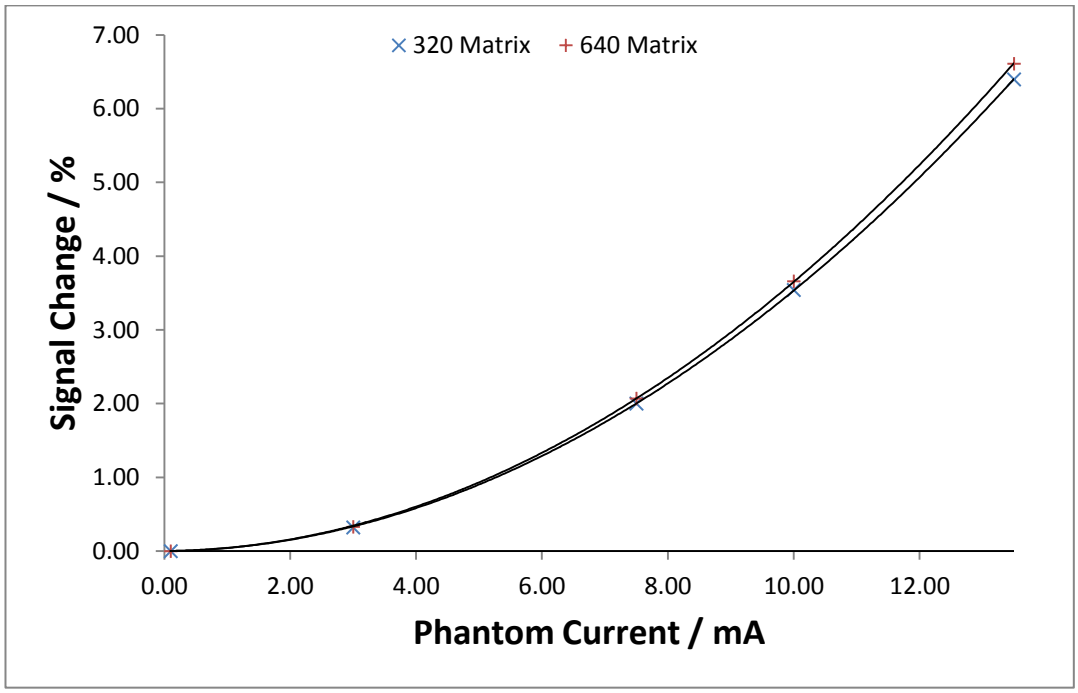

Fig. 4.10 *– Comparison of High Resolution vs Lower Resolution Signal Change Simulations. The two are a very close match which indicates that the high resolution simulation provides a good level of accuracy. Lines of best fit generated to highlight similarity of both simulation results.*

Because of this reassurance it can be safely stated that any differences between simulated and experimental results cannot be down to an insufficiently sampled simulation resolution pattern.

The script for magnetic field calculations is archived in Appendix 3.1.

4.4.2 Conversion of Magnetic Field Matrix to Phase Matrix

The final B_z matrix generated by the magnetic field simulation is converted into a phase (φ_z) matrix of identical dimensions according to:

$$\varphi_Z = B_{Total} * \Delta TE$$

where ΔTE is the echo spacing time between successive pulses.

The result of this is a three dimensional matrix of matching phase change caused by the magnetic field gradient across each point of the matrix.

a) b) c)

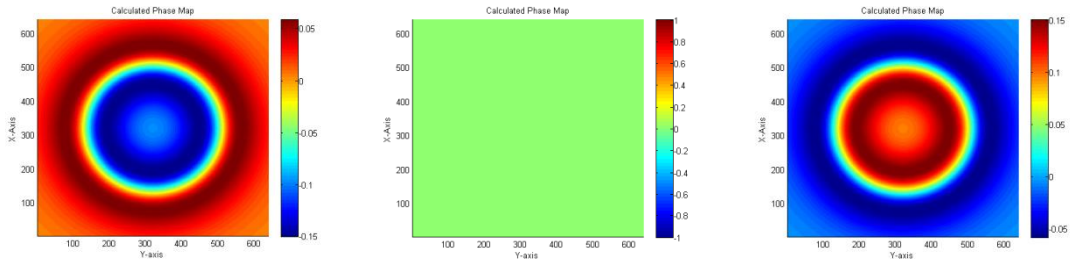

Fig.4.11 *- In the Maxwell configuration, the central slice (z = 60) b) displays a phase difference of zero (I=13.5mA) as expected, whereas slices before and after (a) 59 and c) 61 respectively) show non-zero phases.*

This script is archived in Appendix 3.2.

4.4.3 Resampling of Phase Matrix to Experimental Resolution

The high-resolution phase matrix is then resampled in all dimensions to produce a final phase matrix with pixel voxel resolution equivalent to that of the experimental parameters. Each element in this matrix describes the average change in phase across that element. This summation of individual spin phases also cancels the imaginary parts of Eq. 1.9 leaving the real non-zero component behind to be measured.

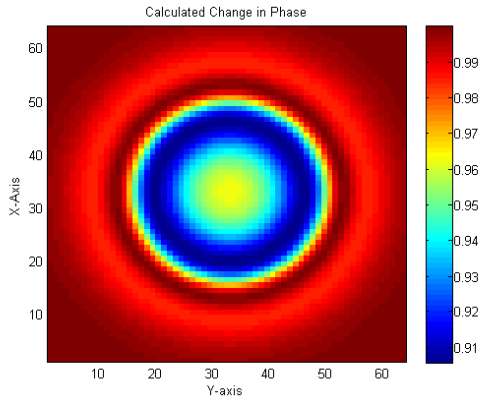

Fig.4.12 *– Resulting map of attenuation where zero attenuation = 1,(z = 6 (I=13.5mA)).*

This script is archived in Appendix 3.3.

4.4.4 Measurement of Simulation Attenuation

ROI measurements are made in the standard way on this final lower resolution phase map, which is effectively a map of signal attenuation. Assuming a signal of 100% when no field is present this is then compared with the ROI attenuated simulation value to calculate a value for ΔS for a specific simulation at a particular current. By running multiple simulations at different current values a sequence of ΔS values van be obtained. From these the standard signal Contrast Response can be measured as with the experimental datasets.

4.5 Comparison of Simulation with Experimental Results

4.5.1 Simulated Signal Attenuation Response

The map of phase attenuation can be used to make ROI measurements in the same manner as with experimental signal change data (See Appendix 1.1). These measurements describe the theoretical pure signal attenuation allowing for the measurement of a theoretical Contrast Response that is comparable with that from experiment. This is shown in Figure 4.13.

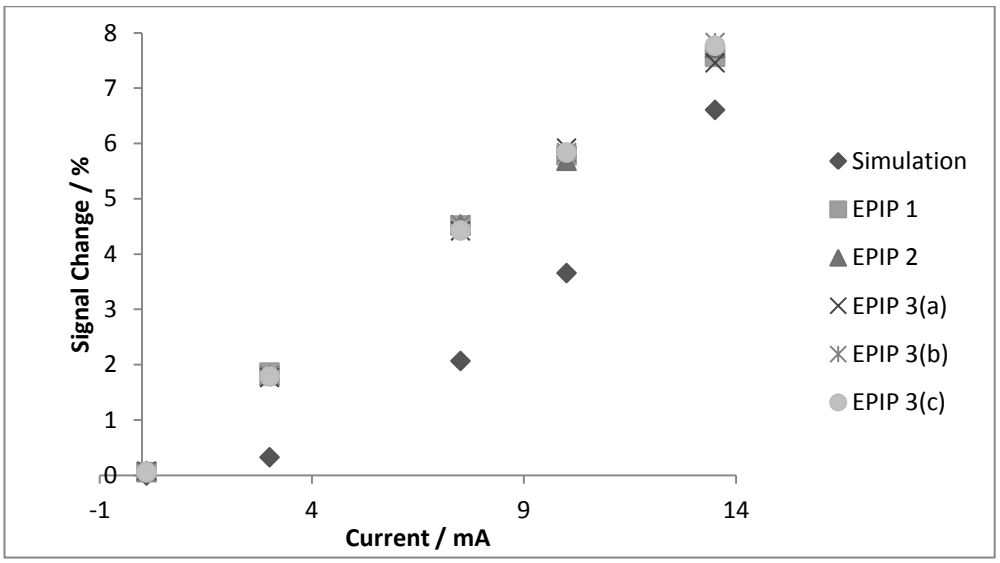

Fig. 4.13 *– Theoretical signal attenuation based on electromagnetic simulation compared with several experimentally measured values.*

There are a number of differences to the experimental data that are immediately obvious.

- Across the current range simulated (matching the experimental range) the signal attenuation is consistently lower than the experimental values gathered with the CAT-CCCS fMRI phantom.
- The theoretical attenuation does not exhibit the strong apparent linearity of the experimental data gathered both in the prototyping phase of the CAT-CCCS phantom (Chapter 3) or in all subsequent studies at multiple sites (Chapters 5 and 6). The initial experimental data with the CAT-CCCS system strongly suggested a linear fit with high Pearson correlation coefficient values. However, this simulated data and the theory outlined behind it suggests this is an assumption and should be considered further.
- The theoretical attenuation does however exhibit an exponential like curve as would be expected from Equation 4.5, where the total resultant attenuation is dependent on a summation of an exponential term involving intra-voxel phase.

Therefore in the experimental data there must be something providing not only an elevation in signal attenuation in this current range, but which is also impacting the behaviour of that attenuation to transform the exponential nature of the magnetic field gradient based attenuation into a linear function.

4.5.2 Influence of ROI Properties

Using the simulation data, the influence of the ROI properties were investigated to see if this might provide clues to this discrepancy.

- **Position of ROI**

  An obvious first step was to investigate if the positioning of the ROI was sufficient to account for the stimulation-experimental discrepancy. Thus far the experimental ROI co-ordinates have been initially set by looking for regions of uniform image intensity, by a combination of manual visual estimation and concurrent minimisation of inter-block transient peaks (see Chapter 3.8.3).

  ROIs in different positions will experience a different magnetic field gradient environment which could lead to differences in signal attenuation based on ROI position. This is to be expected when moving from slice to slice and so moving closer to one coil. The Maxwell configuration of the coils should however ensure an approximate region of cross sectional magnetic field gradient uniformity in the central slice.

  Two ROIs of matching size were compared to test if they produced similar results and so would experience similar magnetic field gradients. One ROI (**Experimental Original**) was positioned at co-ordinates matching the ROI used for experimental data (x=23, y=32 with results outlined as above) and a second (**Centre Original**) was centrally positioned (x=32, y=32). Given the size of the ROI a third ROI positioned in line with the centre and experimental ROI would have taken the ROI outside of the region bounded by the resonator tube in the experiment, thus only two ROIs were compared. Due to the rotational symmetry around the z-axis the results measured from the simulation apply for all matching co-ordinates around the z-axis and so effectively cover the majority of the simulated phantom slice.

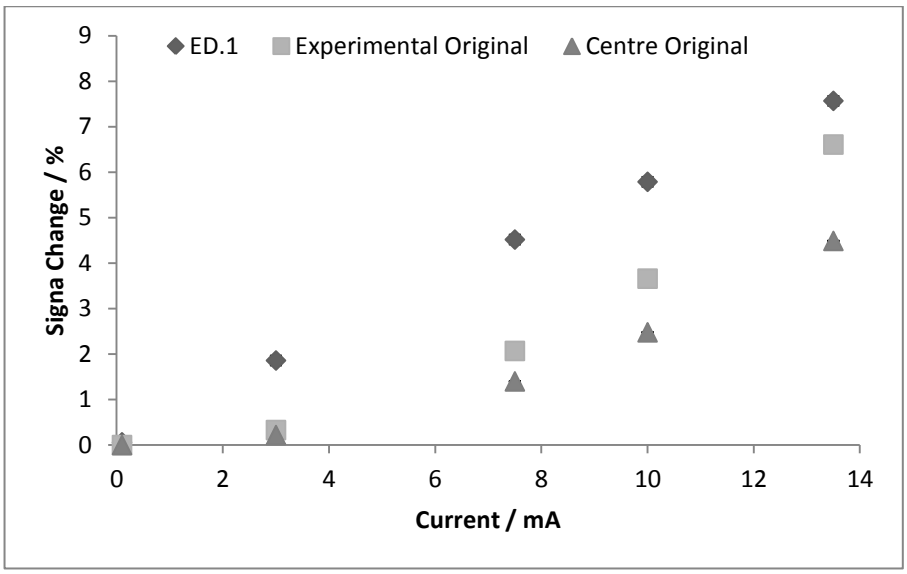

Fig. 4.14 *– ROI |ΔS| results from two different ROIs compared with a typical set of experimental data (Ed.1 (June 2012)). At lowest current values simulation and experimental values for signal change diverse before converging again at higher current values.*

Values for ΔS for both ROIs underestimate the experimental ΔS. Both also still exhibit the exponential rise of signal change expected from theory.

- **Dimensional Properties of ROI**

  Another possible source of discrepancy between theory and experiment concerned the dimensions of the ROI. There are important difference between the shape of the simulated field (perfectly circular) and the phantom cross sectional area (more oblate due to typical EPI distortions in the phase encode direction) as seen in the experimental data. To see if this was having any effect on the results measurements were performed with ROIs of larger (**<dx**) and smaller (**>dx**) dimensions in the vertical direction. These were each tested at both the previously used experimental and central positions.

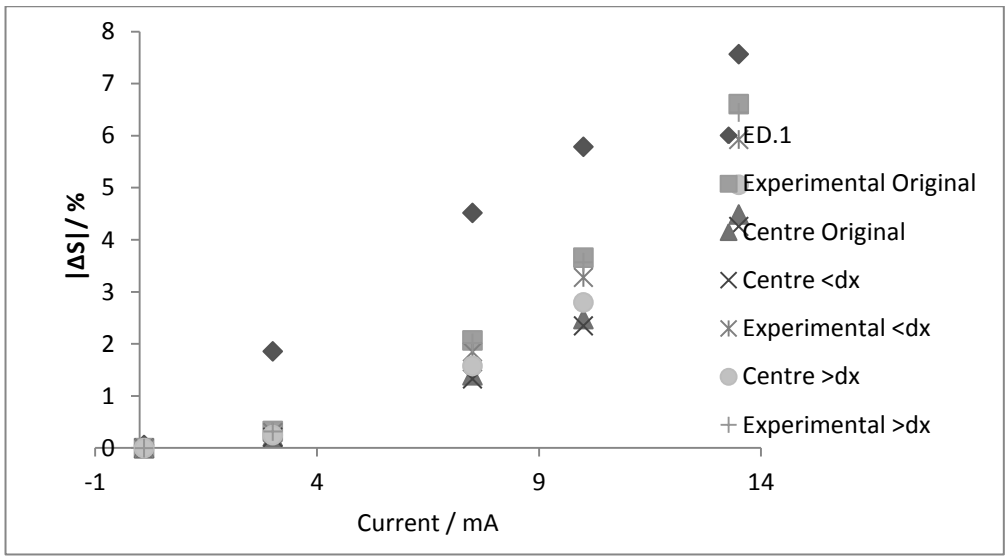

Fig. 4.15 *- ROI |ΔS| results from three different ROIs (ROI = original, with a smaller x-dimension (<dx) and then with a larger x-dimension (>dx) at two different locations as previously). Simulations are also compared with a typical set of experimental data (Ed.1 (June 2012)).*

- As with the change in ROI position the same exponential pattern and undervaluing of ΔS is still apparent in all three different ROIs at both positions. Increasing dx when at centre appears to increase corresponding values of ΔS while decreasing it results in a small drop in ΔS. However the same is not true for the ROI at the experimental co-ordinates. Here an increase in dx makes little difference where as a reduction in dx noticeably lowers ΔS. It is reasonable to conclude that this is because the magnetic field gradient is decreasing relatively less as it moves away from the central axis of the coils, resulting in less apparent change at the experimental co-ordinates compared to the central.

In summary differences in ROI positioning and size do create differences in ΔS. However, measurements produced using the position and size of the ROI used in experimental measurements appear to give the closest match of simulated and experimental signal attenuation. As ROI position and size can effect ROI measurements it is important that they remain consistent across all future experiments. There is robustness to these effects at low current values that increasingly breaks down at high current values.

There is still a large discrepancy in both trend and value between the simulation and experimental results that needs a sufficient explanation.

4.6 High Current Simulations

Further simulations were performed with an increased current range up to 125mA. Although this was a range almost 10 times that used experimentally with the CAT-CCCS phantom it was a similar range to that used by the CAT phantom when powered by a 9V battery (Chapter 3.8). The multisite results from these tests proved highly variable and produced data that exhibited some potentially non-linear trends. However a lack of sufficiently spaced data points presented any definite conclusions from being drawn.

As seen in the earlier studies within the lower experimental current regime ROI positioning produces some small variations in |ΔS|. At high currents the exponential nature of the signal attenuation would magnify these differences and so small changes in ROI position might account for the wide range of |ΔS| trends observed.

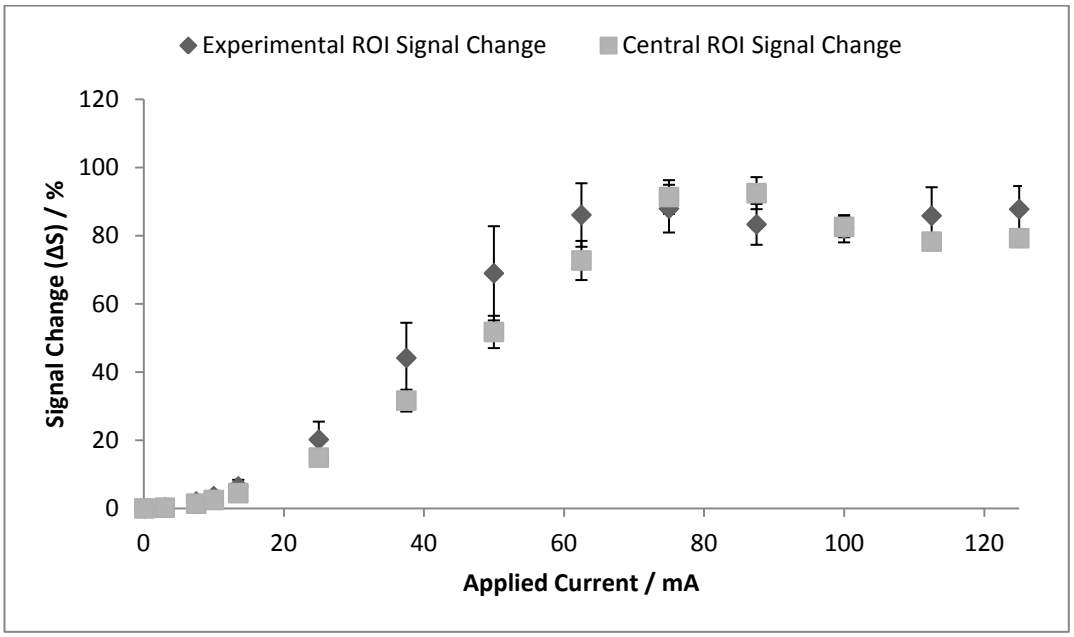

Fig. 4.16 *– Signal change simulations over extended current range for both Experimental and Central ROIs.*

The most obvious result from Fig. 4.15 is that the pattern of signal change is definitely not linear, but rather a SINC function as expected from earlier (Equation 4.8). At high currents the signal approaches near total saturation (~100mA), after which it begins to drop again. There are differences in |ΔS| between the two ROI positions, but this is at a maximum around mid-current values (~60-75mA) and then the two converge again at signal saturation current values. This is unlike the experimental data observed in Chapter 3.8, where the

values of |ΔS| from the different sites were still increasingly divergent from one another at high currents.

Again this suggests that other secondary effects must be occurring to alter the experimental data that are not due to the function of the fMRI phantom itself.

4.7 Addition of Noise to Signal Simulations

Although much has been learnt regarding the properties of the phantom and image analysis process from modelling the operation of the phantom, there is still an unexplained discrepancy between the simulated and experimental measurements of |ΔS|.

A major difference between the simulation and experiment is the lack of any realistic noise component. In experimental measurements the noise level is very low compared to the signal and is generally constant no matter which activation state of the phantom. Therefore experimental fluctuations in noise would not be expected to account for the discrepancy between simulation and experiment.

In order to test this a simple simulation was constructed in MATLAB (Appendix 3.4) that modelled a scaled sinc function to produce a similar signal attenuation output to the full simulations discussed earlier in this chapter (Fig. 4.17)

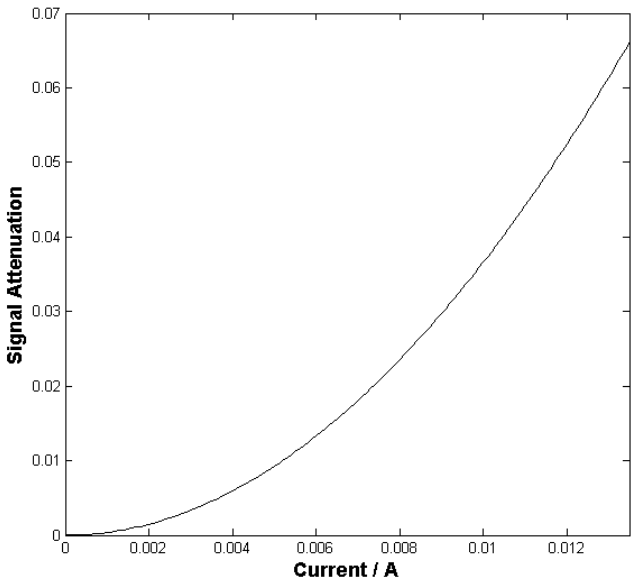

Fig. 4.17 *– Scaled simulated sinc function generated by the script in Appendix 3.4.*

Random noise from a normal distribution was then incorporated to simulate the noise present in an experimental sample and again scaled appropriately using a standard deviation obtained from an experimental data set (Edinburgh June Run 1).

A large number of simulations are run (in this case 100) so that a true sampling of the noise pattern can be obtained to see its likely effect (if any) on the signal attenuation. This generates a final signal attenuation function that takes into account the statistical distribution of the generated noise in the signal on the attenuation. As can be seen in Fig.4.18 the addition of a noise component to the signal attenuation does not alter the underlying shape or scale of the ideal attenuation.

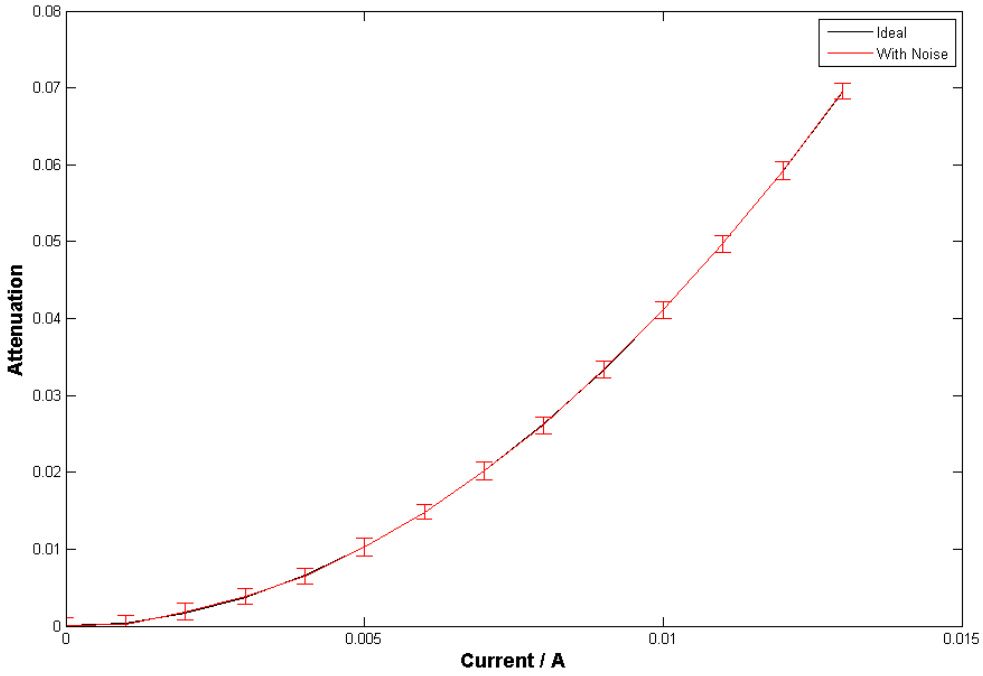

Fig. 4.18 *– 'Noise Sampled' Signal Attenuation function. values (compare noiseless signal function in Fig. 4.17).*

The noise here has been modelled via a Gaussian distribution, as is often used throughout the literature, it would be more accurate to say that it follows a Rician distribution [Gudbjartsson 1995]. This is equivalent to a Gaussian distribution except at exceptionally small SNR values (<2), introducing bias when signal attenuation is very high.

The addition of a realistic noise component to the signal attenuation does not alter the resultant attenuation curve and so is not of any help in trying to resolve the discrepancy

between the experimental and simulated signal change results. The simulated curve remains non-linear and undervalued compared to that of the experimental curve. This difference remains to be adequately explained.

4.8 Chapter Summary

In this chapter operations and performance of the CAT fMRI phantom and aspects of the analysis procedure have both been analysed. Based on first principles the electromagnetic properties of the phantom and its effect on EPI image intensity have been successfully modelled.

While those results have been related to experimental data there are still some discrepancies in the final fit of the simulated data to experimentally derived data. While some of this can be ascribed to ROI properties during the analysis stage, it does not account for all the difference. However, this does not appear to be insurmountable and will probably be overcome with improvements to the phantom model to take into account more realistic aspects of the phantom system as a whole such as electronic noise and signal coupling to the resonator medium. Certainly in the low current regime that has been used with the phantom studies in this project the discrepancy is of limited concern compared to that at higher currents.

Chapter 5 fMRI Phantom Longitudinal Study

5.1 Introduction

In Chapter 3 the development and testing of a satisfactory fMRI phantom was detailed. The final fMRI phantom consists of a carefully positioned pair of wire coils surrounding a resonating medium of Gadolinium doped water. This device is connected to a digitally controlled current system and this is in turn interfaced with the MRI scanner control systems. The success and quality of this final design in terms of repeatability of numerous imaging parameters, including the Contrast Response, SNR and fCNR, gives confidence in the use of the device to study the properties of preclinical scanners.

Two major studies were therefore undertaken using this phantom. These studies are outlined over this and the next chapter.

- **Longitudinal study on Edinburgh preclinical MRI scanner (Chapter 5)**
  This consisted of repeated scanning sessions with the phantom over a period of approximately one year. By performing scans every two months the aim of the study was to both obtain a measure for the long-term stability of an individual scanner and to catalogue the range of behaviours exhibited by that scanner.

- **Multisite Snapshot Study (Chapter 6)**
  This consisted of a second round of phantom testing at other preclinical MRI sites. Unlike previously in the earlier multisite study (Chapter 3.8) where the variability of the current source produced a wide variation in Contrast Response, the properties of the phantom was now well controlled. This would enable a true multisite comparison to be performed, allowing variations between sites that were due to differences in scanner performance to be quantified.

Each of these studies resulted in a range of interesting results that together lead to a conclusion that great caution should be taken in the interpretation and use of data generated by GE-EPI based preclinical fMRI studies.

5.2 Edinburgh Longitudinal Study

The repeated use of the phantom over an extended period builds up an catalogue of scans that can be used to

- Investigate long-term stability of the scanner.
- Study the occurrence and nature of short-term spurious behaviour.
- Provide on-going QA and data integrity support for other concurrently running fMRI phantom studies.

For the first time this will provide an opportunity to experimentally characterise the fMRI performance of a preclinical scanner under operating conditions, without the compounding effects of biological *in vivo* sample variability and associated physiological noise and artefacts.

5.2.1 Study Schedule and Acquisition Details

Data from the testing phase of the Maxwell Coil CAT phantom equipped with the CCCS unit (Chapter 3.11) were used as the initial data for this study. Subsequent scans were taken approximately every two months, dependent on the timetabling of scanner use for other experimental projects and maintenance requirements. During this period there was no major maintenance or system failure except between experiments ED.8 and ED.9 undertaken near the end of the study.

Scans were performed over the period June 2012 – May 2013. This gave almost a full year of coverage of scanner use. This period included typical scanner operations in support of other unrelated projects and also maintenance and repairs to failed equipment where noted. Overall this gives a fair sampling of typical scanner operations over the study period.

Experiment	Date
ED.1	June 2012
ED.2	June 2012
ED.3a	June 2012
ED.3b	June 2012
ED.3c	June 2012
ED.4	August 2012
ED.5	October 2012
ED.6	October 2012
ED.7	December 2012
ED.8	January 2013
ED.9	May 2013

Table 5.1 *– Schedule of Studies for Edinburgh Longitudinal Scans.*

Experiments were conducted and analysis was performed as previously outlined (Chapter 3). A minor change was made in the choice of currents used for Experiment ED.8 as changing scanner properties necessitated an adjustment to current values used in order to maintain like-for-like statistical power to previous experiments. Both functional EPI and anatomical FSEMS scans were performed for each study.

Unless otherwise noted all scans were performed using the previously used rat brain 2-channel phased array coil in partnership with the matching Edinburgh 72mm volume coil. Scans in Ed.6 were performed with only the 72mmm volume coil used in this set up. This was done to confirm both the independence of coil-type on values obtained for $|\Delta S|$ and the Contrast Response and also that SNR and fCNR would be lower utilising the volume coil. This set of experiments was also subsequently used as a match for an experimental set up available on the scanner at King's College London (Chapter 6.3.3).

5.3 Results and Discussion

The results from these experiments are presented and discussed over the rest of this chapter. The results are briefly discussed by image parameter ($|\Delta S|$, SNR, fCNR and Contrast Response) and followed then by a discussion of short term aberrations in behaviour that were intermittently observed within individual experiments. The study is then collectively assessed in order to consider the overall longitudinal performance of GE-EPI on the Edinburgh scanner. For all experiments data tables of discussed imaging parameters are available in Appendix 4.1.

5.3.1 Experiments ED.1-3c

The results from experiments ED.1-3c were previously discussed in detail in Chapter 3.11. In brief summary these experiments showed excellent day-to-day and scan-to-scan repeatability of all relevant measurement parameters including the Contrast Response, SNR and fCNR. Individual measurements of |ΔS| were at times suppressed compared to like-for-like scans at identical current values. Typically this occurred in the first scan of a single day of scans. It also appeared unrelated to the value of current used in the phantom suggesting it was a property of the scanner rather than from any possible interference generated by the phantom itself.

The conclusion from these experiments was that both the Edinburgh scanner and the fMRI phantom itself, when operating with the CCCS, provided a consistent set of results that provided a working basis for continued monitoring of the Edinburgh scanner.

5.3.2 Note on Experiment ED.6

Scans for this Experiment were performed using the Rapid 72mm Volume Coil only i.e. without using the phase array coil for reception as with all others in this study. ED.6 scans were performed immediately after those of ED.5. Between the experiments the phantom was not repositioned and the phased array coil of the previous experiment was left in position so that the results from this experiment are directly comparable to the results of experiment ED.5.

5.3.3 Note on Experiment ED.7

Data was only successfully acquired from four current values. The fifth value was a repeat of the previously used value (0.1mA) due to the phantom being incorrectly reset between scans.

5.3.4 Collective Assessment Discussion

Data tables and figures for imaging parameters sorted by individual Experiment are available in Appendix 4.1 and 4.2 and will be referred to when necessary.

5.3.4.1 Signal Change (|ΔS)

Full tables of values for |ΔS| are contained in Appendix 4.1, but a summary of these results from all experiments in the Longitudinal study is provided in Fig. 5.1 for discussion here.

Signal change values show good consistency from scan to scan suggesting that the performance of the phantom is reliable across long periods of time. Higher current levels in the phantom provide stronger signal changes in resultant MR images as expected. The broad

consistency in values of |ΔS| also suggests that absolute induced signal changes detected by the scanner are also remarkably stable over that same period.

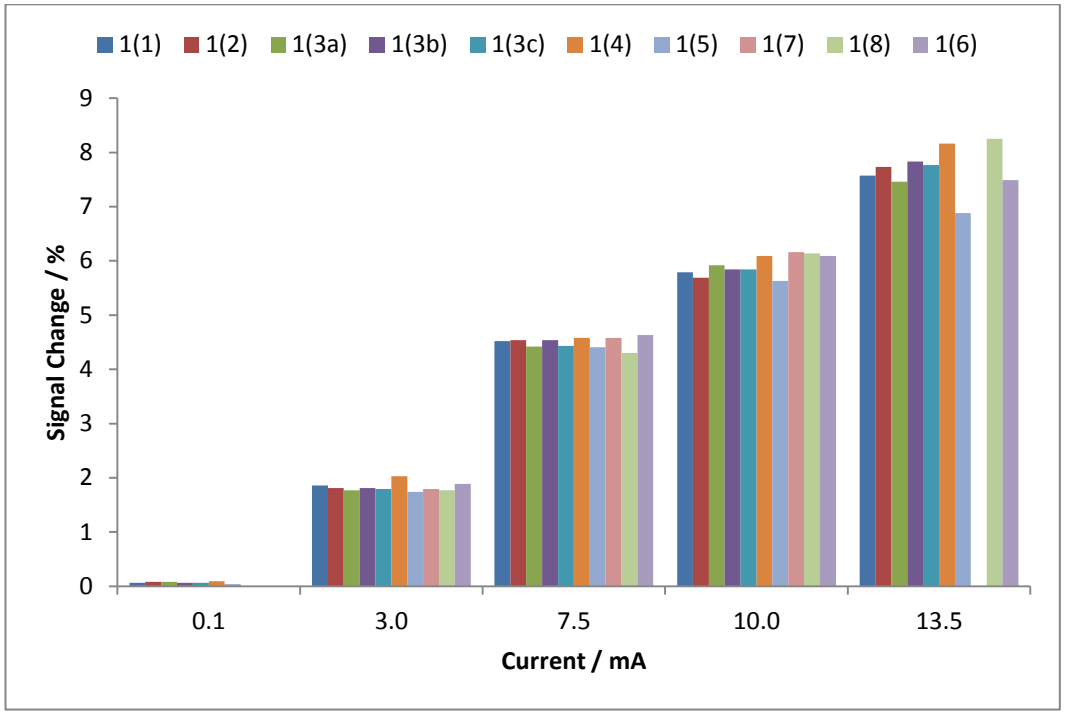

Fig. 5.1 *–Mean |ΔS| values arranged by Phantom current.*

While there is some fluctuation from one experiment to the next overall the values are similar to one another over the successive experiments. The signal change generated from both the PA coil and volume coil experiments are also similar (compare the matching currents from 1(4) and 1(6) for example) as should be expected. The scope of variation is useful to understand as it can put limits on *in vivo* variations and their relevance, if any, to biological signal changes observed.

5.3.4.2 Contrast Response

Across all the experiments the mean |ΔS| per unit of applied current (i.e. the Contrast Response) in the phantom was 0.61 (Standard Deviation ± 0.04) (Fig. 5.2) with no significant differences between experiments. This is a very satisfactory result illustrating the robustness of both the phantom and experimental protocol and calibration over a protracted period despite numerous individual intra-experiment problems and experimental instabilities that are discussed later in this chapter.

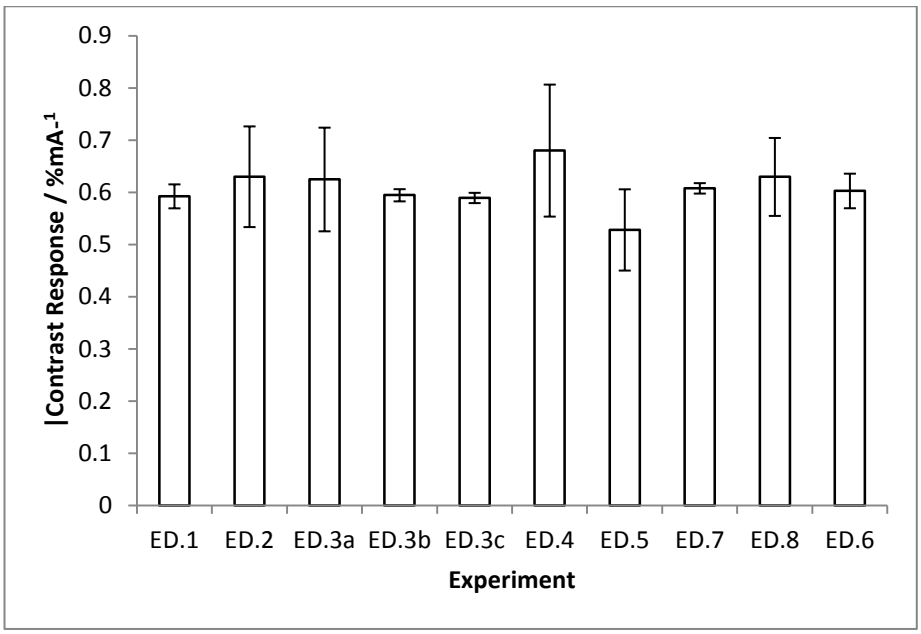

Fig. 5.2 *– Contrast Response results for each Longitudinal Study. Error bars are the associated fitting error.*

Although the error bars in Fig. 5.2 may seem variable in size it should be kept in mind that this is from a sampling of only five current values for each experiment. It would be hoped that with more samples these error bars would reduce in magnitude and standardise in size across future experiments.

Experiment	**Response / % mA^{-1}**	**Standard Error of Fit / % mA^{-1}**	**PCC**	**PCC p-value**
ED.4	0.61	0.01	1.000	<0.0005
ED.5	0.54	0.02	0.995	<0.0005
ED.6	0.58	0.01	0.997	<0.0005
ED.7	0.61	<0.01	1.000	0.003
ED.8	0.61	0.01	0.998	<0.0005

Table 5.2 *– Longitudinal Study Contrast Response Results*

All experiments yielded a highly linear contrast response as expected from the initial set of experiments (ED.1-3c). The value for the Contrast Response does vary across all experiments, but is within a reasonable level of acceptance given the subsequent difference seen at other sites (See Chapter 6).

A low fitting error and high PCC value (and associated p-value) give confidence that the phantom itself is operating as expected.

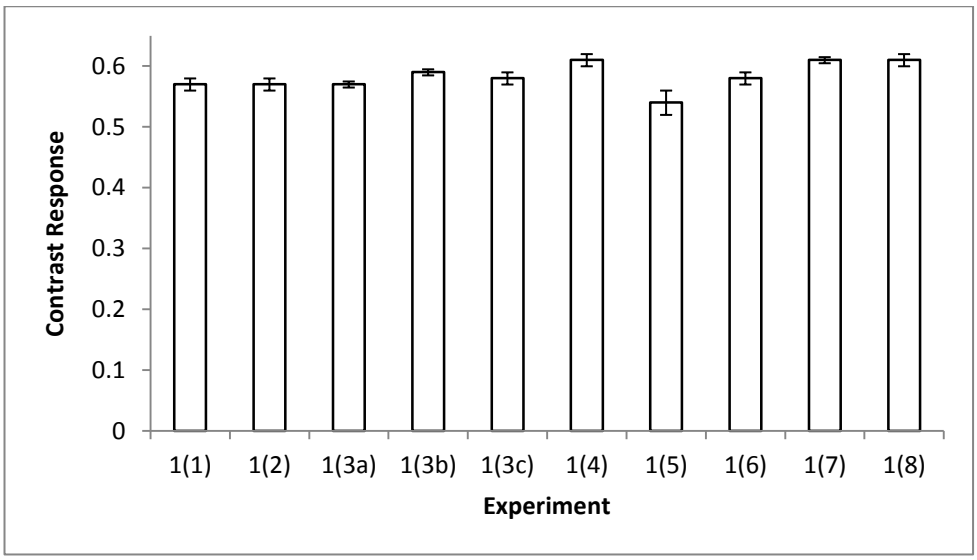

Fig. 5.3 *– Contrast Response to Phantom Signal Change for Longitudinal Study. Error bars represent linear fitting quality from a PCC test.*

The higher level seen in ED.4 could partly be explained by the anomalous behaviour observed in the scans at I = 10mA. Experiment 1(5) shows a noticeable lower value in comparison to the other experiments, presenting both a lower Contrast Response and a higher PCC fitting error value. As detailed in Chapter 5.3.5 there were several significant anomalies in the scanner behaviour during this particular experiment that are probable explanations for the reduced Contrast Response, although the exact cause of these anomalies is unknown. As well as the Contrast Response being generally consistent across the study period, the Standard Error of the fit for the regression line that gives the response is also low in all cases (< 0.01-0.02). This demonstrates that the performance of the phantom and of the analysis procedure is performing well.

The PCC values are also all very high indicating a strongly linear performance of the phantom change in the signal correlated with the phantom current. From theory (Chapter 4) it is known that the signal attenuation is actually non-linear (specifically a sinc function). A near linear function for attenuation probably emerges from the interaction of the dephasing gradient with the Johnson noise of the system. This is probably what is being seen here in the experimental attenuation data. Either way, modelling the experimental data as a linear function to run a PCC test as a measure of scanner stability is well justified experimentally in the current regime used in this study even if the exact theory might not be perfectly linear.

5.3.4.3 Signal-to-Noise Ratio

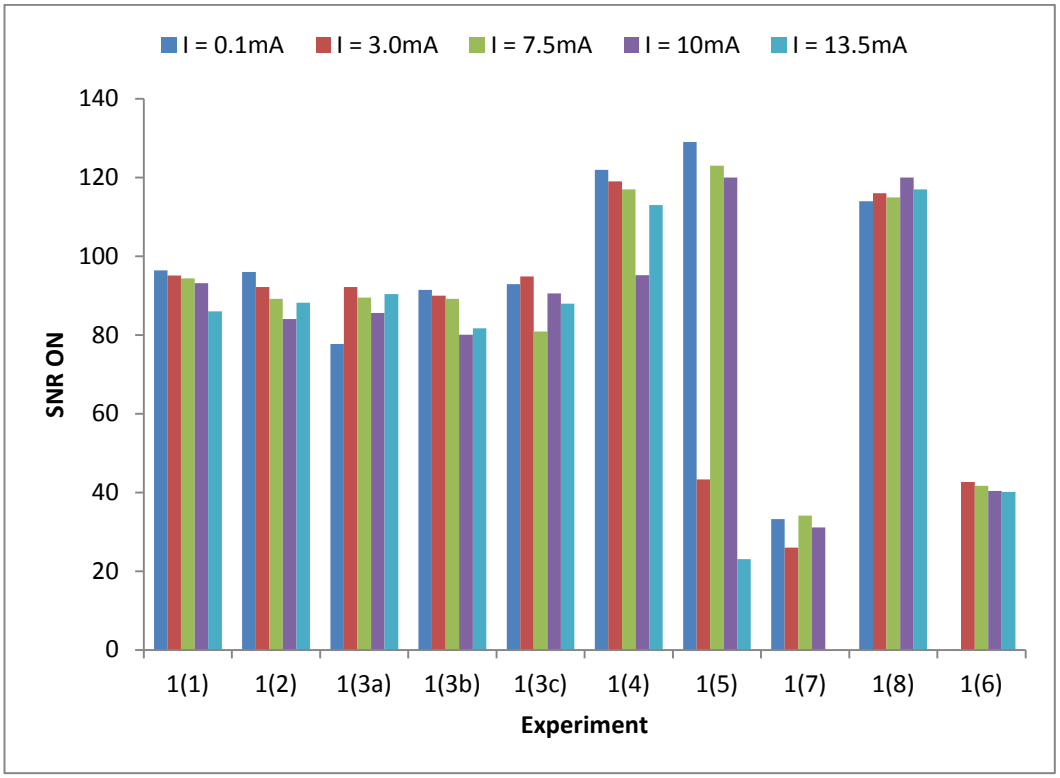

Fig. 5.4 *–SNR for Phantom in ON state*

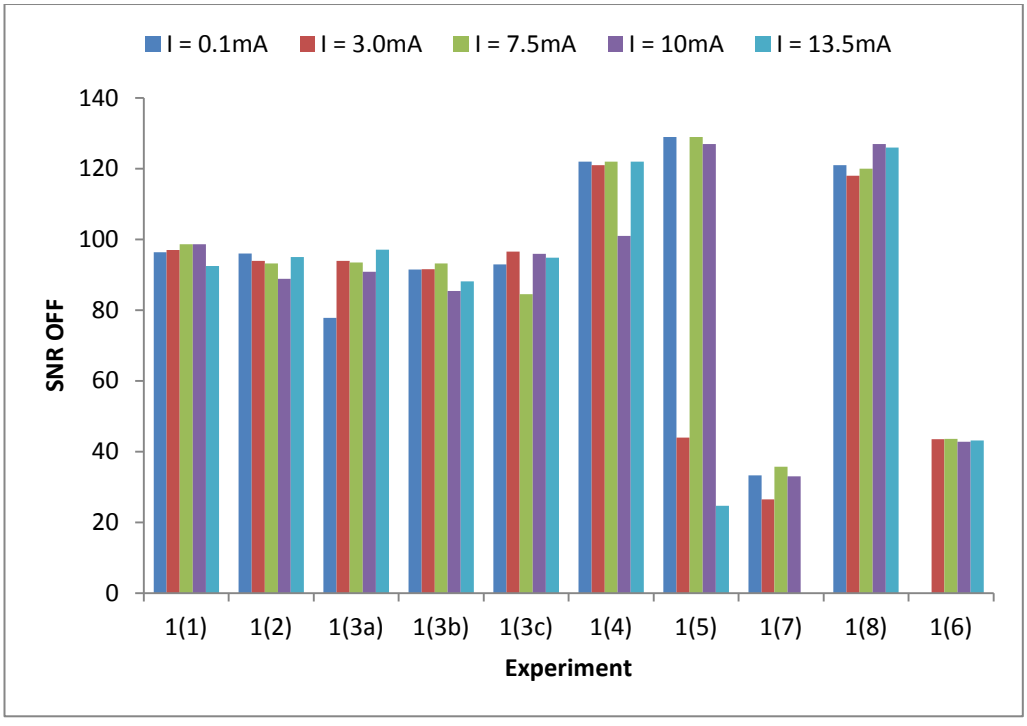

Fig. 5.5 *–SNR for Phantom in OFF state*

In the OFF state SNR stays at an equivalent level across most current values. This is exactly as expected as there is no magnetic field gradient induced signal attenuation occurring in this current state. However, the opposite is true in the ON state and the SNR drops as the MR signal is attenuated by the presence of the magnetic field gradient of the phantom while the background noise level in the system stays constant.

The most striking feature of the SNR when looked at collectively across all experiments in this study was a sudden increase in mean SNR from Experiment ED.4 onwards. This is a ~25% increase, with the only difference between experiments 1-3c and those after being when the data was taken. This SNR increase is sustained across all following Experiments when the SNR is not distorted by other short term effects.

In the OFF state values for mean SNR should be equivalent across all Experiments and current values, since these are based upon the intrinsic levels of signal generated by the phantom and the various background electronic noise sources of the scanner (See Chapter 3.4). There is some variation in this but in general SNR OFF levels hold constant across ED.1-3c and then repeat the jump in SNR seen in the ON state for ED.4-8. This shows that this jump in SNR is not related to the presence nor activation of the phantom itself.

Minor fluctuations in SNR are to be expected from Experiment to Experiment as the electronic noise of the scanner has a randomly influenced component due to the nature of Johnson electronic noise. This is subject to environmental fluctuations such as temperature changes and the physical condition of electronic hardware elements in the system. Between experiments (excepting ED.1-3c), the phantom is also physically removed and then replaced into the scanner. This means that both physical positioning of the phantom in the scanner and slice prescription in VnmrJ is not perfectly identical from one scan to the next which will lead to small changes in SNR. This variation will also be affected by the uniformity of the phantom magnetic field and changes in relative slice position (See Chapter 3.4) between different experiments. These potential sources of experimental variation has been discussed in more detail in Chapter 3 when looking at Experiments ED.1-3c.

As noted before in Experiments ED.1-3c the mean SNR for the first scan of the day for each Experiment continued to be below where it might be expected to be in subsequent experiments when other anomalous behaviour allowed this to be seen (i.e. in ED.4 and ED.8).

5.3.4.4 Functional Contrast-to-Noise Ratio

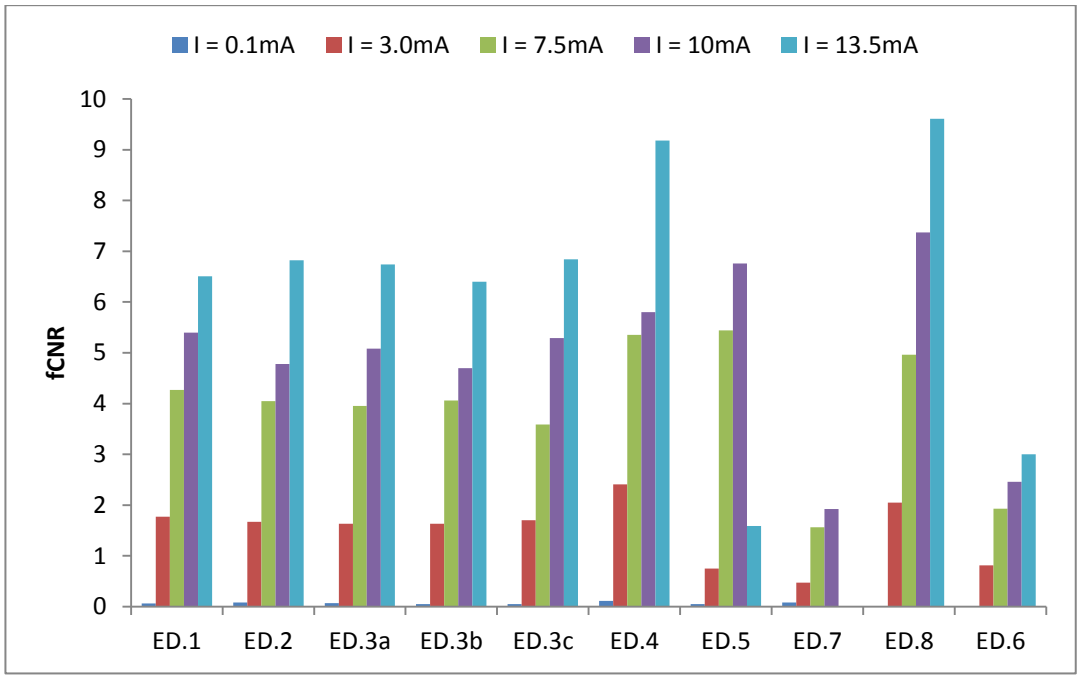

Fig. 5.6 *– fCNR measurements for the Longitudinal Study.*

As expected all experiments yielded an increasing fCNR as phantom current was increased. As anticipated the fCNR for Experiment ED.6 using only the volume coil for signal reception is lower than for the other experiments where a phased array coil was used. It is easy to see in Fig. 5.6 (above) the jump in fCNR going from experiment 1(3c) to 1(4). This is an increase in fCNR is of approximately a third. Like the matching SNR increases from this experiment, the increase in fCNR is maintained over the following experiments. The reduced fCNR values of ED.7 coincide with anomalies seen during the TEP optimisation stage prior to the Experiment start and illustrate quite graphically how such problems can lead to much reduced fCNR and so significance of scanner results.

It is important to note that as the study progressed the detection limit of the phased array experiments appeared to worsen. In later Experiments signal changes associated with current values of 0.1mA were no longer producing statistically significant signal changes (Experiments ED.7 and ED.8). As fCNR is actually higher here than in earlier experiments it is not immediately clear what is causing this effect as the increased fCNR should help further distinguish signal changes from the background noise signal. This suggests that the drop off in detection might not a coil status effect and possibly an artefact from ROI selection and slice/phantom prescription alignment. Alternatively it might be a TEP set up error destroying

low signal change discrimination, with such effects being proportionately more significant at these low current values.

SNR and fCNR values near to the detection limit of a system tend to have larger standard deviations associated with their signal populations compared to other current values. These low current associated values also had higher fCNR per mA values as shown in Fig. 5.7. This suggests a non-linear relationship between fCNR certainty and noise at low current levels. Given the proportionately larger influence on apparent signal changes caused by background electronic noise rather than the gradient field of the scanner it would be unfair to place too much emphasis on these low current values as representing any major deviation of scanner behaviour. Rather they should serve as a warning about over-zealous interpretation of *in vivo* results that also approach the individual detection limit of a scanner at a particular time as revealed by scans using an fMRI phantom.

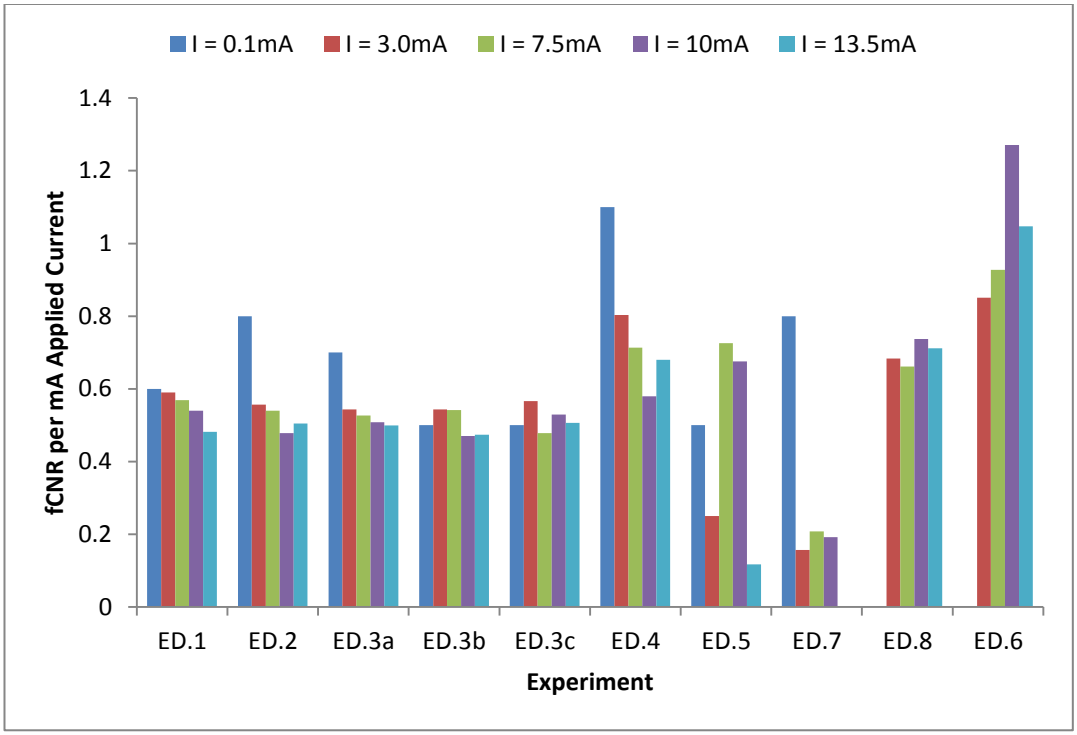

Fig. 5.7 *– Mean fCNR per mA applied current.*

Values for fCNR per mA of applied current should be equal across all current values. In the experimental data such an equivalence occurs rapidly again at current values away from those of the minimum detection threshold. This again suggests great care should be taken when drawing biological conclusions from *in vivo* data as such values are likely to be unfairly disproportionately greater and not given a biological derived true signal.

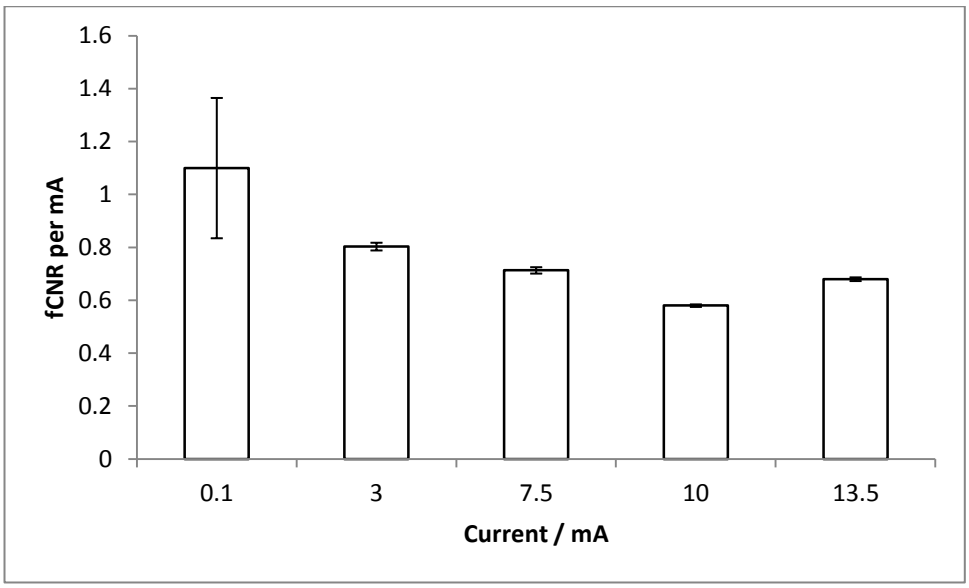

Fig. 5.8 *– fCNR per mA values for Experiment ED.4 illustrating the much larger variation in signal population at very low current values as shown by the much larger associated error at 0.1mA compared to the other current values.*

5.3.5 Intra-Experiment Anomalies

Throughout this study as well as these longer term changes in scanner detection properties a number of shorter term anomalous behaviours were observed in all experiments. Given that these anomalies were so common yet the specifics of them so fleeting it is worth consideration each of them in more detail and how they might impact on both individual Experiments performed and also on potential *in vivo* studies conducted on preclinical MRI scanners.

5.3.5.1 Drop in SNR and fCNR - Experiment ED.4

In this study at I = 10.0mA there is a drop in SNR in both signal states and with the associated fCNR. This drop in fact reduces fCNR to a level almost equivalent to I = 7.5mA. This current value was not run first, so the drop cannot be explained as the previously observed initial drop in imaging parameters described in Chapter 3.11.2. This drop is only seen on this particular set of scans out of the five taken for this scan session. The full plot of Signal vs. Volume data for this scan is provided in Fig. 5.9.

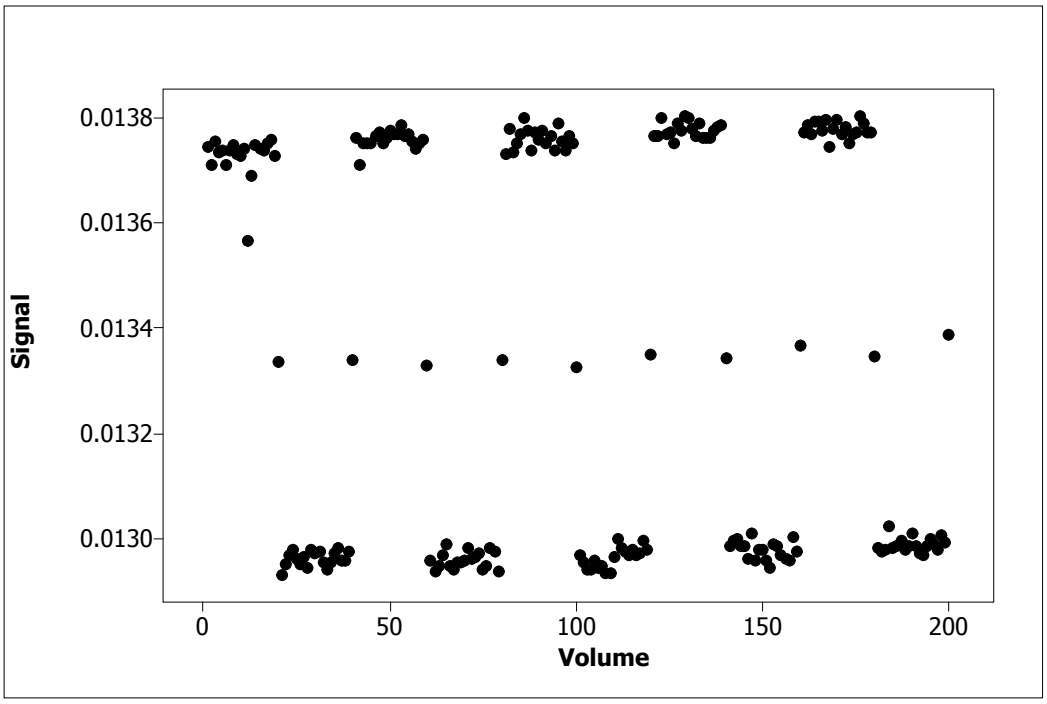

Fig. 5.9 *– Scatterplot of Raw Signal vs. acquisition volume number for experiment ED.4, I = 10.0mA.*

Overall this figure represents what would be typically be considered as a good set of data without any major problems such as large signal level drifts or erratic behaviours that were observed in later scans at other scanner sites. There are a few volumes in the first activation block where signal drops, but these are not a great cause for concern as in other scans there are occasional volumes that also either spike or dip outside the typical signal bounds set by the ON/OFF signal levels of such scans. In this case there is no spiking of that extreme manner and values are within the operational boundaries set by the phantom. The noise similarly exhibits no large erratic changes in behaviour over the duration of the scan.

This drop in SNR and fCNR must therefore be manifesting via a change in the overall signal or noise level of this individual scan. If it is the signal it could indicate either a change in the scanner performance or that of the fMRI phantom. If from the noise, then a scanner fluctuation is the likely source since noise is measured in the images outside of areas containing or strongly influenced by the phantom. When the baseline signal (i.e. the phantom is OFF) and noise values for the ED.4 scans are examined separately (Fig. 5.11 and 5.12) we can see that although the baseline signal is stable across all five scans in this experiment

there is an increase in the noise of 20.5% for this particular scan. This agrees well with the difference between the measured fCNR at 10.0mA in this experiment and that of its nearest equivalent match in alternative experiments (specifically ED.8) which is 21.4%.

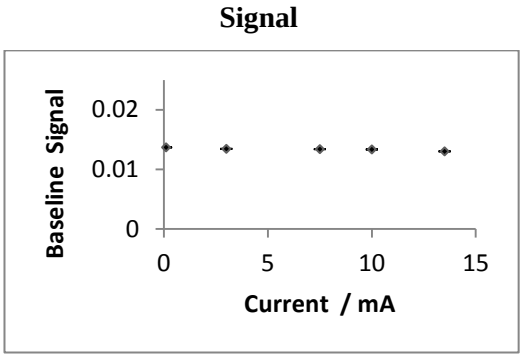

Fig. 5.11 *–Baseline Signal Plat for Exp. ED.4. All signals at the different phantom currents are near identical.*

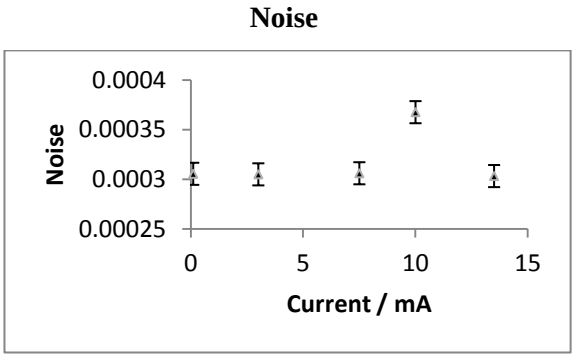

Fig. 5.12 *–Noise Plot for Exp. ED.4. Note the elevated noise level at I=10mA.*

The exact cause of this noise increase is unknown, but it would have to be caused by an effect that lasted only for the duration of the scan as the noise level stayed at this elevated level only for this scan. Speculating, an electronic connection problem might have occurred in the scanner system prior to this scan beginning which increased the noise level in the system. Such a connection problem might have been self-resolving with the start of the next scan as the system reset itself for a new scan. Over the history of the operation of the scanner at Edinburgh such apparent 'self-fixing' of intermittent problems is known to occur and has become an accepted behaviour from the scanner.

5.3.5.2 Signal Steps – ED.4 and ED.8

One anomaly that did occur more than once was what we came to refer to as 'Signal Steps'. In Experiment ED.4 (I = 7.5mA) when the signal time course for this value is examined in detail a 'step' in the signal strength can be seen approximately mid-way through the experimental run (Fig. 5.13). Otherwise the collective behaviour for this current value is in line with expectations.

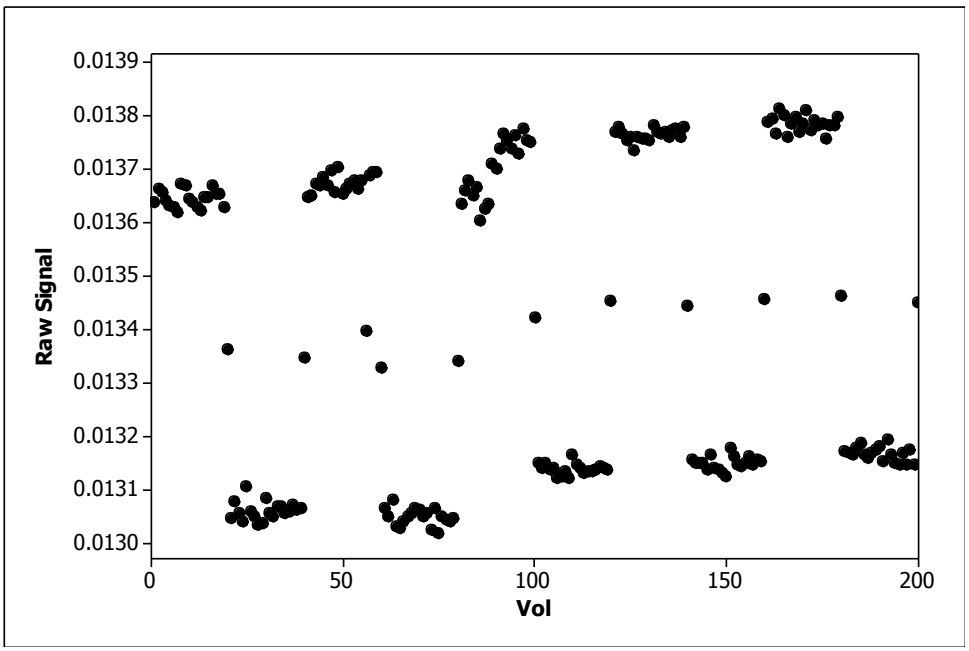

Fig. 5.13 *– Scatterplot of Signal Data Experiment Ed.4 I = 7.5mA illustrating Signal Step Anomaly*

This Signal Step anomaly only represents a signal change of < 1%. This is much less than the change of ~4.5% generated by the switch between the different current states, but it is a real change visible in both phantom activation states. This step is not present in the matching noise trace. The value of |ΔS| pre-step is the same as post-step suggesting the phantom performance hasn't changed and the problem lies in the scanner performance again.

In this particular case there are approximately an equal number of ON and OFF data blocks either side of the step. This results in its effects being averaged across the two states and it is unlikely to directly impact final imaging parameter results. However if an unequal number of blocks in one current state was experienced in a dataset containing a Step Anomaly then this could lead to some differences in comparative data values such as fCNR, particularly if the size of the step was relatively high compared to that of the signal change. If this was to occur on multiple separate animals scanned then they resultant group conclusions would be highly distorted.

The second example comes from Experiment ED.8 at I = 3.0mA where the step anomaly is seen again.

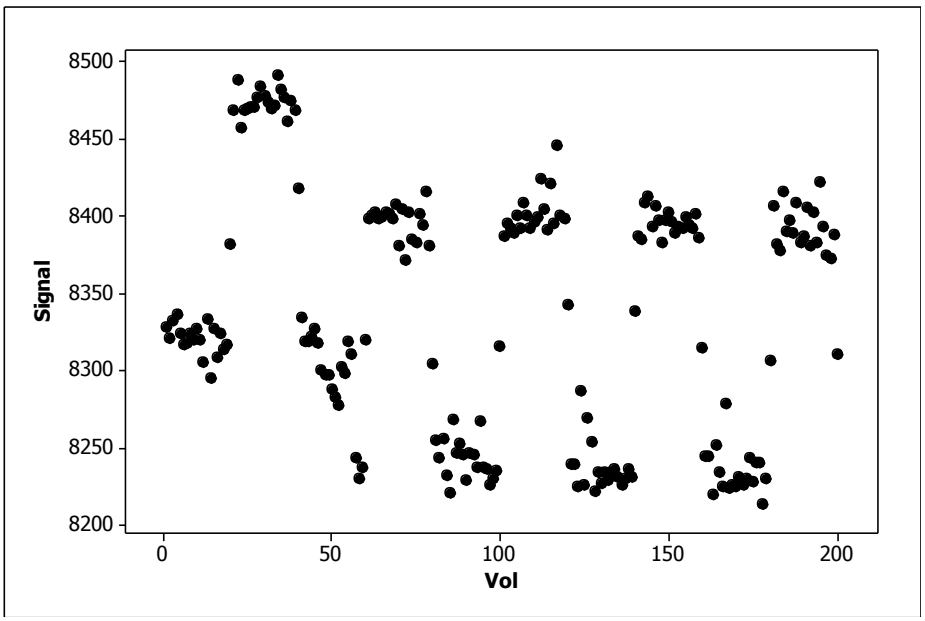

Fig. 5.14 *– ED.8 I = 3.0mA, illustrating the presence of anomalous 'Step' function.*

Unlike in ED.4 the step lowers the Signal in this case rather than raising it suggesting either that the initial signal state was higher than what might be expected or the signal drops later in the experiment. Either way the magnitude of the step change is ~1%, compared to a phantom induced signal change of ~2%. At ~50% of the signal change this step change represents a large proportion of the signal change itself and is illustrative of the potentially distortive effects this anomaly can have on experimental results.

5.3.5.3 Changing Image Parameters During A Study – ED.5

Although this experiment still produced a Contrast Response broadly similar to those of other experiments it was noticeably lower. It also had a larger fitting error and lower PCC value. When the data was fully analysed it also showed suppressed SNR and fCNR for the first two current settings used in the experiment (I = 13.5mA, then I = 3.0mA) compared to similar scans in other Experiments. Both SNR and fCNR increased over the duration of the experiment and had restored to expected levels by the time of the third current setting (I = 0.1mA).

The effect of this reduction in SNR can be visually seen in the signal time courses for this experiment (Fig. 5.15). In Scan 1 (I = 13.5mA) the data trace should look similar to that in Scan 5 (I = 10.0mA) as they are at similar current values. Both currents should show widely separated signal levels with tightly fitting points within each activation state block. Only scans 4 and 5 show this. In Scan 2 (I = 3.0mA) the increased spreading of data points within each current block begins to obscure the current induced signal change. If this was more

severe it is unlikely that a statistically viable signal change could have been discriminated from the data. Scan 3 has not been shown here for clarity as the signal change at this current level (0.1mA) is so low that it can't be easily discriminated visually at the best of times, let alone in this particular case where scanner instabilities may have been further obscuring it.

Scan 1	Scan 2	Scan 4	Scan 5
I = 13.5mA	I = 3.0mA	I = 7.5mA	I = 10.0mA
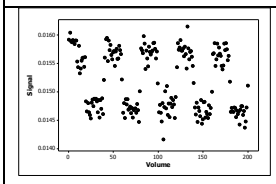	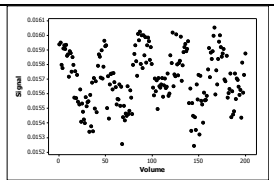	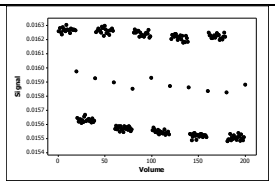	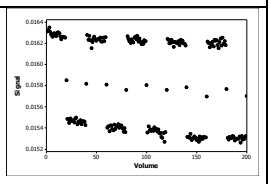

Fig. 5.15 *– Scatterplots of Signal data for Experiment 1(5) showing the improvements in SNR over the duration of the experiment – Noise on each scan gradually reduces.*

Given that the drop in fCNR is accompanied by similar drops in mean SNR in the OFF state it is unlikely that the problem lies with the phantom. Instead the SNR of the scanner itself appears to be temporarily reduced compared to expectations by differing amounts across the successive scans. The values for both the Response and PCC, although slightly different, are broadly similar to what has been observed during other scanning sessions. This further suggests that the source of this unusual variation lies in the scanner hardware rather than the performance of the phantom.

In an *in vivo* study such large decreases in fCNR would swamp out many lesser statistically significant activation events and reduce the significance of the remaining events. This would lead to an under-reporting for such events between subjects scanned during periods of this type of scanner behaviour compared to periods of normal behaviour. If this anomalous behaviour occurs frequently it would have a definite impact on any conclusions based on such mixed results, particularly if groups and/or stimulation presentation is not rigorously randomised or powered sufficiently when scheduling *in vivo* subject scans.

Although *in vivo* fMRI usually involves group comparisons so that the effects of one or two anomalous subjects may have only minor effects on large groups in smaller groups, where anticipated activation differences between groups are minor, such changes in fCNR may have a disproportionate effect on experimental results, interpretations and conclusions.

5.3.5.4 Volume Coil Scans – ED.6

Values for imaging parameters are lower in this experiment compared to those in ED.5. This was expected due to the use of a different coil type that has a lower signal sensitivity associated with it due to the design of the coil. However the Contrast Response and PCC values match well in this data set to the ED.5. This suggests that the contrast effect is independent of coil type used and is dependent only on the magnetic field generated by the phantom.

The gradual decrease in fCNR per mA (Appendix 4.2 - fCNR) was not expected. This decrease while small in absolute terms (going from 0.27 down to 0.22) still represents a relative drop of 18.5% across the current range used. Other experiments showed similar variations, but it is curious that in this particular case it matches the order of increase in applied current.

No significant activations were observed at I = 0.1mA. This is not surprising given the lower coil sensitivity involved and the fact that changes from this current value are only just statistically significant with the more sensitive phased array coil. This result however does provide a neat practical demonstration of the differences between coil configurations that would influence the visibility of signal changes *in vivo* and how this might also effect conclusions drawn with identical biological experimental paradigms but using different coils.

5.3.5.5 Possible Disruption Caused By TEP Speckles – ED.7

The Contrast Response in ED.7 is at the higher end of the range observed in this study, although still at a fairly acceptable level. The PCC however is at a very high value suggesting good performance by the phantom, but it doesn't have as a high a fitting p-value compared to the other experiments, indicating that individual data signal changes were further away from the fitted line than in previously. This is suggestive of performance being quite variable in behaviour across the duration of the scan.

SNR and fCNR values are all very low compared to previous experiments - even to the volume coil experiments of ED.6. Values of $|\Delta S|$ are however in line with those of previous experiments. This again suggests some scan wide drop in signal or noise, rather than any differences in response to the phantom. This decrease in fCNR would also be consistent with the lack of a discernible signal change at 0.1mA in this experiment.

During the setup of this scan the presence of intermittent 'speckles' was noted (Example in Fig. 5.16) during the TEP optimisation stage which were not observed in previous scans.

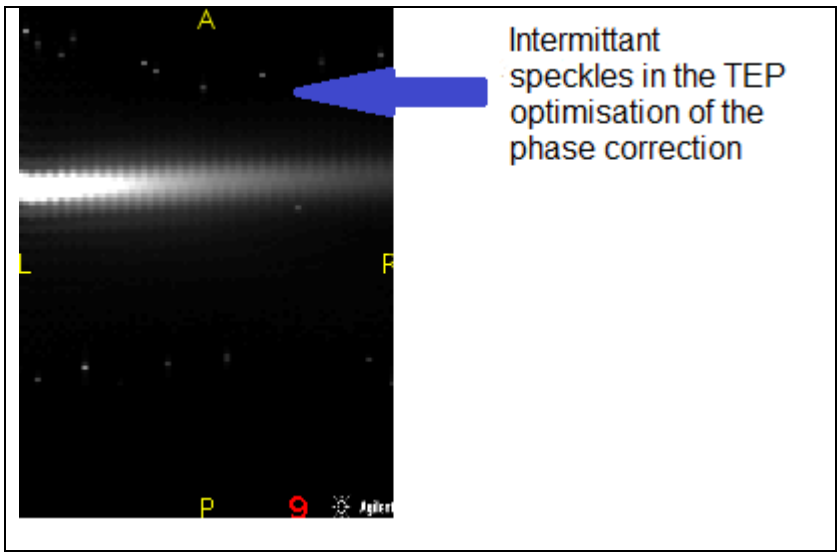

Fig. 5.16 *– Example image of appearance of TEP optimisation speckles.*

Speckles occured throughout the TEP optimisation procedure. This procedure is used to compensate for the temporal differences between the actual and requested start times of gradient waveforms used in the pulse sequence (the so called Gradient Echo Propagation Delay). This is necessary to minimise potential image artefacts caused by this temporal incoherence. Mistiming of this correction can in itself lead to increased artefacts in images [Davies 2005]. The presence of these speckles will produce similar effects to a sub-optimal TEP set up causing imaging changes.

These speckles were not observed in any of the other longitudinal phantom scans at Edinburgh. They were however observed on a single day of *in vivo* scanning for an unrelated GE-EPI project that was performed around the same time as ED.7. However they were no longer present by the time of the next set of phantom experiments (ED.8) a few weeks later. Therefore although this problem appears to have only been a temporary one it was nonetheless persistent across a number of days.

Additional experiences later at both KCL and UCL (See Chapter 6.3.3 and 6.3.4) confirm that these speckles occur at other sites as well. Therefore it would be wise to look for an underlying cause for this problem that would also be common to all sites. Reduced SNR and fCNR parameters were also observed at these sites compared to ‘clean’ experiments in Edinburgh in a similar observation to ED.7.

There was no significant change in signal between the two current states for I = 0.1mA in ED.7. As this experiment had reduced fCNR and the signal change that current value was previously on the limit of detection, it is not surprising that a significant signal change is not

visible in this experiment. This however provides evidences that even at a single location scanner performance can very enough to mask some results previously identifiable at that site.

In the following Experiment (ED.8) SNR levels appear to have been restored to previous levels compared to the lower values obtained in Experiment ED.7. However in this experiment there seems to be a greater amount of variation in SNR as shown in the OFF state so than for previous experiments where it remained more or less level. Signal changes were at expected levels and generated a well-fitted Contrast Response in line with all previous experiments. fCNR increases as expected over the current range for significant detection (I = 1.50 – 13.5mA).

5.3.5.6 Dropped Volumes – ED.8

In the first scan of this Experiment (I = 13.5mA), there were a number of volumes of 'dropped' signal level in the first and fourth blocks of data (Fig. 5.XXX). This is particularly noticeable in the first block rendering the signal points from this block unusable during the image parameter analysis.

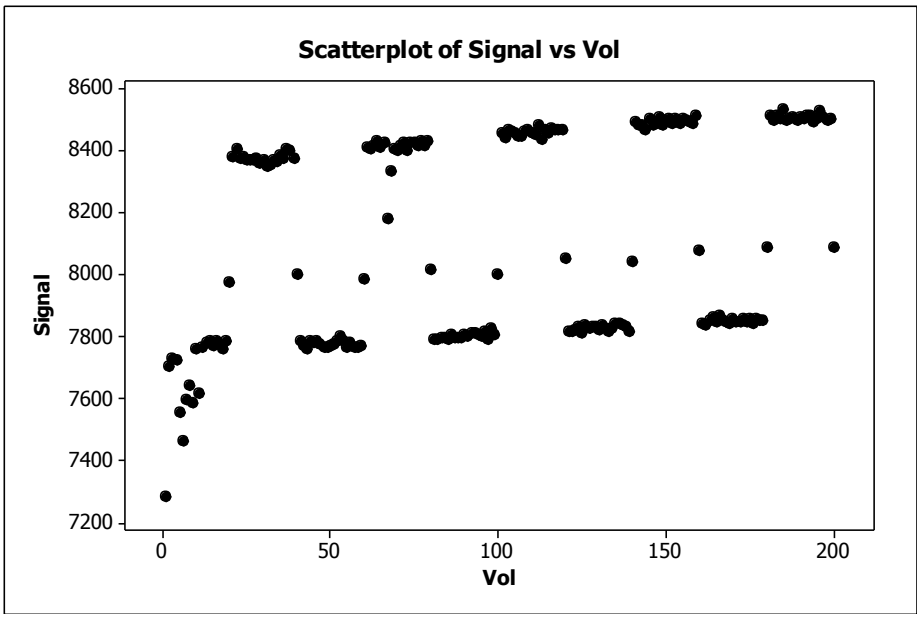

Fig. 5.17 *– ED.8, I = 13.5mA, illustrating signal 'dropping' in the early stages of the scan.*

Although these specific volumes were excluded from the ROI analysis of the experiment data their presence is an example of what may be happening *in vivo* where individual voxel or ROI signal traces are not quality checked in this manner. This underlines the importance

of having some method in place for checking the quality of *in vivo* data before it is processed with semi-automated techniques such as SPM.

5.3.5.7 Equipment Failure – ED.9

Between Experiments ED.8 and ED.9 problems were noticed in non-fMRI phantom projects with both the scanner primary RF transmitter and attenuator boards. This delayed this set of by a number of months more than had been anticipated. The problem was believed to have been repaired before scans in this experiment proceeded. Unfortunately problems appeared to have been persisting or indeed developing anew during this experiment.

Problems were noticed during the initial set up of the experiments with artefact in images already visually present as shown in Fig. 5.18a and 5.18b. For the first time the Streak artefact (see Chapter 2.3.3) also appeared in phantom scans. New ghosting was immediately apparent as was a generally grainier appearance to the image in the background regions outside the phantom suggesting a higher noise level.

a) 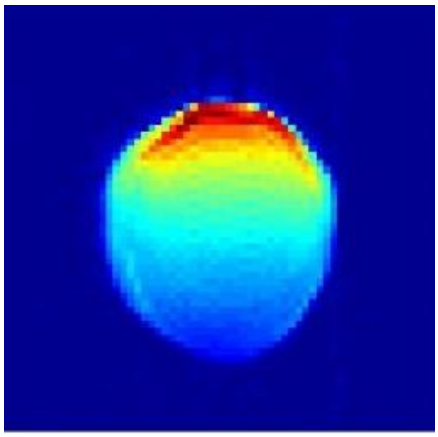 b) 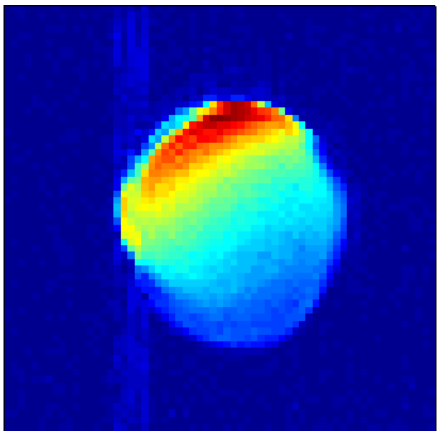

Fig. 5.18 *– Example illustrative images of typical mean signal images from EPIP scans a) ED.4 and b) ED.9 showing increase in artefacts and noise from ED.4 to ED.9.*

Nonetheless scans were attempted and initially all initially seemed fine (volumes 1-150 shown in Fig. 5.19). Beyond this point the signal 'sputtered' and then collapsed. After this point although a signal change was visible the signal had many volumes with signal spikes suggesting fluctuations in signal strength were on going. Signal dips at points of interblock switching also began to appear. If previous observations about these being related to sudden onsets of magnetic field inhomogeneity are correct (See Chapter 3.8.3) then this suggests a problem with intermittent gradient inhomogeneity on the scanner which might also explain the drop in signal if it is dues (or at least partly) if additional dephasing of the signal was occurring due to scanner gradient problems.

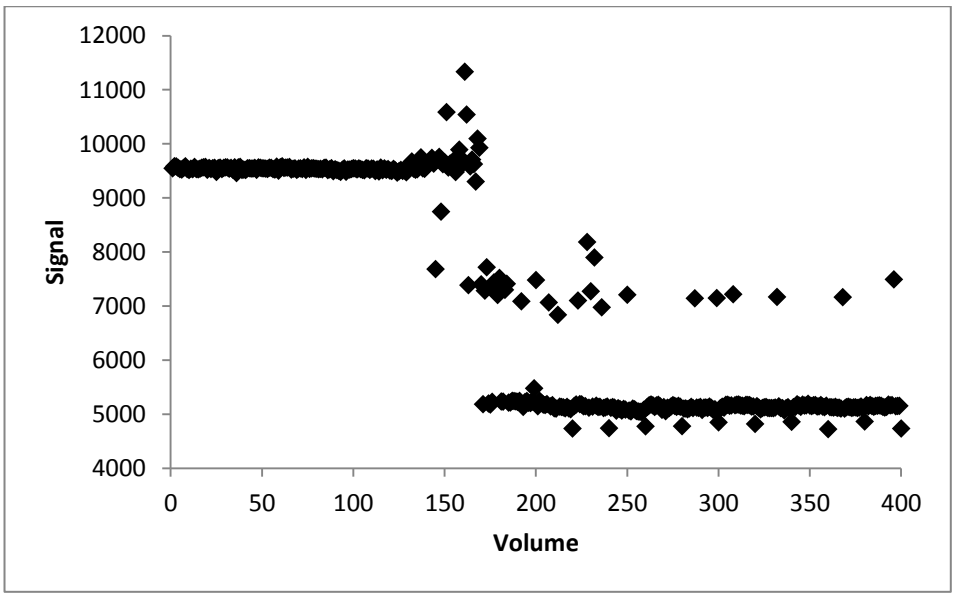

Fig. 5.19 *– Signal trace for two scans taken during ED.9.*

Across the same period the noise behaviour remains fairly constant with no gross abnormalities (Fig. 5.20). The constant noise and collapse in signal suggests that the cause of this change in scanner behaviour is likely to be isolated to either RF transmitters or system gradients that influence the MR signal directly while leaving the background activity of the scanner unaltered.

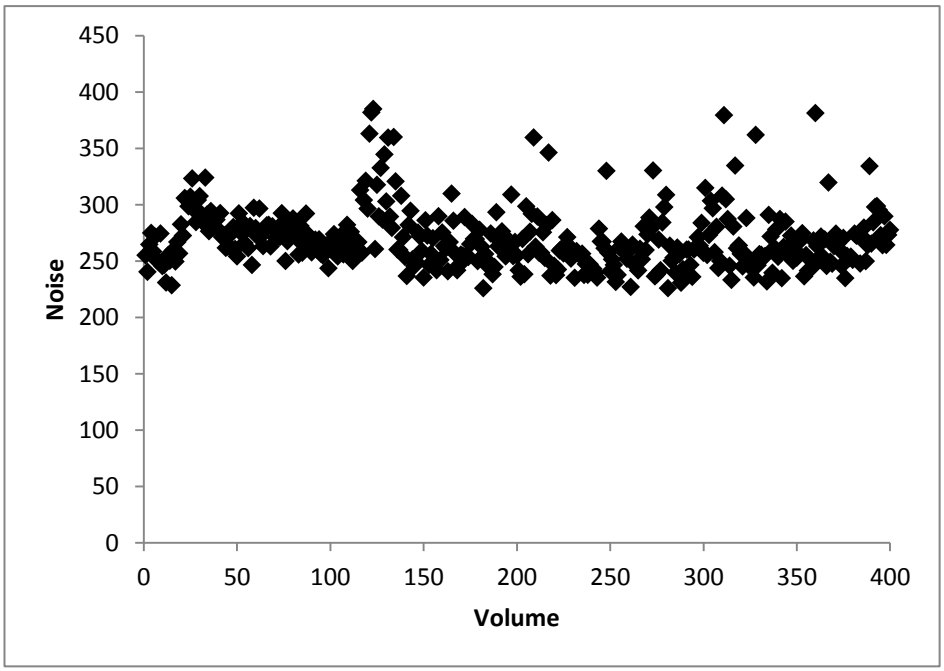

Fig. 5.20 *– Noise trace for matching signal traces in Fig. 5.XXX. Noise behaviour is stable unlike the signal behaviour.*

Again as this way of checking data quality is not a standard procedure on scanners such a problem could happen *in vivo* and go unnoticed meaning separate subjects could effectively be scanned in different scanner environments and thus unwittingly give different results solely due to scanner problems.

5.3.5.8 Changing Detection Limits

Although at the start of the Longitudinal Study all selected current levels generated significantly detectable signal changes as the Study progressed those at the lowest current setting (0.10mA) were no longer detectable even when using the more sensitive phased array coil. Specifically for those from For ED.7 there was no significant signal difference detected between the two current states at I = 0.10mA. Prior to this all phased array coil experiments had managed to see a signal change at this level. No statistically significant signal change at this current value was seen again in any subsequent experiments.

This is particular noteworthy as it would imply that experimental results and subsequent conclusions drawn might be time specific rather than Experiment specific. This would suggest that experimental set ups cannot be replicated across sustained periods.

Current / mA	0.10	3.00	7.50	10.0	13.5
ED.1	Yes	Yes	Yes	Yes	Yes
ED.2	Yes	Yes	Yes	Yes	Yes
ED.3a	Yes	Yes	Yes	Yes	Yes
ED.3b	Yes	Yes	Yes	Yes	Yes
ED.3c	Yes	Yes	Yes	Yes	Yes
ED.4	Yes	Yes	Yes	Yes	Yes
ED.5	Yes	Yes	Yes	Yes	Yes
ED.6	No	Yes	Yes	Yes	Yes
ED.7	No	Yes	Yes	Yes	Yes
ED.8	No	Yes	Yes	Yes	Yes

Table 5.3 – Summary table of signal change detection success.

In Experiment ED.8 an additional measurement was made at 1.50mA to ensure that five usable sets of data would be generated even if the 0.10mA data didn't show a signal change. This was also the first experiment where the initial starting polarity of the switching box on the CCCS had been altered so that the phantom would start in the ON state rather than the OFF as in all previous experiments, but this was not expected to change detection limits.

Although due to equipment failure in experiment ED.9 no firm conclusions can be drawn scans were conducted at a number of points ranging from 0.10mA through to 1.50mA with no successively signal change detections detected. Two non-exclusive conclusions might be drawn from this. Either the degradation in detection limit had reached the point where even a current of 1.50mA was now insufficient to generate a significant change or that the critical equipment failure seen later in this experiment was already having much wider effects on signal and noise behaviours before it totally failed (See Ch. 5.3.5.7).

The loss of low current signal change detection observed earlier in this Study could perhaps then be suggestive as signs of problems with equipment stability and performance that are than manifested as the larger problems seen in ED.9. In this sense performing fMRI quality assurance tests with the fMRI phantom would also lead to earlier warning signs of future problems with wider scanner integrity, allowing such problems to be addressed earlier before critical system failure occurs.

5.4 Chapter Summary

There are three main conclusions to be drawn from this Longitudinal Study:

1. Scanner contrast stability in terms of absolute signal change is excellent across both the short and long term. This provides a great deal of confidence when considering absolute signal changes generated at a single preclinical MRI site over time from GE-EPI experiments and analysis.

2. SNR and fCNR can change across both short and long term periods. Sometimes this can be beneficial (as in the case of fCNR going from ED.3c to ED.4), but often it is detrimental (as in the decreased SNR of days first scans and TEP speckle anomalies. Either way this can lead to varying levels of significance being assigned to different subjects, groups or studies which do not originate from changes in the actual experimental subjects or stimulatory mechanisms, but rather emerge simply from variations in scanner performance at different time points. This altered significance could potential skew conclusions drawn from *in vivo* fMRI studies, where subject numbers are either low and/or neurologically derived signal changes are small. Caution should also be taken with the interpretation of activations at or close to the detection limit of a scanner as these levels seem subject to much wider variations in signal properties.

3. While individual scan behaviour is generally reliable, the presence of various signal steps, drops and single volume spiking could lead to distortions in research conclusions. These effects are likely to be disproportionately greater in studies where experiments utilise lower numbers of EPI volume acquisitions or in group studies with low subject numbers. No single Experiment was completely immune to these effects with at least one of the five scans in each experiment exhibiting non-typical behaviour.

The scans performed in this study represent a small slice of sampling potential. The possibility does exist therefore that these experiments have just been performed at times of anomalous scanner performance - although nothing unusual was reported by facility staff regarding scanner behaviour during the period in which these scans were taken. As is seen in Chapter 6 many of these non-typical effects are also seen in scans taken at other sites. More extensive analysis and experimentation would be needed to confirm levels and frequencies of occurrence of these various problems in order for any firm conclusions regarding the exact causes of the variations in performance observed.

Although clearly useful as a functional neurological technique and with good overall performance, it is recommended a cautious approach is taken to GE-EPIP originated fMRI results. Individual data sets should be checked for anomalies of the types outlined in this chapter before that data set is submitted into pooled group analysis results.

An on-going program of fMRI phantom monitoring should also be implemented to track any further significant shifts in basic imaging parameters. This programme should include regular examination of any further changes in the detection limit of scanner and coil set ups.

Chapter 6 fMRI Phantom Multisite Study

6.1 Introduction

One of the objectives for creating the fMRI phantom was to provide a means for cross checking the performance and calibration of scanners located at different preclinical facilities. This would be able to provide evidence-based assurances that *in vivo* research results emerging from different scanners could be directly compared with one another in a meaningful manner.

The first multisite study (See Chapter 3.8) indicated a wide range of Contrast Response values from the phantom induced magnetic field. This is contrary to what would have been expected from basic theory which suggests that, when properly sampled, the Contrast Response is dependent only on the phantom induced magnetic field gradient and not the properties of an individual scanner (See Chapter 4.2). Replacement of the phantom current source with the CCCS source minimised the variations in the Contrast Response seen in the Edinburgh scan data (See Fig. 5.3.4.2). This suggested that using this new current source the phantom was now able to provide reliable magnetic field gradients across multiple experimental runs. This gave sufficient confidence in phantom performance in order to go ahead with a second multisite study using this new current source to test predictions of phantom behaviour and comparative performance between different scanner sites.

Specifically it is predicted that $|\Delta S|$ will be broadly equivalent at all scanners resulting in an equivalent Contrast Response value between sites. Ideally parameters such as SNR and fCNR would also only very with either choice of MRI coil. Remaining variations and unexpected behaviours could then be attributed solely to changes in scanner or coil behaviour and quality.

6.2 Multisite Study Details

For this study scans were performed at four sites according to Table 6.1. Available coil types varied at the different sites, but provided a good representation and sufficient cross-over in basic type to make reasonable comparisons of performance based on the known properties such coils should relatively possess. Volume coils should give lover values for SNR and fCNR while phase array coils should give higher values and more so as the number of coil elements increases.

Site	B_0 / T	Coil Used	Scanner Manufacturer	Scanner Type
Edinburgh	7.0	Rapid 2 x channel rat brain PA	Agilent Technologies	Direct Drive
Edinburgh	7.0	72mm Volume Coil	Agilent Technologies	Direct Drive
Glasgow	7.0	Rapid 4 x channel rat brain PA	Bruker	BioSpec
Kings College London (KCL)	7.0	72mm Volume Coil	Agilent Technologies	Direct Drive
University College London (UCL)	9.4	Rapid 4 x channel rat brain PA	Agilent Technologies	Direct Drive

Table 6.1 *– Summary of Multisite Snapshot Sites and scanner hardware used.*

All scanners were 7T preclinical scanners, except for the scanner at UCL (Centre for Advanced Biomedical Imaging, University College London, London, UK) which was a 9.4T preclinical scanner and was added to the rosta for this second multisite study. To have a scanner at a higher primary magnetic field strength is actually useful as it provides an experimental check that primary magnetic field strength does not affect the Contrast Response of the phantom. In the first multisite study scans were also taken at Agilent's facility in Yarnton, Oxford but this was unable to be performed this time. Although new scans were planned at this site for this study they were unable to be conducted as the scanner at that site was undergoing a comprehensive upgrade project in the period leading up to the multisite study and was still unavailable at the required time.

All Agilent scanners ran the modified 'epip_pulse' sequence for use with the CCCS power source. At Glasgow the Bruker EPI pulse sequence was similarly modified for use with the CCCS system on the Glasgow scanner.

Location	Date	Experiment
Edinburgh	August 2012	ED.4
Glasgow	October 2012	GL.1
KCL	October 2012	KC.1
UCL	November 2012	UC.1

Table 6.2 *– Experiment Scheduling for Multisite fMRI Phantom Study*

Although Experiment ED.5 (October 2012) is from a close matching time period to match those of the other sites it contains several unusual local site specific anomalies that would preclude it from providing a fair comparative assessment. Because of this in the multisite analysis data from Experiment ED.4 was used as a substitute dataset instead as this provided a more stable and good quality data set. This was the next nearest match in time and which was also of stable quality of behaviour. ED.7 was excluded from being a replacement set of data due to showing the anomalous speckle TEP effect in the TEP setup procedure and associated imaging parameter problems.

6.3 Multisite Study Results and Discussion

Results from this study are summarised below along with a brief discussion on each site. The multisite results are then discussed collectively together and then further in the context of the results from the Edinburgh Longitudinal study.

6.3.1 Edinburgh - ED.4 and ED.6

The data for this comparison was from experiments ED.4 and ED.6. These results have been discussed extensively earlier in this thesis (Chapter 5).

6.3.2 Glasgow - GL.1

The scanner at Glasgow was a Bruker BioSpec system which was equipped with a matching Rapid phased array brain coil as at the Agilent sites of Edinburgh and UCL. The EPI pulse sequence used was also coded by Bruker, but performed the same application using the same physical principles as the Agilent equivalent. Experiments were run with parameters to match those of the Edinburgh Longitudinal study as closely as possible.

As the Bruker EPI pulse sequence does not include an option for individual-volume navigator correction (the Full Triple Referencing option featured on the Agilent EPIP sequence described in Chapter 2.3.3), scans on the Glasgow scanner were performed solely with navigator correction at the start of each scan. This meant that the scans at Glasgow took

only half the time that they did at the other sites. They were however more susceptible to imaging distortions caused by the presence of the phantom wire coils and other B_0 field inhomogeneities.

Shim Gradient strength was also less than at the Agilent sites ($400nTm^{-1}$) and shim coils were physically further away from the sample, all of which limited their ability to create as high quality a shim in comparison to the Agilent scans. This limited the quality of the shim during set up to the point where requests for more rigorous shimming were not acquiesced to due to the site's staff strong feeling that it would be redundant to even attempt it.

Contrast Response

Response / % mA^{-1}	**Standard Error of Fit / % mA^{-1}**	**PCC**	**PCC p-value**
0.54	0.04	0.977	0.004

Table 6.3 *- Contrast Response Results for Experiment GL.1*

The Contrast Response generated in this experiment was comparable to the range outlined by the Edinburgh study in Chapter 5, albeit perhaps at the lower end of this. There was a larger fitting error and higher PCC number indicating a slight deviation from linear performance. This could perhaps be explained by the less rigorous experimental set up performed at this site and the more limited control over scanner gradient optimisation available. Both of these could have increased relative noise levels in the images as well as not correcting for EPI image artefacts as fully as at other sites. This would leave imaging parameters more susceptible to fluctuations in electronic noise and image distortions compared to Agilent scanners running the more sophisticated EPIP corrective options.

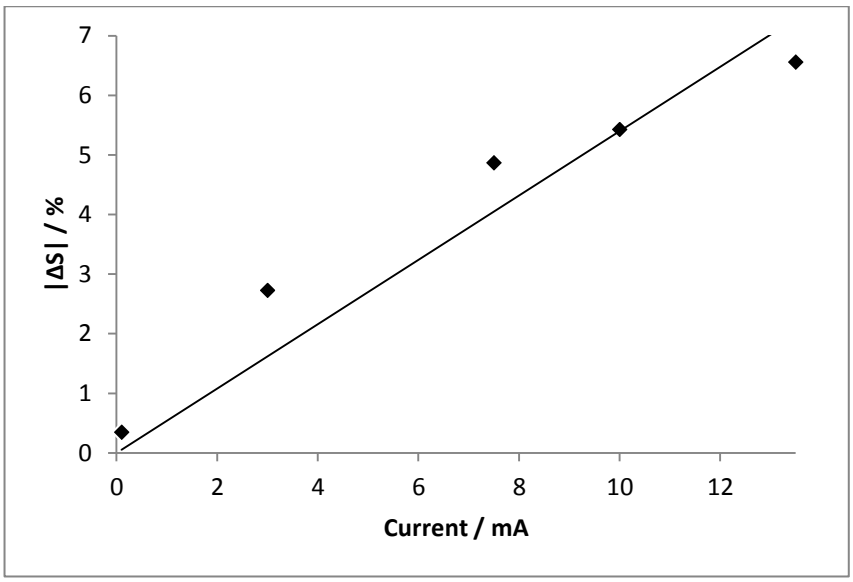

Fig. 6.1 *- |ΔS| for Experiment GL.1 with linear fit line superimposed on experimental data points. Note that very few points lie on the linear line of best fit unlike the examples from the Edinburgh Longitudinal Study (Chapter 5.XXX).*

SNR

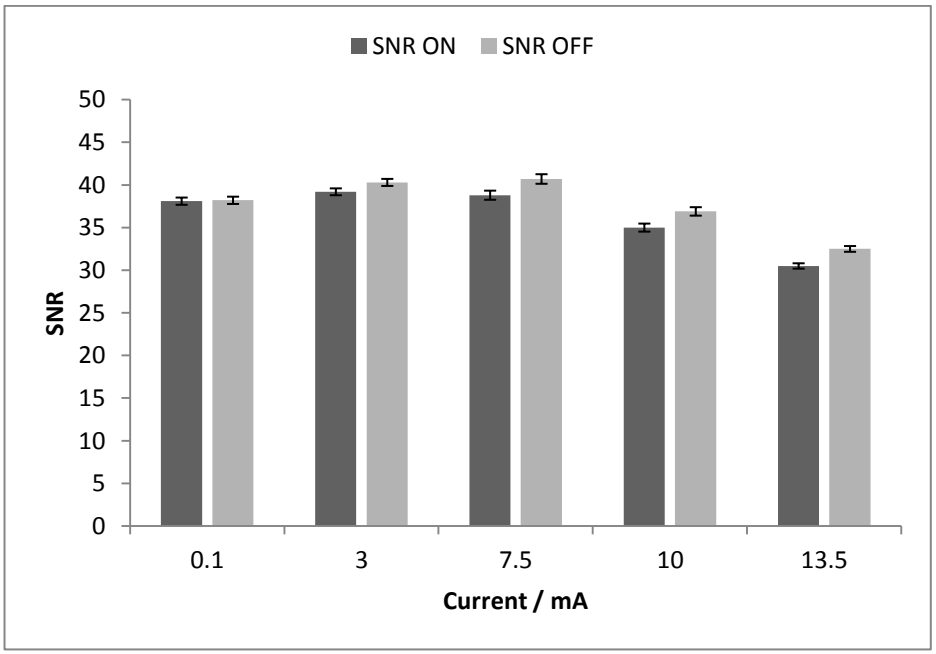

Fig. 6.2 *–SNR Values for both ON and OFF current States for Experiment GL.1*

fCNR

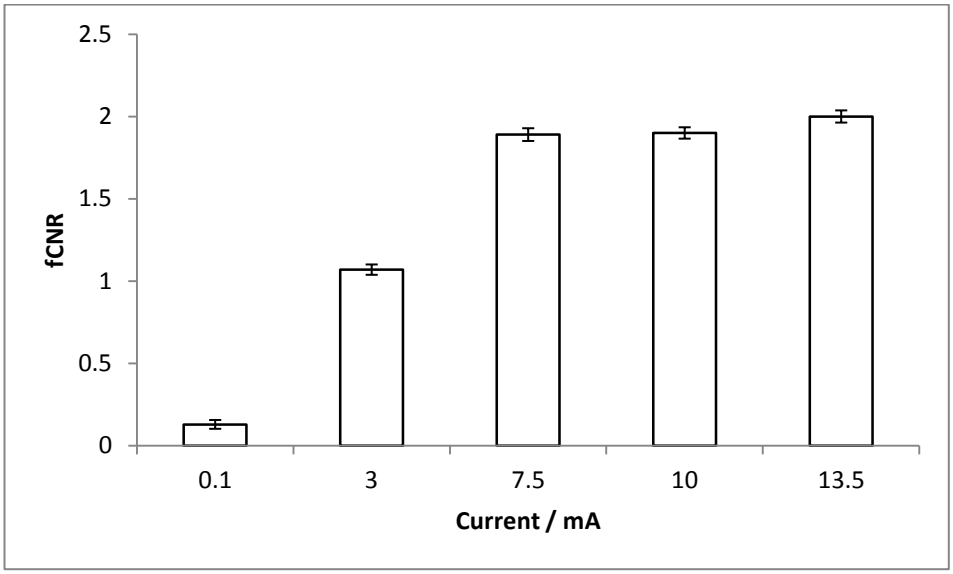

Fig. 6.3 *– Mean fCNR values for Experiment GL.1*

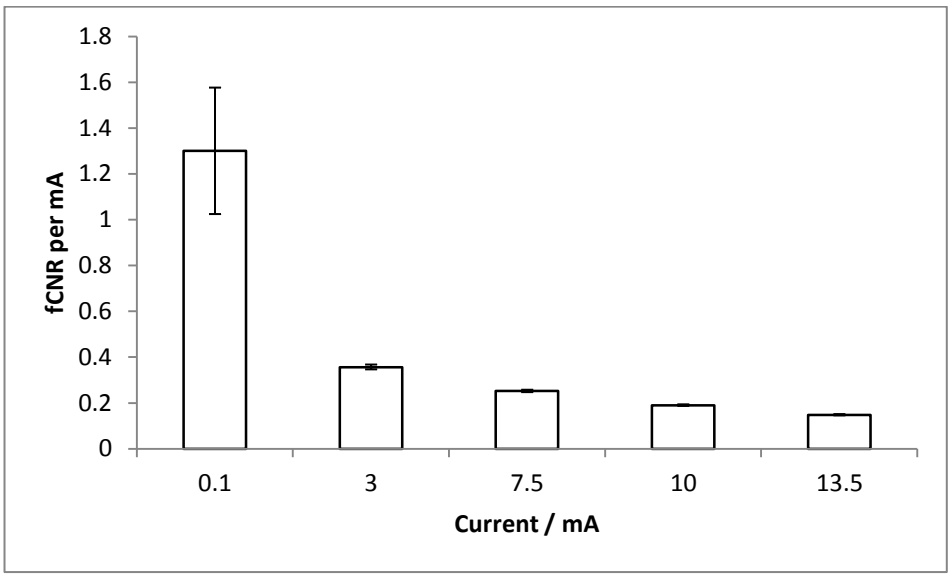

Fig. 6.4 *–fCNR per mA applied current for Experiment GL.1*

Levels of SNR in the OFF current state were not stable on this system and showed variation. SNR levels appeared to be dropping from the third scan onwards. This impacted on fCNR levels to such an extent that they did not show the usual pattern of increasing fCNR with current in the phantom. A likely explanation for these changing SNR and fCNR levels is that the temperature of the gradients on the system was rising and degrading performance. Experience with this particular system from unrelated non-EPI studies [Merrifield 2013a,

2013b] demonstrated that gradient temperatures at this site was often high enough to trip the system several times during a day's scanning when such scanning required a high gradient load. The gradients on this Bruker system are not as strong as those on the Agilent systems and so would have been worked closer to their limits in order to give the same experimental parameter matches of field of view, matrix resolution etc. The system was also running off a lower quality amplifier from a separate Bruker Pharmascan magnet rather than its own which was undergoing repairs at the time.

The inter-block transient volumes observed on Agilent systems utilising the Full Triple Referencing option were not present here on the Bruker scans. This is further evidence suggesting that the appearance of these on Agilent scans is due to the timing of current activation/deactivation connected to the use of the extra pre-volume navigator scans.

6.3.3 Kings College London - KC.1

Unlike the other sites KCL did not have access to a phased array brain coil so scans were taken with just a 72mm volume coil which was also available at Edinburgh. Scans were taken using this coil configuration at both sites (both 7T sites) for direct performance comparison (Experiment ED.6 for Edinburgh scans). For these scans it was predicted that the Contrast Response should be the same as at all the other sites, but because of the use of a different type of coil SNR, fCNR and detection limits would be lower - as seen on the similarly equipped experiment in Edinburgh.

Prior experience at KCL (See Chapter 3.8) suggested that performance of the volume coil at KCL in terms of detection limit would be significantly inferior to that of the matching coil set up in Edinburgh. Because of this, current levels were deliberately chosen to be at a higher level for the KCL scans to ensure an adequate sampling of resulting signal change data points for generating a Contrast Response measurement with the same statistical validity as at the other sites.

The results from KCL present an intriguing case. All results from KCL were heavily dependent on where the ROI was placed in the EPIP images. At other sites this was much less so, as would be expected from the highly uniform dephasing gradient that is generated between the two coils. With the KCL data however as the ROI was moved to different positions on the images, moving left to right (across the frequency encode direction), the value of $|\Delta S|$ changed. As the ROI was swept across, $|\Delta S|$ went from values much higher than normal through to zero change. Inter-block transients exceeding the signal change limits of the phantom effect also became more prominent as the ROI was swept across (Fig. 6.5)

Position of ROI on EPIP Image	Screen grab of signal trend
Left Hand Side Phantom	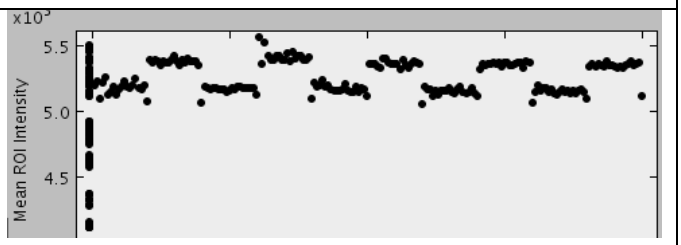
Middle Phantom	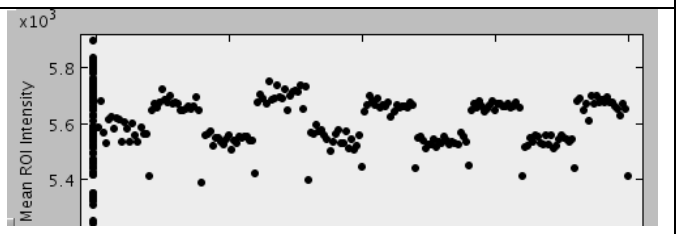
Right Hand Side of Phantom	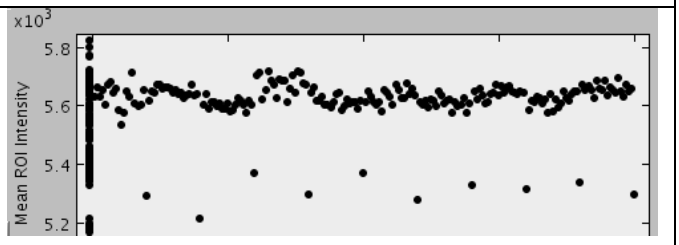

Fig. 6.5 *– Example signal traces of KCL ROI Position based anomaly. As the ROI is moved across the image basic image parameters alter.*

When the Frequency Encode direction was rotated in-plane by 90° this asymmetric effect was still present but now translated into the top-down direction. This pattern is not repeated in the phase encode direction in either prescription orientation.

When an alternative second 72mm coil was used the effect remained present. This suggests that a non-coil related effect is behind this anomaly, potentially something to do with the operation or set up of the gradient profiles. No major problems were noticed during shimming of the system suggesting inadequate shimming was not behind the problem. No significant different geometric distortions were seen in either the EPIP or FSEMS anatomical data from this site. This anomaly remained unexplained beyond speculation regarding unstable or biased gradient setups that may be contributing additional local magnetic field differences onto the phantom's magnetic field.

Because of this problem an adequate ROI with comparative contrast properties was difficult to locate. The following image parameter results and discussion must therefore be taken with that caveat in place. The final ROI position was approximately one third a phantom diameter away from the centre of the usual ROI position (identical in all other experiments), with the

dimensions of the ROI being the same as before and so containing the same number of voxels. This carefully selected ROI was based on finding an ROI that generated similar Contrast Response results and interblock transient behaviour as at other sites and so was a reasonable ROI from which to extract other image parameter values.

Contrast Response

Response / % mA^{-1}	Standard Error of Fit / % mA^{-1}	PCC	PCC p-value
0.57	0.04	0.943	0.016

Table 6.4 *- Contrast Response Results for Experiment KC.1*

SNR

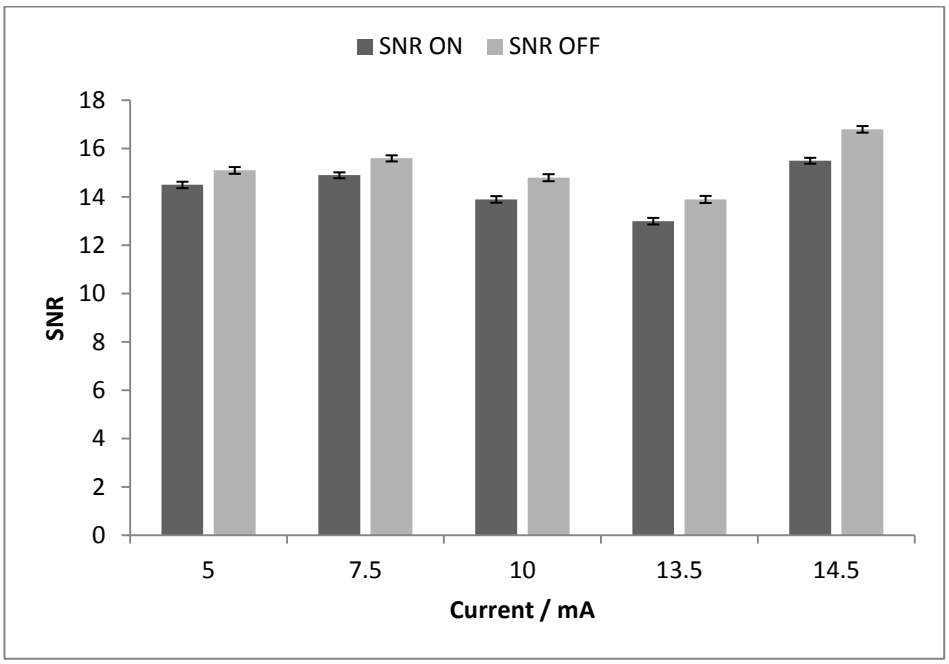

Fig. 6.6 *–SNR Values for both ON and OFF current States for Experiment KC.1*

fCNR

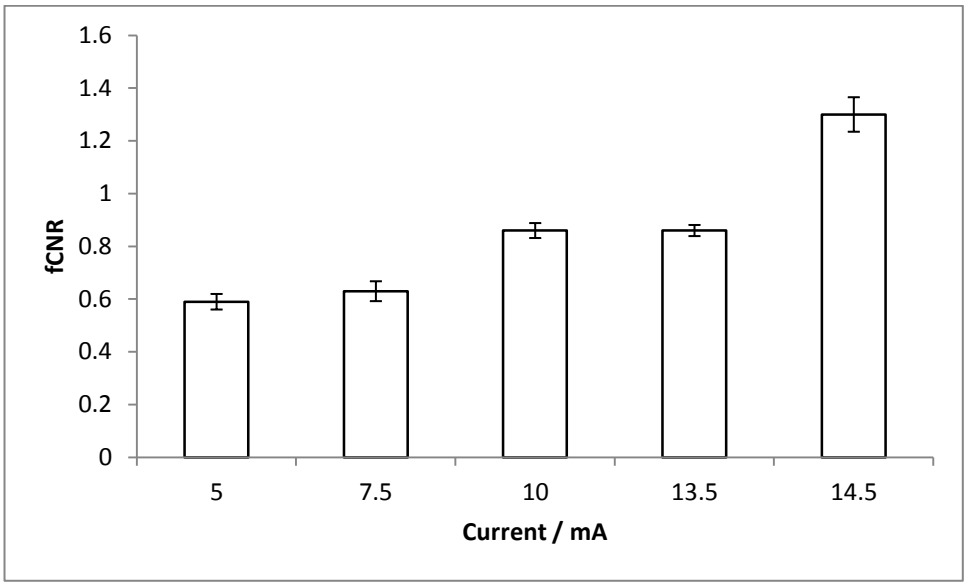

Fig. 6.7 *– Mean fCNR values for Experiment KC.1*

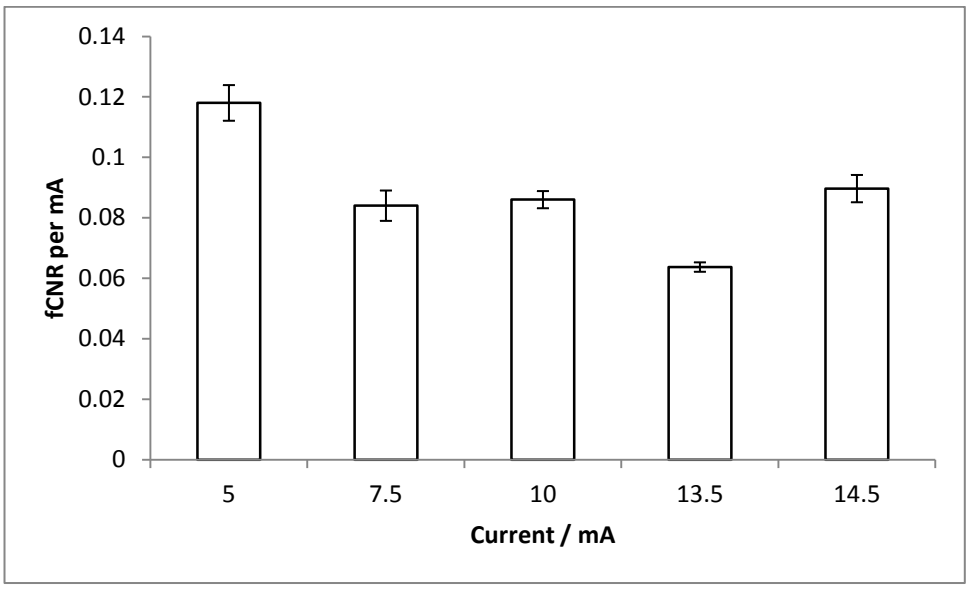

Fig. 6.8 *–fCNR per mA applied current for Experiment KC.1*

The Contrast Response for this particular ROI was in line with those at other sites. SNR is again more variable than at Edinburgh and although fCNR shows an increase with current it is not a smooth rise as seen in Edinburgh. fCNR per mA does plateau as expected at higher current values although individual values are subject to unexplained fluctuations.

Scans at KCL also showed the TEP speckle problem also seen in Experiment ED.7 at Edinburgh. At KCL however the problem was more severe. The speckle problem was more

prominent during the TEP set up screens and was present on both coils used at this site. These TEP problems are perhaps reflected in the greatly reduced levels of both SNR and fCNR seen in the KCL data compared to the matching experiments at Edinburgh in a similar pattern to results in Experiment ED.7.

There were also problems with noise stability during these scans. Examination of noise traces showed intermittent surges and dips in noise for protracted periods before returning to original levels (Fig. 6.11 illustrates a mild noise example). These surges could adversely affect the quality of image parameter data. Data sets exhibiting these changes should strictly be eliminated from any subsequent analysis given a large enough number of EPI volumes affected by these surges. However the performance of the scanner and coils at KCL gave little choice but to proceed and make the best of the data that was obtained.

At KCL the phantom was physically placed into the scanner rotated by 180° compared to all other sites. This appeared to reverse the sign of the signal change in the signal traces (Fig.6.9). Curiously this effect was unable to be replicated at Edinburgh and certainly is not predicted by theory. In fact the theory has no particular regard for the direction of the magnetic field gradient on the final signal attenuation so reversing the gradient should have no effect on the sign of the signal change.

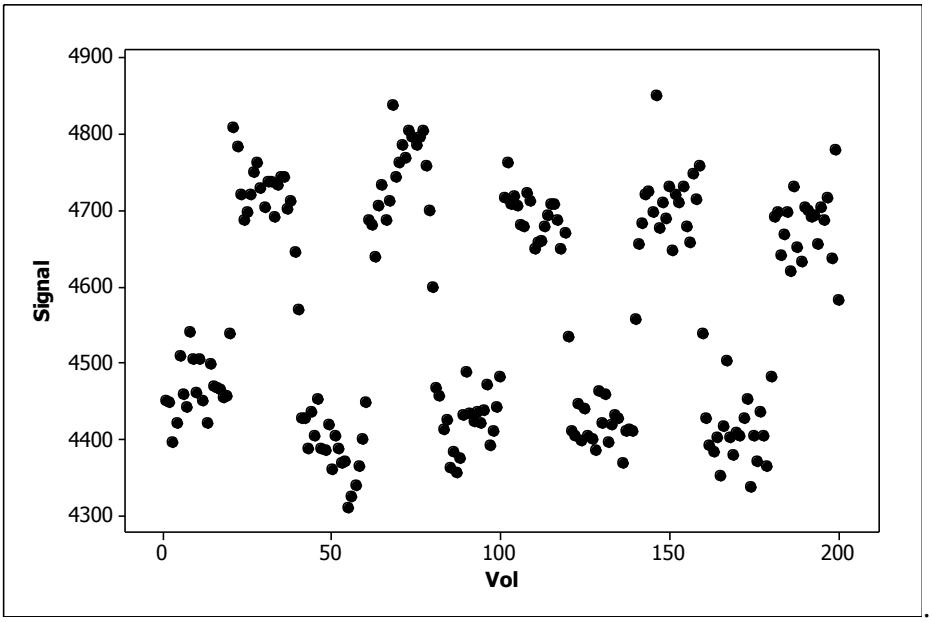

Fig. 6.9 *– Reversal in sign of ΔS seen in all scans at KCL (I = 13.5mA in example shown).*

Another new anomaly was with the data from I = 7.50mA. This data set showed a continuously increasing signal contrast over the duration of the entire scan (Fig. 6.10 below). Although the signals in the ON state (the higher signals for the KCL data) appear relatively stable, the signal in the OFF state drops quickly with volume which acts to increase the signal contrast as the scan progresses. Noise measurements for the same experiment do not show this pattern (Fig. 6.11). It is also possible there is another step anomaly in the first few volume blocks, but the increasing signal contrast of the rest of the scan makes this difficult to reliable ascertain.

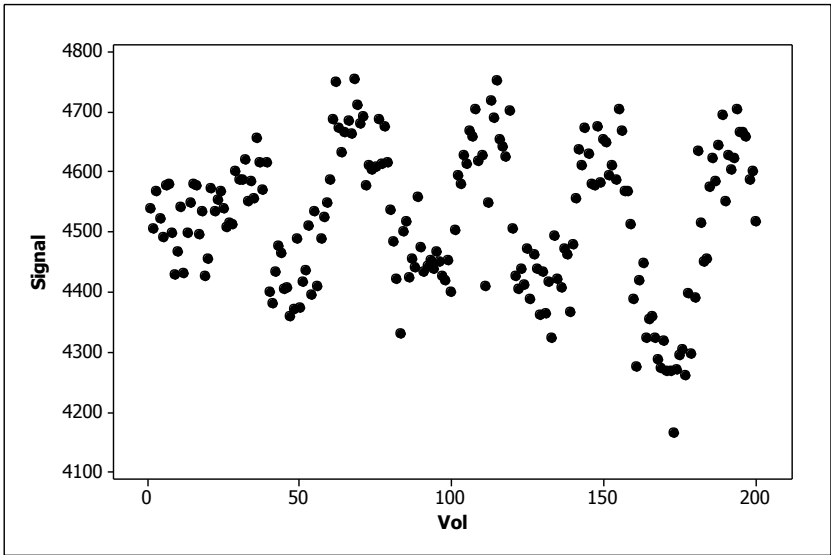

Fig. 6.10 *– Example of increasing signal contrast anomaly - KC.1 I = 7.50mA.*

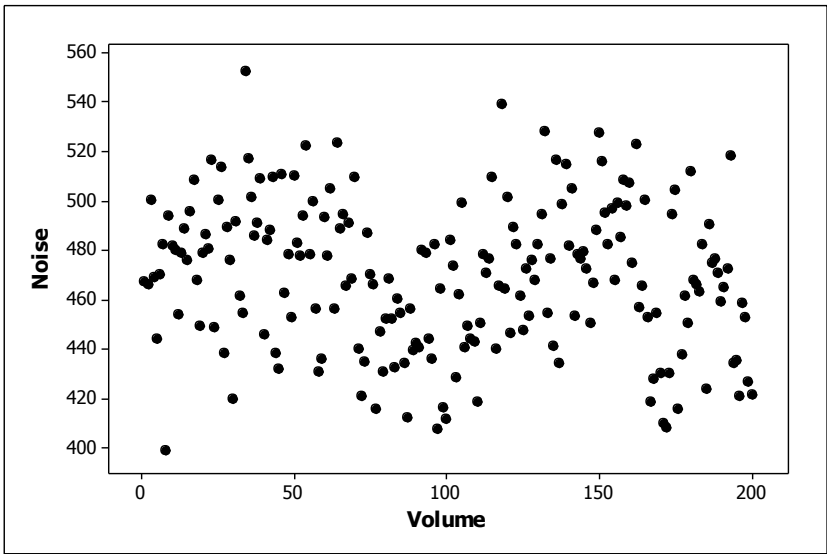

Fig. 6.11 *– Noise values for same scan (KC.1 I = 7.50mA) showing no direct corresponding pattern but a possible dip in noise levels midway through the scan.*

6.3.4 University College London - UC.1

Scans from UCL were of very variable quality. Although the first scan produced data of reasonably good quality, approximately half way through the second scan there was a loss of signal stability. For this reason results are only quantitatively reported from these scans up until this dramatic change in signal quality. Overall however this scans represent a very poor pool of data. Even the first scan shows unusual behaviour with what might be described as a protracted step anomaly lasting the duration of the scan. The UCL results do however provide useful discussion points in the wider context of both the multisite and longitudinal studies.

In the following figure (Fog. 6.12) plots of the UCL data are shown of signal against volume in acquisition order. These show the onset of signal stability degradation which rendered the majority of the data from UCL unusable.

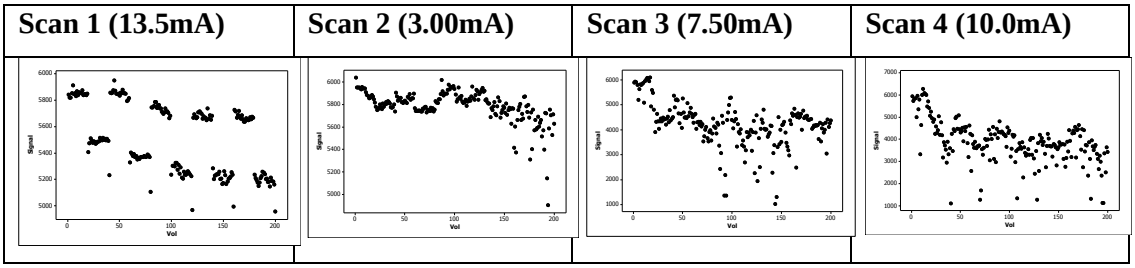

Fig. 6.12 *– Scatterplot illustrations of UC.1 signal values in order of acquisition, illustrating the increasing signal instabilities observed.*

It is difficult to say anything definite about the general behaviour of the UCL scanner in terms of image parameter outputs, due to the variable performance it provided across the total scan session. Expected signal changes were seen at the start of the session, but these were quickly swamped out by scanner instabilities by the end of the session a few hours later. The variations seen over the experiment duration might be typical or exceptional. Correspondence with and conversations with *in vivo* fMRI users of the scanner at UCL suggest that the behaviour is typical of the system at the time these phantom scans were taken.

Noise was also atypical at UCL as there appeared to be a strong interaction between the phantom and the scanner noise (Fig. 6.13). The level of interaction also appeared to change as noise levels fluctuated, often within a single scan. This suggests that possible scanner gradient fields might also be interactive with background electronic noise sampling as well which would distort any biological signal sampling *in vivo*. It is also possible that the phantom itself is for some reason interacting with the scanner set up at this site unlike the

others. While on occasion there has been some evidence of interaction between scanner and phantom as seen in a limited number of examples from both Edinburgh and KCL, it has never been as obvious or consistent as was observed in the UCL data.

Scan 1 (13.5mA)	Scan 2 (3.00mA)	Scan 3 (7.50mA)	Scan 4 (10.0mA)
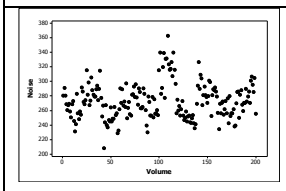	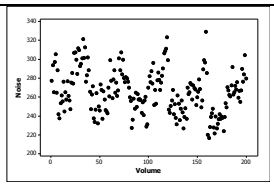	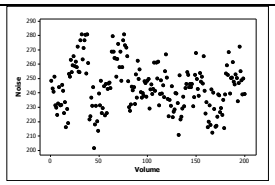	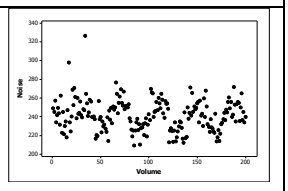

Fig. 6.13 *– Scatterplots of UC.1 noise values, illustrating the increasing signal instabilities observed.*

Because of the selective choosing of useful data points subsequently used to measure image parameter values, all parameter values reported from the UCL phantom data should be treated as tentative. Although they are only estimated for the 'good' data available it is possible that whatever was causing these problems may also have already been affecting the images even in these selected volumes of usable data. Indeed, in the plot for Scan 1 in Fig. 6.13 (above) it is clear that there is already a large drift in signal affecting both phantom current states across the duration of the scan. This is not typical behaviour for other sites.

It should also be noted that although spurious data has been seen in some of the Edinburgh Longitudinal data (Experiments ED.5 and ED.7 for example), the abruptness and consistent nature of the change in data quality in the UCL data has not been seen elsewhere.

Contrast Response

Response / % mA^{-1}	Standard Error of Fit / % mA^{-1}	PCC	PCC p-value
0.62	0.01	1.00	0.020

Table 6.5 *- Contrast Response Results for Experiment UC.1*

The two usable current data sets (I = 13.5mA and the first 4-5 blocks of I = 3.00mA) were analysed in the usual manner. Although two data points is not a sufficient number to obtain any truly meaningful measure of Contrast Response the assumption of an intercept at of 0% signal change at 0.00mA of current provides an additional third point of data allowing for a reasonable Contrast Response to be generated. The final Contrast Response generated is not too far off those off other sites either which is not too surprising if we assume the linear experimental response thus far observed.

SNR

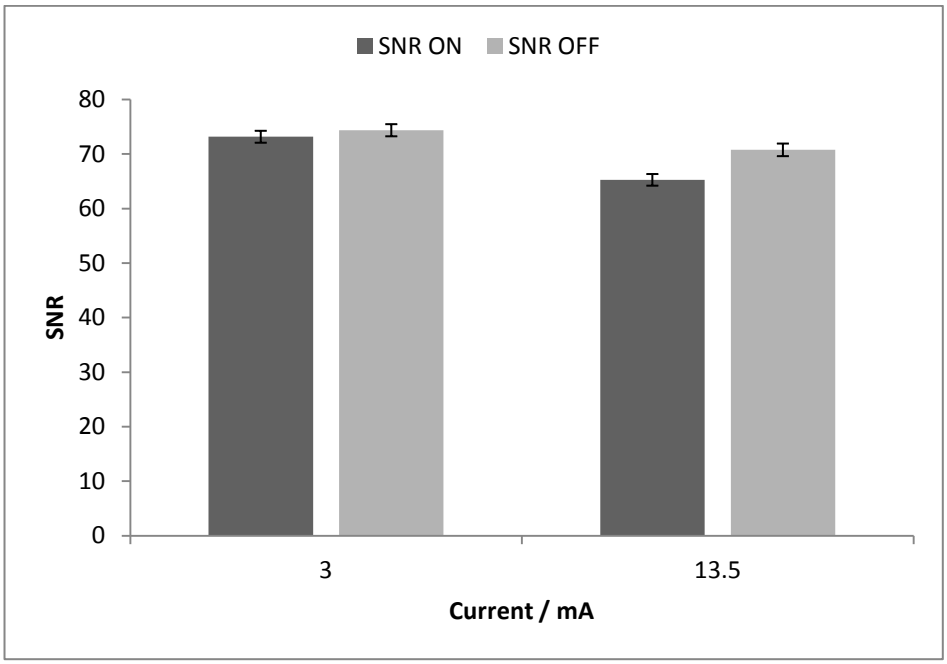

Fig. 6.14 *– Mean SNR Values for both ON and OFF current States for Experiment UC.1.*

fCNR

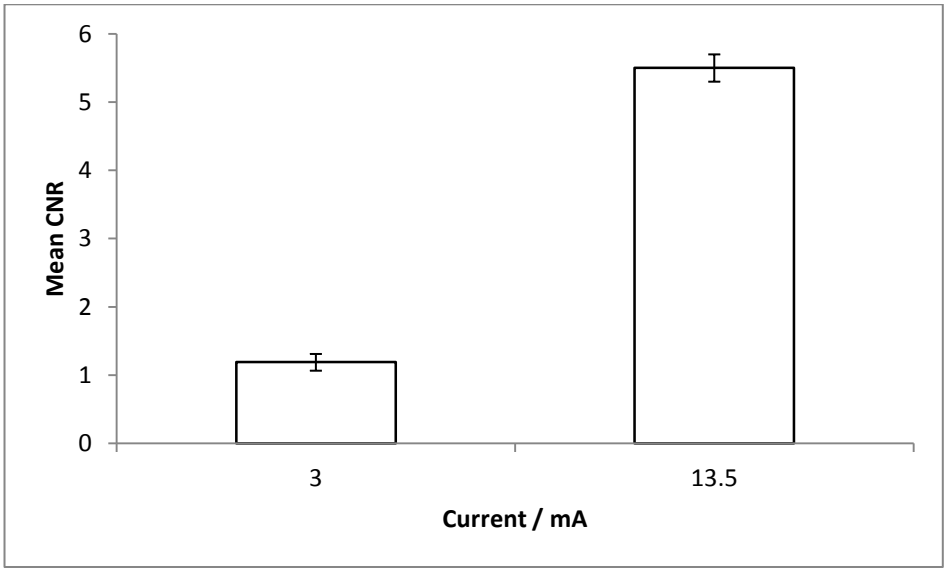

Fig. 6.15 *– Mean fCNR values for Experiment UC.1.*

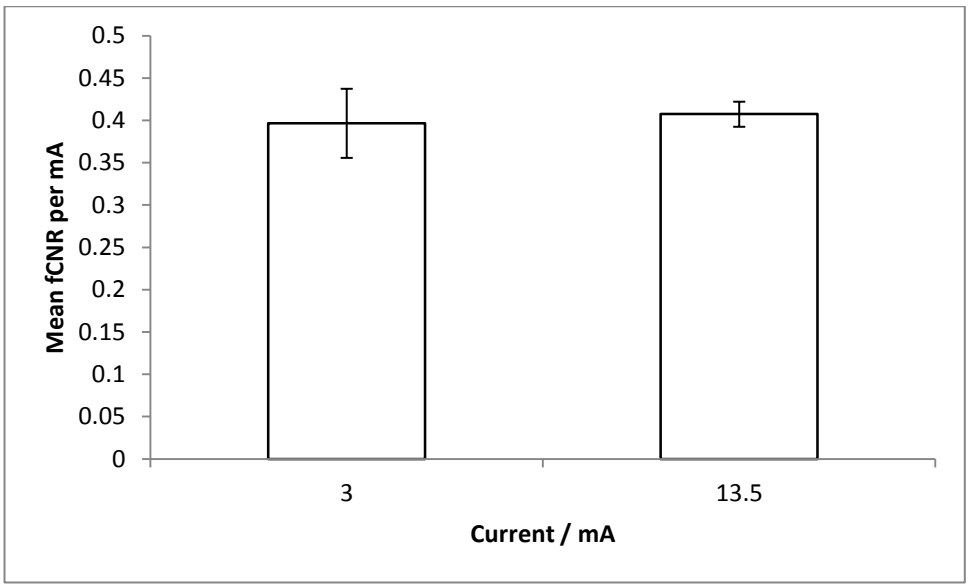

Fig. 6.16 *– Mean fCNR per mA applied current for Experiment UC.1.*

The usable data suggests patterns of response and behaviour in-line with what might be expected – SNR and fCNR increasing and fCNR per mA of applied current giving similar values for the current values used of good data. This suggests that the UCL scanner is capable of producing expected behaviour when operating normally.

Furthermore, although the signal value is variable across the duration of all scans, the actual original starting signal value for each scan was close to the same in all scans, stable or not. This and the sudden onset of signal dispersion shown in Scan 2 suggest that some sort of transitory environmental or mechanical effect is responsible for the degradation of these data sets. This could be as simple as a loose connection in the receiving coil or a gradient connection being jarred loose due to sequence-induced mechanical vibrations or a change in the surrounding environment might be responsible. The UCL scanner is located underground in a region of central London, UK, very close to both extensive over and underground rail networks as well as heavily used roadways. Inadequate building isolation from these influences may result in transitory vibrations being passed along to the scanner infrastructure and to the scanner itself or cumulative effects from protracted exposure to these vibration sources.

The TEP speckle anomaly was also observed during the set up for this Experiment, although its appearance was not as severe as that seen at KCL. Given the other instabilities seen in the images it is unclear to what extent these might have effected imaging parameter results from UCL.

Recently (September 2013) it was verbally reported that a problem with gradient connectors on the rear connector plate of the magnet had been identified since these scans were taken (November 2012) and repairs were then performed. This has apparently improved stability although not as much as users would like. It would be interesting and worthwhile to repeat the scans at UCL under these new operating conditions at some point in the future.

6.3.5 Multisite Comparison Discussion

Mean Images

As part of the manual ROI analysis procedure a mean signal image of the functional phantom data is outputted and can serve as a useful, qualitative guide to the quality of the experimental set up.

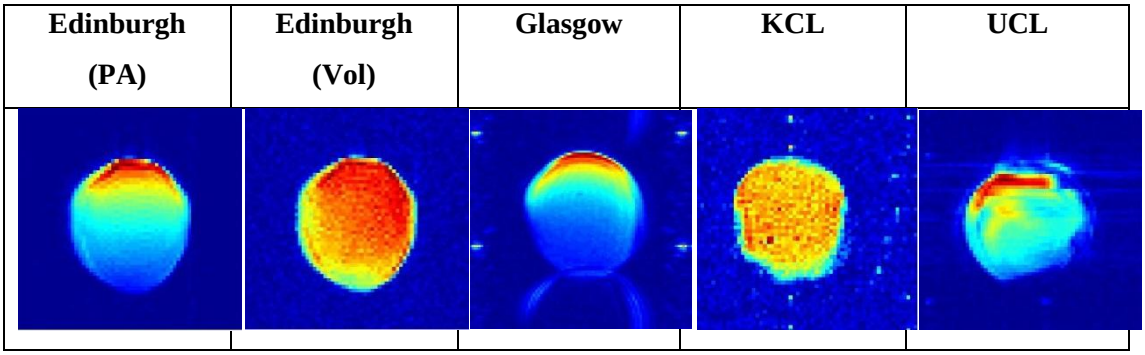

Fig. 6.17 *– Illustrative mean magnitude images from each of the sites visited in the Multisite study. Phase Encode direction is vertical. For PA coils the PA coil is located at the top of the phantom.*

All scanners were optimised as they would be for *in vivo* scans, but displayed a wide variety of final quality. Shim 50% linewidth values also varied across sites with linewidth at Edinburgh being more or less equivalent regardless of coil used and being approximately half of the value of UCL and KCL (See Table. 6.6).

Site	Shim 50% linewidth / Hz
Edinburgh (PA)	28.9
Edinburgh (Vol)	32.0
Glasgow	--
KCL	60.0
UCL	53.0

Table 6.6 *– Final set up shim values for multisite studies. There was no value obtained from Glasgow since it was not a straight forward matter to obtain similar quantitative measurements of water line width on this system. The values for Edinburgh are considerably improved compared to those of other sites.*

The colour gradient in the vertical direction of the images which is visible in the sites using phased array coils is due to the phased array coils giving greater signal sensitivity closer to where the coil elements are physically located. Distortions in shape from the actual circular cross section of the phantom to the elliptical shape seen are seen in the images can be seen and this is a fairly typical EPI artefact (see discussion of EPI artefacts in Chapter 2.2).

The Edinburgh images are more elliptically oblate than images from other sites, but suffer less from other artefacts such as Nyquist ghosting.

The Glasgow mean image shows a strong level of Nyquist ghosting. This is not completely unexpected as the Bruker EPI sequence lacks a per-volume navigator phase correction used in the Agilent scans, relying instead on a single measurement at the start of an entire scan for phase correction. Additionally along the left and right hand sides of the images are four small bright pixel clusters. These vertically oscillated along the edges of the image during the acquisition period. This would have adversely effected noise measurements since they would appear intermittently in the image region encompassing the noise ROI depending on volume acquired.

UCL's mean image shows a very 'choppy' and distorted appearance compared to those of Edinburgh (PA) and Glasgow. There is no smooth signal gradient but rather a non-uniform intensity is presented. Unusually there are also ghosting like artefacts in both the phase and frequency encode dimensions for the UCL images suggestive of major problems since the frequency encode direction is much less sensitive to EPI artefacts than the phase encode direction.

The KCL image shows phase encode distortion, but perhaps more worryingly the presence of several 'bright' pixels away from the phantom itself in regions of what should be pure noise. These additional pixels could be interpreted as activations in an automated analysis and/or distort mean measurements of background noise levels which could well impact on the significance outcomes of activation analysis.

Contrast Response

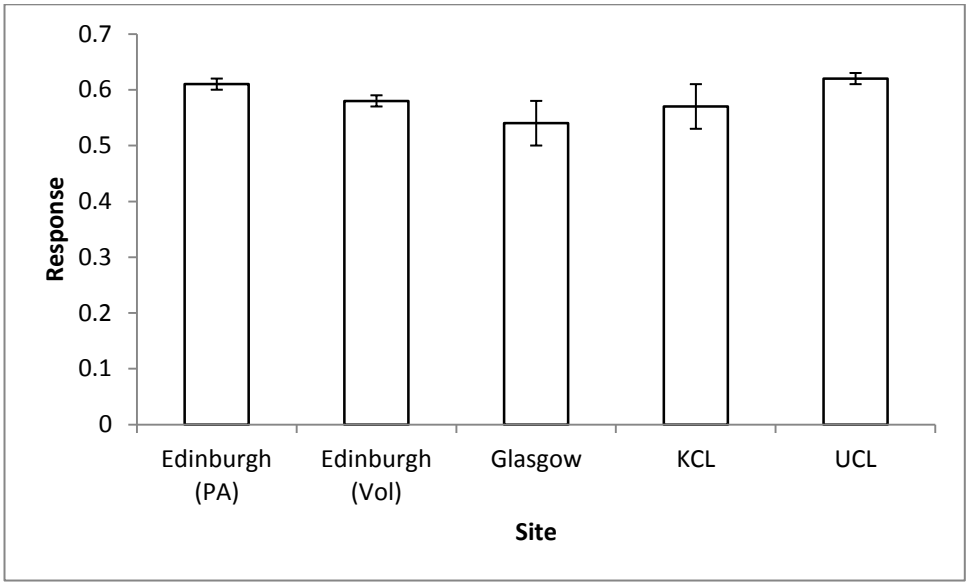

Fig. 6.18 *–Summary of Contrast Response for Multisite Snapshot Study*

The Contrast Response of each scanner and associated coil configuration at the four different sites is broadly comparative across all sites, although there is some variation in the certainty of data fitting. These variations can be explained given the differences in set up procedure and data quality obtained due to site-specific peculiarities. The fitting errors at Glasgow and KCL are noticeably higher than the other sites. Glasgow's scanner had less control over shimming and availability of navigator control. KCL meanwhile had extensive problems with ROI signal returns unseen elsewhere.

The value for the PCC test at each site is also near perfectly linear which is, as seen in the Longitudinal Study, strongly suggestive of a linear performance for the phantom with respect to increased current.

SNR - OFF

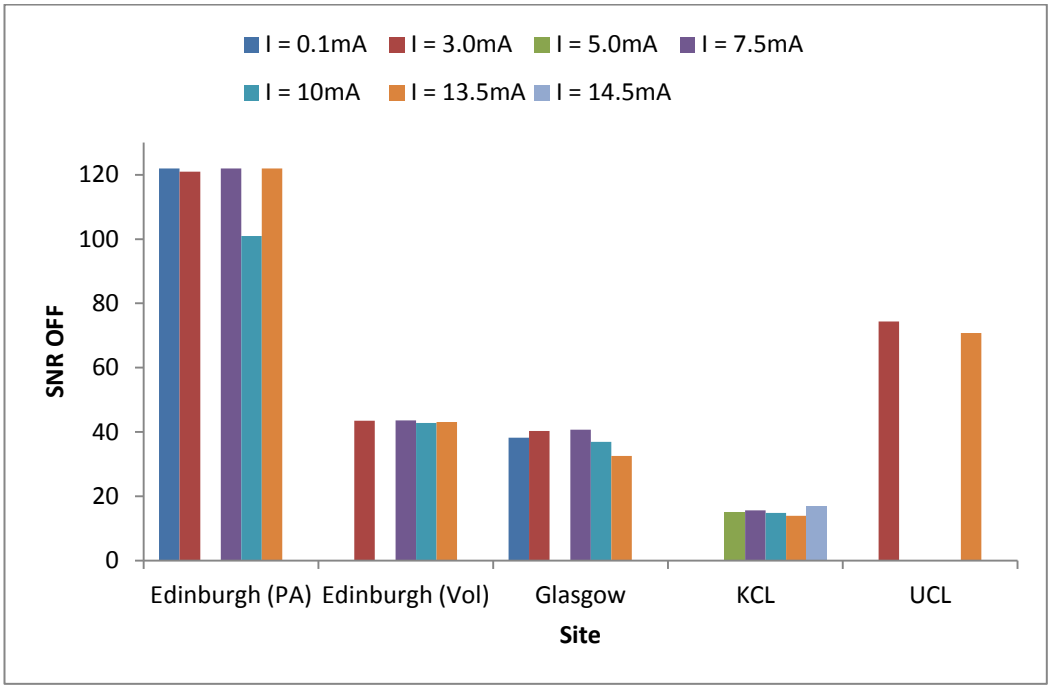

Fig. 6.19 *–SNR values in the OFF state for the Multisite Study arranged by site.*

With the phantom in the OFF state the SNR should be comparative across all current values when similar coils are being used. This should certainly be the case for data gathered at Edinburgh (ED.6) and KCL which had identical coil configurations; however the experimental data shows that it is not. SNR drops off at Glasgow with increasing current while the UCL data is too scant to draw any firm conclusions from. The Glasgow changes could be due to gradient over-heating at this site creating additional noise in a system that is already less optimised than the others and so might have a disproportionately larger effect. There is insufficient data for UCL to speculate on cause. In the case of Edinburgh I = 10mA there is a noticeable drop in SNR, but this has been discussed earlier in Chapter 5.

Additionally, absolute values of SNR should be influenced only by coil configuration used and B_0 field strength. Therefore the expected ordering of SNR level across the sites should be:

1. UCL - 4-channel phase array coil and higher B_0 field strength.
2. Glasgow - 4 channel phase array coil
3. Edinburgh (PA) - 2-channel phase array coil
4. Edinburgh (Vol) and KCL - Volume Coils

However based on experimental phantom results the ordering is somewhat different and is instead:

1. Edinburgh (PA)
2. UCL
3. Edinburgh (Vol)
4. Glasgow
5. KCL

These results strongly suggest that even the presumed baseline operating expectations for fMRI studies; considered from simple first principles, do not match those of experimental evidence. This should have strong consequences for selecting equipment and designing experiments based on prior expectations of coil sensitivity and biological effect sought.

Although there were differences in shim quality between sites (for example UCL and KCL had measured shim values of approximately twice that found in Edinburgh) it would be surprising if *in vivo* this difference alone could be enough to account for such dramatic differences in SNR and fCNR sensitivity ordering. This difference is less than the variability experienced at times with manual shimming techniques. Such a profound effect on image parameter measurements caused by such variation in shim quality must surely have raised questions regarding data quality gathered in *in* vivo scans at a single site before these dedicated multisite tests were performed.

SNR – ON

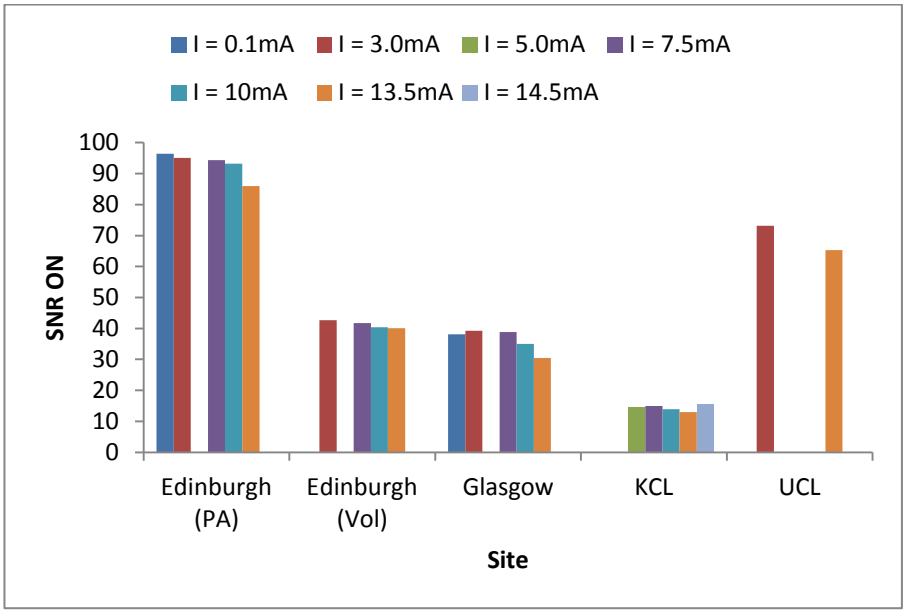

Fig. 6.20 *–SNR for the ON State for the Multisite Study..*

In this state there should be an overall decline in SNR as current increases. This is seen in all sites except at KCL. The same disordering of expected SNR values seen and discussed in the SNR OFF data is reflected here in the SNR ON data.

fCNR

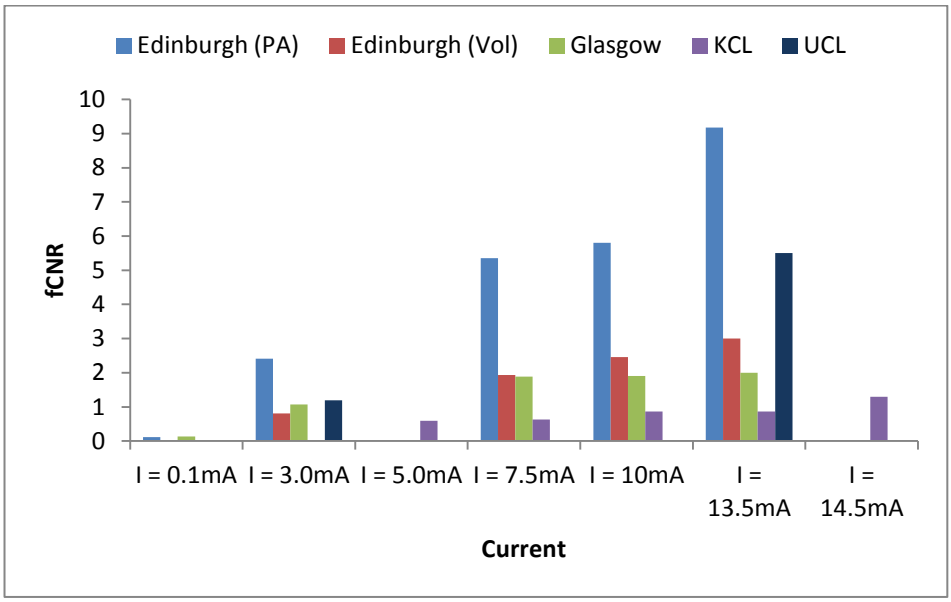

Fig. 6.21 *– fCNR values for different currents from the Multisite Snapshot Study.*

As fCNR is at the heart of producing both quantitative fMRI results and putting bounds on their significance it would be expected that for true comparative performance scanners should be producing identical values of fCNR under identical experimental conditions – as provided by the fMRI phantom. The |ΔS| signal change and overall Contrast Response suggest that the relative signal changes between states are equivalent. However, the fCNR experimentally measured with the phantom however suggest that none of the sites surveyed in this study had equivalent values of fCNR with identical coil configurations nor did they follow expected patterns of behaviour with differing coil configurations.

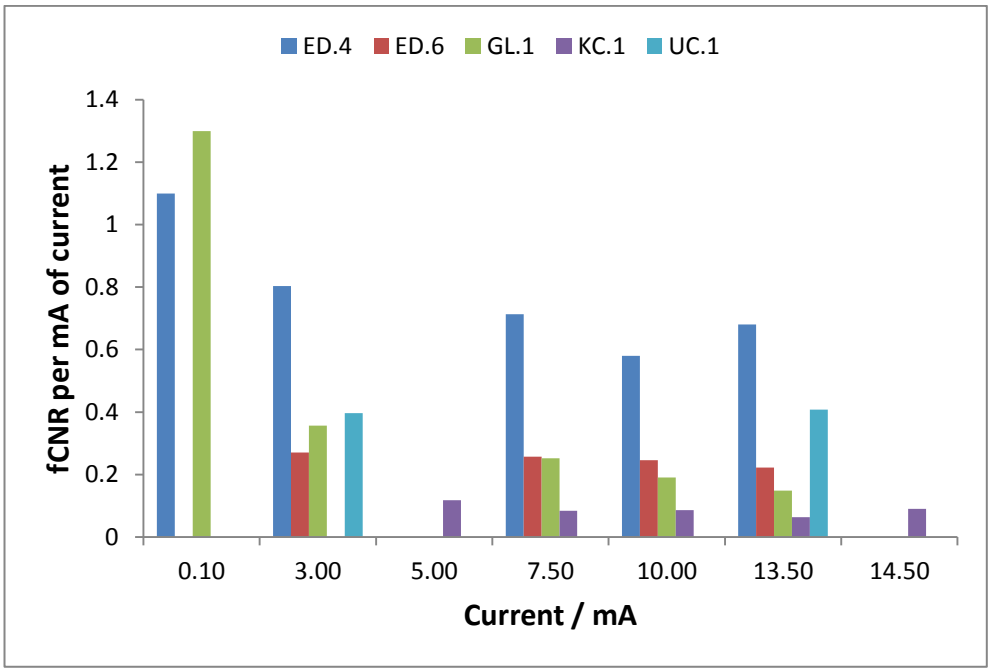

Fig. 6.22 *– fCNR per unit applied current different currents from the Multisite Snapshot Study.*

When fCNR this is looked at as fCNR per unit of applied current (Fig. 6.22) it is even clearer. Although identical values should be returned at 1) each site and 2) between sites with identical coil set ups this is not the case and the mis-ordering of sites noted before is maintained.

These differing image parameter values produced differing signal detection limits as well. While some sites were capable of detecting all the attempted signal changes others did not (as summarised in Table 6.7). Obviously in *in vivo* experiments this would produce results that would have widely differing conclusions as some sites would be detecting some changes that others would not and falsely attributing the lack of or actual detection of these changes

to any interventions or tasks behaviours associated with variations in the animal rather than simply due to scanner performance.

Current / mA	0.10	3.00	5.00	7.50	10.0	13.5	14.5
Edinburgh (PA)	Yes	Yes		Yes	Yes	Yes	
Edinburgh (Volume)	No	Yes		Yes	Yes	Yes	
Glasgow	Yes	Yes		Yes	Yes	Yes	
KCL	No	No	Yes	Yes	Yes	Yes	Yes
UCL	No	Yes				Yes	

Table 6.7 *– Experimentally determined detection limits for the Multisite Study. Green boxes indicate statistically significant signal changes detected. Red values indicate no significant change detected.*

6.5 Multisite General Conclusions

Although data was successfully obtained from all sites, the analysis of that data reveals several worrying trends and concerns.

- Contrast Response and quality of fitting of that data is of a consistent and high quality across all sites tested. This is evidence that absolute contrast measurements between sites are truly comparable.

- SNR and fCNR varied dramatically across sites. Different sites also had different minimum signal detection limits. In an *in vivo* experiment this would result in different significance levels being attached to identical experimental conditions. These effects would also render some signal changes undetectable depending on the site where the experiment was performed. This has clear implications for the biological interpretation and validity of GE-EPI based fMRI data.

  Such differences in fCNR and detection limits would make it very difficult to compare *in vivo* fMRI data between sites as such data is usually reported as in terms of statistical significance and cluster the size of statistically significantly ‘activated’ pixel clusters, rather than as absolute in signal percentage changes as has been investigated with the phantom in this project.

- Individual scanner behaviour is also variable in the short-term across the duration of both a day and at times an individual scan within a day. As with the Edinburgh

Longitudinal Study (Chapter 5) it was not possible to get a single day's worth of optimal scans during this study from any individual site.

- General image geometric quality was highly variable across sites. This is most likely the result of different levels of magnetic inhomogeneity correction and shimming at different sites.

- The sites with the problems of most concern were also those currently performing the most GE-EPI imaging – specifically KCL and UCL. In the Longitudinal Study at Edinburgh increasing problems were beginning to be detected in EPI quality and associated imaging parameters as EPI usage at that site started to accumulate as more phantom scans were performed and GE-EPI was deployed on other projects using that scanner.

- There were no BOLD-like over- or undershoots observed at any site. This is starkly in opposition to Renvall's proposal that these are an intrinsic part of fMRI phantom performance rather than due to the biological processes of brain function and associated blood usage as is the prevailing scientific opinion [Renvall 2009b].

6.6 Chapter Summary

This study, taken across a range of preclinical MRI sites, reports a wide range of scanner behaviours and anomalies that have clear implications for *in vivo* data validity and scanner quality assurance. While some imaging parameters are pleasingly universal across sites the measurements of others are out of pattern with what might be expected from experimental availability and scanner rating.

The greatest sites of concern are, frustratingly, also those most widely utilising GE-EPI fMRI. This, alongside the evidence from Chapter 5 that suggests a degradation of fMRI quality over time with usage, is indicative of a self-compromising nature to the technique in terms of scan quality. This reinforces the need for regular monitoring and maintenance of the equipment to be used for such studies to keep final data integrity at acceptable levels.

While this study provides only a snapshot of behaviour for a small sampling of sites, the range of problems encountered at all sites provides good grounds for the need for further and expanded fMRI monitoring at all preclinical MRI sites utilising the technique.

Chapter 7 Conclusions and Future Work

7.1 Small Animal EPI

Compared to some other MRI sequences such as FSEMS or FLASH, GE-EPI is a more difficult sequence to work with, requiring patience and experience in order to produce good quality GE-EPI images which can then be used in meaningful fMRI studies. This is especially so when performing such scans with preclinical scanners and subjects. Even so, due to the sensitive nature of the sequence images, are not guaranteed to be free of artefacts for every subject scanned. Measures used to reduce such image artefacts such as multishot imaging increase the total acquisition time of the scan and lower the temporal resolution of the scan. These problems can themselves be mitigated by using a compressed multishot sequence, but this had a large impact on image SNR. In the world of GE-EPI nothing is perfect, only manageable.

One of the most persistent artefacts needing elimination from *in vivo* EPI images on the Edinburgh scanner was the streak artefact. Although careful positioning of the animal within the field of view of the scan often visually eliminated these artefacts, there might still be a residual presence present enough to distort fMRI activation results. These effects have been observed both on other scanners involved in this project and also elsewhere (personal correspondence). Thus far groups contacted regarding this artefact simply ignore it and proceed as if it were not present. This is neither personally satisfying nor scientifically robust.

Concern at the apparent variability of results, combined with the lack of uniformity and rigour in analysis techniques across different imaging sites and the temperamental multi-step set up optimisation methodology outlined in Chapter 2 led us to ask the basic question of do preclinical *in* vivo fMRI studies produce reliable results? And hence justify associated scientific conclusions and use of animal subjects?

The first step in answering these questions was to investigate whether the images generated and captured by a scanner were themselves as robust as has been assumed up until now. This rapidly became the central question of this project, as reliable and comparative image acquisition is fundamental to all other subsequent questions regarding fMRI studies.

7.2 fMRI Phantom

The different studies in this project, developing and using fMRI phantoms, have revealed a number of previously undetected effects that give significant cause for concern surrounding

the implementation of GE-EPI based fMRI using animal subjects. These effects are likely to be currently impacting on the conclusions of *in vivo* preclinical fMRI studies.

The studies here have also identified interesting data that may help explain a range of other apparently contradictory results proposed by different investigators in regards to BOLD-based HRF interpretation and the potential for direct neuronal imaging.

7.2.1 fMRI Phantom Design

For widespread deployment as a standardised QA device the manufacturing process of the phantom would have to be improved. Although any firm evidence for the influence of manufacturing variations on image results is stil an open question, in the CAT phantom used in this study the alignment of the wire coils on the main body of the resonator was slightly skewed. This resulted in a final phantom coil geometry that was non-ideal. The final angle was slight and approximately equal for both coils which could result in a 'shifted' region of maximum signal uniformity. The ROI sampling region however, is still well within the central region of the coils where gradient effects are reasonably uniform within the low current regime used. Because of this the effect from this misalignment can be assumed to be minimal. In any future phantoms that are constructed any coil specific assembly deviations should be minimised to give added assurance given the presence of block-block transient spiking in slices that are off-centre.

7.2.2 fMRI Phantom Procedure

One factor that was only able to be controlled in a limited fashion was the positioning of the phantom in the scanner. Although an identical methodology was followed each time and at each site it is difficult to guarantee that the phantom is positioned in exactly the same position each time. Although in many ways this represents the similar situation *in vivo* it is another variable that could in theory be controlled during phantom scans. To allow for this the resonator design should be altered and/or the production of a suitable holding system specific for the fMRI phantom must be constructed such that the phantom can be positioned with good repeatability in the scanner every time.

However, given the overall similarity of the signal response across sites and experiments it is unlikely that minor changes in coil positioning were a significant factor in the much larger changes observed in results such as fCNR and SNR so is perhaps not a factor of too much concern.

7.2.3 fMRI Phantom Data Analysis

The relationship between ROI size and SNR (and therefore also of fCNR) will have an impact on the results of QA since SNR ∝ pixel volume [Edelstein 1986]. By enlarging the ROI to include more individual pixels the mean ROI signal becomes less influenced by the noise fluctuations of individual pixels. This places minimum constraints on the number of pixels composing the ROI in order for it to give a statistically robust signal sample from the image. This in turns constrains the minimum physical size of the phantom resonator given that MRI scanners are limited in the minimum pixel size that they can practically produce.

Along with construction issues and ROI positioning concerns, the requirement for a large population of pixels excludes the WIT based design since it produces a magnetic field that rapidly decays away after only 2-3 pixels distance [Renvall 2006]. This allows a maximum sampling region of approximately nine pixels versus the ROI used in the CAT tests that contains a hundred pixels.

7.2.4 BOLD Signal Interblock Transients

In similar results to Renvall's previous work, when phantoms in this project were operating from a battery supplied current source, spikes and/or dips in signal strength were observed at the beginning and end of 'stimulation' periods. Renvall has uniquely proposed that these phantom-originated observed spikes are identical or significant contributors to the signal under- and overshoots observed in *in vivo* BOLD fMRI studies [Renvall V. 2009b].

If this is correct then it would place the current understanding of the biological dynamics of the BOLD HRF function and its underlying physiological basis into serious question. This would have significant implications for our understanding of brain function and mechanism. Indeed Renvall's suggestion has already led to some in the biological community picking up on these concerns and beginning to consider them as sources of unexpected deviations or anomalies in fMRI derived HRF data [Loggia 2012].

However, when the CAT fMRI phantom was powered by the alternative CCCS system, these spikes were not observed at any sites. Spikes could be detected in the signal pattern only when the analysis ROI was deliberately placed off centre in the z-direction, into a region of weighted gradient imbalance. On occasion when using a particularly poor system that was already showing other anomalies (such as the later scans at UCL) transients were sometimes detected in the central imaging region. This implies that in such phantoms their origin is connected both to gradient inhomogeneities and current source instability rather than being a necessary feature of *in vivo* fMRI scanning as suggested by Renvall.

Also of note in Renvall's experiments are both the lower number of pixels within his ROIs and also the use of much larger slice thicknesses and pixel sizes. Together this not only reduce his statistical power and make his results more subject to spurious noise events, but would also increase the difficulty of placing his ROI in a precise fashion at the proper geometric centre of the two coils used in his phantom. This off-centred position could cause his ROI to experience additional field inhomogeneity effects and thus is a possible likely explanation for the appearance of the transient spiking observed in those experiments.

These effects, rooted in the nature of the phantom design and scanner set up, are likely to be at the root of his transient observations - as has also been observed in data from this project when it has been deliberately misanalysed in a comparative fashion.

It is also unclear what, if any, physical connection between phantom transients and HRF over- and undershoots actually is. Beyond a very crude pictorial similarity between the two Renvall offers no other explanation connecting the two. At the present time given the lack of a plausible shared mechanism at work between phantom induced signals and BOLD biological responses it is inappropriate and potentially hasty to be considering modifying current understanding of the HRF function in terms of biological dynamics in order to incorporate phantom field induced effects.

In addition it should be noted that it is also easy to generate spurious transient spikes in phantom data by convolving the signal data with a HRF response function rather than the simpler box car function used in the analysis of the data in this project. From Renvall's publications [Renvall 2006, 2009a, 2009b] and PhD thesis [Renvall 2010] it is unclear exactly how he analysed his data, what response function he used or even how he selected for his ROI location.

7.3 Implications of fMRI Phantom Results

7.3.1 Contrast Detection Limits

Over the duration of the longitudinal study degradation in the contrast detection limit of the scanner at Edinburgh was observed. Although stable across the first few months by the end of the study the limit had increased from ~0.07% (June 2012) to >0.75% by the final set of scans (ED.9, May 2013). Over this period the signal response stayed within an acceptable range suggesting that the change in detection limit is linked to noise rather signal generation problems. The intermittent reliability in scanner behaviour across the study makes it difficult

to precisely track the rate of this change with the data sets currently obtained; however a definite rise in detection threshold was observed.

This change in detection limit is possibly linked to cumulative use of the EPI. Sites that were heavy users of the sequence were found to not only have lower detection limits, but poorer fCNR values and increases in the occurrences and severity of other image artefact problem. Further agreement of this is suggested via the low level of signal change able to be detected at Glasgow where EPI is not regularly used. The initial low levels observed at Edinburgh also agree with this since the EPI sequence was rarely used at that site before this project began.

More data would be required to conclusively prove and quantify a firm relationship between scanner usage and detection limit degradation. These initial observations are suggestive of such a relationship, but the precise nature of that relationship is still unclear. In the meantime the real changes in the detection limit at Edinburgh and the differences seen across multiple preclinical MRI scanners suggest that caution should be taken when comparing results of fMRI studies between centres.

As observed using the phantom, shifting detection limits over time are likely to mask some occurrences of low level activation data. This would also occur during *in vivo* studies as well. The result of this would be undetected neural activity at one time point compared to another. This under-detection would be due to changes in the scanner rather than by any differences in animal model or task-based effects. Without prior knowledge of scanner behaviour it would be impossible to distinguish between these three sources when making final conclusions.

It is also unclear whether the approximate detection limits measured in this project represent sharp cut off points or if there is a region of uncertainty around the limit that could further skew results detected near the limits. The necessity for repeat scanning at low current levels and the notably elevated $fCNRmA^{-1}$ values at low current values in the longitudinal study plus greater variation of ΔS at low current values across sites suggest the effective nature of this uncertain region may indeed not simply be an absolute cut off point. If so this would necessitate a cautious approach to any results near a scanner's detection limit, perhaps to the point of deliberately excluding particularly low signal change values.

As the Signal Response fit is near identical across all studies, changes in signal are unlikely to be solely at the root cause of the detection limit changes. This suggests that the variation comes primarily from increases in the noise of the system, possibly due to physical

mechanical degradation of coils and associated electronics due to the heavy operational demands placed on them by the EPI sequence. Possible sources of detection degradation via system noise increase might include:

- **Vibrational Induced Degradation in Coil Performance.**
  EPI generates a lot of mechanical vibration combined via a rapidly oscillating magnetic field. In theory this vibration could, over time, loosen contacts between coil components. Researchers at KCL reported improved *in* vivo results when either padding out their coil to give a tighter fit in the bore of the scanner and/or rotating the Phase Encode direction by 90° which would also rotate the vibration direction, reducing the mechanical strain on coil components already preferentially strained in one direction.
- **Degradation in Gradient Performance.**
  For similar reasons to coils, gradient hardware may also lose performance capability over time. If this was the cause it might not be apparent in currently conducted annual QA checks conducted by suppliers as such checks may not push gradient systems as hard as necessary to replicate EPI-based *in vivo* scenarios.
- **Environmental Changes.**
  Variable temperatures and humidity levels in MRI facilities may impact on equipment performance by altering levels of thermally induced noise in the electronic systems of scanners. Although suppliers rate their equipment over a range of environmental conditions such conditions are not always met and can be difficult to maintain at steady levels. These effects may occur on a temporary basis, potential skewing a single set of scans or alternatively may also damage equipment in the long term. Environmental effects may also be locally induced by the heavy use of MRI equipment itself. Such effects might potentially explain the reduced SNR values seen in first scans of the day seen in a number of sessions in this project.

The particular nature of coil and gradient degradation rates might be site unique, depending on the construction materials and quality of techniques applied at the time of component manufacture and assembly. Without direct, systematic involvement of appropriate suppliers to test equipment at the point of manufacturing, partnered with continued monitoring by researchers on-site it is unlikely that these effects can be properly quantified to identify an origin cause.

It is also unknown whether the running of other types of sequences contributes to any potential system degradation between functional scans, although EPI usage is likely to be a stronger factor in any degradation due to its high operational demands.

The best outcome from these concerns may, unfortunately, be merely raised awareness of these potential issues. Long term monitoring of systems may allow for the establishment of quality guidelines as to when to repair or replace degraded equipment, possibly established around the expected signal changes provided by *in vivo* data.

7.3.2 Variation in SNR and fCNR

The magnitude of the observed differences in SNR and fCNR in both the longitudinal and multisite studies is especially concerning, especially when combined with the observed instability of even individual scan sessions. This combined with the wide diversity of signal and noise behaviours observed across the four scanner sites calls into serious question not just the subsequent interpretation of preclinical GE-EPI based fMRI results, but also whether the basic experimental images acquired can be truly reliable and so useful.

That both the longitudinal and multisite studies show striking SNR and fCNR variations across both short and long term timescales is particularly concerning. Alongside possible loss of low-signal change events from detection limit changes, differences in SNR and fCNR would substantially alter the perception of relative signal changes under identical experimental conditions from one study to the next, or from one scan to the next and between scanner sites. This would undermine the basic principle of experimental replication with regard to all GE-EPI fMRI studies involving animal scanners.

The ability to generate reliable and believable image data, in a repeatable manner, which then guides interpretation and conclusions, is fundamental to scientific research. If preclinical fMRI is not at a standard where this is possible then its continued widespread use as an experimental tool is seriously called into question.

7.4 Implications for the use of Animals in fMRI experimentation and Scientific Studies

The observed variability and unexpected poor imaging quality observed calls into question the practical usefulness of preclinical *in vivo* results. While undoubtedly real signal changes originating in neural-based physiological activity changes are being detected, questions are raised over the usefulness of such signal changes in what appears to be a diverse range of scanner performance.

Particular concerned is noted for studies that for whatever reasons are performed intermittently over long periods of time where scanner performance may significantly change during that time. The significance of any signal change would be altered between the start and end point of a study and variations in detection limits would ultimately mask many previously measurable weaker signal changes. Comparing relative non-absolute signal measurements between papers and scanner sites is also questionable given the range of scanner performance.

Given the existing legal and ethical framework demanding scientific experiments using animals produce useful scientific data it is questionable whether it is morally or legally permissible to continue to use animals in such experiments. The results of this project suggest that improvements in the performance and reliability of preclinical scanners must be implemented before GE-EPI based fMRI studies are further conducted in live animal subjects. For those preclinical fMRI studies currently proceeding the likelihood of scanner performance producing an effect on results must be considered in any conclusions drawn from generated results.

7.5 Recommendations

While the first recommendation might be for the halting of GE-EPI fMRI *in vivo* experiments, this is unlikely to happen without intervention from relevant oversight bodies. For fMRI studies that do proceed, the results of this project should be borne in mind. Given the variability in scanner performance seen it is important to adjust experimental procedures to take this into account and to try to mitigate the potential effects of that variability on any *in vivo* studies.

Specifically:

- **Pre- and Post-*in vivo* QA Scans.**
  Before animals are scanned the performance of the scanner should be checked with the fMRI phantom. This should also be done after *in vivo* scanning is complete. Results should then be compared to previously obtained measurements on the same scanner to provide a longer term context from which to judge the scanner's performance across the duration of a study. This also has the advantage of pre-running the system to prepare it for *in vivo* scanning. This is important given numerous examples in this project that have shown decreased SNR on the first scan of the day on many occasions.

Obviously this would add both time and cost to a study, but when the alternative is not validating your study data and so rendering it unjustifiable and/or out of any comparative context it should only be a minimal extra obligation. A universally recognised system of rating these phantom scans to approve or disapprove scans would also need to be clarified.

- **fMRI Phantom Result Reporting**

  It would be helpful if preclinical fMRI studies were to report scanner properties concurrently in published reports alongside *in vivo* results. Until scanners can be optimised to give reliable standardised results this would go some way towards providing greater critical oversight to fMRI result reporting. Reported phantom measures for a particular scanner should include values for image quality and stability (such as the Signal Response and $fCNRmA^{-1}$) over the duration of a study, as well as longer term performance of the scanner. Perhaps most importantly a measurement of the detection limit of the scanner should be included to enable an outside researcher to assess what BOLD effects a scanner may or may not be ultimately sensitive to.

- **Compressed Timetable for *in vivo* scanning**

  fMRI studies should be conducted across as short a time period as possible to attempt to reduce the potential any medium or long term changes in scanner behaviour may have on results.

- **Randomisation of Groups**

  While this should already be happening as part of a study design it is worth reemphasising here. Proper randomisation of study groups will mitigate the potential for systematic bias in results due to changes in scanning performance over time. If, as we suspect, noise on the Edinburgh scanner was increasing over time, raising the detection limit, then this calls for caution when designing experimental groups of animals in studies. Groups should be mixed so that a difference in signal response between two groups are attributable solely to biological effects and not to increased degradation over time of scanner performance with one group scanned at a later time point disproportionately affected.

- **Increase Group Sizes**

  Although at first this might seem contradictory to the aim of Reduction within the 3Rs animal welfare strategy, it is important to pre-empt any possible drop in group numbers from data judged via phantom pre/postscans to be unusable. Additionally if at the review stage of a publication an editor asks for group sizes to be increased it may not be possible to provide like-for-like scans at that later time as it would be difficult to justify adding in additional data that might be skewed by scanner performance differences at that point. An exception to this would of course be if scans with the phantom were shown to be giving identical results (by all measures) to when the original scans were performed. Group sizes should be increased to a point that strikes a balance between conservative numbers for welfare purposes while adequate maintaining statistical power if a reasonable number of subjects must be excluded from the study in question.

7.6 Future Work

There are a number of areas that future work could focus on that would not only investigate the basic MRI phenomena discovered throughout this project, but also establish fMRI phantoms as a valuable QA procedure in fMRI practice and publication.

- **Streak Artefact Correction**

  Although measures taken with *in vivo* subjects in this study were able to reduce these particular streak artefacts they were a persistent problem, reappearing and disappearing between subjects. Their cause would seem to be rooted in pseudo-gradient effects caused by intra- voxel effects in voxels containing an abrupt air/tissue interface (such as around the ear canals). This pseudo-gradient effect appears to disrupt signal phase encoding resulting in an altered signal along the phase encode line of the problem element.

  There have been recent successful suggestions in the literature on how to compensate for these phase encode disruptions [Chung 2012] on clinical systems. Implementation of a similar methodology on preclinical systems should eliminate these effects.

- **Implementation of Standard fMRI QA Reporting**

  A lack of good quality QA information in general seems to be a problem at preclinical MRI centres, whereas most clinical centres have successfully

incorporated QA into their daily routines. While there are practical considerations that may hinder the wider uptake of QA testing at preclinical centres there are many benefits in doing so. This study has highlighted that fMRI QA in particular should be readily adopted across those sites engaged in fMRI studies and preferably at all preclinical sites. Standard QA measures can also be extracted from the fMRI phantom data as well.

- **fMRI Reporting**

  Any major fMRI conference or journal will reveal a wide range of mismatched methods when reporting fMRI experimental parameters and results. Arguably there needs to be a more widespread standardised format for reporting the set-up and results of fMRI experiments in a similar manner to the ARRIVE guidelines for animal research in general [Kilkenny 2010]. Suggested formats for this have been made, but they have yet to be widely adopted or discussed [Poldrack 2008].

- **Continual Site Monitoring**

  Longer term usage of the fMRI phantom and protocol by sites already involved in these project would enable a catalogue of data to be accumulated that would not only serve as a QA record for an individual site, but also provide clues to help identify sources of scanner variation.

  Retesting after repairs and upgrades to individual sites may also yield useful information. For example UCL have reported repairs to their gradient cabling since fMRI phantom scans were performed there and user concerns at that site regarding signal stability at this site have since dropped. KCL has also recently seen an end to heavy construction work adjacent to their facility which might result in reductions of intermittent environmental vibrational sources of noise.

- **Expanded Multisite Survey**

  Although four sites were included in the existing multisite survey group there are many other preclinical sites located in the UK and globally that could form part of a more comprehensive test group. Currently it could be the case that we have an unfair sampling of sites and the majority have the high quality results of Edinburgh and Glasgow, with KCL and UCL being particularly anomalous (perhaps due to heavy use of EPI).

With Agilent's recently announced withdrawal from the preclinical MRI market it is important to sample more Bruker manufactured scanners. Ideally access to freshly commissioned systems at the install or even factory point would provide a basic reference point for subsequent monitoring.

- **Identify Variation Sources**

  Although changes and variations in imaging parameters have been observed across sites their exact sources still need to be identified. Given the complexity of scanner systems and the currently lack of relevant data this will be difficult to do, but ultimately worthwhile.

  A program of investigation should include:

  - **Coil Quality Survey**

    A collection of identical coils from a single manufacturer should be tested at a single site to compare performance in equipment that is intended to be identical. This should provide some understanding as to how much of the variation observed is system specific and how much is coil specific.

  - **Coil Supplier Survey**

    All coils at sites tested in this project where supplied by Rapid Biomedical. However there are other manufacturers of MRI coils and a range of coils that might typically be used for fMRI studies should be tested at a single site. Ideally again these coils should also be tested at other sites as well.

  - **Cryocoil Coil Test**

    For systems that are suitably equipped, the fMRI phantom and protocol should be tested in partnership with a cryogenically cooled (and stabilised) coil. This would provide a useful test bed with minimum thermal noise in the receiver further allowing discrimination of variation sources.

  - **Environmental Influence Experimentation**

    Identical scans should be run at a site with environmental conditions deliberately varied to try to induce or reduce imaging parameter variations in the system. Ideally this should occur at a number of sites to see if effects are universal or specific to a single site.

- **Intervention**

  Once likely source candidates have been identified experimental adjustment of these mechanisms should be undertaken and tested with the phantom. In this manner their effects on scan outputs can be minimised in a more controllable manner.

It is probable that multiple sources of variation are interacting in unique ways on different systems which could make it very difficult to fully implement a comprehensive program of corrective measures on every system. However there may be some sources common to each system that could correct for at least some of the variation observed if they could be identified and negated.

- **Investigate Nature of Detection Limit**

  While the existence of varying detection limits has been established by this project, the exact nature and influences on those limits remains to be established. Controlled testing of phantom parameters on a finer scale near to those limits should be performed as well as monitoring for changings in those limits.

- **Phantom Theory**

  Further work should refine the MATAB modelling scripts of the phantom (Chapter 4) in order to bring a closer agreement between experiment and theory. This would not only give greater understanding with regard to cause of any variations in experimental results, but provide a development platform for a range of test devices based on the initial CAT principle.

- **Streamline Data Analysis**

  There is currently a bottleneck in the testing procedure as currently the data must go through several manually adjusted steps and multiple scripts and procedures. This process is time consuming and subject to some user error at times. Ideally much of this could be integrated into a single automated script which would provide a more efficient throughput and minimise the time needed for processing of phantom data. Such a process would also aid the attractiveness of the project when engaging new sites in studies.

- **Other fMRI sequences**

  The stability of other commonly used pulse sequences in fMRI such as spin-echo EPI or accelerated non-EPI spin echo techniques remains to be evaluated. With the CAT phantom design used in this project signal changes are not present in spin-echo based sequences. To successively evaluate these sequences would require the design of another fMRI phantom suited to spin echo imaging.

- **Effect on Resting State fMRI Connectivity Analysis**

  Given the increasing popularity of resting state fMRI studies that are utilising GE-EPI as their imaging sequence it is worth considering developing some way to systematically test how the effects of sequence variability might also be affecting resting state results. A possible way to do this would be to construct a 'network' of multiple phantoms that could be activated in a controlled and variable fashion to simulate a crude functional network.

- **fMRI Phantom as Imaging Design Tool**

  Using contrasts derived from tissue samples or theory, the phantom could be used to optimise or design imaging settings for required BOLD-like contrasts before *in vivo* subjects are placed within the scanner.

- **In vivo QA monitoring**

  The original intent of designing an fMRI phantom was to insert it within the field of view of an animal being scanned. This would have provided an ideal control signal to provide an independent measure during a scan to eliminate any system or stimulus bias in the processing of the resultant data.

  With the CAT design this was not practical due to the close-quarters brain coils used across the different sites. If researchers were willing or able to sacrifice some data quality and use larger MRI coils so that the CAT design could be safely accommodated it could still prove viable.

- **Development of neuronal fMRI Techniques**

  As discussed in Chapter 1, to date, trials designed to image neuronal action potential firing directly with MRI have produced mixed results across a wide range of experimental methodologies. These suggested action potential derived signal

changes are at the very edge of theoretical detection in both clinical and preclinical scanning environments [Hatada 2005].

The potential to access a much more direct measurement of neuronal activity than the BOLD effect is a strong incentive to investigate this area further. The increasing use of cryogenically cooled (and stabilised) MRI detection coils also increases the potential for success in this area.

The fMRI phantom is ideally placed to assist in the validation and any sequence development to achieve this goal given that it can be adjusted to produce magnetic field changes of the same strength are expected from neuronal action potentials.

The results provided by this study also suggest that any current failures to detect neuronal activation that have been published in the literature might be due to variation in scanner performance – particularly the variation of detection limit - rather than because of any particular failure in a biological set up. The evidence of abnormal behaviour near detection thresholds would also suggest that we should be unsurprised at getting mixed results from low fCNR regions such as those we would expect from direct neuronal imaging experiments.

- **Clinical fMRI Phantom**

  This study has only involved studying the properties of GE-EPI in relation to fMRI applications on preclinical scanners. Although preclinical fMRI is a rapidly emerging technique, fMRI began and is currently used far more widely in human studies on clinical MRI scanners.

  Clinical MRI systems have had more financial resources and development time invested into their designs, but it should be remembered that they too work at the limits of current designs and researchers will continue to push them to those limits. Given that the variations seen across the preclinical scanners in this study are likely to come from a combination of interacting problems and sources, it is not unreasonable to consider that such sources of performance variation might also be present at clinical sites.

  As such it should be considered a priority that similar studies to those performed here should also be conducted on clinical scanners to check for and to quantify any such variations. With access to scanners and willing participation by MRI centres this could be done relatively swiftly. To accomplish this all that would need to be

changed from the current phantom design would be the dimensions of the signal resonator and associated pixel and ROI sizes.

The dimensions for this clinical-scale resonator could be upscaled from the preclinical design to ensure equivalent statistical sampling in terms of number of pixels sampled. Field calculations to induce matching signal changes can then be approximately computed from the existing MATLAB scripts (Chapter 4) with an adjusted geometry of the resonator and number of turns of wire per coil altered appropriately for clinical systems.

7.7 Final Conclusions

The phantom device designed and deployed for this project has shown that the current widely used MRI pulse sequence for preclinical fMRI studies, GE-EPI, does not provide universally reliable results. Because of this it is recommended that such scans are either put on hold until MRI scanners are fully calibrated and tested so that they give stable and meaningful results across duration of use. Scanners should also be adjusted to provide consistent data between sites. Reliability of short-term scanner behaviour must also be improved to properly maximise the return of scientific data from live animal subjects.

Where scans continue relevant phantom QA data should be provided to help place any *in vivo* results into a universal bench-marked context. To achieve these goals significant further investigation should be undertaken on preclinical MRI scanners. Clinical scanners should also be evaluated in a similar manner to investigate their performance as well.

This study illustrates the value of rigorous experimental evidence, testing and continually challenging accepted scientific norms in new ways. By subjecting the most basic criteria of fMRI studies – that of shared acquisition properties providing universal image stability and comparability - to a novel experimental analysis this project has shown that, perhaps, much has been assumed but not yet adequately assessed in the field thus far.

"See now the power of truth; the same experiment which at first glance seemed to show one thing, when more carefully examined, assures us of the contrary."

- Galileo Galilei, 1638.

Discourses and Mathematical Demonstrations Relating to Two New Sciences

Appendix 1.1 Method for Measurement of SNR and fCNR in Images

1. MR images acquired on scanner (FDF format)

2. Resultant image stack is converted offline to Analyse image format.

3. Two ROIs are prescribed onto a slice in the image stack via a MATLAB script (provided by Prof. Ian Marshall) – one in a signal region and the other in a noise region.

a) b) c)

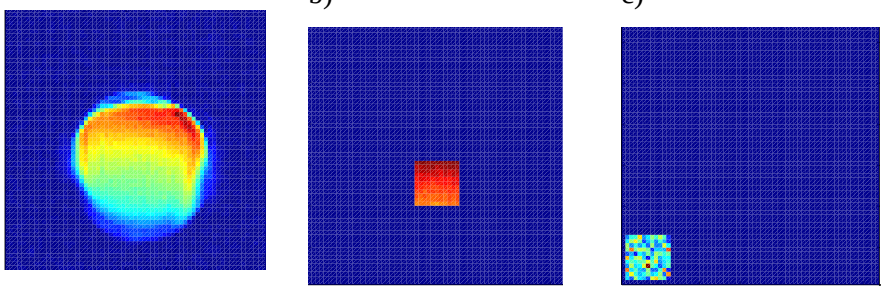

Example Image

Signal ROI selection within the main body of the phantom

Noise ROI positioned outside the body of the phantom and to the side away from any phase encode ghosting.

4. Measurements of ROI mean and standard deviation are made for the slice in each volume of the image stack.

5. Signal measurements are sorted into appropriate groups depending on the phantom current state.
6. Descriptive statistics are generated for $Signal_{ON}$, $Signal_{OFF}$ and Noise ROIs.

7. Students t-test is used to check for statistically significant differences between $Signal_{ON}$ and $Signal_{OFF.}$ ($P \leq 0.05$).

8. SNR for each signal state is simply $SNR_{ON} = \frac{Mean\ Signal_{ON}}{Mean\ Noise}$ or $SNR_{ON} = \frac{Mean\ Signal_{ON}}{Mean\ Noise}$ depending on the current state of the phantom [Magnotta 2006].

9. fCNR for is calculated as$fCNR = \frac{Signal_{\ OFF} - Signal_{ON}}{Mean\ Noise}$ [Geissler 2007].

Appendix 2.1 Data Tables for WIT fMRI Phantom Design

Current / mA	**2.29**	**2.74**	**4.81**	**19.15**	**33.0**	**49.7**	**107**
|ΔS| / %	2.83	3.06	6.05	11.7	14.2	5.26	48.0
S1NR – ON	61.9	72.9	62.1	59.7	53.9	59.4	36.4
S2NR – OFF	63.7	75.2	66.1	67.6	62.8	62.7	70.0
fCNR	1.81	2.29	3.93	7.89	8.88	2575	33.9

Table A3.1 – Summary of Results from Initial Trial of fMRI Phantom WIT Design

Appendix 2.2 Data Tables for CAT fMRI Phantom Design

Current / mA	**0.13**	**0.90**	**1.61**	**5.01**	**13.3**
Signal Change / %	0.12	0.86	1.43	4.18	10.9
S1NR – ON	42.2	42.6	41.6	43.1	35.8
S2NR – OFF	42.2	42.9	42.2	44.9	40.0
fCNR	0.05	0.36	0.60	1.80	3.88

Table A3.2 – Summary Results for fMRI Phantom Design 2 – Multicoil CAT Design.

Appendix 2.3 Data Tables for Battery Helmholtz Coil Phantom Multisite Study

Signal Change

Current / mA	0.90	1.61	5.01	13.3
Edinburgh / %	0.25	0.55	1.81	5.54
Glasgow / %	0.58	0.72	1.76	10.3
KCL / %	-	-	1.80	2.43
Agilent / %	0.27	0.53	1.27	2.35

Table A3.3.1 – Multisite results for $|\Delta S|$ from Design 3 at four different preclinical MRI sites

Contrast Response

Site	Contrast Response	Standard Error	PCC
Edinburgh	0.41	0.01	1.00
Glasgow	0.72	0.08	0.98
Kings College London	0.21	0.05	0.93
Agilent (Oxford)	0.19	0.02	0.99

Table A3.3.2 – Multisite Contrast Response from the fMRI Phantom.

S1NR - OFF

Current / mA	0.90	1.61	5.01	13.3
Edinburgh	168	172	166	168
Glasgow	28.9	30.4	31.7	31.9
KCL	-	-	95.1	93.9
Agilent	155	152	158	155

Table A3.3.3 – Multisite SNR values with the phantom in the OFF state.

S2NR - ON

Current / mA	0.90	1.61	5.01	13.3
Edinburgh	168	171	163	159
Glasgow	28.7	30.2	31.2	28.9
KCL	-	-	93.2	91.7
Agilent	155	151	156	152

Table A3.3.4 – Multisite SNR values with the phantom in the ON state.

Functional Contrast-to-Noise Ratio

Current / mA	0.90	1.61	5.01	13.3
Edinburgh	0.42	0.93	2.94	8.81
Glasgow	0.17	0.22	0.55	2.98
KCL	-	-	1.69	2.24
Agilent	0.43	0.80	1.98	3.56

Table A3.3.5 – Multisite fCNR values from the fMRI phantom.

Appendix 2.4 Data Tables for CAT + CCCS fMRI Phantom Design

Signal Change (|ΔS|)

Current / mA	0.10	3.00	7.50	10.0	13.5
EPIP 1	0.06	1.86	4.52	5.79	**7.57**
EPIP 2	0.08	1.81	4.54	**5.69**	7.73
EPIP 3(a)	**0.08**	1.77	4.42	5.92	7.46
EPIP 3(b)	0.06	1.81	4.54	**5.84**	7.83
EPIP 3(c)	0.06	1.79	**4.43**	5.84	7.77

Table A3.4.1 – Experimental Results for |ΔS| from Final Coil Test study.

Contrast Response

Experiment	Response	Standard Error of Fit	PEC
EPIP 1	0.57	0.01	1.00
EPIP 2	0.57	0.01	1.00
EPIP 3(a)	0.57	<0.01	1.00
EPIP 3(b)	0.59	<0.01	1.00
EPIP 3(c)	0.58	0.01	1.00

Table A3.4.2 – Summary of Signal Response for Final Coil Testing. The high PCC values indicate a near perfect linear fit to the data.

S1NR - ON

Current / mA	0.10	3.00	7.50	10.0	13.5
EPIP 1	96.4	95.1	94.4	93.2	**86.0**
EPIP 2	96.0	92.2	89.2	**84.1**	88.2
EPIP 3(a)	**77.7**	92.2	89.5	85.6	90.4
EPIP 3(b)	91.5	**90.0**	89.2	80.1	81.7
EPIP 3(c)	92.9	94.9	**80.9**	90.6	88.0

Table A3.4.3 – Experimental Results for SNR with the phantom activated during the Final Coil Test study.

S2NR – OFF

Current / mA	0.10	3.00	7.50	10.0	13.5
EPIP 1	96.4	97.0	98.6	98.6	**92.5**
EPIP 2	96.0	93.9	93.2	**88.9**	95.0
EPIP 3(a)	**77.8**	93.9	93.5	90.9	97.1
EPIP 3(b)	91.5	**91.6**	93.2	85.4	88.1
EPIP 3(c)	92.9	96.6	**84.5**	95.9	94.8

Table A3.4.3 – Experimental Results for SNR with the phantom deactivated during the Final Coil Test study.

Contrast-to-Noise (fCNR)

Current / mA	**0.10**	**3.00**	**7.50**	**10.0**	**13.5**
EPIP 1	0.06	1.77	4.27	5.40	**6.51**
EPIP 2	0.08	1.67	4.05	**4.78**	6.82
EPIP 3(a)	**0.07**	1.63	3.95	5.08	6.74
EPIP 3(b)	0.05	**1.63**	4.06	4.70	6.40
EPIP 3(c)	0.05	1.70	**3.59**	5.29	6.84

Table A3.4.4 – Experimental Results for fCNR from Final Coil Test study.

Appendix 3.1 MATLAB script for Coil Magnetic Field Simulations

```
%01/12/13 - Calculates B for a Single Loop Helmholtz Coil%

%reset%

clear all;

%parameter set up%

I=112.5e-3;
R=7.5e-3;
L=7.5e-3;
perm=(4*(pi*10.^-7));

coilconstant1=((perm*I*R)/(4*pi)); %coil constants for coil 1
coilconstant2=((perm*-I*R)/(4*pi)); %coil constants for coil 2

stepsinplane=input('Number of steps in plane? '); %Specify number of
steps to calculate in plane (i.e. the image matrix) axis%
stepsz=input('Number of steps along z axis? '); %Specify number of
steps to calculate along z-axis axis%

%hard set FOV parameters

FOVinplane=25.6e-3;
FOVzaxis=14*1e-3;

inplaneresolution=FOVinplane/stepsinplane;
zresolution=FOVzaxis/stepsz;

%setting up current elements for numerical integration

currentelements=input('Number of current elements? '); %How many
divisions to segment the field loop into%
dphi=((2*pi)/currentelements); %Individual angle for each current
element in radians

%interate along z-axis%

for j=1:stepsz;
    z=(j-(stepsz/2))*zresolution;

%interate along y-axis%

for k=1:stepsinplane;
    y=(k-(stepsinplane/2))*inplaneresolution;

%interate along x-axis%

for l=1:stepsinplane;
    x=(l-(stepsinplane/2))*inplaneresolution;
```

```
%combine x and y%

inplaneposition=sqrt((y.^2)+(x.^2));

%loop for calculating Bz Field of Current Loops

for i=1:currentelements;
    phi=i*dphi;
        dBz1(i)=coilconstant1*((((R-
(inplaneposition*(sin(phi))))*dphi)/(((R.^2)+(inplaneposition.^2)+((
z-(L/2)).^2)-(2*inplaneposition*R*((sin(phi)))))^(3/2))));
        dBz2(i)=coilconstant2*((((R-
(inplaneposition*(sin(phi))))*dphi)/(((R.^2)+(inplaneposition.^2)+((
z+(L/2)).^2)-(2*inplaneposition*R*((sin(phi)))))^(3/2))));

end

%Calclulating total Bz at Point P

Bz=(sum(dBz1))+(sum(dBz2));

Btotal(j,k,l)=Bz;

end
end
end

%display a slice of Bz

Bdisplay=squeeze(Btotal(stepsz/2,:,:));
pcolor(Bdisplay);

colormap jet
shading flat
ylabel('X-Axis')
xlabel('Y-axis')
title('Calculated Magnetic Field Strength / T')
colorbar
```

Appendix 3.2 MATLAB script for Magnetic Field to Phase Calculation

```
clear all;

%Specify time between echos in seconds

deltaTE=input('TE? ');

gamma=267.513e6;

%Load magnetic field simulation matrix

load
'C:\Users\gmerrifi\Documents\PhD\Phantom_Theory\scripts\results\high
_res\112_5_mA\Bz_matrix.mat';

%Calculating phase change (phiz)%

phasez=gamma*Btotal*deltaTE;

%display a slice of the change in phase

phasezdisplay=squeeze(phasez(70,:,:));
pcolor(phasezdisplay);

colormap jet
shading flat
ylabel('X-Axis')
xlabel('Y-axis')
title('Calculated Change in Phase')
colorbar
```

Appendix 3.3 MATLAB script for Phase Summation Calculation.

```
%Script for summing phase changes from high res to scanner
resolution

clear all;

%Load phase matrix

load
'C:\Users\gmerrifi\Documents\PhD\Phantom_Theory\scripts\results\high
_res\112_5_mA\Phasez_matrix.mat';

zdimension=140;
xdimension=640;
ydimension=640;

%Specify high resolution voxel to low resolution voxel ration

xfactor=10;
yfactor=10;
zfactor=10;

%Number of high resolution voxels in scanner resolution voxel

N=xfactor*yfactor*zfactor;

%TOTAL PHASE CALCULATION

%Calculate voxel exponential value

voxelphase=exp(1i*phasez);


%Set up loops

%interate along x

for j=1:(zdimension/zfactor);        %Number of new elements
    zposition=(j-1)*zfactor+1;       %starting position of new
element

%interate along y%

for k=1:(xdimension/xfactor);
    xposition=(k-1)*xfactor+1;

%interate along z%

for l=1:(ydimension/yfactor);
    yposition=(l-1)*yfactor+1;
```

```
%Sum high res N voxels to one low res voxel

totalphase(j,k,l)=abs(sum(sum(sum(voxelphase(zposition:(zposition+zf
actor-1),xposition:(xposition+xfactor-
1),yposition:(yposition+yfactor-1))))));

end
end
end

%Divide by N for final phase map

finalphase=totalphase/N;

%Display final phase map

finalphasedisplay=squeeze(finalphase(((zdimension/zfactor)/2),:,:));
pcolor(finalphasedisplay);

colormap jet
shading flat
ylabel('X-Axis')
xlabel('Y-axis')
title('Calculated Change in Phase')
colorbar

%Save final phase map

save('C:\Users\gmerrifi\Documents\PhD\Phantom_Theory\scripts\results
\finalphase', 'finalphase')
```

Appendix 3.4 MATLAB Script for Addition of Noise to Signal

```
%Script for adding guassian noise to sinc function

close all;
clear all;

%% Generate  current values
startcurrent=0;
maxcurrent=13.5e-3;

attenuationScaleFactor=250;
current=startcurrent:1e-3:maxcurrent;

%% Noise Distribution details
stdev_noise=0.000783666
no_of_loops=100;                %Number of times to run simulation

%% Calculate attenuation without noise
signal_off = ones(size(current));
signal_on = 1 - attenuationScaleFactor*(1-(sinc(current)));
attenuation_ideal = -(signal_on - signal_off); %attenuation without
noise

%% Calculate attenuation with noise. Do this multiple times then
calculate the mean + SD
attenuation_noisy=nan(no_of_loops,size(current,2));
for iLoop=1:no_of_loops
    signal_off_noise=abs(signal_off +
stdev_noise*(randn(size(current)))); %add noise to "off" signal and
take magnitude
    signal_on_noise=abs(signal_on +
stdev_noise*(randn(size(current)))); %add noise to "on" signal and
take magnitude
    attenuation_noisy(iLoop,:)=-(signal_on_noise -
signal_off_noise); %attenuation with noise
end
attenuation_noisy_mean=mean(attenuation_noisy,1);
attenuation_noisy_sd=std(attenuation_noisy,1);

%% Display plots

figure(1)
subplot(1,2,1)
plot(current, attenuation_ideal,'k-')
hold on
errorbar(current,attenuation_noisy_mean,attenuation_noisy_sd,'r-')
legend('ideal','with noise','Location','NorthWest');
xlabel('current / A'); ylabel('attenuation');

subplot(1,2,2)
plot(current,attenuation_ideal,'k-
',current,attenuation_noisy_mean,'r-')
legend('ideal','with noise','Location','NorthWest');
xlabel('current / A'); ylabel('attenuation');
```

Appendix 4.1 Data and Error Tables for fMRI Phantom Longitudinal Study

Signal Change

PA Coil

Site	I = 0.1mA	I = 3.0mA	I = 7.5mA	I = 10mA	I = 13.5mA
ED.1	0.06	1.86	4.52	5.79	7.57
ED.2	0.08	1.81	4.54	5.69	7.73
ED.3a	0.08	1.77	4.42	5.92	7.46
ED.3b	0.06	1.81	4.54	5.84	7.83
ED.3c	0.06	1.79	4.43	5.84	7.77
ED.4	0.09	2.03	4.58	6.09	8.16
ED.5	0.04	1.74	4.41	5.63	6.88
ED.7	--	1.79	4.58	6.16	Not Recorded

Table A5.1.1 –Experimental values for |ΔS| across a period of 12 months on the Edinburgh Scanner

I / mA	0.01	0.10	1.50	3.00	7.50	10.0	13.5
|ΔS|	--	--	1.14	1.77	4.30	6.14	8.25

Table A5.1.2 – Values for |ΔS| Experiment ED.8 on the Edinburgh Scanner

I / mA	0.10	3.00	7.50	10.0	13.5
|ΔS|	--	1.89	4.63	6.09	7.49

Table A5.1.3 – Values for |ΔS| Experiment ED.6 on the Edinburgh Scanner

|ΔS| per mA of Current

I / mA	0.10	3.00	7.50	10.0	13.5
ED.1	**0.60**	**0.62**	**0.60**	**0.58**	**0.56**
ED.2	**0.80**	**0.60**	**0.61**	**0.57**	**0.57**
ED.3a	**0.80**	**0.59**	**0.59**	**0.59**	**0.55**
ED.3b	**0.60**	**0.60**	**0.61**	**0.58**	**0.58**
ED.3v	**0.60**	**0.60**	**0.59**	**0.58**	**0.58**
ED.4	**0.90**	**0.68**	**0.61**	**0.61**	**0.60**
ED.5	**0.40**	**0.58**	**0.59**	**0.56**	**0.51**
ED.7		**0.60**	**0.61**	**0.62**	

Table A5.1.4 – Values for |ΔS| per mA of Current

Contrast Response

Site	Response	Standard Error of Fit	PCC	PCC p-value
ED.1	0.57	0.01	0.999	
ED.2	0.57	0.01	0.999	
ED.3a	0.57	<0.01	0.999	
ED.3b	0.59	<0.01	1.000	
ED.3c	0.58	0.01	1.000	
ED.4	0.61	0.01	1.000	<0.0005
ED.5	0.54	0.02	0.995	<0.0005
ED.6	0.58	0.01	0.997	<0.0005
ED.7	0.61	<0.01	1.000	0.003
ED.8	0.61	0.01	0.998	<0.0005

Table A5.1.5 – Data for Response of Scanner in Longitudinal Study

S1NR – ON

I / mA	0.10	3.00	7.50	10.0	13.5
ED.1	96.4	95.1	94.4	93.2	86.0
ED.2	96.0	92.2	89.2	84.1	88.2
ED.3a	77.7	92.2	89.5	85.6	90.4
ED.3b	91.5	90.0	89.2	80.1	81.7
ED.3c	92.9	94.9	80.9	90.6	88.0
ED.4	122	119	117	95.2	113
ED.5	129	43.3	123	120	23.1
ED.7	33.2	26.0	34.1	31.1	Not Recorded

Table. A5.1.6 – Mean SNR Measurements when phantom ON for the Longitudinal Study.

I / mA	0.01	0.10	1.50	3.00	7.50	10.0	13.5
Mean SNR	121	114	123	116	115	120	117

Table. A5.1.7 – Mean SNR Measurements when phantom ON for the Experiment ED.8.

I / mA	0.10	3.00	7.50	10.0	13.5
Mean SNR	--	42.7	41.7	40.4	40.1

Table. A5.1.8 – Mean SNR Measurements when phantom ON for the Experiment ED.6.

S2NR - OFF

I / mA	0.10	3.00	7.50	10.0	13.5
ED.1	96.4	97.0	98.6	98.6	92.5
ED.2	96.0	93.9	93.2	88.9	95.0
ED.3a	77.8	93.9	93.5	90.9	97.1
ED.3b	91.5	91.6	93.2	85.4	88.1
ED.3c	92.9	96.6	84.5	95.9	94.8
ED.4	122	121	122	101	122
ED.5	129	44.0	129	127	24.7
ED.7	33.3	26.5	35.7	33.0	Not Recorded

Table. A5.1.9 – Mean SNR measurements when phantom OFF for the Longitudinal Study.

I / mA	0.01	0.10	1.50	3.00	7.50	10.0	13.5
Mean SNR	121	114	124	118	120	127	126

Table. A5.1.10 – Mean SNR measurements when phantom OFF for the Experiment ED.8.

I / mA	0.10	3.00	7.50	10.0	13.5
Mean SNR	--	43.5	43.6	42.8	43.1

Table. A5.1.11 – Mean SNR measurements when phantom OFF for the Experiment ED.6.

fCNR

I / mA	0.10	3.00	7.50	10.0	13.5
ED.1	0.06	1.77	4.27	5.40	**6.51**
ED.2	0.08	1.67	4.05	**4.78**	6.82
ED.3a	0.07	**1.63**	3.95	5.08	6.74
ED.3b	0.05	1.63	4.06	**4.70**	6.40
ED.3c	0.05	1.70	3.59	5.29	6.84
ED.4	0.11	2.41	5.35	5.80	**9.18**
ED.5	0.05	0.75	5.44	6.76	**1.59**
ED.7	0.08	**0.47**	1.56	1.92	Not Recorded

Table. A5.1.12 – Mean fCNR measurements for the Longitudinal Study.

I / mA	0.01	0.10	1.50	3.00	7.50	10.0	13.5
Mean fCNR	0.10	0.00	1.40	2.05	4.96	7.37	**9.61**

Table. A5.1.13 – Mean fCNR Measurements for the Experiment ED.8.

I / mA	0.10	3.00	7.50	10.0	13.5
Mean fCNR	--	0.81	1.93	2.46	**3.00**

Table. A5.1.14 – Mean fCNR measurements when phantom OFF for the Experiment ED.6.

Error Tables

ED.4

Current / mA	0.1	3	7.5	10	13.5
Error in Sig. Diff.	±2.83E-06	±4.24E-06	±8.60E-06	±2.83E-06	±0.00
Error S1NR	±1.09	±1.06	±1.05	±0.70	±1.02
Error S2NR	±1.09	±1.08	±1.09	±0.74	±1.10
Error CNR	±0.03	±0.04	±0.09	±0.05	±0.09
Error in CNR per mA	±0.27	±0.02	±0.01	±0.00	±0.01

Error values for Experiment ED.4.

ED.5

Current / mA	0.1	3	7.5	10	13.5
Error in Sig. Diff.	±2.82E-06	±1.77E-05	±5.83E-06	±8.06E-06	±2.267E-05
Error S1NR	±1.02	±1.44	±0.98	±0.94	±0.73
Error S2NR	±1.02	±1.47	±1.02	±0.99	±0.78
Error CNR	±0.02	±0.05	±0.06	±0.08	±0.06
Error in CNR per mA	±0.24	±0.02	±0.01	±0.01	±0.00

Error values for Experiment ED.5

.

ED.6

Current / mA	0.1	3	7.5	10	13.5
Error in Sig. Diff.	±2.83E-06	±1.77E-05	±5.83E-06	±8.06E-06	±2.267E-05
Error S1NR	±1.02	±1.44	±0.98	±0.94	±0.73
Error S2NR	±1.02	±1.47	±1.02	±0.99	±0.78
Error CNR	±0.02	±0.05	±0.06	±0.08	±0.06
Error in CNR per mA	±0.24	±0.02	±0.01	±0.01	±0.00

Error values for Experiment ED.6.

ED.7

Current / mA	0.1	3	7.5	10
Error in Sig. Diff.	±11.43	±10.6	±10.6	±9.76
Error S1NR	±0.67	±0.51	±0.69	±0.69
Error S2NR	±0.67	±0.52	±0.73	±0.73
Error CNR		±0.03	±0.05	±0.057
Error in CNR per mA		±0.01	±0.01	±0.01

Error values for Experiment ED.7.

ED.8

Current / mA	0.1	1.5	3	7.5	10	13.5
Error in Sig. Diff.	±2.74	±2.32	±5.33	±1.94	±2.21	±3.91
Error S1NR	±0.82	±0.75	±0.80	±0.73	±0.63	±0.66
Error S2NR	±0.82	±0.75	±0.81	±0.76	±0.67	±0.71
Error CNR		±0.04	±0.08	±0.04	±0.05	±0.08
Error in CNR per mA		±0.02	±0.02	±0.01	±0.01	±0.01

Error values for Experiment ED.8.

Appendix 4.2 Additional Figures for Experiments in Longitudinal Study

SNR

Summary figures for various SNR experimental measurements performed across the Edinburgh Longitudinal Study (Chapter 5).

Exp.	Signal-to-Noise Ratio (SNR)
ED.4	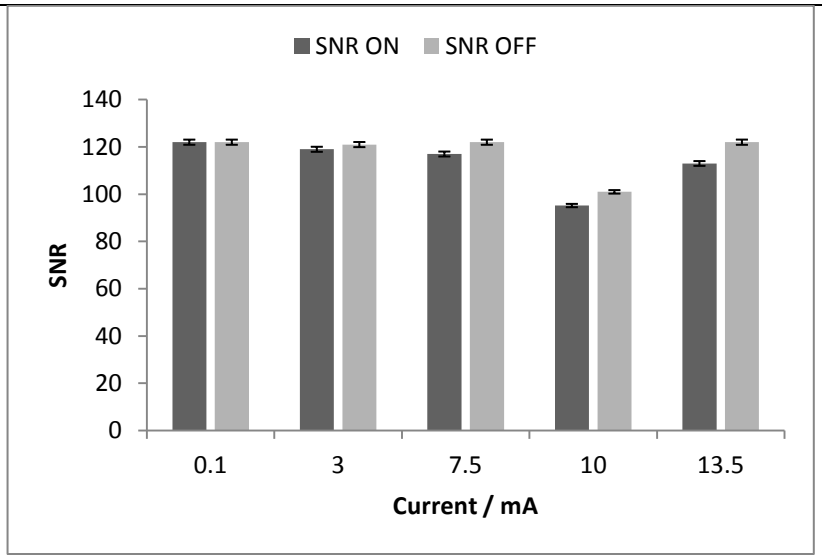
ED.5	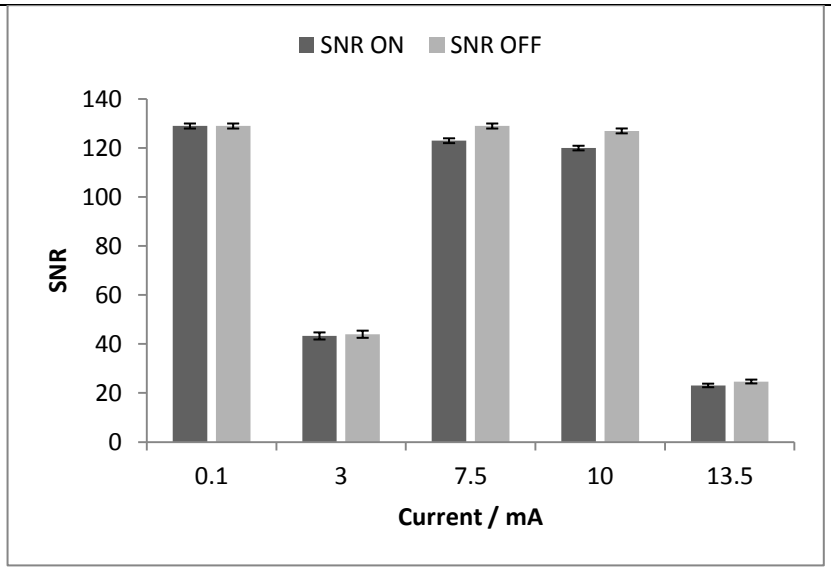

ED.6	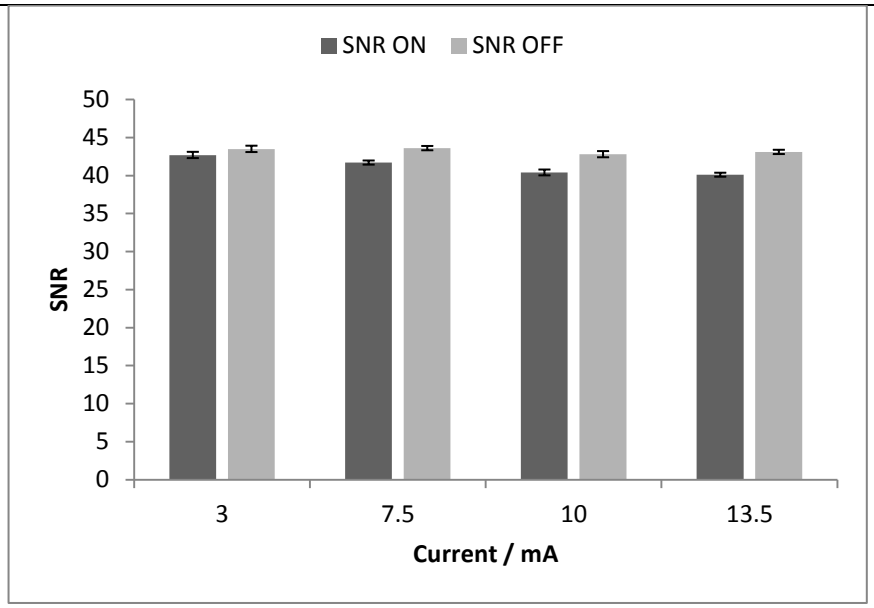 SNR ON SNR OFF SNR 50 45 40 35 30 25 20 15 10 5 0 3 7.5 10 13.5 Current / mA
ED.7	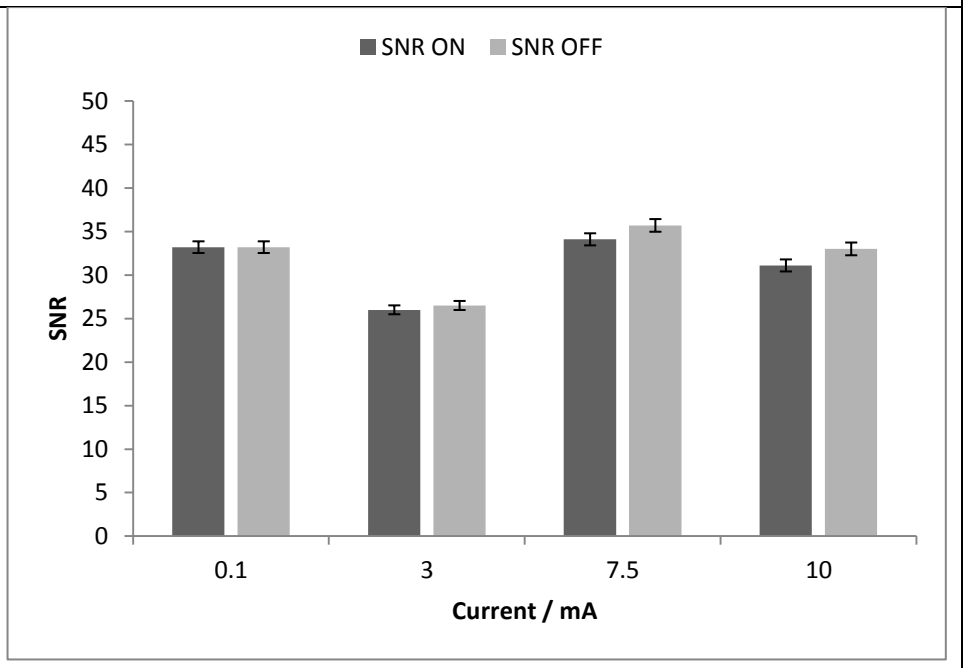 SNR ON SNR OFF SNR 50 45 40 35 30 25 20 15 10 5 0 0.1 3 7.5 10 Current / mA

ED.8	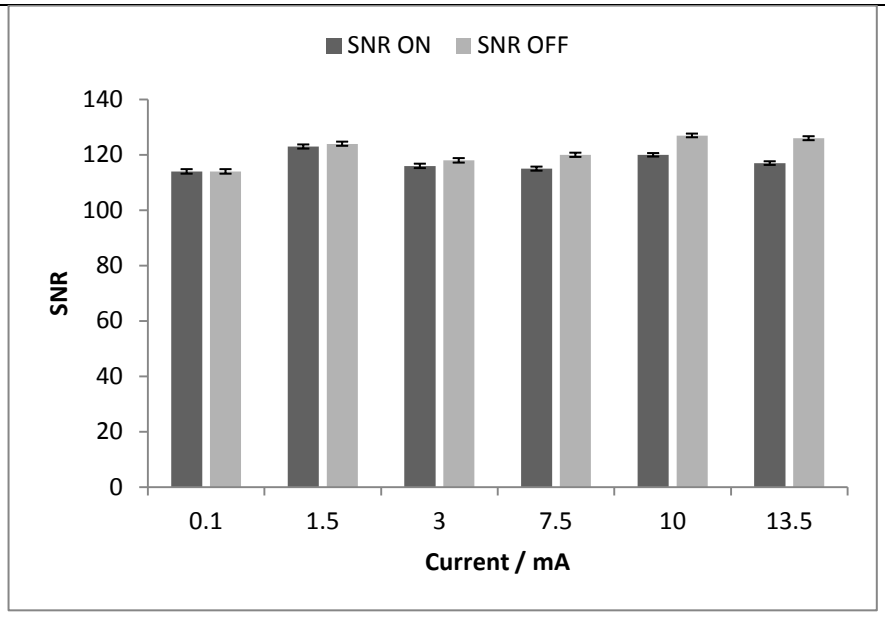
ED.9	No Data

fCNR

Summary figures for various fCNR experimental measurements performed across the Edinburgh Longitudinal Study (Chapter 5).

Exp.	**fCNR**
ED.4	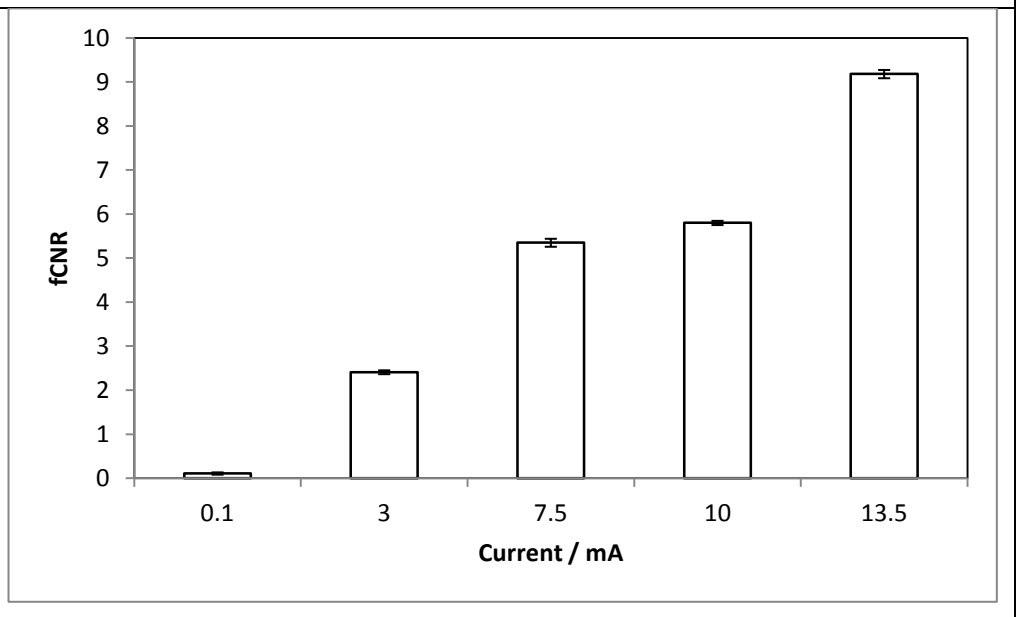

ED.5

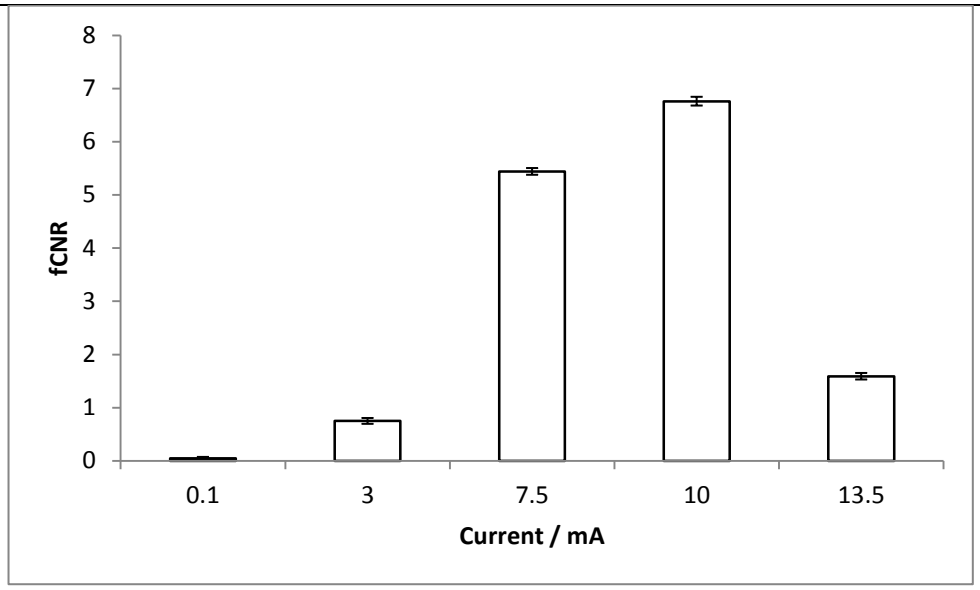
8
7
6
5
4
3
2
1
0
fCNR
0.1
3
7.5
10
13.5
Current / mA

ED.6

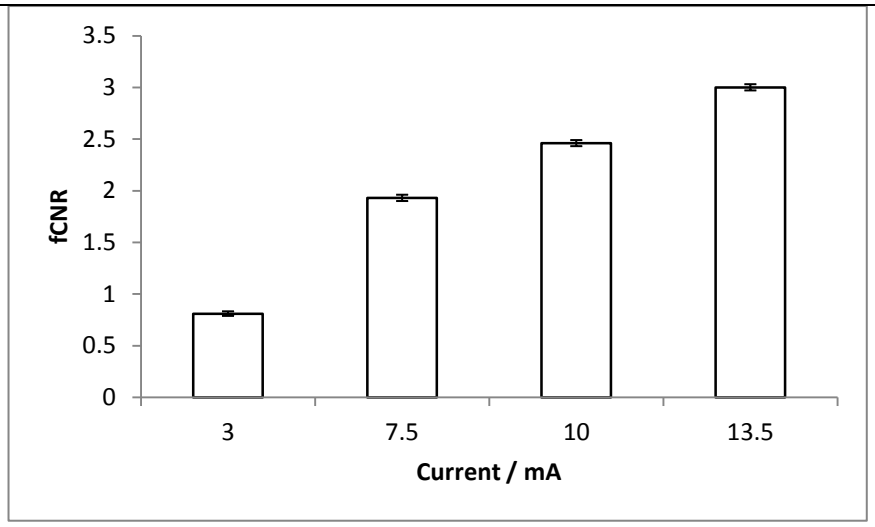
3.5
3
2.5
2
1.5
1
0.5
0
fCNR
3
7.5
10
13.5
Current / mA

ED.7

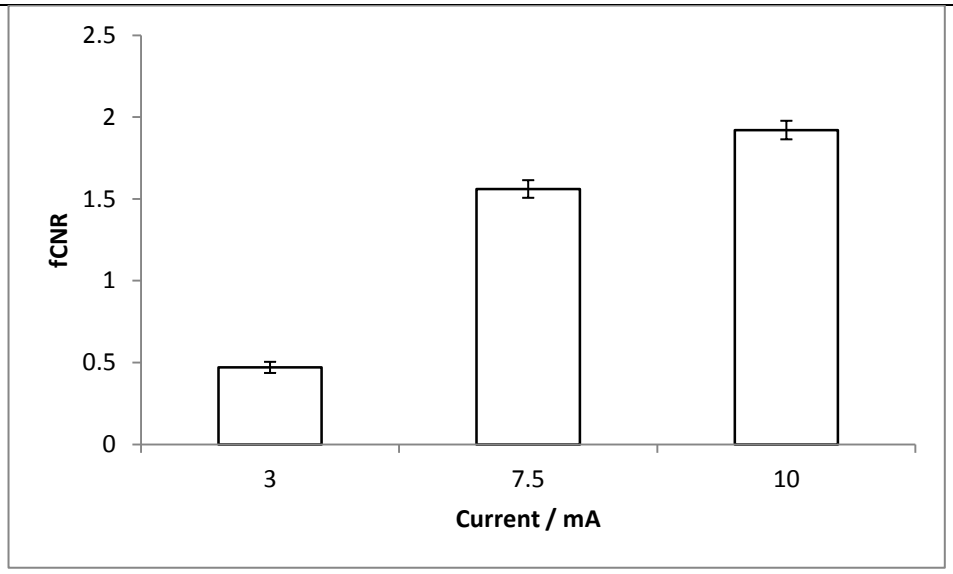
2.5
2
1.5
1
0.5
0
fCNR
3
7.5
10
Current / mA

ED.8	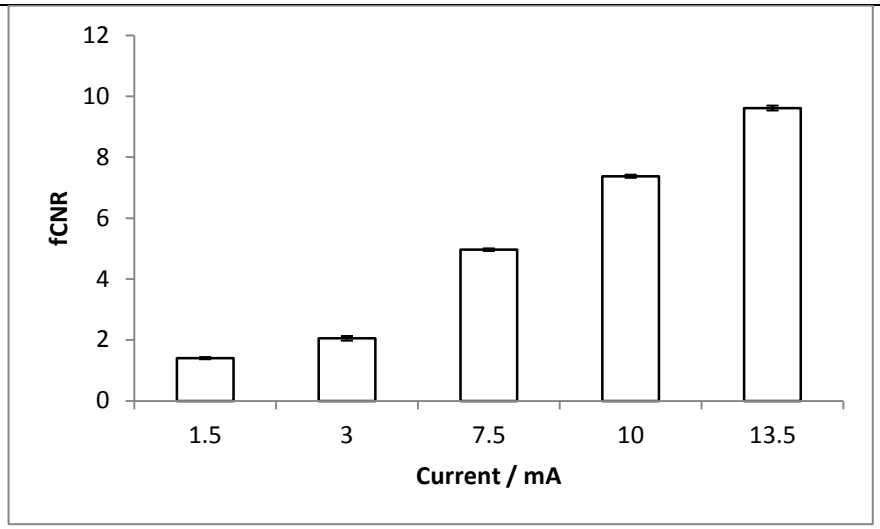
ED.9	

fCNR per mA

Summary figures for various fCNR per unit applied Current experimental measurements performed across the Edinburgh Longitudinal Study (Chapter 5).

Exp.	**fCNR**
ED.4	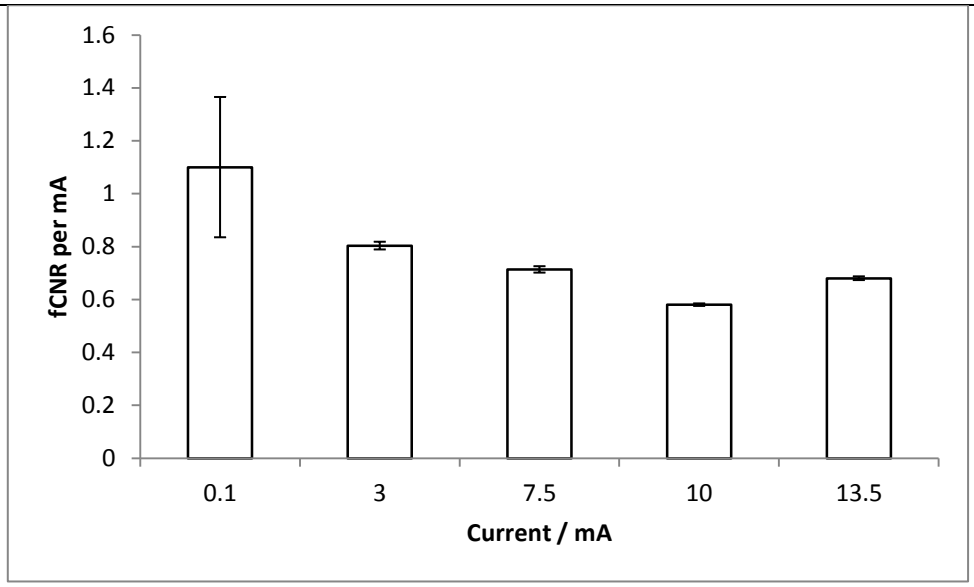

ED.5

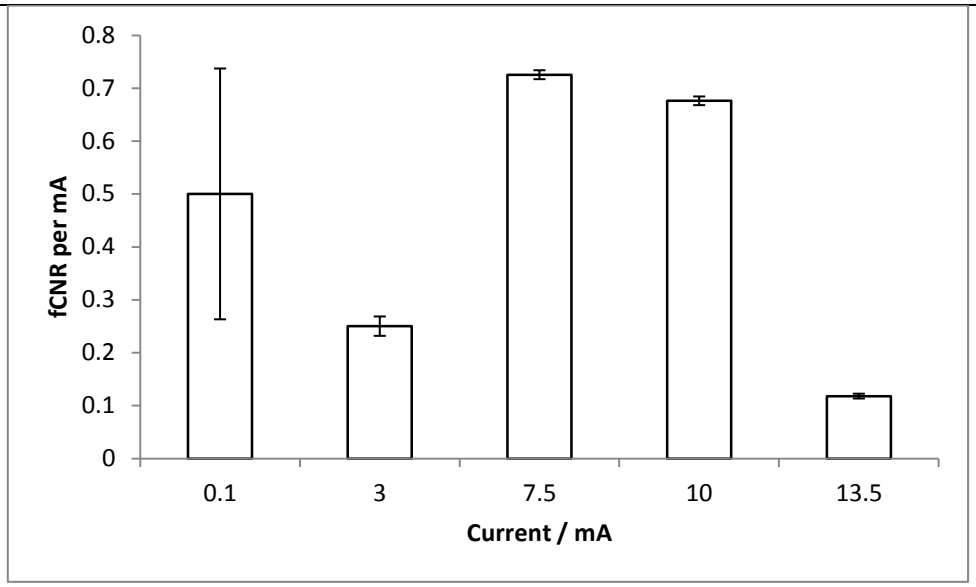
0.8
0.7
0.6
0.5
0.4
0.3
0.2
0.1
0
fCNR per mA
0.1
3
7.5
10
13.5
Current / mA

ED.6

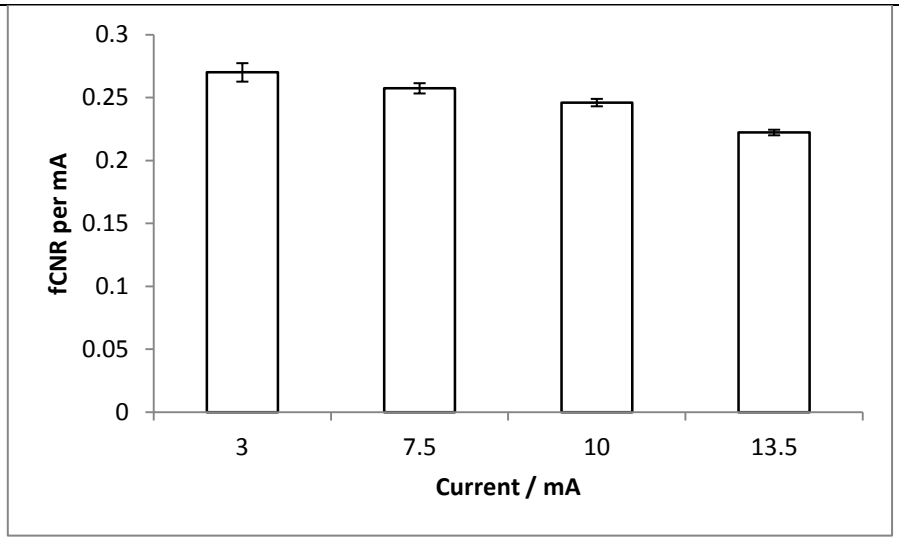
0.3
0.25
0.2
0.15
0.1
0.05
0
fCNR per mA
3
7.5
10
13.5
Current / mA

ED.7

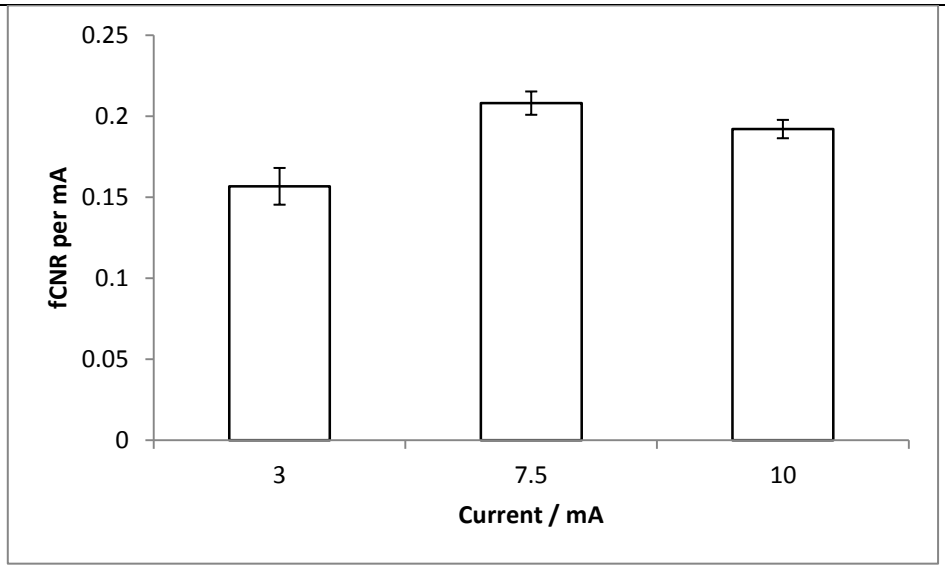
0.25
0.2
0.15
0.1
0.05
0
fCNR per mA
3
7.5
10
Current / mA

ED.8	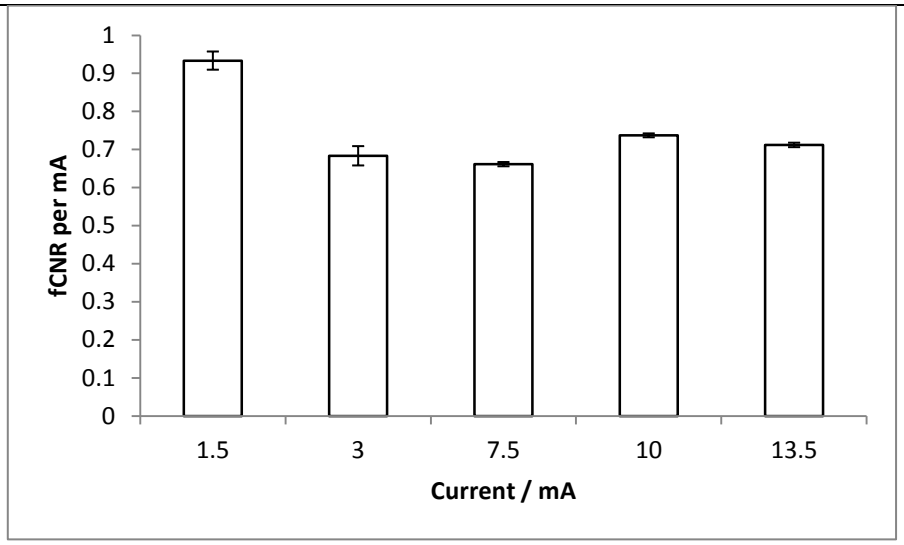
ED.9	No Data.

Appendix 5.1 Data and Error Tables for fMRI Phantom Mulisite Study

Results

Signal Change (%)

Current / mA	0.10	3.00	5.00	7.50	10.0	13.5	14.5
Edinburgh (PA)	0.09	2.03		4.58	6.09	8.16	
Edinburgh (Vol)	--	1.89		4.63	6.09	7.49	
Glasgow	0.35	2.73		4.87	5.43	6.56	
KCL			4.11	4.23	6.17	6.64	8.35
UCL		1.62				8.43	

Table 6.1.1 – Signal Change results (|ΔS|) for the Multisite Snapshot Study

Contrast Response

Site	Response	Standard Error of Fit	PCC	PCC p-value
Edinburgh (PA)	0.61	0.01	1.00	<0.0005
Edinburgh (Vol)	0.58	0.01	1.00	<0.0005
Glasgow	0.54	0.04	0.98	0.004
KCL	0.57	0.04	0.94	0.016
UCL	0.62	0.01	1.00	0.020

Table 6.1.2 – Response data for the Multisite Snapshot Study

SNR – ON

Current / mA	0.10	3.00	5.00	7.50	10.0	13.5	14.5
Edinburgh (PA)	96.4	95.1		94.4	93.2	86.0	
Edinburgh (Vol)	--	42.7		41.7	40.4	40.1	
Glasgow	38.1	39.2		38.8	35.0	30.5	
KCL			14.5	14.9	13.9	13.0	15.5
UCL		73.2				65.3	

Table 6.1.3 – Mean SNR values in the ON state data for the Multisite Snapshot Study

SNR - OFF

Current / mA	0.10	3.00	5.00	7.50	10.0	13.5	14.5
Edinburgh (PA)	122	121		122	101	122	
Edinburgh (Vol)	--	43.5		43.6	42.8	43.1	
Glasgow	38.2	40.3		40.7	36.9	32.5	
KCL			15.1	15.6	14.8	13.9	16.8
UCL		74.4				70.8	

Table 6.1.4 – Mean SNR values in the OFF state for the Multisite Snapshot Study

fCNR

Current / mA	0.10	3.00	5.00	7.50	10.0	13.5	14.5
Edinburgh (PA)	0.11	2.41		5.35	5.80	9.18	
Edinburgh (Vol)	--	0.81		1.93	2.46	3.00	
Glasgow	0.13	1.07		1.89	1.90	2.00	
KCL			0.59	0.63	0.86	0.86	1.30
UCL		1.19				5.50	

Table 6.1.5 – Mean fCNR values for different currents from the Multisite Snapshot Study

fCNR per mA current in phantom

Current / mA	0.10	3.00	5.00	7.50	10.0	13.5	14.5
Edinburgh (PA)	1.1	0.80		0.71	0.58	0.68	
Edinburgh (Vol)		0.27		0.26	0.25	0.22	
Glasgow	1.3	0.36		0.25	0.19	0.15	
KCL			0.12	0.08	0.09	0.06	0.09
UCL		0.40				0.41	

Table 6.1.6 – Mean fCNR per mA of applied current values for different currents from the Multisite Snapshot Study

Error Tables

GL.1

Current / mA	0.1	3	7.5	10	13.5
Error in Sig. Diff.	±3.85	±4.13	±3.76	±3.60	±5.13
Error S1NR	±0.43	±0.40	±0.54	±0.47	±0.32
Error S2NR	±0.43	±0.41	±0.56	±0.50	±0.34
Error CNR	±0.027	±0.03	±0.04	±0.03	±0.04
Error in CNR per mA	±0.28	±0.01	±0.01	±0.00	±0.00

Error Table for Experiments performed on the scanner at the University of Glasgow (Chapter 6.3.2).

KC.1

Current / mA	5.00	7.50	10.0	13.5	14.5
Error in Sig. Diff.	±8.92	±11.1	±8.62	±6.48	±17.7
Error S1NR	±0.13	±0.12	0.14	±0.14	±0.12
Error S2NR	±0.14	±0.13	0.15	±0.15	±0.14
Error CNR	±0.03	±0.04	0.03	±0.02	±0.07
Error in CNR per mA	±0.01	±0.01	0.00	±0.00	±0.00

Error Table for Experiments performed on the scanner at King's College London (Chapter 6.3.3).

UC.1

Current / mA	3.0	13.5
Error in Sig. Diff.	±9.57	±14.5
Error S1NR	±1.09	±1.07
Error S2NR	±1.11	±1.15
Error CNR	±0.12	±0.20
Error in CNR per mA	±0.04	±0.01

Error Table for Experiments performed on the scanner at University College London (Chapter 6.3.4).

References

[Ahrens 2013] Ahrens ET and Bulte JWM. (2013) Tracking immune cells in vivo using magnetic resonance imaging. Nature Reviews Immunology 13, 755–763 doi:10.1038/nri3531

[Axmacher 2009] Axmacher, Nikolai. (2009) The specific contribution of neuroimaging versus neurophysiological data to understanding cognition. Behavioural brain research 200:1 -6

[Ashburner 2012] Ashburner J. (2012) SPM: A history, NeuroImage, Volume 62, Issue 2, ISSN 1053-8119, http://dx.doi.org/10.1016/j.neuroimage.2011.10.025.

[Ashby 2011] Ashby F. G. (2011) Statistical Analysis of fMRI Data, Chapter 5. The MIT Press, Cambridge.

[Belliveau 1991] Belliveau JW, Kennedy DN, McKinstry RC, Buchbinder BR, Weisskoff RM, Cohen MS, Vevea JM, Brady TJ, Rosen BR, (1991). Functional mapping of the human visual cortex by magnetic resonance imaging. Science 254(5032):716-9. pubmed/1948051

[Benveniste 2002] Benveniste H, Blackband S. MR microscopy and high resolution small animal MRI: applications in neuroscience research, Progress in Neurobiology, Volume 67, Issue 5, ISSN 0301-0082, http://dx.doi.org/10.1016/S0301-0082(02)00020-5.

[Bernstein 2004a] Bernstein MA, King FK and Zhou XJ (2004. Handbook of MRI Pulse Sequences, Elsevier Academic Press (London) pp. 726-732

[Bernstein 2004b] Bernstein MA, King FK and Zhou XJ (2004. Handbook of MRI Pulse Sequences, Elsevier Academic Press (London) pp. 351-353

[Bethapudi 2013] Imaging at London 2012 summer Olympic Games: analysis of demand and distribution of workload. Bethapudi S, Budgett R, Engebretsen L, O'Connor P. Br J Sports Med. 2013 Sep;47(13):850-6. doi: 10.1136/bjsports-2013-092345. Epub 2013 Jul 23.

[Bianciardi 2009] Bianciardi M, Fukunaga M, van Gelderen P, Horovitz SG, de Zwart JA, Shmueli K, Duyn JH. (2009) Sources of functional magnetic resonance imaging signal fluctuations in the human brain at rest: a 7 T study. Magn Reson Imaging. 27(8):1019-29. doi: 10.1016/j.mri.2009.02.004.

[Biswal 1995] Biswal B, Yetkin FZ, Haughton VM, Hyde JS. (1995) Functional connectivity in the motor cortex of resting human brain using echo-planar MRI. Magn Reson Med 34:537–541.

[Bodurka 1999] Bodurka J, Jesmanowicz A, Hyde JS, Xu H, Estkowski L, Li SJ. (1999) Current-induced magnetic resonance phase imaging. J Magn Reson.137 (1):265-71.

[Bodurka 2002] Bodurka, J. and Bandettini, P. A. (2002), Toward direct mapping of neuronal activity: MRI detection of ultraweak, transient magnetic field changes. Magn Reson Med, 47: 1052–1058. doi: 10.1002/mrm.10159

[Brett 2002] Brett M., Anton J., Valabregue R. and Poline J. (2002) Region of interest analysis using an SPM toolbox. 8th International Conference on Functional Mapping of the Human Brain, June 2-6, 2002, Sendai, Japan. NeuroImage, Vol 16, No 2.

[Brydges 2012] Brydges NM, Hall L, Nicolson R, Holmes MC, Hall J (2012) The Effects of Juvenile Stress on Anxiety, Cognitive Bias and Decision Making in Adulthood: A Rat Model. PLoS ONE 7(10): e48143. doi:10.1371/journal.pone.0048143

[Brydges 2013] Brydges NM, Whalley HC, Jansen MA, Merrifield GD, Wood ER et al. (2013) Imaging conditioned fear circuitry using awake rodent fMRI. PLoS One ;8 (1): e54197. doi: 10.1371/journal.pone.0054197

[Buxton 2002] Buxton RB (2002). Introduction to Functional Magnetic Resonance Imaging Principles and Techniques, Cambridge University Press, Cambridge pp. 290-294

[Callaghan 2006a] Callaghan PT. (2006) Principles of Nuclear Magnetic Resonance Microcopy, Oxford Science Publications p.93

[Callaghan 2006b] Callaghan PT. (2006) Principles of Nuclear Magnetic Resonance Microcopy, Oxford Science Publications p.94

[Chacko 2000] Chacko VP, Aresta F, Chacko SM and Weiss RG. (2000) MRI/MRS assessment of in vivo murine cardiac metabolism, morphology, and function at physiological heart rates. American Journal of Physiology - Heart and Circulatory Physiology Vol. 279:. H2218-H2224

[Cheng 2006] Cheng H, Zhao Q, Duensing GR, Edelstein WA, Spencer D, Browne N, Saylor C, Limkeman M. (2006) SmartPhantom — an fMRI simulator. Magnetic Resonance Imaging, Volume 24, Issue 3, ISSN 0730-725X, http://dx.doi.org/10.1016/j.mri.2005.12.012.

[Chung 2012] Chung JY., Han Y., Cho Z., and Park H. (2012) A correction method for streak artifacts in gradient-echo EPI using spin-echo EPI reference data. MAGMA 25(3): 205-13 DOI 10.1007/s10334-011-0289-0

[Davies 2005] Nigel P. Davies NP and Jezzard P. (2005) Calibration of Gradient Propagation Delays for Accurate Two-Dimensional Radiofrequency Pulses. Magnetic Resonance in Medicine 53:231–236

[De Martino 2011] De Martino F, Esposito F, van de Moortele PF, Harel N, Formisano E, Goebel R, Ugurbil K, Yacoub E. (2011) Whole brain high-resolution functional imaging at ultra high magnetic fields: an application to the analysis of resting state networks. NeuroImage 57:1031–1044.

[Deane-Drummond 2009] Deane-Drummond CE and Clough D (*Eds*). (2009) Creaturely Theology: On God, Humans and Other Animals. SCM Press, London.

[Deichmann 1992] Deichmann R and Haase A. (1992) Quantification of T1 values by SNAPSHOT-FLASH NMR Imaging. JMR 96: 608-612

[Dichter 2012] Dichter, G. (2012) Functional magnetic resonance imaging of autism spectrum disorders. Dialogues in clinical neuroscience. 14:319-351

[Dobbins 2003] Dobbins RL and Malloy CR. (2003) Measuring in-vivo metabolism using nuclear magnetic resonance. Current Opinion in Clinical Nutrition and Metaboli Care 6(5):501 PMID 12913667

[Edelstein 1986] Edelstein WA, Glover GH, Hardy CJ and Redington, RW. (1986) The Intrinsic Signal-to-Noise Ratio in NMR Imaging. Magnetic Resonance in Medicine 3:604-6I8

[Fain 2007] Fain, SB., Korosec, FR., Holmes, JH., O'Halloran, R., Sorkness, RL. and Grist, TM. (2007), Functional lung imaging using hyperpolarized gas MRI. J. Magn. Reson. Imaging, 25: 910–923. doi: 10.1002/jmri.20876

[Ferris 2006] Ferris, C.F., M. Febo, F. Luo, K Schmidt, M. Brevard, P Kulkarni, T. Messenger, J. Harder, J.A. King. (2006) Functional magnetic resonance imaging in conscious animals: A new tool in behavior neuroscience research Journal of Neuroendocrinology 18:307-318.

[Fox 2012] Fox PT, The coupling controversy, NeuroImage, Volume 62, Issue 2, ISSN 1053-8119, http://dx.doi.org/10.1016/j.neuroimage.2012.01.103.

[Friedman 2006] Friedman, L. and Glover, G. H. (2006), Report on a multicenter fMRI quality assurance protocol. J. Magn. Reson. Imaging, 23: 827–839. doi: 10.1002/jmri.20583

[Friedman 2008] Friedman L, Stern H, Brown GG, Mathalon DH, Turner J, Glover GH, et al., (2008) Test–retest and between-site reliability in a multicenter fMRI study. Hum. Brain Mapp. 29, 958–972.

[Friston 2007] Friston KJ, Ashburner JT, Kiebel SJ, Nichols TE, Penny, WD, 2007. Statistical Parametric Mapping: the Analysis of Functional Brain Images. Elsevier/Academic Press.

[Fu 2008] Fu, CHY, Williams, SCR, Cleare, AJ, Scott, J, Mitterschiffthaler, MT, Walsh, ND, Donaldson, C, Suckling, J, Andrew, C, Steiner, H & Murray, RM. 2008 Neural responses to sad facial expressions in major depression following cognitive behavioral therapy. Biological Psychiatry, 64: 505 - 512.

[Gadian 1985] Gadian DG. (1985) NMR and its Applications to Living Systems, Oxford University Press, pp. 147.

[Geissler 2007] Geissler, A., Gartus, A., Foki, T., Tahamtan, A. R., Beisteiner, R. and Barth, M. (2007), Contrast-to-noise ratio (CNR) as a quality parameter in fMRI. J. Magn. Reson. Imaging, 25: 1263–1270. doi: 10.1002/jmri.20935

[Gradin 2010] Gradin V, Gountouna V-E, Waiter G, Ahearn TS, Brennan D, Condon B, et al. (2010) Between- and within-scanner variability in the CaliBrain study n-back cognitive task. Psychiatry Res. 184, 86–95.

[Griffiths 1999] Griffiths DJ, Introduction to Electrodynamics, Prentice Hall (1999), pp. 215

[Gudbjartsson 1995] Gudbjartsson H and Patz S. (1995) The Rician Distribution of Noisy MRI Data. Magn Reson Med. 1995 December ; 34(6): 910–914.

[Guilfoyle 2006] Guilfoyle DN and Hrabe J (2006), Interleaved snapshot echo planar imaging of mouse brain at 7.0T, NMR in Biomedicine 2006; 19:108-115

[Guilfoyle 2013] Guilfoyle DN, Gerum SV, Sanchez JL, Balla A, Sershen H, Javitt DC, Hoptman MJ. (2013) Functional connectivity fMRI in mouse brain at 7T using isoflurane. J Neurosci Methods. 2013 Apr 15;214(2):144-8. doi: 10.1016/j.jneumeth.2013.01.019.

[Hamilton 2011] Hamilton, D. R., Sargsyan, A. E., Martin, D. S., Garcia, K. M., Melton, S. L., Feiveson, A. and Dulchavsky, S. A. (2011), On-Orbit Prospective Echocardiography on International Space Station Crew. Echocardiography, 28: 491–501. doi: 10.1111/j.1540-8175.2011.01385.x

[Hamilton 2012] Hamilton, DR. et al. (2012) Cardiac and vascular responses to thigh cuffs and respiratory manoeuvres on crewmembers of the International Space Station. Journal of applied physiology [8750-7587] vol:112 iss:3 pg:454 -62

[Hampel 2011] Hampel, Harald. (2011) Recent developments of functional magnetic resonance imaging research for drug development in Alzheimer's disease. Progress in Neurobiology 95: 570-578.

[Hatada 2005] Hatada T, Sekino M, Ueno S. Finite element method-based calculation of the theoretical limit of sensitivity for detecting weak magnetic fields in the human brain using magnetic-resonance imaging. Journal of Applied Physics, vol.97, no.10, doi: 10.1063/1.1861553

[Heller 2006] Heller R, Stanley D, Yekutieli D, Rubin N, Benjamini Y. (2006) Cluster-based analysis of FMRI data, NeuroImage, Volume 33, Issue 2. ISSN 1053-8119, http://dx.doi.org/10.1016/j.neuroimage.2006.04.233.

[Horikawa 2013] T. Horikawa, M. Tamaki, Y. Miyawaki, Y. Kamitani. (2013) Neural Decoding of Visual Imagery During Sleep. Science 340 (6132), 639-642 DOI:10.1126/science.1234330

[Huang 2013] Huang J. (2013) Detecting neuronal currents with MRI: A human study. Magn Reson Med. 2013 Mar 8. doi: 10.1002/mrm.24720.

[Hutton 2011] Hutton C, Josephs O, Stadler J, Featherstone E, Reid A, Speck O, Bernarding J, Weiskopf N. (2011) The impact of physiological noise correction on fMRI at 7T, NeuroImage, Volume 57, Issue 1. ISSN 1053-8119, http://dx.doi.org/10.1016/j.neuroimage.2011.04.018.

[Iacovella 2011] Iacovella V, Hasson U. (2011) The relationship between BOLD signal and autonomic nervous system functions: implications for processing of “physiological noise”, Magnetic Resonance Imaging, Volume 29, Issue 10, ISSN 0730-725X, http://dx.doi.org/10.1016/j.mri.2011.03.006.

[Jackson 2011] Jackson, SJ, Hussey, R, Jansen, MA, Merrifield, GD, Marshall, I, MacLullich, A, Yau, JLW & Bast, T. 2011, 'Manganese-enhanced magnetic resonance imaging (MEMRI) of rat brain after systemic administration of MnCl(2):: Hippocampal signal enhancement without disruption of hippocampus-dependent behavior' Behavioural Brain Research, vol 216, no. 1, pp. 293-300.

[Jaffer 2012] U. Jaffer, M. Aslam, V. Kasivisvanathan, R. Patni, M. Midwinter, N. Standfield, Evaluation of rapid training in ultrasound guided tourniquet application skills, International Journal of Surgery, Volume 10, Issue 9, 2012, Pages 563-567, ISSN 1743-9191, http://dx.doi.org/10.1016/j.ijsu.2012.08.019.

[Jansen 2004] Assessment of myocardial viability by intracellular 23Na magnetic resonance imaging. Circulation 11/2004; 110(22):3457-64. Maurits A Jansen, Jan G Van Emous, Marcel G J Nederhoff, Cees J A Van Echteld

[Jenkinson 2012] Jenkinson M, Beckmann CF, Behrens TE, Woolrich MW, Smith SM. FSL. NeuroImage, 62:782-90, 2012

[Jiang 2013] Jiang, X., Lu, H., Shigeno, S., Tan, L.-H., Yang, Y., Ragsdale, C. W. and Gao, J.-H. (2013), Octopus visual system: A functional MRI model for detecting neuronal electric currents without a blood-oxygen-level-dependent confound. Magn Reson Med. doi: 10.1002/mrm.25051

[Johnson 1999] Johnson G, Wadghiri YZ, Turnbull DH (1999). 2D Multislice and 3D MRI sequences are often equally sensitive. Magn. Reson. Med. 41: 824-828

[Kannurpatti 2003] Kannurpatti, S. S., Biswal, B. B. and Hudetz, A.G. (2003), Regional dynamics of the fMRI-BOLD signal response to hypoxia-hypercapnia in the rat brain. J. Magn. Reson. Imaging, 17: 641–647. doi: 10.1002/jmri.10311

[Kida 2011] Kida I, Iguchi Y, Hoshi Y. (2011) Blood oxygenation level-dependent functional magnetic resonance imaging of bilateral but asymmetrical responses to gustatory stimulation in the rat insular cortex, NeuroImage, Volume 56, Issue 3, 1 ISSN 1053-8119, http://dx.doi.org/10.1016/j.neuroimage.2011.03.007.

[Kilkenny 2010] Kilkenny C, Browne WJ, Cuthill IC, Emerson M, Altman DG (2010) Improving Bioscience Research Reporting: The ARRIVE Guidelines for Reporting Animal Research. PLoS Biol 8(6): e1000412. doi:10.1371/journal.pbio.1000412

[Lazar 2008] Lazar NA. (2008) The Statistical Analysis of Functional MRI Data (Chapter 5), Springer, New York.

[Lewin 2002] Lewin, W. 8.02 Electricity and Magnetism, Spring 2002. (MIT OpenCourseWare: Massachusetts Institute of Technology), http://ocw.mit.edu/courses/physics/8-02-electricity-and-magnetism-spring-2002 (Accessed 10 Dec, 2013). License: Creative Commons BY-NC-SA

[Loggia 2012] Marco L. Loggia, Robert R. Edwards, Jieun Kim, Mark G. Vangel, Ajay D. Wasan, Randy L. Gollub, Richard E. Harris, Kyungmo Park, Vitaly Napadow. (2012) Disentangling linear and nonlinear brain responses to evoked deep tissue pain. Pain 153: 2140-2151 DOI: 10.1016/j.pain.2012.07.014

[Lowe 2007] Lowe, AS, Beech, JS & Williams, S. (2007), 'Small animal, whole brain fMRI: innocuous and nociceptive forepaw stimulation' NeuroImage, vol 35, no. 2, pp. 719 - 728.

[Magnotta 2006] Magnotta VA, Friedman L; FIRST BIRN. (2006) Measurement of Signal-to-Noise and Contrast-to-Noise in the fBIRN Multicenter Imaging Study. J Digit Imaging. 2006 Jun;19(2):140-7.

[Mansfield 1977] Mansfield P. (1977) Multi-planar image formation using NMR spin echoes. Journal of Physics C: Solid State Physics 10:L55–L58

[Marshall 1998] Marshall I. (1998) Pulse Sequences for Steady-State Saturation of Flowing Spins. Journal of Magnetic Resonance Volume 133, Issue 1, Pages 13–20

[McGonigle 2012] McGonigle DJ. (2012) Test–retest reliability in fMRI: Or how I learned to stop worrying and love the variability, NeuroImage, Volume 62, Issue 2, ISSN 1053-8119, http://dx.doi.org/10.1016/j.neuroimage.2012.01.023.

[Merrifield 2013a] Merrifield GD, Mullin J, Gallagher L and Holmes WM. (2013) In vivo High-Field Magnetic Resonance of Spiders. Proc. Intl. Soc. Mag. Reson. Med. 21.

[Merrifield 2013b] Merrifield GD, Mullin J, Tucker CS, Denvir MA and Holmes WM. (2013) Development of Cardiac MRI for Studying Zebrafish Models of Cardiovascular Disease. Proc. Intl. Soc. Mag. Reson. Med. 21

[Mezer 2009] Mezer A, Yovel Y, Pasternak O, Gorfine T, Assaf Y. (2009) Cluster analysis of resting-state fMRI time series. Neuroimage 45(4):1117-25. doi:10.1016/j.neuroimage.2008.12.015.

[Min 2011] Gastric distention induced functional magnetic resonance signal changes in the rodent brain. (2011) Min DK, Tuor UI, Chelikani PK. Neuroscience 179:151–158

[Mitterschiffthaler 2006] Mitterschiffthaler MT, Ettinger U, Mehta MA, Mataix-Cols D and Williams S. (2006) Applications of functional magnetic resonance imaging in psychiatry. Journal of Magnetic Resonance Imaging 23: 851-861.

[Murphy 2007] Murphy K, Bodurka J, Bandettini PA. (2007) How long to scan? The relationship between fMRI temporal signal to noise ratio and necessary scan duration, NeuroImage, 34 (2) 15: 565-574, http://dx.doi.org/10.1016/j.neuroimage.2006.09.032.

[Nagal 1974] Nagal T. (1974) What Is It Like to Be a Bat? The Philosophical Review , Vol. 83, No. 4, pp. 435-450

[Nobel Prize 2003] "The Nobel Prize in Physiology or Medicine for 2003 - Press Release". Nobelprize.org. Nobel Media AB 2013. Web. 21 Oct 2013. <http://www.nobelprize.org/nobel_prizes/medicine/laureates/2003/press.html>

[Ordidge 1999] Ordidge R. (1999) The development of echo-planar imaging (EPI): 1977-1982. Magnetic Resonance Materials in Physics, Biology and Medicine 9 (1999) 117-121

[Olsrud 2008] Olsrud J, Nilsson A, Mannfolk P, Waites A, Ståhlberg F. (2008) A two-compartment gel phantom for optimization and quality assurance in clinical BOLD fMRI, Magnetic Resonance Imaging, 26 (2) 2, http://dx.doi.org/10.1016/j.mri.2007.06.010.

[Park 2006] Park TS, Lee SY, Park JH, Cho MH and Lee SY. (2006) Observation of the fast response of a magnetic resonance signal to neuronal activity: a snail ganglia study. Physiol. Meas. 27 181 doi:10.1088/0967-3334/27/2/008

[Petersen 2006] Non-invasive measurement of perfusion: a critical review of arterial spin labelling techniques, E T PETERSEN, MSc, I ZIMINE, PhD, Y-C L HO, MSc and X GOLAY, PhD, The British Journal of Radiology, 79 (2006), 688–701

[Peetersa 2001] R.R. Peetersa, I. Tindemansa, E. De Schutterb, A. Van der Lindena. (2001) Comparing BOLD fMRI signal changes in the awake and anesthetized rat during electrical forepaw stimulation. Magnetic Resonance Imaging 19: 821–826

[Pessoa 2002] Pessoa L, Gutierrez E, Bandettini PA, Ungerleider LG. (2002) Neural Correlates of Visual Working Memory: fMRI Amplitude Predicts Task Performance, Neuron, Volume 35, Issue 5, 29 ISSN 0896-6273, http://dx.doi.org/10.1016/S0896-6273(02)00817-6.

[Petersen 2006] Petersen ET, Zimine I, Ho YC, Golay X. Non-invasive measurement of perfusion: a critical review of arterial spin labelling techniques. Br J Radiol. 79 (944): 688-701.

[Poldrack 2008] Poldrack RA., Fletcher PC., Henson RN, Worsley KJ., Brett M. et al.. (2008) Guidelines for reporting an fMRI study. NeuroImage 40: 409-414. doi: 10.1016/j.neuroimage.2007.11.048

[Rawlinson 1941] Rawlinson WA. (1941) The effect of oxidizing agents on haemocyanin. Australian Journal of Experimental Biology and Medical Science 19, 137–141; doi:10.1038/icb.1941.22

[Ray 2012] The neurobiology and neural circuitry of cognitive changes in Parkinson's disease revealed by functional neuroimaging. (2012) Ray NJ, Strafella AP. Movement Disorders 27: 1484-1492 DOI: 10.1002/mds.25173

[Reichert 2005] Reichert IL, Robson MD, Gatehouse PD, He T, Chappell KE, Holmes J, Girgis S, Bydder GM. (2005) Magnetic resonance imaging of cortical bone with ultrashort TE pulse sequences. Magn Reson Imaging. 23 (5): 611-8.

[Renvall 2006] Ville R., Raimo J., and Riitta H. (2006). Functional phantom for fMRI: a feasibility study. Magnetic Resonance Imaging 24 (3): 315-320

[Renvall 2009a] Renvall V. (2009) Functional magnetic resonance imaging reference phantom. Magnetic Resonance Imaging 27: 701–708. doi:10.1016/j.mri.2008.11.007

[Renvall 2009b] Renvall V. and Hari R. (2009) Transients may occur in functional magnetic resonance imaging without physiological basis. PNAS 106: (48) 20510-20514 doi:10.1073/pnas.0911265106

[Renvall 2010] Renvall V. (2010) Studying Functional Magnetic Resonance Imaging with Artificial Imaging Objects. Aalto University. http://lib.tkk.fi/Diss/2010/isbn9789526030814/

[Sargsyan 2006] Sargsyan, AE, Dulchavsky SA, Jones JA, Hamilton DR, Roden SK, Melton SL, Martin D, Garcia K, and Duncan JM. (2006) Abdominal imaging with ultrasound on the International Space Station. Aviation Space and Environmental Medicine 77, no. 3 248.

[Schröder 2011] Schröder L. and Faber C. (*eds*). (2011) In Vivo NMR Imaging Methods and Protocols, Human Press, e-ISSN 1940-6029

[Sekino 2009] Sekino M. Ohsaki H. Yamaguchi-Sekino S. Ueno S. (2009) "Toward Detection of Transient Changes in Magnetic-Resonance Signal Intensity Arising From Neuronal Electrical Activities," *IEEE Transactions on Magnetics*, vol.45, no.10, doi: 10.1109/TMAG.2009.2022954

[Steward 2005] Steward CA, Marsden CA, Prior MJW, Morris PG and Shah YB. (2005) Methodological considerations in rat brain BOLD contrast pharmacological MRI. Psychopharmacology 180: 687–704 DOI 10.1007/s00213-005-2213-7

[Storey 2006] Storey N, Electronics a Systems Approach, 3rd Edition (2006) pp.16. Pearson Education Limited, Harlow, England.

[van Beek 2004] van Beek, EJR., Wild, JM, Kauczor, H.-U., Schreiber, W., Mugler, JP. and de Lange, EE. (2004), Functional MRI of the lung using hyperpolarized 3-helium gas. J. Magn. Reson. Imaging, 20: 540–554. doi: 10.1002/jmri.20154

[van Zijl 1994] van Zijl et al, (1994). Optimised Shimming for High-Resolution NMR Using Three-Dimensional Image-Based Field Mapping. J. Mag. Res. Series A 111: 203-207

[White 2011] White BR, Bauer AQ, Snyder AZ, Schlaggar BL, Lee J-M, et al. (2011) Imaging of Functional Connectivity in the Mouse Brain. PLoS ONE 6(1): e16322. doi:10.1371/journal.pone.0016322

[Xia 2013] Xia J. (2013) Neuronal Current MRI in the Octopus Visual System, ,Proc. Intl. Soc. Mag. Reson. Med. 21

[Xiong 2003] Xiong, J., Fox, P. T. and Gao, J.-H. (2003), Directly mapping magnetic field effects of neuronal activity by magnetic resonance imaging. Hum. Brain Mapp., 20: 41–49. doi: 10.1002/hbm.10124

[Xu F 2010] XuF, Uh J, Brier MR, Hart Jr J, Yezhuvath US, Gu Hong, Yang Y and Lu H. (2010) The influence of carbon dioxide on brain activity and metabolism in conscious

humans. Journal of Cerebral Blood Flow & Metabolism 31, 58–67; doi:10.1038/jcbfm.2010.153

[Xu 2012] Xu F, Liu P, Pascual JM, Xiao G, Lu H. (2012) Effect of hypoxia and hyperoxia on cerebral blood flow, blood oxygenation, and oxidative metabolism. J Cereb Blood Flow Metab. 2012 Oct;32(10):1909-18. doi: 10.1038/jcbfm.2012.93.

[Zhakor, 1991] Zhakor A. Weisskoff R. and Rzedzian R (1991). Optimal Sampling and Reconstruction of MRI signals resulting from sinusoidal gradients. IEEE Trans. Signal Proc. 39: 2056-2065

[Zheng 2010] Zheng ZZ, Munhall KG, and Johnsrude IS. (2010) Functional Overlap between Regions Involved in Speech Perception and in Monitoring One's Own Voice during Speech Production. Journal of Cognitive Neuroscience, Vol. 22, No. 8.